

---

# Galaxy Populations in Galaxy Clusters Selected by the Sunyaev-Zeldovich Effect

Alfredo Andrés Zenteno Vivanco

---





---

# Galaxy Populations in Galaxy Clusters Selected by the Sunyaev-Zeldovich Effect

Alfredo Andrés Zenteno Vivanco

---

Dissertation an der Fakultät für Physik  
Dissertation at the Faculty of Physics

der Ludwig-Maximilians-Universität München  
of the Ludwig Maximilian University of Munich

für den Grad des  
for the degree of

Doctor rerum naturalium

vorgelegt von Alfredo Andrés Zenteno Vivanco  
presented by Alfredo Andrés Zenteno Vivanco

aus Concepción, Chile  
from Concepción, Chile

München, den 09.12.2013





1<sup>st</sup> Evaluator: Prof. Dr. Joseph Mohr

2<sup>nd</sup> Evaluator: Prof. Dr. Andreas Burkert

Date of the oral exam: 24.02.2014



*To the memory of Crystal Marie Brasseur*



# Zusammenfassung

Wir präsentieren eine Studie über die Galaxienpopulation in massereichen Galaxienhaufen, ausgewählt aufgrund ihrer Signatur im Sunyaev–Zel’dovich Effekt (SZE). Die Auswahl mittels des SZE ist annähernd massenlimitiert, d.h. das untere detektierbare Massenlimit variiert nur geringfügig mit der Rotverschiebung, wodurch der SZE eine ideale Auswahlmethode für ein Studium der Entwicklung von Galaxien innerhalb einer Haufenumgebung ist. Wir beginnen diese Arbeit mit einer Einführung in den SZE, einer Vorstellung des Südpolteleskops (SPT) mittels dessen der SZE gemessen werden kann, sowie des Forschungsprojekts, innerhalb dessen diese Arbeit entstanden ist. Im Folgenden präsentieren wir dann die Studien zur Galaxienpopulation, die der Kern dieser Doktorarbeit sind.

In Kapitel 3 präsentieren wir die erste großskalige Folgestudie eines mittels des SZE ausgewählten Galaxienhaufen–Samples. Von 224 Galaxienhaufen–Kandidaten des Samples werden 158 Haufen durch Beobachtungen im Optischen bestätigt und deren photometrische Rotverschiebungen bestimmt. Wir finden eine Rotverschiebungsspanne von  $0.1 \lesssim z \lesssim 1.35$ , was unsere Erwartung, daß Samples, die aus dem SZE–Signal selektiert wurden, ein großes Rotverschiebungsintervall abdecken, bestätigt. Ein Vergleich zwischen der Signifikanz  $\xi$  der Haufenselektion auf Basis der SZE–Detektion und der Reinheit des Samples demonstriert, daß das SPT eine sehr saubere SZE–Auswahl liefert: Die Bestätigungsrate des Samples beträgt 70% bei  $\xi > 4.5$  und erreicht 100% bei  $\xi > 6$ . In 146 Haufen identifizieren wir die roten hellsten Haufengalaxien (red Brightest Cluster Galaxies, rBCGs) mittels der red-sequence–Technik. Wir vergleichen in unseren Haufen die räumliche Verteilung der rBCGs im Bezug zum SZE–Haufenschwerpunkt mit der Verteilung eines anhand von Röntgenstrahlung ausgewählten Samples. Wenn die Methode zur Identifizierung der rBCGs ähnlich ist, stellt sich heraus, daß auch die Verteilung der rBCGs beider Samples identisch ist. Da die rBCG–Verteilung durch Verschmelzung von Galaxien in der Haufenpopulation beeinflusst wird, bedeutet dies, daß Samples beider Auswahlmethoden (SZE und Röntgen) ähnliche Indizien für kontinuierliche Akkretion liefern.

Anschließend analysieren wir die optischen Eigenschaften der ersten vier SZE–ausgewählten Haufen im Detail. Diese Haufen sind in einem für das gesamte SPT–Sample repräsentativen Rotverschiebungsintervall verteilt. Für jeden Haufen verwenden wir aus Röntgenbeobachtungen gewonnene Massenabschätzungen und spektroskopische Rotverschiebungen, um die projizierten Virialradien zu bestimmen. Wir finden Navarro–Frenk–White (NFW) Dichteprofile, die mit den Galaxienverteilungen kompatibel sind, und ermitteln Konzentrationsparameter ähnlich derer röntgenausgewählter Haufen. Des Weiteren studieren wir die Leuchtkraftfunktionen (LFs) der Haufen und vergleichen ihre charakteristischen Helligkeiten in jedem *griz*–Filter mit einem einfachen Sternenpopulationsmodell (Simple Stellar Population, SSP) und stellen deren Übereinstimmung fest. Um die Steigung  $\alpha$  am schwachen Ende der Leuchtkraftfunktion besser bestimmen zu können, nutzen wir die Voraussagen des SSP–Modells für die charakteristische Leuchtkraft als Funktion von Wellenlängenband und Rotverschiebung, und fitten eine Schechter–Funktion an die individuellen Leuchtkraftfunktionen der Haufen. Die Ergebnisse ergeben Werte für  $\alpha$ , die konsistent sind mit den Werten, die in Studien publiziert wurden, welche auf Haufen basieren, die rein optisch oder anhand ihrer Röntgenstrahlung identifiziert wurden. Weiterhin bestimmen wir den Anteil blauer Galaxien innerhalb der

Virialregion jedes Haufens und finden, daß Haufen bei sehr hohen Rotverschiebungen reicher an blauen Galaxien sind als ihre Gegenstücke bei niedrigen Rotverschiebungen. Die Fehler in diesen Messungen sind jedoch groß genug um auch kompatibel zu sein mit einem Szenario, in dem sich der Anteil der blauen Galaxien nicht mit der Rotverschiebung entwickelt. Dieser Trend wird auch in anderen optischen Studien gefunden. Zusammenfassend zeigt unsere Pilotstudie, daß Galaxienverteilungen in SZE–ausgewählten Haufen sich nicht von den Verteilungen in durch andere Kriterien ausgewählten Haufen unterscheiden.

In Kapitel 5 präsentieren wir eine systematische Studie der Entwicklung der Galaxienpopulation in den 26 massereichsten SZE–ausgewählten Haufen aus dem  $2500 \text{ deg}^2$  Beobachtungsbereich des SPT. Wir erzeugen SSP–Modelle für jede Kombination von Teleskop und Filter aus den optischen Folgebeobachtungen. Wir kombinieren die radialen Profile einerseits unter Verwendung aller Galaxien innerhalb der Virialradien sowie unter ausschließlicher Verwendung der roten Galaxien und finden, daß die Verteilung der roten Galaxien geringfügig konzentrierter ist als die Verteilung unter Berücksichtigung aller Galaxien. Weiterhin kombinieren wir auch die Leuchtkraftfunktionen aller Galaxien und fitten eine Schechter–Funktion an das Ergebnis. Die resultierenden Werte für die charakteristischen Leuchtkräfte  $m^*$ , für die Galaxiendichte  $\phi^*$  bei ebendieser  $m^*$ , sowie für  $\alpha$  sind konsistent mit den Literaturwerten. Des Weiteren studieren wir die Entwicklung der Galaxienpopulation im Detail und finden, daß die Entwicklung von  $m^*$  mit der Rotverschiebung in guter Übereinstimmung mit sich passiv entwickelnden SSP–Modellen ist. Wenn  $m^*$  an das SSP–Modell gekoppelt wird, zeigt ein Fit an die Leuchtkraftfunktion keinen Trend in  $\phi^*$  und einen  $2\sigma$ –Trend in  $\alpha$ , wobei Haufen bei hoher Rotverschiebung ein flacheres  $\alpha$  besitzen. Mit allen Parametern der Leuchtkraftfunktion zur Verfügung können wir die Halobesetzungsfunktion (Halo Occupation Number, HON) untersuchen. Wir fitten die HON mit einem Potenzgesetz  $N = N_0 \times (M/M_{\text{pivot}})^s (1+z)^\gamma$ , wobei wir für die Steigung  $s$  die Literaturwerte übernehmen, da unser Haufensample nur einen kleinen Massenbereich abdeckt. Die gemessene Normalisierung  $N_0$  ist konsistent mit der Normalisierung aus der Literatur bei gleicher Steigung. Weiterhin finden wir Hinweise auf Entwicklungstrends in der HON auf einem  $2\sigma$ –Level, wobei SZE–ausgewählte Haufen bei hoher Rotverschiebung weniger Galaxien pro Masseneinheit haben als ihre Gegenstücke bei niedrigen Rotverschiebungen.

Das Abschlußkapitel bildet eine Zusammenfassung der Ergebnisse dieser Doktorarbeit und skizziert zukünftige Forschungsrichtungen.

# Abstract

We present a study of the galaxy populations in massive galaxy clusters selected by their Sunyaev–Zel’dovich Effect (SZE) signatures. Selection via the SZE is approximately mass-limited where the mass limit varies only slightly with redshift, making it an ideal selection method for studying the evolution of the galaxy content of clusters. We begin by introducing the SZE, the South Pole Telescope (SPT), and the larger research project in which this Thesis is embedded. We then present the core galaxy population studies of this Thesis.

In Chapter 3, we present the first large-scale follow-up of an SZE-selected galaxy cluster sample. Of 224 galaxy cluster candidates in the sample, we optically confirm 158 clusters and measure their photometric redshifts. We find a redshift range of  $0.1 \lesssim z \lesssim 1.35$ , confirming our expectation that samples selected by their SZE signal yield a large range of cluster redshifts. A comparison between the cluster SZE detection significance ( $\xi$ ) and the purity of the sample demonstrates that the South Pole Telescope (SPT) produces a very clean SZE selection: the confirmation rate of the sample is 70% at  $\xi > 4.5$  and reaches 100% at  $\xi > 6$ . In 146 clusters, we identify the red Brightest Cluster Galaxies (rBCG) using the red sequence technique. We compare the spatial distribution of the rBCGs with respect to the SZE cluster centroid in our clusters with that from an X-ray-selected sample. We find that if the method of identifying the rBCG is similar, the SZE rBCG distribution is indistinguishable from the rBCG distribution in an X-ray selected sample. Because the rBCG distribution is affected by merging in the cluster population, this indicates that SZE and X-ray selected samples exhibit similar evidence for continued accretion.

We then analyze the optical properties of the first four SZE-selected clusters in detail. These clusters are distributed in a redshift range representative of the entire SPT sample. For each cluster we use X-ray mass estimation and spectroscopic redshifts to define the projected virial radius. We then find Navarro-Frenk-White (NFW) profiles compatible with the galaxy distributions and recover concentration parameters similar to the values found for X-ray-selected clusters. We also study the cluster luminosity functions (LFs) and compare their characteristic luminosities in each *griz* band to a Simple Stellar Populations (SSP) model, finding them in agreement. To better constrain the faint end slope  $\alpha$ , we adopt the SSP model prediction for the characteristic luminosity as a function of band and redshift and fit a Schechter function to the individual cluster LFs. The results reveal values of  $\alpha$  that are consistent with those published for optically- and X-ray-selected clusters. We also measure the blue galaxy fraction within the virial region of each cluster, finding high-redshift clusters to be richer in blue galaxies than their low-redshift counterparts. However, the measurement errors from this study are large enough to be consistent with no evolution of blue galaxy fraction. This trend is similar to results found in other optical studies. In summary, our initial study shows that the galaxy populations of SZE-selected clusters do not differ from galaxy populations of clusters selected by other means.

In Chapter 5 we present a systematic evolutionary study of the galaxy populations in the 26 most massive SZE-selected clusters from the 2500 deg<sup>2</sup> SPT footprint. We create SSP models for each combination of telescope and bandpass used for the optical follow-up. We stack the radial profile using all of the galaxies within the virial radius as well as using only the red sequence galaxies. We find profiles from the latter galaxy set are slightly more concentrated.

We stack the luminosity functions of all galaxies and fit the result to a Schechter Function. The resulting values for the characteristic luminosity  $m^*$ , the density of galaxies  $\phi^*$  at the characteristic  $m^*$ , and  $\alpha$  are consistent with literature values. We then study the evolution of the galaxy population in detail and find that the redshift evolution of  $m^*$  is in good agreement with the passively evolving SSP models. If  $m^*$  is fixed to the SSP models, an LF fit reveals no trend for  $\phi^*$  and a  $2\sigma$  trend for  $\alpha$ , where clusters at high redshift have a shallower  $\alpha$ . With all LF parameters in hand, we explore the Halo Occupation Number (HON). We fit the HON to the power law relation  $N = N_0 \times (M/M_{\text{pivot}})^s (1+z)^\gamma$ , fixing the slope  $s$  to the literature value given the comparatively small range in mass in this cluster sample. The measured normalization  $N_0$  is consistent with the normalization found in the literature with this same slope. We also find evidence for evolutionary trends in the HON at the  $2\sigma$  level, where SZE selected high redshift clusters have fewer galaxies per unit mass than their low redshift counterparts.

In the concluding chapter, we provide a summary of the results presented in this Thesis and outline future directions of research.



# Contents

<b>Zusammenfassung</b>	<b>ix</b>
<b>Abstract</b>	<b>xi</b>
<b>Contents</b>	<b>xv</b>
<b>List of Figures</b>	<b>xviii</b>
<b>List of Tables</b>	<b>xix</b>
<b>1 Introduction</b>	<b>1</b>
<b>2 Galaxy Clusters, the Sunyaev–Zel’dovich Effect, and the South Pole Telescope</b>	<b>15</b>
2.1 First Results: Method confirmation . . . . .	17
2.2 First Data Release Results . . . . .	19
2.3 Second Data Release Results . . . . .	21
2.4 Third Data Release Results . . . . .	22
2.5 X-ray Studies of SPT SZE selected Galaxy Clusters . . . . .	25
2.6 Weak Lensing Results . . . . .	29
2.7 Special clusters . . . . .	29
2.8 Submillimeter Galaxies . . . . .	31
2.9 Conclusion . . . . .	31
<b>3 Redshifts, Sample Purity, and BCG Positions SPT Galaxy Clusters on 720 Square Degrees</b>	<b>33</b>
3.1 Abstract . . . . .	33
3.2 Introduction . . . . .	34
3.3 Discovery & Followup . . . . .	35
3.3.1 SPT Data . . . . .	35
3.3.2 Optical/NIR Imaging . . . . .	36
3.3.3 Spectroscopic Observations . . . . .	39
3.4 Methodology . . . . .	39
3.4.1 Photometric Redshifts . . . . .	41

3.4.2	NIR Overdensity Estimates for Unconfirmed Candidates . . . . .	47
3.4.3	Identifying rBCGs in SPT Clusters . . . . .	49
3.5	Results . . . . .	49
3.5.1	Redshift Distribution . . . . .	50
3.5.2	Purity of the SPT Cluster Candidates . . . . .	52
3.5.3	rBCG Offsets in SPT Clusters . . . . .	53
3.6	Conclusions . . . . .	57
3.7	Notable clusters . . . . .	59
<b>4</b>	<b>A Multiband Study of the Galaxy Populations of the First Four SZ selected Galaxy Clusters</b>	<b>67</b>
4.1	Abstract . . . . .	67
4.2	Introduction . . . . .	68
4.3	Observations and Data Reduction . . . . .	69
4.3.1	Blanco Cosmology Survey . . . . .	69
4.3.2	Completeness . . . . .	70
4.4	Basic Properties of these SPT Clusters . . . . .	72
4.4.1	Redshifts . . . . .	73
4.4.2	Cluster masses . . . . .	74
4.5	Cluster Galaxy Populations . . . . .	75
4.5.1	Radial distribution of galaxies . . . . .	75
4.5.2	Luminosity functions . . . . .	79
4.5.3	Halo Occupation Number . . . . .	85
4.5.4	Blue fractions . . . . .	87
4.6	Conclusions . . . . .	90
<b>5</b>	<b>Galaxy Populations in the 26 most massive Galaxy Clusters in the South Pole Telescope SZE Survey</b>	<b>93</b>
5.1	Abstract . . . . .	93
5.2	Introduction . . . . .	94
5.3	Observations and Data Reduction . . . . .	95
5.3.1	mm-wave Observations . . . . .	95
5.3.2	Redshifts and Cluster Masses . . . . .	96
5.3.3	Optical Imaging . . . . .	97
5.3.4	Completeness . . . . .	99
5.4	Cluster Galaxy Populations: tools . . . . .	99
5.4.1	Radial Distribution of Galaxies . . . . .	99
5.4.2	Luminosity Function . . . . .	101
5.4.3	Simple Stellar Population Models . . . . .	105
5.4.4	Simulated Catalogs . . . . .	105
5.5	Results . . . . .	107
5.5.1	Radial Profile . . . . .	107
5.5.2	Luminosity Function . . . . .	107
5.5.3	Halo Occupation Number . . . . .	112
5.6	Conclusions . . . . .	114
<b>6</b>	<b>Summary &amp; outlook</b>	<b>117</b>

<b>Bibliography</b>	<b>142</b>
<b>Acknowledgments</b>	<b>143</b>
<b>Curriculum vitae</b>	<b>145</b>



# List of Figures

1.1	Velocity-Distance relation as discovered by Hubble. . . . .	6
1.2	Redshift-distance relationship fit for different cosmological models. . . . .	6
1.3	ESA/Planck Universe Energy content . . . . .	7
1.4	Planck CMB temperature map. . . . .	8
1.5	Planck CMB Angular power spectrum. . . . .	8
1.6	BAO from Eisenstein et al. (2005) . . . . .	10
1.7	Vikhlinin et al. (2009) mass function . . . . .	11
1.8	Bullet Cluster . . . . .	12
1.9	Combination of different cosmological probes . . . . .	13
2.1	Distortion in the CMB due to the thermal SZE. . . . .	16
2.2	The South Pole Telescope. . . . .	17
2.3	CMB decrement of the first blind SZE cluster detections. . . . .	18
2.4	Optical images of the first four SZE selected clusters with the SPT . . . . .	19
2.5	First cosmology analysis on a SZE selected cluster sample. . . . .	20
2.6	Richness in SZE-selected Clusters . . . . .	21
2.7	Rarity of the 26 most massive galaxy clusters in the SPT footprint. . . . .	23
2.8	$Y_{\text{SZ}} - Y_{\text{X}}$ relation from Andersson et al. (2011). . . . .	26
2.9	$Y_{\text{SZ}} - M_{500}$ relation from Andersson et al. (2011). . . . .	26
2.10	Projected BCG / X-ray centroid offset as function of the surface brightness concentration. . . . .	27
2.11	BCG in a cool core cluster with massive star formation. . . . .	28
2.12	Redshift evolution of cooling properties. . . . .	30
3.1	Photometric versus spectroscopic redshift for 47 confirmed SZ-selected clusters. . . . .	43
3.2	Weighted mean photometric redshift versus spectroscopic redshift. . . . .	46
3.3	Photometric versus spectroscopic redshift from <i>Spitzer</i> IRAC 3.6 $\mu\text{m}$ -4.5 $\mu\text{m}$ colors. . . . .	47
3.4	Redshift histogram of 158 confirmed clusters. . . . .	50
3.5	Purity estimates from the optical/NIR followup compared to simulations. . . . .	51
3.6	rBCG / SPT candidate position offsets for 146 systems. . . . .	54
3.7	Normalized cumulative distribution of rBCG / SPT candidate position offsets. . . . .	56
4.1	Completeness of the BCS coadds for the SPT-CL J0516-5430 field. . . . .	71
4.2	Masses and redshifts of the SPT cluster sample. . . . .	72

---

4.3	Radial profiles for the red galaxy population to $0.36L^*$ . . . . .	76
4.4	$m^*$ resulting from Schechter function fits to the luminosity function. . . . .	78
4.5	Luminosity function with best fit Schechter function for SPT-CL J0516-5430. . . . .	81
4.6	Luminosity function with best fit Schechter function for SPT-CL J0509-5342. . . . .	81
4.7	Luminosity function with best fit Schechter function for SPT-CL J0528-5300. . . . .	82
4.8	Luminosity function with best fit Schechter function for SPT-CL J0546-5345. . . . .	82
4.9	68% confidence region for the LF parameters for each cluster / band combination. . . . .	83
4.10	Halo occupation number within each band for each cluster. . . . .	86
4.11	Color magnitude diagram for galaxies around each cluster. . . . .	88
4.12	Blue fraction versus redshift using the populations from Fig. 4.11. . . . .	90
5.1	Mass-redshift distribution of Williamson et al. (2011) sample. . . . .	95
5.2	Stacked radial profiles. . . . .	102
5.3	Evolution of the concentration parameter. . . . .	103
5.4	Individual and stacked luminosity function. . . . .	108
5.5	Evolution of the luminosity function parameters. . . . .	111
5.6	Halo Occupation Number for a fixed slope . . . . .	113

# List of Tables

2.1	Mass Scaling Relations . . . . .	22
2.2	R12 Cosmological constraints . . . . .	24
3.1	Optical and infrared imagers . . . . .	37
3.2	Spectroscopic Follow-Up . . . . .	40
3.3	All candidates above $\xi = 4.5$ in 720 deg <sup>2</sup> of the SPT-SZ survey. . . . .	61
4.1	Completeness limits for each tile for each filter for 90%/50% completeness . .	71
4.2	X-ray masses, spectroscopic redshifts and cluster parameters. . . . .	74
4.3	HON parameters . . . . .	84
5.1	SPT Cluster List. . . . .	96
5.2	Optical imagers . . . . .	99





# Chapter 1

## Introduction

The beginning of the 20<sup>th</sup> century was an exciting time. Along with a new theory of gravitation (Einstein, 1916) and its non-static solutions (Friedmann, 1922; Lemaître, 1931; Robertson, 1933), the works of astronomers such as Vesto Slipher and Edwin Hubble revealed a Universe greater and more dynamic than their predecessors imagined. The observational proof that fuzzy objects known as nebulae were in fact new kinds of objects that lay beyond the Milky Way Galaxy produced a new picture of our Universe (Slipher, 1913; Stromberg, 1925; Hubble, 1929). With this discovery a fundamental change took place: the long-standing paradigm of a static Universe changed to one that is a dynamic and brought forth an entire new discipline in extragalactic astronomy.

The first catalogs of galaxies date back to the 18<sup>th</sup> century with the work of Charles Messier (Messier, 1781) and F. Wilhelm Herschel (Herschel, 1785). From Paris, Messier recorded the positions and diameters of “star clusters” and what were back then referred to as *nebulae*. From England, Wilhelm Herschel discovered thousands of nebulae and recognized several nearby galaxy clusters and groups. Herschel and Messier were the first to recognize a concentration of nebulae in the direction of the Virgo and Coma clusters, which would later become become the most studied galaxy clusters in astronomy. There is no greater example of the impact that these clusters had on astronomy than the work of Fritz Zwicky on the Coma cluster in 1933. Zwicky used spectroscopic observations to find the motions of the galaxies in order to estimate the mass of the cluster. The results revealed for the first time the need for some form of dark matter to explain the high velocities of galaxies at large radii (Zwicky, 1933). Since then, large samples of galaxy clusters have been compiled (e.g. Abell, 1958; Zwicky et al., 1968). Even early on, clusters of galaxies acquired an important status for our understanding of the Universe in general and cosmology in particular.

## Galaxy Clusters Components

Galaxy clusters are the largest gravitationally collapsed structures, consisting of hundreds to thousands of galaxies and masses of  $10^{14}M_{\odot} - 10^{15}M_{\odot}$ . Although clusters were recognized early on due to their remarkable agglomeration of objects bright in optical light, stars constitute only about 2-4% of the Cluster mass. Intracluster gas only contributes between 8-15% to the total cluster mass (Gonzalez et al., 2013). The majority of the cluster mass is neither in form of stars, gas, nor any other form of baryonic matter. The remaining 85% of the mass

is in form of an unknown component that we identify as Dark Matter. We describe the main cluster components in detail below.

## Galaxies

Clusters are unique places to study galaxies because they provide a volume-limited sample of galaxies. The two first clusters to have their galaxy populations characterized were the Coma and Virgo clusters. The galaxy luminosity segregation in both clusters was reported in several papers (Zwicky, 1942, 1951; Reaves, 1966; Rood & Turnrose, 1968; Rood, 1969; Rood & Abell, 1973). Here, the brightest galaxies were found in the cores of the clusters and the general population luminosity was found to diminish with cluster-centric radius (Oemler, 1974). The works of Rood (1969) and Rood & Abell (1973) showed the importance of the luminosity function and the color-magnitude diagram as statistical tools to look at the overall changes in the galaxy populations as well as to understand the formation of the stellar component. The luminosity function describes the number of galaxies per luminosity bin and therefore informs us about the galaxy populations in a statistical manner. Examples of luminosity functions are shown Fig. 4.5 and Fig. 5.4.

When plotting a cluster's member galaxies on a color-magnitude diagram (CMD) a sequence of red galaxies forms a clearly-defined ridge. The placement of this ridge is determined by the redshifted location of the 4000Å break in typical galaxy spectra (Baum, 1959; Rood, 1969; Visvanathan & Sandage, 1977) as well as the collective age of the stars in the member galaxies. The tight scatter of the red sequence in the CMD suggests a single, short formation epoch of the cluster's stellar component at very high redshift ( $z \gtrsim 2 - 3$ ) that is collectively aging (e.g. De Lucia et al., 2004; Rudnick et al., 2012). The red sequence slope or tilt is driven by the metallicity, with larger and brighter galaxies redder (higher metallicity) as their deeper potential wells allows them to retain more metals. Several examples of the red sequence at various redshift using different colors is shown in Fig. 4.11.

Galaxies also provide a means to estimate the cluster mass. The most direct measurement is via the cluster's line-of-sight velocity dispersion. Assuming the galaxies are dynamically relaxed, they act as collisionless particles tracing the cluster's gravitational potential. The method provides a direct estimation of the total cluster mass with measurement errors on the order of  $\approx 20\%$ , as long as systematics are kept under control (Saro et al., 2013).

The number of galaxies in a cluster, (known as the cluster's richness), can also be used to estimate the cluster's mass. However, this method first requires calibration on a set of clusters with known mass and is therefore dependent on other mass estimation techniques. Furthermore the resulting measurement errors are comparatively large. A richness versus mass plot is shown in Fig. 2.6.

## Intracluster light

The first detection of Intra-cluster light (ICL) dates to 1952, when Zwicky found intergalactic stars and groups of stars in the Coma cluster (Zwicky, 1952). A general definition of ICL is that it is light from stars not bound to identified galaxies. Simulations have shown that this diffuse stellar component comes from tidal stripping during galaxy mergers. Typically half of these stars come from the Brightest Cluster Galaxy (BCG), a quarter come from tidal interaction of less massive galaxies, and the remaining quarter come from dissolved galaxies (e.g. Murante et al., 2007). The majority of the observable ICL is found near the core of the

cluster, where the BCG commonly resides. Therefore, in galaxy clusters where the BCG sits near the center, the BCG and ICL must be decomposed. A two-component model for the BCG and the ICL is found to be a good fit (e.g. Gonzalez et al., 2005). In such cases, the ICL represents between 80-90% of the total light of the two components within 300 kpc.

## Gas component

After the suggestion that hot, intracluster gas must fill clusters (Limber, 1959), Felten et al. (1966) estimated that a thermalized gas in the Coma cluster would have a temperature around  $\approx 7 \times 10^7 \text{K}$ . The source of this heat comes from adiabatic collapse of the gas in the cluster's deep potential well. At these temperatures, the gas is fully ionized and free electrons suffer Coulomb interactions with the ions, emitting x-rays in the keV energy range (known as thermal *bremsstrahlung* radiation). This x-ray emission was first observed by the *Uhuru* satellite from the *Aerobee* 150 rocket Data in the 2-8 keV range from *Uhuru* revealed extended emission in rich clusters with luminosities of  $10^{43} - 10^{44} \text{ ergs s}^{-1}$  (Gursky et al., 1972). The evidence of the x-ray emission as thermal bremsstrahlung became stronger as the x-ray luminosity was found to be highly correlated with cluster velocity dispersion, pointing to a connection to the size of the cluster potential through the virial theorem (Solinger & Tucker, 1972).

Under the assumption of hydrostatic equilibrium, the gas temperature provides a good estimate of the cluster virial mass via the relation  $M \propto T_{\text{gas}}^{3/2}$ . Furthermore, the x-ray luminosity can be used as a mass proxy as it is connected to the gas temperature as  $L_X \propto T_{\text{gas}}^2$  (Giodini et al., 2013). A third way to measure the cluster mass using the intracluster gas is to measure how the hot electrons distort Cosmic Microwave Background photons by inverse Compton scattering. This phenomenon is known as the Sunyaev–Zel’dovich Effect (SZE) and discussed in more detail in Chapter 2.

## Dark Matter

The first evidence of Dark Matter (DM) in the Universe appeared from spectroscopic observations of the Coma cluster. Zwicky (1933) used the virial theorem to argue that the velocity dispersion of galaxies in the Coma cluster, observed to be on the order of 1500 to 2000 km/sec, indicates that the cluster must have an average density of 400 times the mass derived from observations of the luminous matter. Additional evidence of DM came from observations of galaxy rotations curves. Babcock (1939) studied the kinematics of the Andromeda galaxy noticing that rotation curves approached a constant angular velocity in the outer spiral arms. Babcock (1939) also reported that such velocities would imply a mass-to-light ratio of about 50, attributing the large mass estimation to “the outer parts of the spiral on the basis of the unexpectedly large circular velocities of these parts”. Further evidence based on galaxy rotation curves strengthens the need for DM in galaxies (e.g. Seielstad & Whiteoak, 1965; Roberts, 1969; Rubin & Ford, 1970).

The possibility that the unseen DM in galaxies takes a form of baryonic dark objects was explored by several projects such as MACHO, OGLE, and EROS. They searched for *MAssive Compact Halo Objects* (MACHO) like brown dwarfs and planets to test if their abundance could explain the observed missing mass. MACHOs can be detected from the magnification of bright objects as they cross our line-of-sight, due to gravitational lensing. Several searches were carried out, using the Andromeda Galaxy, the Galactic bulge, and the Magellanic clouds

as background sources. While they were successful in finding some candidate objects, the results only account for  $\approx 20\%$  of the missing mass (Alcock et al., 1997; Udalski et al., 1997; Alcock et al., 2000; Afonso et al., 2003; Tisserand et al., 2007; Garg, 2008).

With the list of baryonic candidates exhausted, other forms of matter are explored. Some of the DM candidates include Weakly Interacting Massive Particles (WIMPs), Axions, nonthermal WIMPs or WIMPzillas, Q-balls, gravitinos, etc. Whatever their true nature, nonbaryonic DM particles would at least have to be collisionless, cold, and behave like a fluid.

In recent investigations, galaxy clusters have provided striking evidence of the nature of DM. This is achieved by measuring the gravitational lensing of background galaxies due to the space-time distortions from a massive, foreground galaxy cluster. A statistical analysis of the distorted shapes of the background galaxies allows us to extract the total mass of the foreground cluster. Because DM is the dominant source of cluster mass, the distortions are assumed to be caused primarily by DM. Therefore this kind of analysis can reveal how the DM is distributed within a cluster. One of the most famous exhibits of this technique is the Bullet Cluster, a system where two clusters are colliding. By complementing the background-galaxy shape measurements with x-ray observations, the three main components of the cluster are traced: x-rays follow the gas, shape measurements of background galaxies indicate where the bulk of the (dark) matter is, and optical images shows where the galaxies are located. The three different components are depicted in Fig. 1.8. Here, it is clearly shown that the DM distribution derived from shape measurements of background galaxies does not follow the collisional gas component, but rather the collisionless component traced by the galaxies.

## Galaxy Clusters and other Cosmological Probes

Once the dynamical nature of the Universe was established, its understanding and characterization became a goal. This required new, cosmological probes, such as galaxies (e.g. Hubble, 1929; Lemaître, 1931; Bender et al., 1998), galaxy clusters (e.g. Wang & Steinhardt, 1998; Haiman et al., 2001; Reichardt et al., 2013), supernova type Ia (e.g. Hamuy et al., 1993; Schmidt et al., 1998; Riess et al., 1998; Perlmutter et al., 1999), the Cosmic Microwave Background (CMB) (e.g. Smoot et al., 1992; Komatsu et al., 2011; Planck Collaboration et al., 2013), and Baryon Acoustic Oscillations (e.g. Eisenstein & Hu, 1998; Sánchez et al., 2012). Utilizing multiple probes is important as each cosmological probe reveals different aspects of the evolution of the Universe and each is subject to different systematics. Together, they form the current picture of cosmology and is the context within which this thesis was developed. In this chapter we introduce the cosmological probes used in this thesis.

### Type Ia Supernova

In 1998, two teams lead by Adam Riess (Riess et al., 1998) and Saul Perlmutter (Perlmutter et al., 1999) searched for the rate of deceleration of the universe, using a set of high redshift supernovae (SNe). However, instead of a decelerating Universe, they discovered that the Universe is actually accelerating.

To trace the dynamics of the universe, distances and redshifts of objects spanning a range of distances are needed. While the redshift can be obtained precisely from the object's spectra, the distance is more tricky. To determine the distance, scientists use a class of objects with known intrinsic luminosity to serve as *standard candles* to which distances can be measured.

Some examples of standard candles are *Cepheids* (used by Hubble, see Feast & Walker, 1987, for a review), Planetary Nebulae (e.g. Ciardullo et al., 2002, and references therein) and Type Ia Supernovae (SNIa). Because brighter objects can be observed further away, the greater the luminosity of a standard candle, the greater the importance for tracing the dynamics of the Universe. Among all known standard candles, SNIa are the most luminous, with a peak observed energy of  $\sim 10^{43} \text{ ergs/sec}$ . This is so bright that it outshines its host galaxy for a few days, providing us a brief window for observation from very far away.

Although SNe are extremely luminous events, they are not exactly standard candles, as their peak luminosities have intrinsic scatter of about  $\approx \pm 0.7$  in BVI. The key is to *make* them a standard candle by correcting their peak luminosity. Phillips (1993) found that the decay in magnitude that a SNIa suffers within 15 days is highly correlated with the absolute magnitude at the peak of the light curve. Using this information the peak luminosity can be corrected and therefore the absolute magnitude can be standardized. More sophisticated methods have been developed (e.g. Multicolor Light Curve Shape Method (MLCS), “stretch factor”; Riess et al., 1998; Perlmutter et al., 1999) but they share the same principle.

Once the SNIa are calibrated and their redshifts are determined, it is possible to find out how the Universe is evolving applying the following formula to a set of observed standard candles:

$$m - M = -2.5 \log \left( \frac{L}{4\pi d_L^2} \right) + 2.5 \log \left( \frac{L}{4\pi (10 \text{ pc})^2} \right) = 5 \log \frac{d_L}{10 \text{ pc}}, \quad (1.1)$$

where  $d_L$  is the *luminosity distance* which is a function of redshift and chosen cosmology. In the *local* Universe  $d_L$  can be described simply as  $cz/H_0$ , where  $H_0$  is the Hubble parameter and corresponds to the rate of expansion of the Universe. At cosmological scales  $d_L$  for a flat Universe is expressed as

$$d_L = (1+z)^2 D_A(z) = c(1+z) \int_0^z \frac{dz'}{H(z')} = \frac{c(1+z)}{H_0} \int_0^z \frac{dz'}{\Omega_M(1+z')^3 + \Omega_\Lambda}. \quad (1.2)$$

In such a Universe,  $\Omega_M$  is the matter energy density at redshift zero and  $\Omega_\Lambda$  is an unknown energy component (*Dark Energy*). Thus, eq. 1.1 becomes:

$$m - M = 5 \log \frac{c(1+z)/H_0 \int_0^z \frac{dz'}{\Omega_M(1+z')^3 + \Omega_\Lambda}}{10 \text{ pc}} \quad (1.3)$$

Fig. 1.2 shows the data presented in Riess et al. (1998) along with eq. 1.3 evaluated for two closed Universes, a pure matter-dominated one and a pure  $\Lambda$ -dominated one, as well as a fiducial, open Universe with only matter ( $\Omega_M = 0.2$  and  $\Omega_\Lambda = 0.0$ ). All curves use a Hubble parameter of  $H_0 = 65.2$ . The results clearly show that we are not living in a open, matter-dominated Universe! For a review see Clocchiatti (2011).

## The Cosmic Microwave Background

The Cosmic Microwave Background (CMB) radiation is the light that has freely streamed since a redshift of  $\sim 1100$ , when the Universe first cooled to a temperature below 3000 K. At that temperature, photons were no longer energetic enough to keep hydrogen and helium atoms ionized, and the two atoms *recombine*. This period is also known as the epoch of

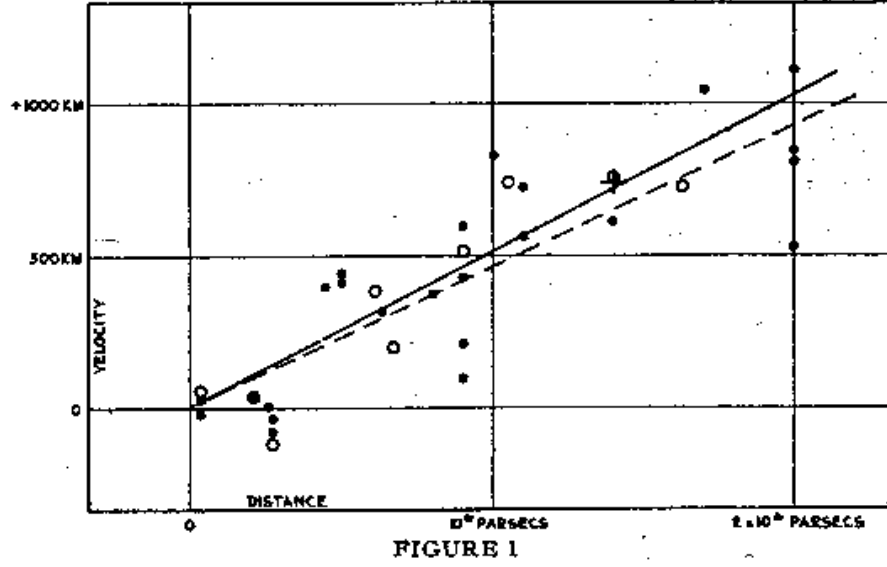


**Figure 1.1:** Diagram showing the nature of the dynamical universe by Hubble. The scientific concept of the Universe as an eternal and immutable entity gives away to a dynamical (and more interesting) Universe.

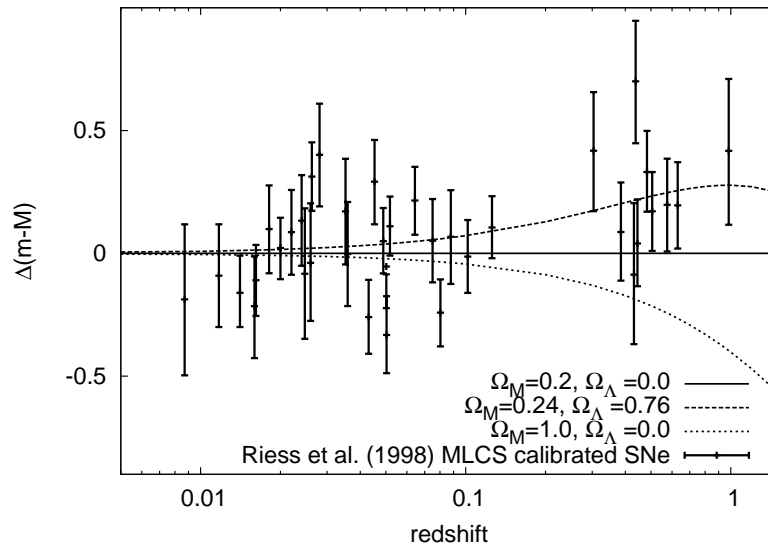


**Figure 1.2:**  $\Delta m$  from Riess et al. (1998). The best fit for a flat cosmology is the solid line with  $H_0 = 65.2$ ,  $\Omega_M = 0.24$  and  $\Omega_\Lambda = 0.76$ . We have reproduced the fits using eq. 1.3

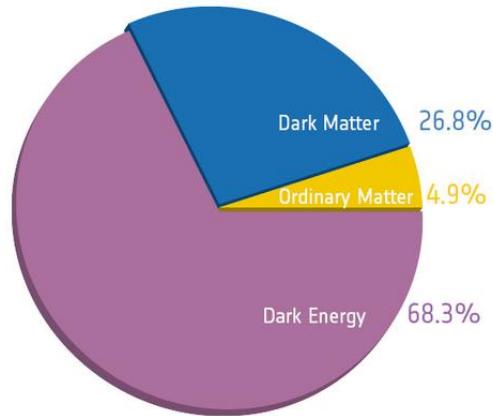


**Figure 1.3:** Composition of the universe according to the ESA/Planck mission results. Credit: ESA/Planck

the last scatter. Before the last scattering the photons were in equilibrium and produced a blackbody spectrum with a temperature measured today of 2.73 K (Fixsen et al., 1996). This last scattering radiation was predicted as early as 1948 (Alpher et al., 1948) and observed in McKellar (1941, without realizing) and Penzias & Wilson (1965, without intending).

Although highly homogeneous, the CMB has anisotropies at the  $\Delta T/T \sim 10^{-5}$  level (Smoot et al., 1992). Between the time of inflation and last scattering, the Baryonic matter was ionized and coupled to the radiation. In this state, it behaved as a fluid and supported sound waves (Peebles & Yu, 1970; Sunyaev & Zel'dovich, 1970). However, DM was not coupled and began to clump together, forming deeper and deeper gravitational potentials and planting the primordial seeds for the large-scale structure of the present day. The photon-baryon fluid interacts with the DM potential wells, where the battle between gravity and pressure causes the baryons to oscillate, creating acoustic waves. The wavelengths of these waves are harmonics of the fundamental scale set by the distance that the sound waves travel in the time between the formation of the potential wells and recombination.

Statistically those waves at maximum compression and rarefaction are the acoustic peaks that we observe in the CMB angular power spectrum of the temperature maps as traced by the light (Planck Collaboration et al., 2013, see Fig. 1.5). The heights and positions of such acoustic peaks provide insights into the content and geometry of the Universe. Predictions from varying cosmologies can be generated using numerical codes such as CMBFAST (Seljak & Zaldarriaga, 1996) or CAMB (Lewis et al., 2000). The results can be compared to observations to discern the validity of the tested cosmology. In this way, CMB experiments like WMAP (Komatsu et al., 2011; Bennett et al., 2012) and *Planck* (Planck Collaboration et al., 2013) have rendered a detailed description of the Universe we live in.

## Baryon Acoustic Oscillations

The Baryon Acoustic Oscillations describe the characteristic length of the first acoustic peak as it reaches recombination at the speed of sound. After recombination, the photons travel

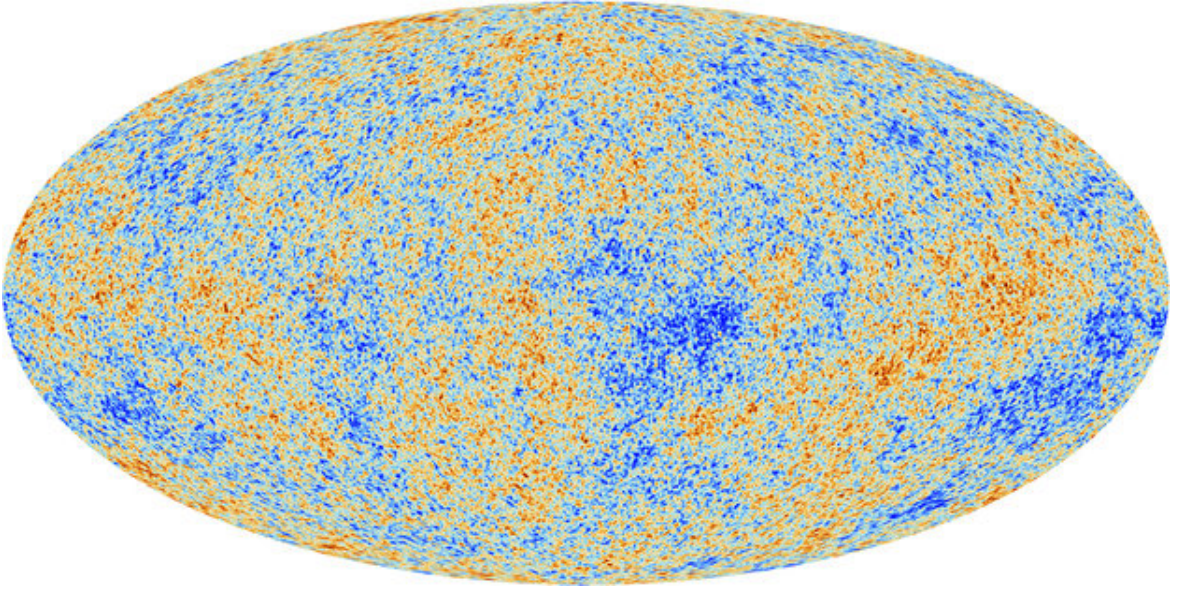


**Figure 1.4:** CMB temperature map. Credit: ESA/Planck.

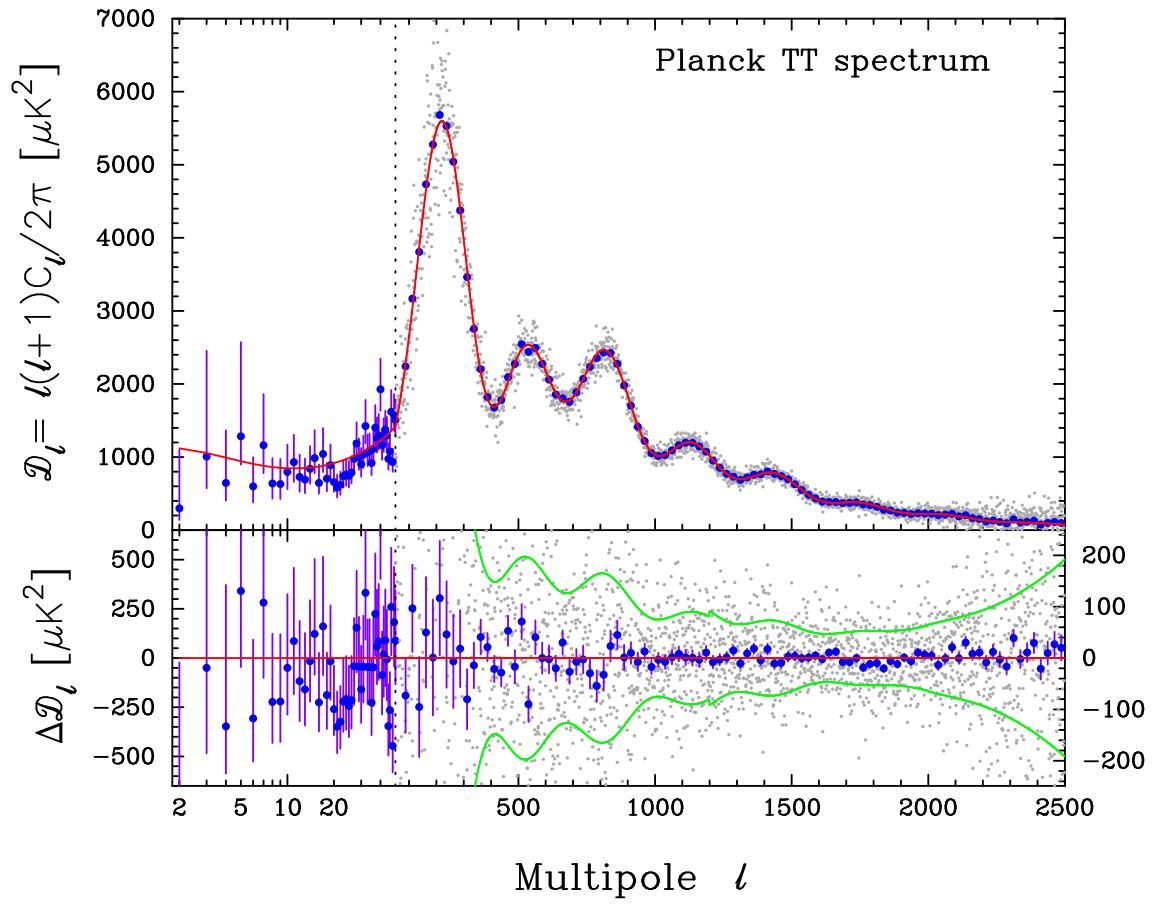


**Figure 1.5:** Planck Temperature power spectrum (Planck Collaboration et al., 2013). Credit: ESA/Planck



freely, ending the wave propagation and freezing the baryon overdensity at a characteristic length. The baryon overdensity grows over cosmological time, creating gravitationally collapsed systems such as galaxies. A complete, all-sky map of galaxies can be traced using the correlation function enhancement at a distance given by (e.g. Eisenstein & Hu, 1998; Percival et al., 2007):

$$r_s(z_*) = \frac{1}{H_0 \Omega_M^{1/2}} \int_0^{a_*} \frac{c_s}{(a + a_{\text{eq}})^{1/2}} da,$$

where  $c_s$  is the sound speed,  $a$  is the scale factor  $(1+z)^{-1}$ ,  $a_*$  is the value at recombination and  $a_{\text{eq}}$  is the value at matter-radiation equality. This distance ( $\Delta\chi$ ) is around 150 (comoving) Mpc in current cosmology and can be connected to observables through

$$\Delta\theta = \frac{\Delta\chi}{d_A(z)},$$

where  $\Delta\theta$  is the angular size in the sky. This in turn can be connected to the luminosity distance via the angular distance:

$$d_A(z) = \frac{d_L}{(1+z)^2},$$

where  $d_L$  is given in eq. 1.2. As the evolution of the standard ruler is a function of the expansion rate,  $H(z)$ , and the two redshifts at which the distances were measured, we can write:

$$c\Delta z = H(z)\Delta\chi.$$

In this way, from purely geometrical considerations, we can measure  $H(z)$  which depends on cosmological parameters as follows:

$$\frac{H^2(z)}{H_0^2} = \Omega_M(1+z)^3 + \Omega_r(1+z)^4 + \Omega_k(1+z)^2 + \Omega_\Lambda(1+z)^{-3(1+w)}$$

This geometrical test has been successfully applied: By measuring the large-scale correlation function on a spectroscopic sample of 46,748 Luminous Red Galaxies (LRG) from the Sloan Digital Sky Survey with a typical redshift of 0.35, Eisenstein et al. (2005) presented the first clear detection of the acoustic peak (see Fig. 1.6) along with its cosmological implications. An updated version can be found in Sánchez et al. (2012).

## Galaxy Clusters

Galaxy clusters are the largest collapsed objects in the Universe. Hundreds to thousands of galaxies crowd together in deep potential wells, largely defined by Dark Matter (see Fig. 1.8). In this way, galaxy clusters trace the distribution of the mass in the Universe as well as the position of the initial density fluctuations. Because of these characteristics, galaxy clusters are a powerful probe for cosmological studies (Albrecht et al., 2006).

In the cosmological context, galaxy clusters are sensitive to the rate of the formation of structures which depends on the dynamical behaviour and mass content of the Universe. By simply using the abundance and the redshift distribution of clusters of galaxies as a function of mass, several cosmological parameters can be extracted (e.g. Haiman et al., 2001; Holder et al., 2001). However, to extract cosmological parameters, the observed redshift evolution of

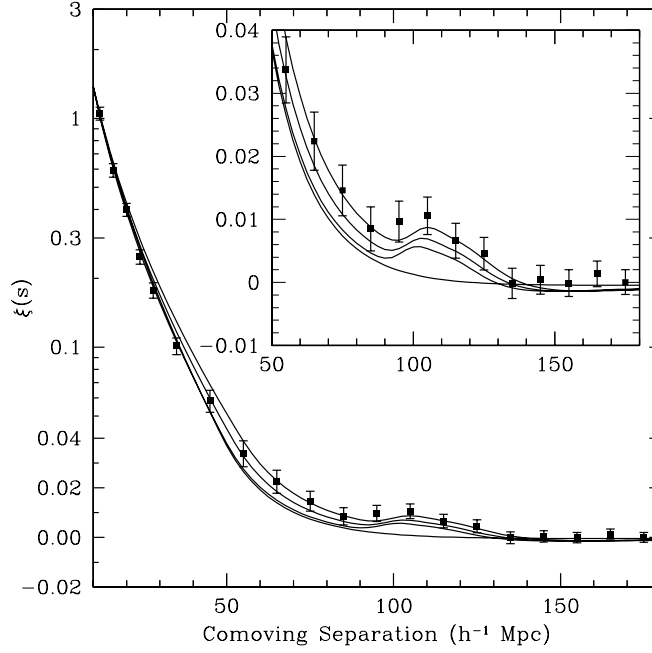


**Figure 1.6:** From Eisenstein et al. (2005): Large-scale redshift-space two-point correlation function of the SDSS Luminous Red Galaxy sample. The Baryon Acoustic Peak detection shown here confirms the theoretical prediction.

the cluster mass function per volume surveyed must be compared to its theoretical prediction for a given cosmology (e.g. Vikhlinin et al., 2009, see Fig. 1.7). An analytical description of the predicted number density of collapsed objects of a mass  $M$  at a redshift  $z$  in the linear regime is provided by the Press-Schechter mass function (Press & Schechter, 1974):

$$\frac{dn}{dM} = -\sqrt{\frac{2}{\pi}} \frac{\bar{\rho}_m}{M} \frac{\delta_c}{\sigma_M^2} \frac{d\sigma_M}{dM} \exp\left(-\frac{\delta_c^2}{2\sigma_M^2}\right),$$

where  $\bar{\rho}_m$  is the mean matter density,  $\delta_c$  is the linear density contrast (1.686 for spherical collapse) and  $\sigma_M$  is the variance of the density fluctuation field at scale  $M$  (see eq. 1.6).

Currently, the mass function that is used for cluster cosmology is derived from numerical simulations, such as the Tinker et al. (2008) mass function:

$$\frac{dn}{dM} = f(\sigma_M) \frac{\bar{\rho}_m}{M} \frac{d\ln\sigma_M^{-1}}{dM}, \quad (1.4)$$

with  $f(\sigma_M)$  parametrized as

$$f(\sigma_M) = A \left[ \left( \frac{\sigma_M}{b} \right)^{-a} + 1 \right] e^{-c/\sigma_M^2}, \quad (1.5)$$

where the values for  $A$ ,  $a$ ,  $b$ , and  $c$  are  $0.186 \times (1+z)^{-0.14}$ ,  $1.47 \times (1+z)^{-0.06}$ ,  $2.57 \times (1+z)^{-0.011}$  and 1.19, respectively ( $-0.011$  was obtained by evaluating  $10^{-(0.75/\log_{10}(\Delta/75.))^{1.2}}$  assuming  $M = M_{\Delta, \text{mean}} = M_{200, \text{mean}}$ ).

Also,  $\sigma_M$  is

$$\sigma_M^2 = \int P(k) \hat{W}(kR) k^2 dk, \quad (1.6)$$

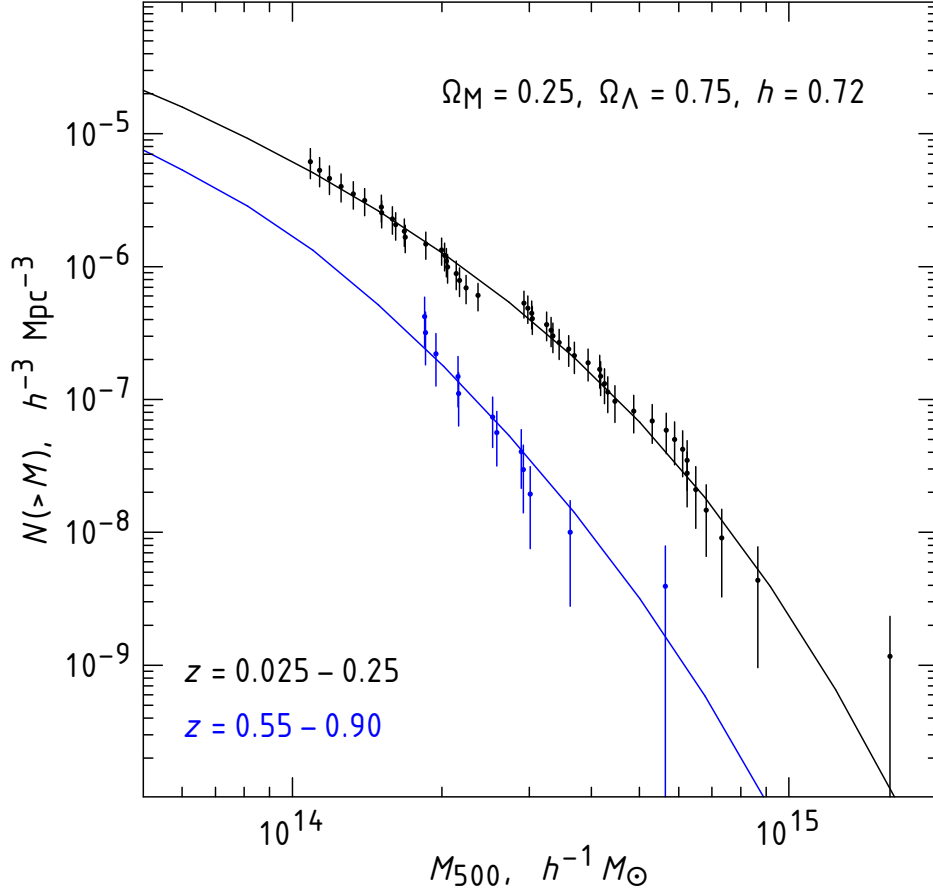


**Figure 1.7:** From Vikhlinin et al. (2009), showing the evolution of the mass function given  $\Lambda$ CDM cosmology (solid lines) and the observed cluster abundance distribution (points). Notice the exponential decrement of high mass high redshift clusters. Those cluster are specially sensitive to the cosmology and as such they are excellent probes to recover cosmological parameters.

where  $P(k)$  is the linear matter power spectrum,  $k$  the wavenumber, and  $\hat{W}$  is the Fourier transform of the real space top-hat window function of radius  $R$ . In this way,  $\sigma_M$  is a function of a scale or mass given  $M \propto R^3$ . Notice that with a scale invariant power spectrum  $P(k) \propto k$ ,  $\sigma_M$  becomes  $\propto k^2$ . This implies that at higher scales (or mass)  $\sigma_M$  is lower. Due to the effect of  $\sigma_M$  in eq. 1.5, the number of high mass clusters is expected to rapidly decrease at higher and higher masses (see eq. 1.4). This can be seen clearly in Fig. 1.7.

The observable is the average number of clusters of a given mass above a minimum value at a redshift  $z$  observed over a  $d\Omega$  solid angle (Haiman et al., 2001):

$$\frac{dN}{dzd\Omega}(z) = \left( \frac{dV}{dzd\Omega}(z) \int_{M_{\min}(z)}^{\infty} dM \frac{dn}{dM} \right) \quad (1.7)$$

By comparing eq. 1.4 to observations, through eq. 1.7, cosmological parameters are extracted.

In comparison to SN and BAO techniques, which are purely geometrical, Clusters of Galaxies

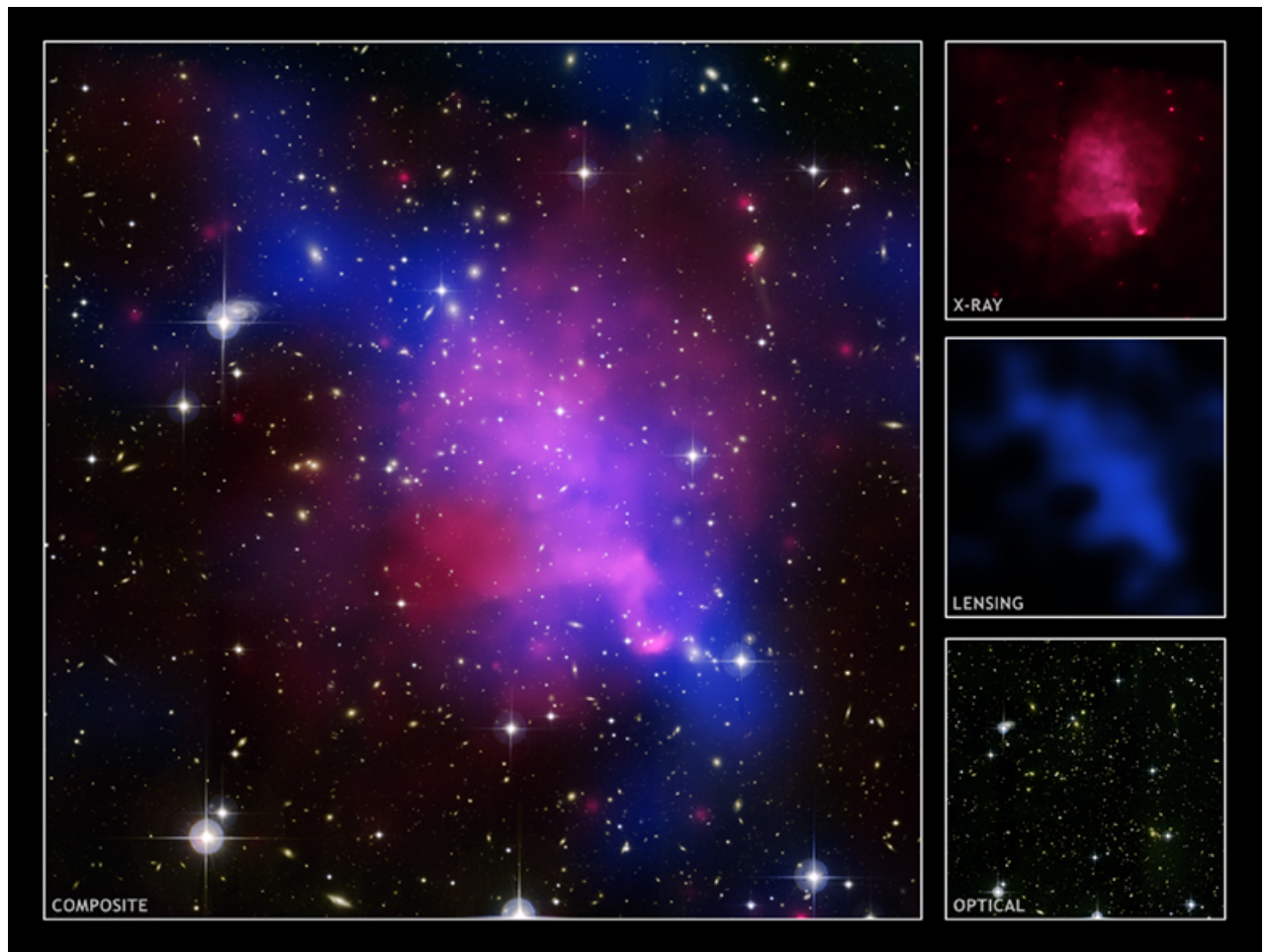


**Figure 1.8:** The Bullet Cluster: By using different observational techniques, the different matter components of the galaxy cluster can be seen, the Dark Matter is traced by the weak lensing observation, the baryon gas is traced by the X-rays and the baryons in form of galaxies and stars are seen in optical wavelength. Source: Chandra X-ray observatory site, Harvard University.

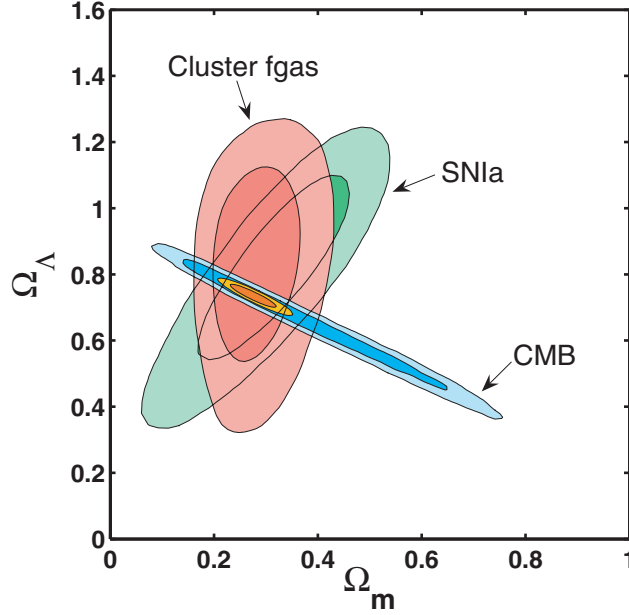


**Figure 1.9:** Combining different probes we constrain  $\Omega_\Lambda$  and  $\Omega_m$ .

are sensitive to the geometry and the growth of structure.

Each cosmological probe has unique problems and advantages, and characterize from a different perspective the Universe. The combination of probes and how they constraint the  $\Omega_M - \Omega_\Lambda$  plane can be seen in Fig 1.9.

## Organization

This thesis is based on work done as part of the South Pole Telescope collaboration. In Chapter 2 we summarize the main scientific results of this collaboration where the author of this thesis has contributed in different degrees. In Chapter 3 we analyze the third data release, estimate photometric redshifts, identify the Brightest Cluster Galaxies, and compare their distribution to the that from other selection methods such as X-rays. In Chapter 4 we perform a study of the first four blindly SZ-selected galaxy clusters, comparing their optical properties to those of galaxy clusters selected by other means. In Chapter 5 we extend this study of optical properties to a larger sample of the 26 most massive galaxy clusters in the SPT footprint (Williamson et al., 2011) and additionally study the redshift evolution of the galaxy population. Finally, Chapter 6 provides a summary of the results and an outlook for subsequent work for the future.



# Galaxy Clusters, the Sunyaev–Zel’dovich Effect, and the South Pole Telescope

The thermal Sunyaev–Zel’dovich effect (SZE) was predicted in 1972 in a paper by R.A. Sunyaev and Y.B. Zel’dovich (Sunyaev & Zel’dovich, 1972). The effect is a distortion in the CMB spectrum due to inverse Compton scattering of CMB photons by hot electrons in the intracluster medium. Only about  $\sim 1\%$  of the CMB photons are scattered, so the effect is subtle and can be hard to measure. Neglecting relativistic correction, the fractional change in the temperature can be written as

$$\frac{\Delta T_{\text{SZE}}}{T_{\text{CMB}}} = f(x)y = f(x) \int n_e \frac{k_B T_e}{m_e c^2} \sigma_T dl, \quad (2.1)$$

where  $y$ , the Compton  $y$ -parameter, is a function of the Thomson cross-section  $\sigma_T$ , the electron number density  $n_e$ , the electron temperature  $T_e$ , the Boltzmann constant  $k_B$ , and the electron rest mass energy  $m_e c^2$ . The integral is taken along the line of sight.  $f(x)$ , which is a function of the reduced frequency ( $x = \frac{h\nu}{k_B T}$ ), is

$$f(x) = \left(x \frac{e^x + 1}{e^x - 1} - 4\right)(1 + \delta_{\text{SZE}}(x, T_e)). \quad (2.2)$$

The intensity of the SZE effect signal is given by

$$\Delta I_{\text{SZE}} = \frac{x^4 e^x}{e^x - 1} f(x) I_0 y. \quad (2.3)$$

From Eq. 2.1 it can be seen that the distortion is independent of redshift and depends on the value of the integrated pressure of the cluster, which itself depends on the size of the cluster’s potential well, which is determined by the cluster mass. This is the reason why cluster surveys based on the SZE signal are so powerful.

Although a powerful selection method, the SZE is hard to observe. We show the effect of hot cluster electrons on the CMB spectrum in Fig. 2.1. In this Figure we have scaled down the blackbody spectrum of the CMB by a factor of 100 and plotted how the SZE would change it. From this Figure, it is clear that the effect is subtle even if the blackbody spectrum is just 1% of its actual value. Because the change in the spectrum is so small, it was several

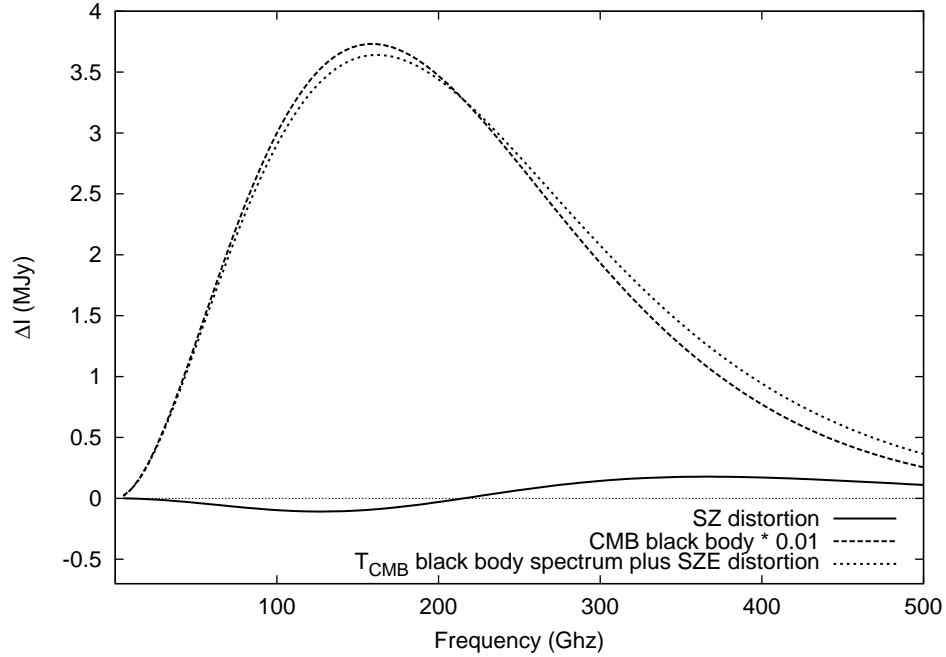


**Figure 2.1:** The distortion that would be introduced to the CMB by the SZE of a massive cluster, with the black body scaled down to 1% of its normal values, which exemplify how hard it is to measure this effect. The distortion is in the order of few hundreds  $\mu\text{K}$ .

decades from the prediction of this phenomenon for the technology to achieve the sensitivity levels needed to detect it. That level of sensitivity, on the order of few tens of  $\mu\text{K}$ , have been achieved by telescopes such as the South Pole Telescope (Carlstrom et al., 2011) and the Atacama Cosmology Telescope (Marriage et al., 2011), allowing for the blind discovery of clusters via the SZE signal for the first time.

The South Pole Telescope (SPT Carlstrom et al., 2002, 2011) is a 10m off-axis millimeter-wavelength telescope located at the geographical South Pole (see Fig 2.2). With a 1 arcmin angular resolution it is designed to search for galaxy clusters at all redshifts. The SPT receiver consists of a bolometer array of 960 elements in 95, 150 and 220 GHz bands. The 95 GHz and 150 GHz bands are used to detect decrements in the CMB map and the 220 GHz band is used as a null band (see Fig 2.1). From those bands, the 150 GHz band has the lowest sensitivity at  $18\mu\text{K arcmin}$ —a large contributor of noise—and as such it is typically used for cluster detection. Observations began in 2007 and was completed by the end of 2011, covering a footprint of  $2500 \text{ deg}^2$ .

As mentioned above, a sample selected by the SZE consists of clusters independent of redshift down to a limiting mass. As we have seen in § 1.4, such sample is exactly what is required in order to do cosmology with galaxy clusters. However, there is one element yet missing. As shown in Eq. 1.7, the abundance of clusters per redshift is needed, but clusters detected via the SZE is independent of redshift. Therefore an external redshift measurements is needed. This is primarily achieved with photometric redshifts using optical and near infra-red broadband imaging observations. Ultimately, many clusters are followed-up with spectroscopic





**Figure 2.2:** The South Pole Telescope. Credit: Daniel Luong-Van

observations and redshifts can be improved.

In preparation for the first results of the SPT Survey, an optical campaign was carried out. The Blanco Cosmology Survey (BCS), completed in 2009, consisted of 60 nights, covering an  $80 \text{ deg}^2$  area in the sky. The footprint was distributed in two patches, one at  $(\alpha, \delta) = (5 \text{ hr}, -55^\circ)$  and the other at  $(23 \text{ hr}, -55^\circ)$  (J2000) Desai et al. (2012b). The first scientific results of the SPT survey utilized photometric redshifts determined from the deep observations of the BCS survey.

In the following subsection we summarize the main scientific results within the SPT collaboration.

## 2.1 First Results: Method confirmation

The first blind SZE cluster detections were published in Staniszewski et al. (2009). It corresponded to the 4 most significant detections found in CMB maps of  $\approx 40 \text{ deg}^2$ . For the detection, only the 150 GHz map was used because it has the highest sensitivity. The other two maps were cross-checked to verify detections (the 80 GHz map can be used to verify there is a source and the 225 GHz map can be used to check against false positives, see Fig. 2.3).

The cluster-finding methodology applies spatial filters on the CMB maps in Fourier space. To

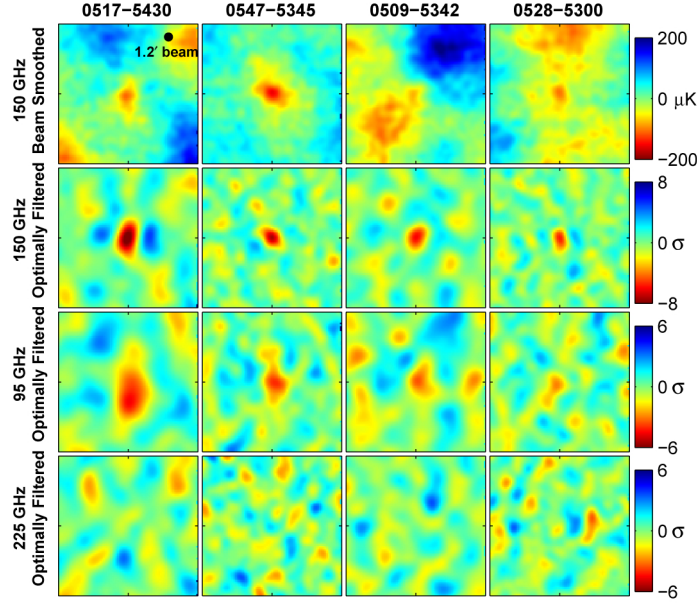


**Figure 2.3:** First blind SZE cluster detections from Staniszewski et al. (2009). Red are cold spots versus the hot blue spots. It can be seen that, while the cluster shows decrements in the 90GHz and the 150 GHz bands, there is no signal in the 220 GHz band where the null is .

enhance the signal-to-noise ratio, the spatial filters have morphologies similar to that expected for SZE galaxy clusters:

$$\phi = \frac{S^T N^{-1}}{\sqrt{S^T N^{-1} S}}, \quad (2.4)$$

where  $\phi$  is the match filter,  $N$  the noise covariance matrix (including non-SZE foregrounds) and  $S$  is the source template which contains the morphology information. An example of a source template is a  $\beta$ -model:

$$\Delta T_{\text{SZE}}(\theta) = \Delta T_0 (1 + \theta^2 / \theta_{\text{core}}^2)^{(1-3\beta)/2}, \quad (2.5)$$

where  $\theta$  is the angular distance from the line-of-sight through the center of the cluster,  $\theta_{\text{core}}$  is the core radius, and  $\Delta T_0$  is the peak signal. By combining this with noise information for the observation (e.g., primary CMB signal, instrument and atmospheric noise, point sources), the significance of a detection can be estimated.

The highest significance detections were confirmed optically with one of the pre-observed BCS target areas (centered at R.A  $5^h 30^m$  and decl.  $-53^\circ$ ) and became the first blind discovery of galaxy clusters selected via the SZE signal. BCS images of the galaxy clusters are shown in Fig. 2.4.

Besides confirming the presence of galaxy clusters, the BCS data allowed for redshift estimations of those clusters. Cluster redshifts were estimated in two ways: once by using the artificial neural network ANNz (Collister & Lahav, 2004) and another by using red sequence models Song et al. (2012a). The artificial neural network was trained on several

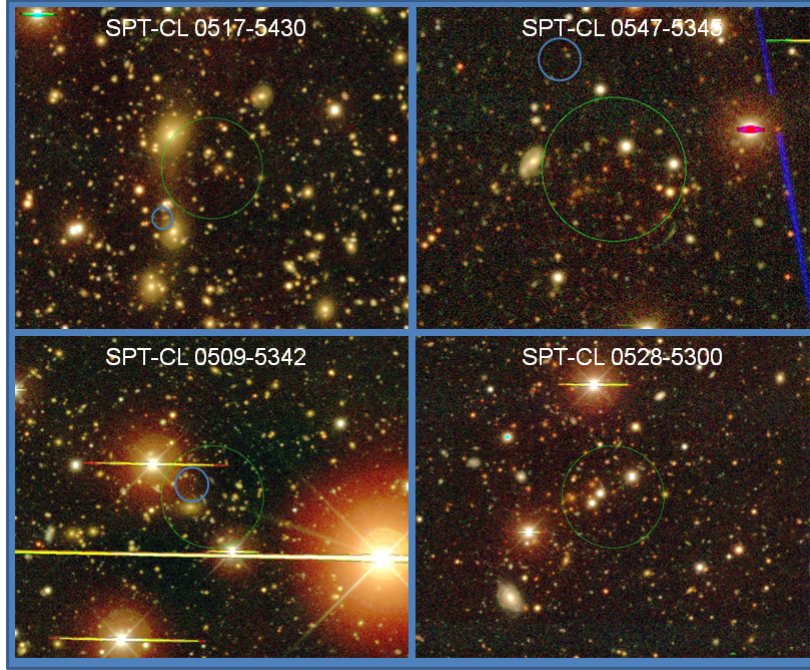


**Figure 2.4:** Blanco Cosmology Survey optical images for the first blind SZE cluster detections.

spectrophotometric fields observed during the BCS observation run and applied to the entire BCS cluster candidate catalog. The results produce accurate photometric redshifts out to  $z \approx 0.9$ . Red sequence models produce photometric redshifts by subtracting the photometric redshift histograms of galaxies within each cluster area from the histogram from the cluster background. The results reveal significant peaks at the clusters' redshifts. Additionally, cluster redshifts were predicted using passively evolving Simple Stellar Population (SSP) models (BC03, Bruzual & Charlot, 2003) given a Salpeter IMF and a formation redshift of  $z \approx 3$ .

## 2.2 First Data Release Results

The first cluster sample release comprises 21 clusters observed in 178 deg<sup>2</sup> surveyed in 2008 (Vanderlinde et al., 2010, V10 hereafter). From this sample, 12 detections were newly discovered clusters. The data processing and source extraction is very similar to that in V10, using only the 150 GHz band with a noise level of 18  $\mu$ K arcmin.

One of the characteristics of an SZE selected cluster sample is the well-understood selection function. By adding the SPT characteristics and observation strategy to simulations, V10 was able to estimate catalog completeness. The results showed the sample completeness to be nearly 100% above  $M_{200} \approx 5 \times 10^{14} M_{\odot} h^{-1}$  at  $z = 0.6$ , pushing the mass selection a bit lower at higher redshifts.

Along with a well-understood selection function, the cluster mass is required. The integrated SZ flux  $Y_{SZ}$  is predicted to be a tight proxy for cluster mass (e.g. Nagai et al., 2007) and can be obtained by integrating a  $\beta$ -profile (Eq. 2.5). In the SPT case, the 1 arcmin beam is not

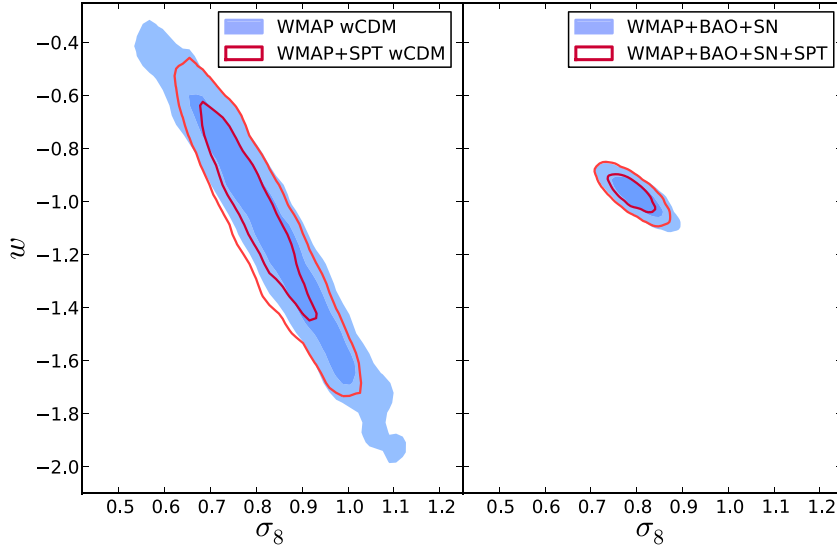


**Figure 2.5:** (Vanderlinde et al., 2010): First cosmology analysis on a SZE selected cluster sample. Combined with WMAP the errors in  $w$  are improved by 1.5

small enough to resolve  $\theta_c$ , and  $Y_{SZ}$  is poorly estimated. Under these conditions, a better quantity for mass estimation is the signal-to-noise ratio. Signal-to-noise maps are constructed by dividing each map by its noise (which is constant across SPT maps). The cluster signal-to-noise ( $\xi$ ) then is estimated as the highest signal-to-noise value associated with the cluster decrement, across all filter scales. However,  $\langle \xi \rangle$  (the average of  $\xi$  over many noise realizations) is a biased estimator of the significance. An unbiased significance estimator is found to be  $\zeta = \sqrt{\langle \xi \rangle^2 - 3}$  (for details see Appendix B in V10).

To use  $\zeta$  as a mass proxy, a calibration is required. The scaling relation between  $\langle \xi \rangle$  and mass is assumed to have the form:

$$\zeta = A \left( \frac{M}{5 \times 10^{14} M_\odot h^{-1}} \right)^B \left( \frac{1+z}{1.6} \right)^C. \quad (2.6)$$

The parameters  $A$ ,  $B$ , and  $C$  are found after fitting this equation to simulations:  $A = 6.01$ ,  $B = 1.31$  and  $C = 1.6$ . Once optically estimated redshifts (High et al., 2010) are determined, the cluster sample can be used for finding cosmological parameters. The Tinker mass function (Tinker et al., 2008) was used along with the matter power spectra computed by CAMB (Lewis et al., 2000), following § 1. The most significant result is when the SPT catalog is combined with the WMAP7 results, under a flat,  $\Lambda$ CDM cosmology, the precision on  $\sigma_8 = 0.81 \pm 0.09$  and  $w = -1.07 \pm 0.29$  is improved by 50% (see Fig. 2.5).

Besides using simulations, another way to calibrate the cluster mass is by using other cluster observables such as the  $Y_X$  signature in the X-ray. This parameter is the product of the cluster gas mass and temperature and can be used as a mass proxy. By including such extra information, Benson et al. (2013) extended the cosmological analysis presented by V10, on the same cluster sample.



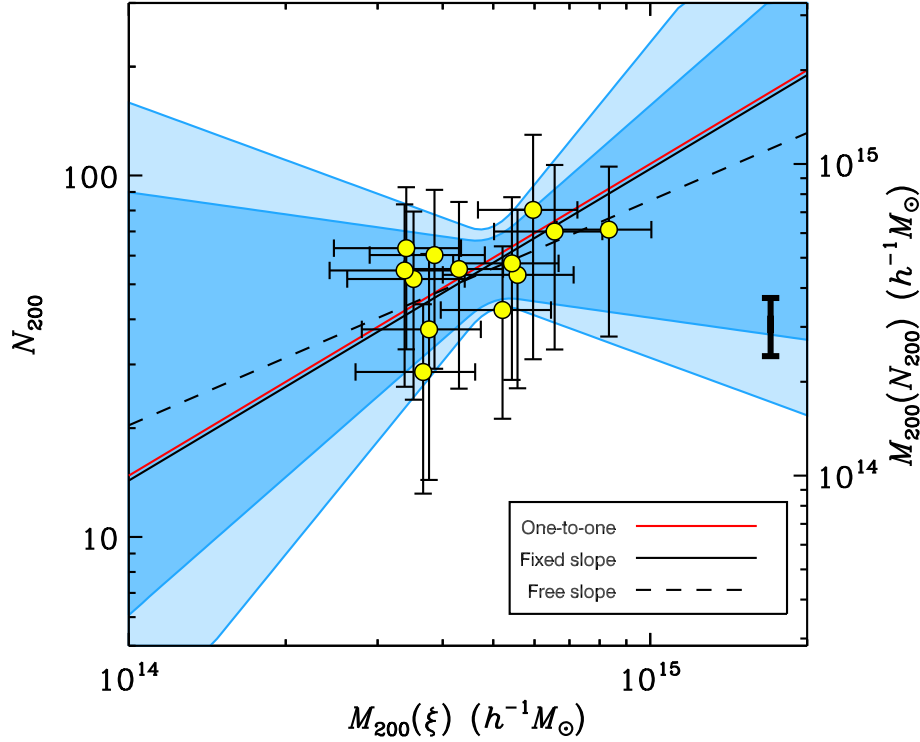


**Figure 2.6:** (High et al., 2010): Richness measurement on SZ selected clusters. Y-axis shows  $N_{200}$ , defined as the number of galaxies within  $R_{200}$ , and  $M_{200}$  defined as a function of  $N_{200}$  given published scaling relations (Reyes et al., 2008). X-axis shows the cluster mass estimated from SPT significance,  $\xi$ . In the darker blue the  $1\sigma$  contours are shown, assuming zero intrinsic richness-mass scatter while the lighter version correspond to  $1\sigma$  contours assuming 35% intrinsic richness-mass scatter. The dashed line is the best fit with slope and normalization free to float, the solid red line is the one-to-one relation, while the solid black line is obtained by fixing the slope and fitting for the normalization.

The release by V10 was accompanied by an optical effort reported in High et al. (2010). The optical companion used BCS and targeted Magellan observations to identify candidates, estimate photometric redshifts, and, for a subsample, obtain spectroscopic redshifts. Also, for the first time, richness measurements in SZE selected clusters were obtained. The main results can be seen in Fig. 2.6, where masses derived from a richness relation (Reyes et al., 2008) are compared to the V10 masses. It can be seen that, when the slope and intercept are left free (best-fit, dashed line and  $1\sigma$  area in dark blue), the result is consistent with a 1-to-1 relation between  $M_{200}(N_{200})$  and  $M_{200}(\xi)$  at the  $1\sigma$  level. Unfortunately, is very large (see also Fig. 5.6).

## 2.3 Second Data Release Results

The Second Data Release corresponds to a mix of deep and shallow observations over the total  $2500 \text{ deg}^2$  footprint which, given the sensitivity, correspond to the most massive systems in the SPT area. Williamson et al. (2011) presented the 26 galaxy clusters consisting of 14 known clusters and 12 new discoveries, with a wide redshift range ( $0.098 \leq z \leq 1.132$ ) and with masses of  $M_{200, \text{mean}} \geq 9.8 \times 10^{14} h_{70}^{-1} M_{\odot}$ . The masses were estimated as in V10 (§ 2.2),

**Table 2.1:** Mass Scaling Relations

Depth	A	B	C	Scatter
V10 sample	6.01	1.31	1.60	0.21
Full survey	7.50	1.32	1.64	0.21
Preview	3.50	1.29	0.87	0.16

with slightly different values for  $A$ ,  $B$ , and  $C$  in Eq. 2.6 (see Table 2.1).

As the mass function falls exponentially in the high-mass end (see Eq. 1.5), this sample is well-suited to test cosmological models. Furthermore, even a single massive cluster, especially at high redshift, can falsify the current cosmological paradigm. To test this possibility, Mortonson et al. (2011) predicted the likelihood of finding a cluster of a given mass at a given redshift given the current observations and cosmological model. By comparing exclusion limits at 95% to observations such as SPT-CL J0546–5345 (Brodwin et al., 2010), Mortonson et al. (2011) showed that such clusters do not rule out  $\Lambda$ CDM cosmology. Following the framework of Mortonson et al. (2011) exclusion curves, Williamson et al. (2011) presented the whole sample (Fig. 2.7), showing no individual cluster lying above the 95% exclusion line.

A detailed study of the optical properties of this sample is presented in Chapter 5.

## 2.4 Third Data Release Results

The most recently reported sample of the SPT results was published in Reichardt et al. (2013) on 720 deg<sup>2</sup>. It comprises 224 cluster candidates with 158 confirmed clusters that have a significance of  $\xi \geq 4.5$ . The median redshift of confirmed clusters in the sample is  $z = 0.55$ , and the highest redshift cluster is at  $z = 1.37$ . From the 158 confirmed clusters, 117 are newly discovered, totaling 144 newly discovered clusters by the SPT survey to date.

From a subsample of 100 clusters with  $\epsilon > 5$  (95% purity) and  $z > 0.3$ , cosmological parameters are derived. Following Benson et al. (2013), the cosmological parameters are obtained by using Monte Carlo Markov chain (MCMC) methods. As a key piece of knowledge, the connection between observable and mass depends on the assumed cosmology. To consider this dependence, the MCMC method fits simultaneously for both the SZ and the X-ray scaling relations and the cosmology. Also, information from several cosmological probes such as CMB, BAO, local measurements of  $H_0$ , and SNe is included. The cosmological parameters are shown in Table 2.2.

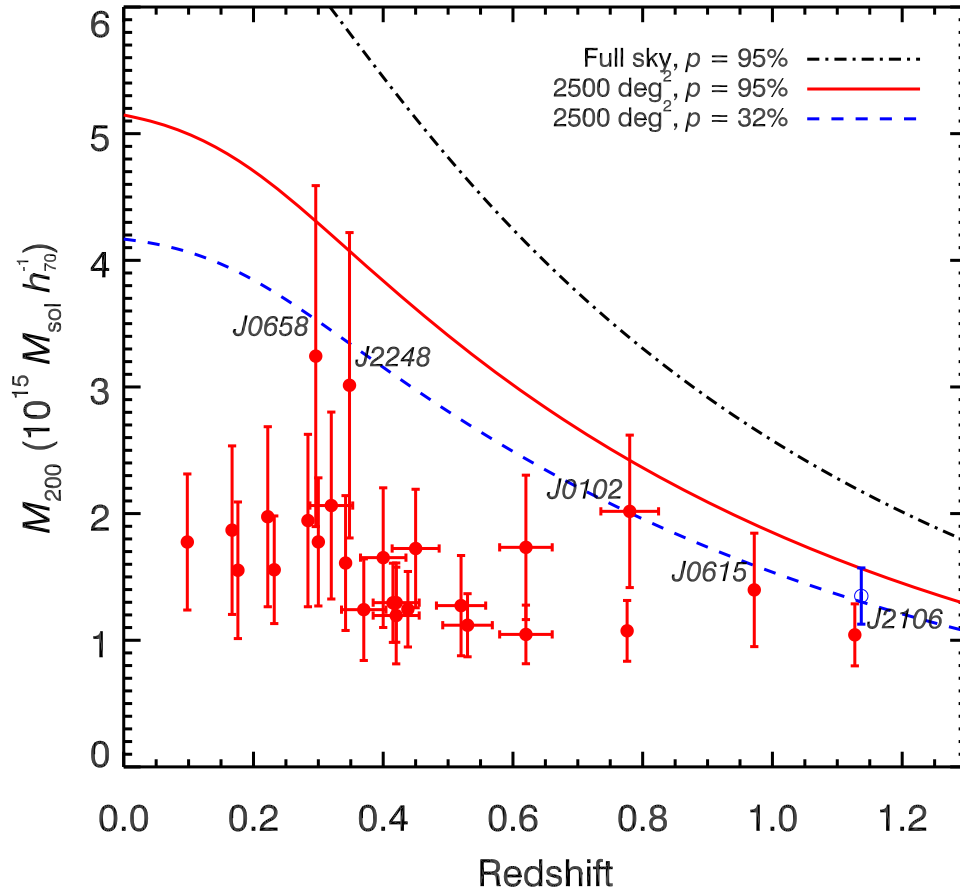


**Figure 2.7:** The 26 most massive clusters in the SPT footprint along with rarity curves showing agreement with current  $\Lambda$ CDM cosmology. Red solid line shows the mass above which a cluster at a given redshift is less than 5% likely to be found in the 2500 deg<sup>2</sup> SPT survey region in 95% of the  $\Lambda$ CDM parameter probability distribution. The black dash-dotted line is the equivalent for the whole sky. The blue line shows that SPT-CL J2106-5844 has less than 5% likely **Un-reworded**

**Table 2.2:** R12 Cosmological constraints

	$\Lambda$ CDM		wCDM		$\sum m_\nu$	
	CMB	+SPT <sub>CL</sub>	CMB + BAO + $H_0$ + SNe	+ SPT <sub>CL</sub>	CMB + BAO + $H_0$	+ SPT <sub>CL</sub>
$\Omega_c h^2$	$0.1109 \pm 0.0048$	$0.1086 \pm 0.0031$	$0.1140 \pm 0.0041$	$0.1104 \pm 0.0029$	$0.1113 \pm 0.0030$	$0.1113 \pm 0.0025$
$\sigma_8$	$0.808 \pm 0.024$	$0.798 \pm 0.017$	$0.840 \pm 0.038$	$0.807 \pm 0.027$	$0.775 \pm 0.041$	$0.766 \pm 0.028$
$\Omega_m$	$0.267 \pm 0.026$	$0.255 \pm 0.016$	$0.269 \pm 0.014$	$0.262 \pm 0.013$	$0.274 \pm 0.016$	$0.275 \pm 0.015$
$H_0$	$70.71 \pm 2.17$	$71.62 \pm 1.53$	$71.20 \pm 1.49$	$71.15 \pm 1.51$	$69.83 \pm 1.36$	$69.76 \pm 1.31$
$w$			$-1.054 \pm 0.073$	$-1.010 \pm 0.058$	$< 0.44$	$< 0.38$
$\sum m_\nu$						

Cosmological constraints results from Reichardt et al. (2013). Results shown for three models with and without the SPT cluster sample.



A companion paper describing the optical effort with this data release, was published (Song et al., 2012b) and is part of this thesis. We refer the reader to Chapter 3 for details.

## 2.5 X-ray Studies of SPT SZE selected Galaxy Clusters

To trace the evolution of the Universe with cluster abundances, it is important to have three ingredients: a cluster sample with a well-understood selection function, cluster redshifts, and cluster masses. An SZE selected sample such as the SPT survey is expected to be nearly redshift independent and mass limited, so the selection function is easy to understand. This survey also has optical/NIR follow-up in Staniszewski et al. (2009); High et al. (2010); Song et al. (2012b), which provide spectroscopic and photometric redshifts. The third ingredient is the cluster masses. Simulations show that the observable that correlates with cluster mass with very low scatter is the cluster's Temperature  $\times$  Gas Mass (Kravtsov et al., 2006). As the SZ intensity is proportional to the line-of-sight integrated gas pressure, the SZ signal integrated over the cluster extent is expected to be tightly correlated with the cluster mass. In § 2.2, § 2.3, and § 2.4 the mass calibration made no use of the SZ flux but the signal-to-noise was employed as the observable. This is due to the 1 arcmin SPT resolution which is comparable to the cluster projected size. At that scale, the  $\theta_c$  in the  $\beta$ -model (Eq. 2.5) cannot be properly recovered except in the largest (as projected along the sky) clusters, making the SZ flux poorly estimated. The SZ flux measurements can be improved by the use of a profile extracted from external observations such as the X-ray gas density profile (Melin et al., 2006). Furthermore, X-ray hydrostatic mass measurements can be compared to those SZ masses calibrated with simulations. With those goals in mind, Andersson et al. (2011) selected the 15 most significant clusters from V10 ( $\xi \geq 5.4$ ) and used their X-ray profiles (a modified  $\beta$ -model multiplied by a temperature profile) to recover the integrated Comptonization  $Y_{SZ}$  of each cluster. The ratio between the *observed*  $Y_{SZ}$  versus  $Y_X$  render a normalization of  $0.82 \pm 0.07$  which is  $1.5\sigma$  lower than the expectation from the ratio of the *predicted*  $Y_{SZ}$  and  $Y_X$  of  $0.91 \pm 0.01$  and the value  $0.924 \pm 0.004$  from the literature (Arnaud et al., 2010). However, the *predicted*  $Y_{SZ}$  values were obtained from the X-ray density and temperature profiles and, due to the different weighting of the temperature profile, the ratio was not expected to be 1. The ratio between the SZ and X-ray mass is  $0.78 \pm 0.06$  and is shown in Fig. 2.8.

If the comparison between  $Y_{SZ}$  and  $M_{500,Y_X}$  is drawn, the following equation is fit

$$Y_{SZ} = 10^A \left( \frac{M_{500,Y_X}}{3 \times 10^{14} M_\odot} \right)^B E(z)^{2/3} M_\odot keV,$$

with  $A = 10^{14.06}$  and  $B = 1.67 \pm 0.29$ .

These X-ray results point to a tight correlation between SZ observables and mass as measured by X-rays. It also illustrates the prominent role X-ray observations have in calibrating the SZ signal. This calibration is key to ultimately extract cosmological parameters from cluster abundances as a function of redshift.

X-ray studies of SPT clusters have been fruitful in other aspects beyond SZ calibration or cosmology. For example, the SZ sample is an excellent opportunity to study the evolution of

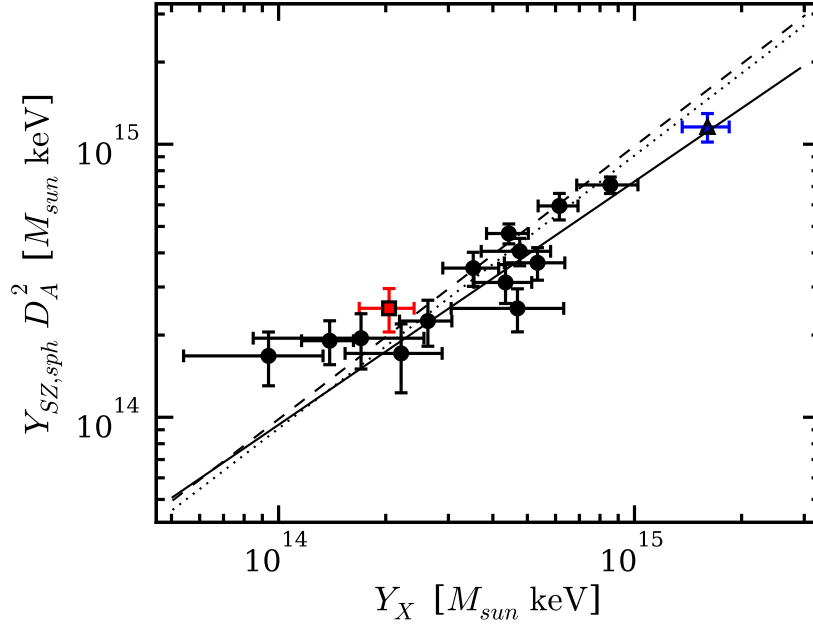


**Figure 2.8:** Solid line is the best fit relation, dashed line is the equality relation and dotted line is the expectation from Arnaud et al. (2010) with a normalization ratio of 0.924.

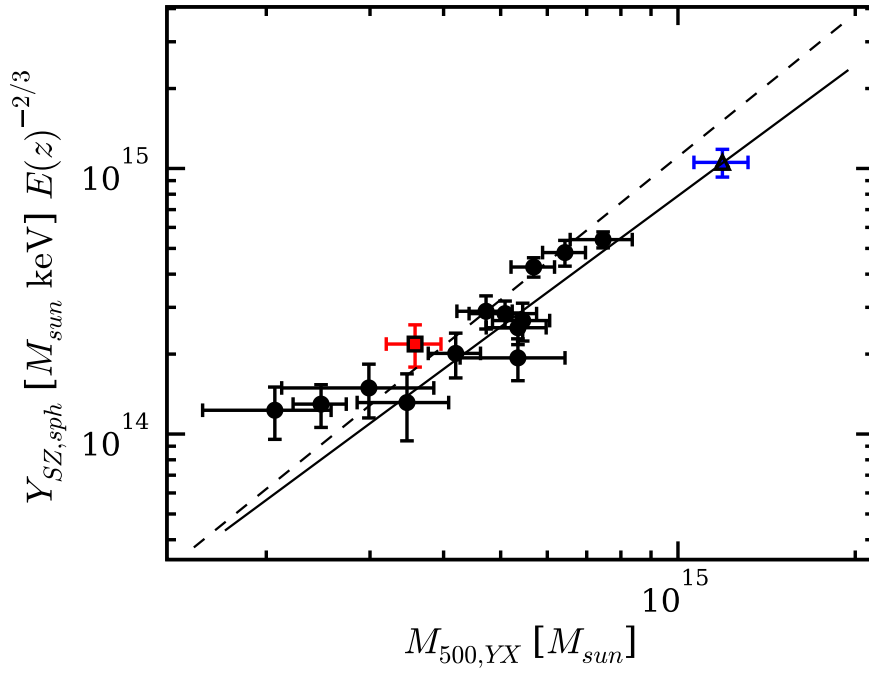


**Figure 2.9:**  $Y_{SZ} - M_{500}$  relation for the Andersson et al. (2011) sample. The plot show illustrate...

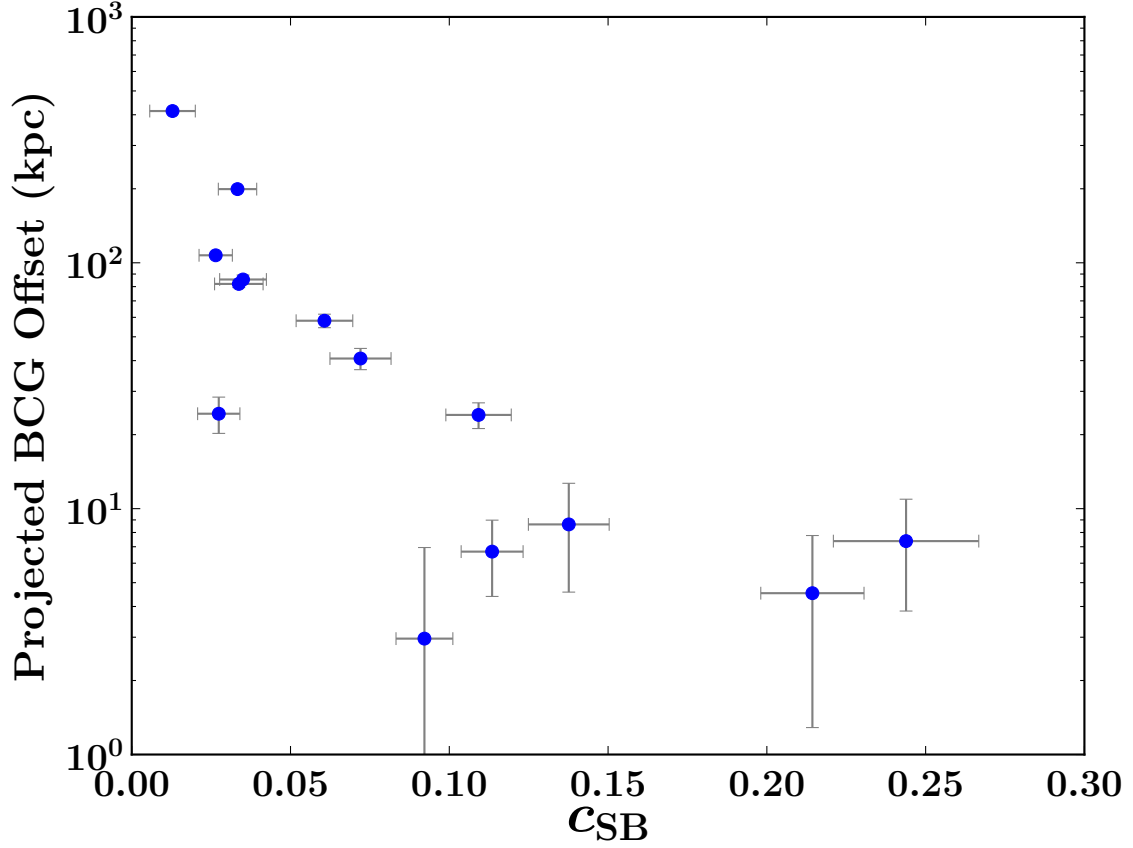


**Figure 2.10:** Projected offset between the BCG and the X-ray centroid as a function of the surface brightness concentration.

cool-core clusters and their effect in the cluster BCG. Semler et al. (2012) used 13 clusters selected from 178 deg<sup>2</sup> of the SPT footprint that were followed-up with X-rays observations with *Chandra*. Using the surface brightness concentration (defined as  $c_{SB} = F_{r<40 \text{ kpc}}/F_{r<400 \text{ kpc}}$ ) as a proxy for cool-core strength, they found the high-redshift distribution of cool-core clusters selected via the SZE is statistically consistent with that of X-ray-selected samples. However, the sample of Semler et al. (2012) includes the two strong cool-core clusters at  $z \geq 0.5$ , the first discovery of such objects. They also found a correlation of BCG–X-ray centroid offset with  $c_{SB}$  which indicate that the presence of a cool core correlates with the dynamical state of a cluster (see Fig. 2.10).

The connection between cool cores and the central galaxy is an important one. As the intracluster hot gas loses energy through *Bremsstrahlung* radiation, it cools, falling to the cluster core. As the gas is accreted and cooled, mass deposition on the order of  $1000 M_{\odot} \text{ yr}^{-1}$  is expected in the center. This tremendous mass deposition rate is expected to fuel large amounts of star formation in the central galaxy. However, with only a exceptions, high star formation rates are not observed (e.g. Fabian, 1994). One of the exceptions is SPT-CLJ2344–4243, also known as the Phoenix cluster (see fig. 2.11). At a redshift of  $z = 0.596$ , SPT-CLJ2344–4243 shows an extremely strong cooling flow on the order of  $M_{\text{cool}} = 3820 \pm$

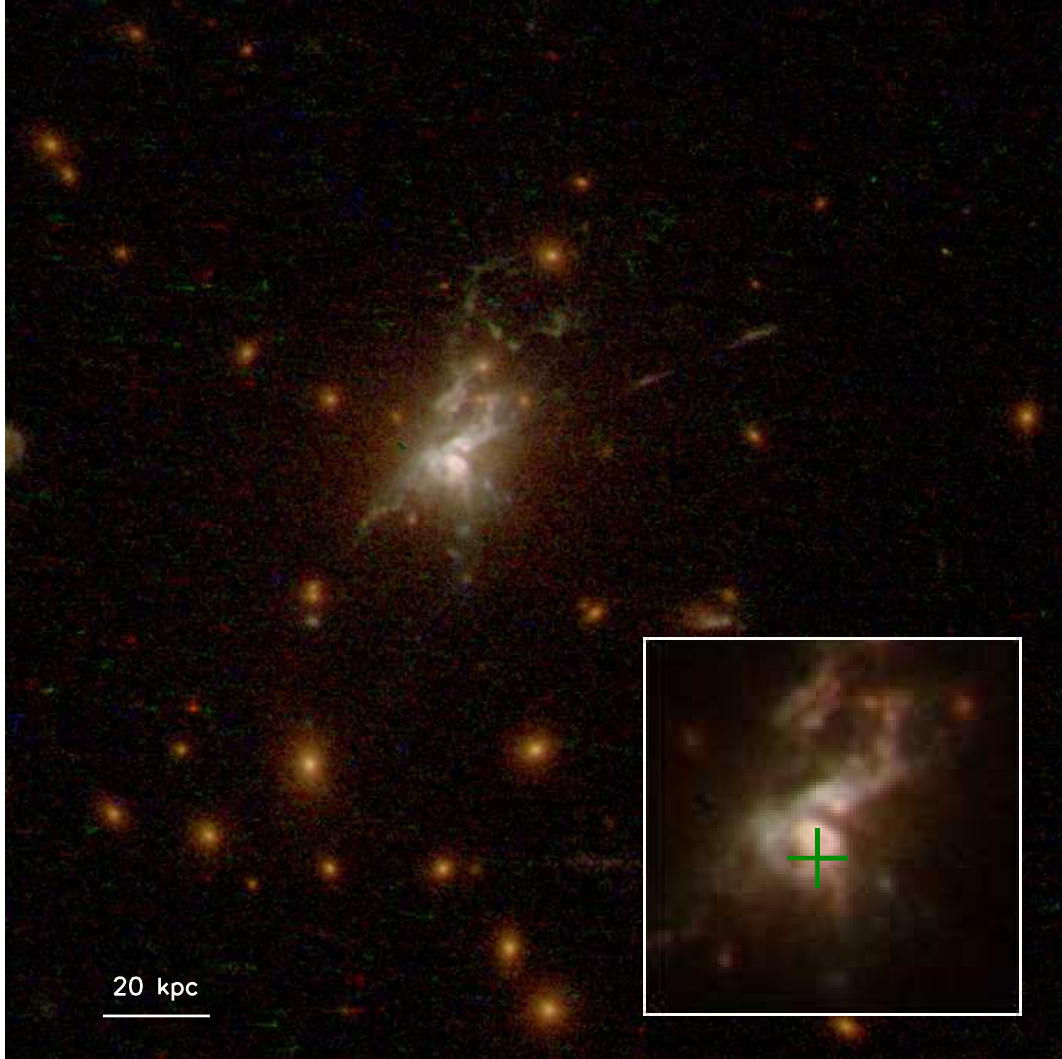


**Figure 2.11:** BCG in a cool core cluster with massive star formation

$539 M_{\odot} \text{ yr}^{-1}$  with the BCG experiencing a massive star formation rate of  $740 \pm 160 M_{\odot} \text{ yr}^{-1}$  (McDonald et al., 2012a, 2013). The sole existence of a cluster with such high levels of cooling points to the possibility of a brief phase of massive BCG growth through accretion of intracluster gas rather than galactic merging events.

Expanding on the work of Semler et al. (2012), McDonald et al. (2013) used 83 SPT clusters in a redshift range of  $0.3 < z < 1.2$ . The clusters were observed as part of a *Chandra* X-ray Visionary Project to measure X-ray properties of the most massive clusters detected in the first 2000  $\text{deg}^2$  of the SPT survey. McDonald et al. (2013) present the cluster cooling properties such as the central cooling time, central entropy and mass deposition rate. Their results show no evolution of such properties (see Fig. 2.12), revealing that the mechanism that balance the cooling flow (e.g., feedback from active galactic nuclei) is stable over very long timescales. Their results also reveal that for clusters that show cooling signatures their central density increases by a factor of 10 during the same period of time with the consequent

increase in surface brightness.

## 2.6 Weak Lensing Results

As mentioned above, a crucial part of SZ cluster cosmology is the mass-observable calibration. One of the best techniques to measure the cluster mass is to observe the gravitational bending of the surrounding space. The strength of the weak lensing (WL) technique is that it probes the total (projected) mass and is insensitive to the dynamical state of the cluster (i.e., the lens). Several studies on individual SPT clusters have been carried out (e.g. McInnes et al., 2009; Gruen et al., 2013a,b). Within the SPT collaboration, High et al. (2012) carried out a pilot study on 5 SPT clusters comparing WL to SZ masses. The main result is a WL/SZ mean spherical mass ratio of  $1.10 \pm 0.24$  measured within  $R_{500,WL}$  or  $1.07 \pm 0.18$  when it is measured within  $R_{500,SZ}$ . Weak lensing scaling relations are crucial for calibrating  $Y_{SZ}$  and efforts in this direction are currently being undertaken (Dietrich et al., *in prep.*).

Where galaxy clusters are in particularly fortuitous alignment with a bright background source, strong lensing (SL) analyses can be produced. While the techniques cannot be applied to most clusters, these results they produce are generally more precise than WL analyses. Buckley-Geer et al. (2011) studied a single cluster SPT-CL J2351–5452 with a beautiful Einstein ring which they name *The Elliot Arc*. In this system the lens is at  $z = 0.3838$  and the arc is at  $z=0.9057$ . Combining WL, SL plus velocity dispersion, SPT-CL J2351–5452 is estimated to have a mass of  $M_{200} = 5.1 \pm 1.3 \times 10^{14} M_{\odot}$ .

## 2.7 Special clusters

As a mass-limited survey, the SPT sample contains the most massive clusters in the Universe. The number of massive clusters can be used to constrain cosmology or to falsify it. Finding an extremely massive cluster at high redshift could expose a contradiction between the expansion history and the prediction of the growth of large-scale structure by the  $\Lambda$ CDM model (Mortonson et al., 2011). Using SPT clusters, this scenario is briefly discussed in Brodwin et al. (2010) and quantitatively analysed in Foley et al. (2011). Foley et al. (2011) reported on SPT-CL J2106–5844, a cluster at redshift 1.132 and discovered within the 2500 deg<sup>2</sup> SPT survey footprint. They show a probability of 7% of finding a single cluster with the same or greater mass and redshift as SPT-CL J2106–5844 within current cosmology. This corresponds to a likelihood of finding just one such cluster in the entire sky. Furthering this analysis, following Mortonson et al. (2011), Williamson et al. (2011) plot mass versus redshift for the 26 most massive clusters in the entire SPT footprint and compare the results to probability curves of levels where the  $\Lambda$ CDM model is falsified (see Fig. 2.7).

Another special cluster is SPT-CL J0205–5829, which lies at  $z = 1.322$ . At the time of discovery it was the highest spectroscopically confirmed SPT cluster (Stalder et al., 2013). Currently SPT-CL J2040–4451 holds that honor with a redshift of  $z = 1.478$  (Bayliss et al., 2013). However, neither of these are massive enough to falsify  $\Lambda$ CDM cosmology. In terms of galaxy evolution, Brodwin et al. (2010); Foley et al. (2011) and Stalder et al. (2013) at redshifts 1.067, 1.132, and 1.322 respectively, show a similar picture with a well-established red sequence and no star formation. However, the highest redshift cluster, SPT-CL J2040–4451, at  $z = 1.478$ , seems to change this picture. Using the same galaxy selection method for spectroscopic

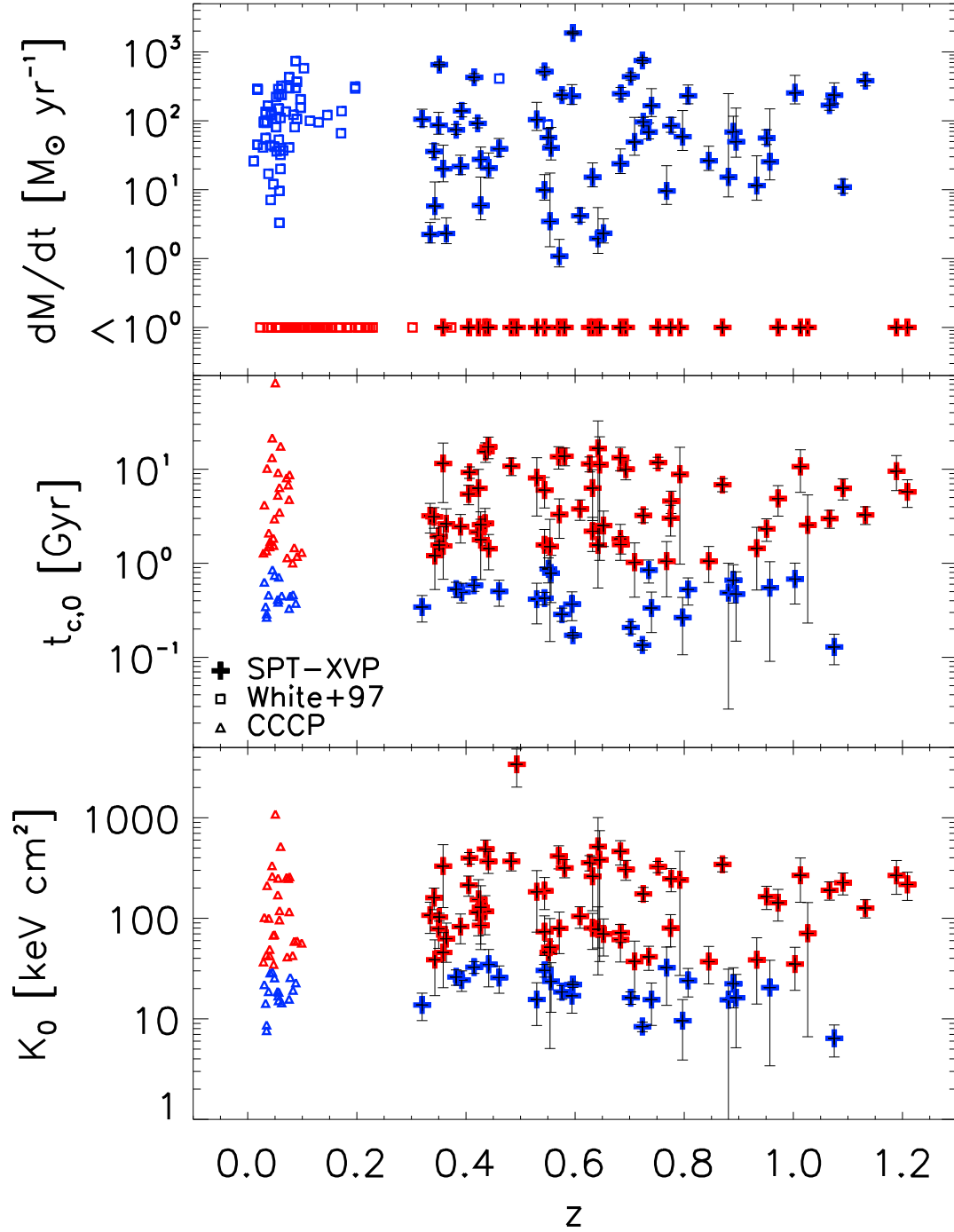


Figure 2.12: Redshift evolution of cooling properties

observations as the other three clusters, 15 of the 59 spectra of SPT-CLJ2040–4451 member galaxies show interesting star formation features. This is interesting because several papers such as Mancone et al. (2010); Brodwin et al. (2013) claim that at  $z \gtrsim 1.4$ , clusters are still in the process of assembling their galaxy population. These authors suggest the possibility that at that redshift, there is a transition in star formation that takes place. As the SPT sample grows, we are expecting to be able to test this picture with a larger cluster sample, focusing on galaxies that are in the bottom of the cluster potential well, a prime spot to access the gas required for star formation (as we have seen in an spectacular way in McDonald et al. (2012a,b)).

## 2.8 Submillimeter Galaxies

Point sources are common in the SPT CMB maps. For example, AGNs were a source of noise that was expected. While AGNs are found in the SPT CMB maps, they are not the only point sources found. With the use of the three SPT bands, AGNs show a flat or decreasing brightness with decreasing wavelength ( $S \propto \lambda^{-1}$ ). On the other hand, sources with increasing brightness with decreasing wavelength were also found ( $S \propto \lambda^{-3}$ ). These are identified as emission from dusty star forming galaxies. This unexpected discovery is related to lensed submillimeter galaxies or SMG. The first analyses of these objects in the SPT survey were published in Vieira et al. (2010). Within  $87 \text{ deg}^2$  (Vieira et al., 2010) found 141 synchrotron-dominated sources (AGNs) and 47 dust-dominated sources (SMGs). Most of the significant AGNs that were discovered were previously published in radio catalogs.

## 2.9 Conclusion

As we have seen, the SZE is fulfilling its promise as a powerful tool to test cosmological models as well as to constrain cosmological parameters. The cluster sample assembled is also well suited for astrophysical studies such as cool core evolution and star formation in the central BCGs. Furthermore, a research front for which the SPT sample is also ideally suited is the study of galaxy formation and evolution. Clusters have a long history as laboratories for the study of galaxy properties, and an SZE-selected sample has the power to reveal, in a consistent and statistically significant manner, evolutionary trends in the galaxy population as well as the mechanisms that shape them. In the following Chapters we present our efforts to characterize the galaxy populations and their evolution within the SPT galaxy cluster sample.





# Redshifts, Sample Purity, and BCG Positions for the Galaxy Cluster Catalog from the first 720 Square Degrees of the South Pole Telescope Survey

## 3.1 Abstract

We present the results of the ground- and space-based optical and near-infrared (NIR) follow-up of 224 galaxy cluster candidates detected with the Sunyaev-Zel'dovich (SZ) effect in the 720 deg<sup>2</sup> of the South Pole Telescope (SPT) survey completed in the 2008 and 2009 observing seasons. We use the optical/NIR data to establish whether each candidate is associated with an overdensity of galaxies and to estimate the cluster redshift. Most photometric redshifts are derived through a combination of three different cluster redshift estimators using red-sequence galaxies, resulting in an accuracy of  $\Delta z/(1+z) = 0.017$ , determined through comparison with a subsample of 57 clusters for which we have spectroscopic redshifts. We successfully measure redshifts for 158 systems and present redshift lower limits for the remaining candidates. The redshift distribution of the confirmed clusters extends to  $z = 1.35$  with a median of  $z_{\text{med}} = 0.57$ . Approximately 18% of the sample with measured redshifts lies at  $z > 0.8$ . We estimate a lower limit to the purity of this SPT SZ-selected sample by assuming that all unconfirmed clusters are noise fluctuations in the SPT data. We show that the cumulative purity at detection significance  $\xi > 5$  ( $\xi > 4.5$ ) is  $\geq 95\%$  ( $\geq 70\%$ ). We present the red brightest cluster galaxy (rBCG) positions for the sample and examine the offsets between the SPT candidate position and the rBCG. The radial distribution of offsets is similar to that seen in X-ray-selected cluster samples, providing no evidence that SZ-selected cluster samples include a different fraction of recent mergers than X-ray-selected cluster samples.

GALAXIES: CLUSTERS: GENERAL — GALAXIES: DISTANCES AND REDSHIFTS — COSMOLOGY: OBSERVATIONS

## 3.2 Introduction

In November 2011, the South Pole Telescope (SPT; Carlstrom et al., 2011) collaboration completed a 2500 deg<sup>2</sup> survey, primarily aimed at detecting distant, massive galaxy clusters through their Sunyaev-Zel'dovich (SZ) effect signature. In Reichardt et al. (2013, R13 hereafter), the SPT team presented a catalog of 224 cluster candidates from 720 deg<sup>2</sup> observed in the 2008-2009 seasons. In this work, we present the optical and near-infrared (NIR) follow-up observations of the cluster candidates reported in R13, mainly focusing on follow-up strategy, confirmation and empirical purity estimate for the cluster candidates, photometric redshift estimations of confirmed clusters, and the spatial position of the red brightest cluster galaxies. Galaxy clusters have long been used for the study of structure formation and cosmology (e.g., Geller & Beers, 1982; White et al., 1993). Soon after the discovery of the cosmic acceleration (Schmidt et al., 1998; Perlmutter et al., 1999), it became clear that measurements of the redshift evolution of the cluster mass function could provide a powerful tool to further understand the underlying causes (Wang & Steinhardt, 1998; Haiman et al., 2001; Holder et al., 2001; Battye & Weller, 2003). More precise theoretical investigations (Majumdar & Mohr, 2003; Hu, 2003; Majumdar & Mohr, 2004; Molnar et al., 2004; Wang et al., 2004; Lima & Hu, 2005, 2007) identified the key challenges associated with cluster surveys, which include: (1) producing large uncontaminated samples selected by an observable property that is closely related to the cluster mass, (2) measuring cluster redshifts for large samples and (3) precisely calibrating the cluster masses.

Competitive approaches to producing large cluster samples include optical multiband surveys (e.g., Gladders & Yee, 2005; Koester et al., 2007), infrared surveys (e.g., Eisenhardt et al., 2008; Muzzin et al., 2008; Papovich, 2008), X-ray surveys (e.g., Finoguenov et al., 2007; Pacaud et al., 2007; Vikhlinin et al., 2009; Finoguenov et al., 2010; Mantz et al., 2010; Fassbender et al., 2011; Lloyd-Davies et al., 2011; Šuhada et al., 2012), and millimeter-wave (mm-wave) surveys (Vanderlinde et al., 2010; Marriage et al., 2011; Planck Collaboration et al., 2011b; Reichardt et al., 2013). The mm-wave surveys capitalize on the cluster SZ effect signature, which is produced by the inverse Compton scattering of cosmic microwave background photons by the energetic electrons within the cluster (Sunyaev & Zel'dovich, 1972). The surface brightness of the SZ effect is redshift-independent, making SZ surveys a particularly powerful tool for identifying the most distant clusters. It is typical for X-ray and mm-wave surveys to have accompanying multiband optical imaging to enable photometric redshift measurements; these multiband optical data also enable a second stage of cluster candidate confirmation, verifying the purity estimation of the X-ray or SZ-selected cluster samples.

Ideally, one would coordinate an SZ survey with a deep, multiband optical survey over the same region; indeed, the Dark Energy Survey (DES<sup>1</sup>; Cease et al., 2008; Mohr et al., 2008) and the SPT are coordinated in this way. Because of the different development timelines for the two projects, it has been necessary to undertake extensive cluster-by-cluster imaging follow-up for SPT using a series of ground-based telescopes together with space-based NIR imaging (from *Spitzer* and *WISE*). The NIR data are of particular importance in the confirmation and redshift estimation of the  $z > 1$  massive galaxy clusters, which are especially interesting for both cosmological studies and studies of the evolution of clusters themselves. Pointed observations were used in High et al. (2010, H10 hereafter) to provide redshift and richness

---

<sup>1</sup>[www.darkenergysurvey.org](http://www.darkenergysurvey.org)

estimates of the SZ detections of Vanderlinde et al. (2010), and subsequently by Williamson et al. (2011) and Story et al. (2011).

Cluster samples from high-resolution SZ surveys can be also used to explore the evolution of cluster properties as a function of redshift. Previous studies using X-ray-selected clusters have identified a correlation between the dynamical state of a cluster and the projected offset between the X-ray centers and the brightest cluster galaxy (e.g., Katayama et al., 2003; Sanderson et al., 2009; Haarsma et al., 2010; Fassbender et al., 2011; Stott et al., 2012). In principle, SZ-selected clusters can serve as laboratories to search for this correlation also, if the spatial resolution of SZ detections is high enough to detect the significance of offsets between the SZ centers and the brightest cluster galaxies. Systematic comparison between X-ray and SZ samples will indicate if the selection of the two methods differs in terms of the dynamical state of clusters.

This paper is structured as follows: we briefly describe the SPT data and methods for extracting the cluster sample in §3.3.1. In §3.3.2, we provide details of the follow-up strategy, as well as data processing. §3.4 is dedicated to a detailed description of the analysis of our follow-up data, including redshift estimation using optical and *Spitzer* data, the derivation of redshift lower limits for those systems that are not confirmed, and the selection of red brightest cluster galaxies (rBCGs) in the clusters. Results are presented in §5.5 and discussed further in §3.6. Throughout this paper, we use the AB magnitude system for optical and NIR observations unless otherwise noted in the text.

### 3.3 Discovery & Followup

#### 3.3.1 SPT Data

Here we briefly summarize the analysis of the SPT data and the extraction of cluster candidates from that data; we refer the reader to R13 and previous SPT cluster publications (Staniszewski et al., 2009; Vanderlinde et al., 2010; Williamson et al., 2011) for more details. The SPT operates in three frequency bands, although only data from the 95 GHz and 150 GHz detectors were used in finding clusters. The data from all detectors at a given observing frequency during an observing period (usually 1-2 hours) are combined into a single map. The data undergo quality cuts and are high-pass filtered and inverse-noise-weighted before being combined into a map. Many individual-observation maps of every field are co-added (again using inverse noise weighting) into a full-depth map of that field, and the individual-observation maps are differenced to estimate the map noise. The 95 GHz and 150 GHz full-depth maps of a given field are then combined using a spatial-spectral matched filter (e.g., Melin et al., 2006) that optimizes signal-to-noise on cluster-shaped objects with an SZ spectral signature. Cluster candidates are identified in the resulting filtered map using a simple peak detection algorithm, and each candidate is assigned a signal-to-noise value based on the peak amplitude divided by the RMS of the filtered map in the neighborhood of the peak. Twelve different matched filters are used, each assuming a different scale radius for the cluster, and the maximum signal-to-noise for a given candidate across all filter scales is referred to as  $\xi$ , which we use as our primary SZ observable. In 2008, the 95 GHz detectors in the SPT receiver had significantly lower sensitivity than the 150 GHz array, and the cluster candidates from those observations are identified using 150 GHz data only; the candidates from 2009 observations were identified using data from both bands. The data from the two observing seasons yielded a total of 224 cluster candidates with  $\xi \geq 4.5$ —the sample discussed

here.

### 3.3.2 Optical/NIR Imaging

The cluster candidates detected using the method described above are followed up by optical and, in many cases, NIR instruments. In this section, we describe the overall optical/NIR follow-up strategy, the different imaging and spectroscopic observations and facilities used, and the data reduction methods used to process the raw images to catalogs.

#### Imaging Observations

The optical/NIR follow-up strategy has evolved since the first SPT-SZ candidates were identified. Originally we imaged regions of the sky with uniformly deep, multiband observations in *griz* optical bands to confirm SZ detections and estimate redshifts as in Staniszewski et al. (2009). For the first SPT cluster candidates, we used imaging from the Blanco Cosmology Survey (BCS; Desai et al., 2012b) to follow up candidates in parts of the 2008 fields. The BCS is a 60-night,  $\sim 80 \text{ deg}^2$  NOAO survey program carried out in 2005-2008 using the Blanco/MOSAIC2 *griz* filters. The BCS survey was completed to the required depths for  $5\sigma$  detection at  $0.4L^*$  within  $2''3$  apertures up to  $z \sim 1$ . The goal of this survey was to provide optical imaging over a limited area of the SPT survey to enable rapid optical follow-up of the initial SPT survey fields.

For clusters outside the BCS region we initially obtained deep *griz* imaging on a cluster-by-cluster basis. But as the SPT survey proceeded and the cluster candidate list grew, it became clear that this strategy was too costly, given the limited access to follow-up time. Moreover, eventually the full SPT region will be imaged to uniform  $10\sigma$  depths of  $\text{mag} \sim 24$  in *griz* by the DES. We therefore switched to an adaptive strategy of follow-up in which we observed each SPT cluster candidate to the depth required to find an optical counterpart and determine its redshift.

For each SPT cluster candidate, we perform an initial pre-screening of candidates using the Digitized Sky Survey (DSS)<sup>2</sup>. We examine DSS images using 3 bands<sup>3</sup> for each cluster candidate to determine whether it is “low- $z$ ” or “high- $z$ ,” where the redshift boundary lies roughly at  $z = 0.5$ . We find that this visual classification identifies spectroscopically and photometrically confirmed SPT clusters out to  $z=0.5$  in the DSS photographic plates. We use the DSS designation to prioritize the target list for the appropriate telescope, instrument and filters with which we observe each candidate. Specifically, candidates that are clearly identified in DSS images are likely to be low- $z$  clusters and are designated for follow-up observations on small-aperture (1m-2m) telescopes. Otherwise, candidates are classified as high- $z$  candidates and therefore designated for large-aperture (4m-6.5m) telescopes. The various ground- and space-based facilities used to collect optical/NIR imaging data on SPT clusters are summarized in Table 3.1. Each telescope/instrument combination is assigned a numeric alias that is used to identify the source of the redshift data for each cluster in Table 3.3.

For the  $\geq 4\text{m}$ -class observations, we use an adaptive filter and exposure time strategy so that we can efficiently bracket the cluster member galaxy’s 4000Å break to the depth required for redshift estimation. In this approach we start with a first imaging pass, where each candidate is observed in the *g*, *r*, and *z* bands to achieve a depth corresponding to a  $5\sigma$  detection of a

---

<sup>2</sup><http://archive.stsci.edu/dss/>

<sup>3</sup><http://gsss.stsci.edu/SkySurveys/Surveys.htm>

**Table 3.1:** Optical and infrared imagers

Ref. <sup>a</sup>	Site	Telescope	Aperture (m)	Camera	Filters <sup>b</sup>	Field	Pixel scale (")
1	Cerro Tololo	Blanco	4	MOSAIC-II	<i>griz</i>	36' × 36'	0.27
2	Las Campanas	Magellan/Baade	6.5	IMACS f/2	<i>griz</i>	27.4 × 27.4	0.200
3	Las Campanas	Magellan/Clay	6.5	LDSS3	<i>griz</i>	8.3 diam. circle	0.189
4 <sup>c</sup>	Las Campanas	Magellan/Clay	6.5	Megacam	<i>gri</i>	25' × 25'	0.16
5	Las Campanas	Swope	1	SITe3	<i>BVRI</i>	14.8 × 22.8	0.435
6	Cerro Tololo	Blanco	4	NEWFIRM	<i>K<sub>s</sub></i>	28' × 28'	0.4
7		Spitzer Space Telescope	0.85	IRAC	3.6μm, 4.5μm	5.2 × 5.2	1.2
8		WISE	0.40		3.4μm, 4.6μm	47' × 47'	6

**Notes:** Optical and infrared cameras used in SPT follow-up observations.

<sup>a</sup> Shorthand alias used in Table 3.3.

<sup>b</sup> Not all filters were used on every cluster.

<sup>c</sup> Megacam data were acquired for a large follow-up weak-lensing program.

0.4 $L^*$  galaxy at  $z = 0.8$ ,  $\sim 23.5$  mag and 21.8 mag in  $r$  and  $z$  bands respectively, based on the Bruzual & Charlot (2003) red-sequence model (for more details about the model, see § 3.4.1). Observations are also taken in a single blue filter for photometric calibration using the stellar locus (discussed in §3.3.2). For candidates with no obvious optical counterpart after first-pass observations, a second-pass is executed to get to  $z = 0.9$ ,  $\sim 23$  mag and 22 mag in  $i$  and  $z$  bands respectively.

If the candidate is still not confirmed after the second-pass in  $i$  and  $z$  bands, and is not covered by the *Spitzer*/IRAC pointed observations described below, we attempt to obtain ground-based NIR imaging for that candidate using the NEWFIRM camera on the CTIO Blanco telescope. The data presented here are imaged with NEWFIRM during three observing runs in 2010 and 2011, yielding  $K_s$  data for a total of 31 candidates. Typical observations in  $K_s$  consist of 16 point dither patterns, with 60 second exposures divided among 6 coadds at each dither position. Median seeing during the 2010 runs was 1''.05; during the 2011 run observing conditions were highly variable and the seeing ranged from 1''.05 to 2''.6 with median seeing  $\sim 1''.2$ .

We note that most of the galaxy cluster candidates in this work with significance  $\xi > 4.8$  were imaged with *Spitzer* (Werner et al., 2004). More specifically, *Spitzer*/IRAC (Fazio et al., 2004) imaging has been obtained for 99 SZ cluster candidates in this work. The on-target *Spitzer* observations consist of 8×100 s and 6×30 s dithered exposures at 3.6μm and 4.5μm, respectively. The deep 3.6μm observations should produce 5 $\sigma$  detections of passively-evolving 0.1 $L^*$  cluster galaxies at  $z = 1.5$  at  $z = 1.5$  ( $\sim 17.8$  mag (Vega) at  $z = 1.5$ ).

For some of the NIR analysis, we augment the data from our *Spitzer* and NEWFIRM observations with the recently released all-sky Wide-field Infrared Survey Explorer (*WISE*; Wright et al., 2010) data. Finally, we note that a few of the clusters were observed with Magellan/Megacam to obtain weak gravitational lensing mass measurements (High et al., 2012). These data are naturally much deeper than our initial followup imaging.

## Data Processing

We use two independent optical data processing systems. One system, which we refer to as the PHOTPIPE pipeline, is used to process all optical data except Magellan/Megacam data,

and the other, which is a development version of the Dark Energy Survey data management (DESDM) system, is used only to process the Blanco/Mosaic2 data. PHOTPIPE was used to process optical data for previous SPT cluster catalogs (Vanderlinde et al., 2010; High et al., 2010; Williamson et al., 2011); the DESDM system has been used as a cross-check in these works and was the primary reduction pipeline used in Staniszewski et al. (2009).

The basic stages of the PHOTPIPE pipeline, initially developed for the SuperMACHO and ESSENCE projects and described in Rest et al. (2005), Garg et al. (2007), and Miknaitis et al. (2007), include flat-fielding, astrometry, coadding, and source extraction. Further details are given in H10. In the DESDM system (Ngeow et al., 2006; Mohr et al., 2008; Desai et al., 2012b), the data from each night first undergo detrending corrections, which include cross-talk correction, overscan correction, trimming, bias subtraction, flat fielding and illumination correction. Single epoch images are not remapped to avoid correlating noise, and so we also perform a pixel-scale correction that brings all sources on an image to a common photometric zeropoint. For  $i$  and  $z$  bands we also carry out a fringe correction. Astrometric calibration is done by using the AstrOmatic code **SCAMP** (Bertin, 2006) and the USNO-B catalog. Color terms to transform to the SDSS system rely on photometric solutions derived from observations of SDSS equatorial fields during photometric nights (Desai et al., 2012b). In both pipelines, coaddition is done using **SWarp** (Bertin et al., 2002). In the DESDM system the single epoch images contributing to the coadd are brought to a common zeropoint using stellar sources common to pairs of images. The final photometric calibration of the coadd images is carried out using the stellar color-color locus as a constraint on the zeropoint offsets between neighboring bands (e.g., High et al., 2009), where the absolute photometric calibration comes from 2MASS (Skrutskie et al., 2006). For  $griz$  photometry the calibration is done with reference to the median SDSS stellar locus (Covey et al., 2007), but for the Swope data using Johnson filters, the calibration relies on a stellar locus derived from a sequence of models of stellar atmospheres from PHOENIX (Brott & Hauschildt, 2005) with empirically measured CCD, filter, and atmosphere responses. Cataloging is done using SExtractor (Bertin & Arnouts, 1996), and within the DESDM catalogs we calibrate *mag\_auto* using stellar locus. Quality checks of the photometry are carried out on a cluster by cluster basis using the scatter of stars about the expected stellar locus and the distribution of offsets in the single-epoch photometry as a function of calibrated magnitude (so-called photometric repeatability tests). Poor quality data or failed calibrations are easily identified as those coadds with high stellar locus scatter and or high scatter in the photometric repeatability tests (see Desai et al., 2012b).

NEWFIRM imaging data are reduced using the FATBOY pipeline (Eikenberry et al., 2006), originally developed for the FLAMINGOS-2 instrument, and modified to work with NEWFIRM data in support of the Infrared Bootes Imaging Survey (Gonzalez et al., 2010). Individual processed frames are combined using **SCAMP** and **SWarp**, and photometry is calibrated to 2MASS.

*Spitzer*/IRAC data are reduced following the method of Ashby et al. (2009). Briefly, we correct for column pull-down, mosaic the individual exposures, resample to  $0''.86$  pixels (half the solid angle of the native IRAC pixels), and reject cosmic rays. Magnitudes are measured in  $4''$ -diameter apertures and corrected for the 38% and 40% loss at  $3.6\mu\text{m}$  and  $4.5\mu\text{m}$  respectively due to the broad PSF (see Table 3 in Ashby et al., 2009). The *Spitzer* photometry is crucial to the measurement of photometric redshifts for clusters at  $z \gtrsim 0.8$ , as described in §3.4.1.

The acquisition and processing for the initial weak lensing Megacam data is described in detail in High et al. (2012). These data are reduced separately from the other imaging data using

the Smithsonian Astrophysical Observatory (SAO) Megacam reduction pipeline. Standard raw CCD image processing, cosmic-ray removal, and flat-fielding are performed, as well as an additional illumination correction to account for a low-order scattered light pattern. The final images are coadded onto a single pixel grid with a pixel scale of  $0''.16$  using **SWarp**. Sources are detected in the coadded data in dual-image mode using **SExtractor**, where the  $r$  band image serves as the detection image. The photometry is calibrated by fitting colors to the stellar locus, and color-term corrections are accounted for in this step. The color term is roughly  $0.10(g - i)$  for the  $g'$  band,  $-0.02(g - i)$  for the  $r'$  band, and  $-0.03(g - i)$  for the  $i'$  band.

### 3.3.3 Spectroscopic Observations

We have targeted many of the SPT clusters with long-slit and multi-object spectroscopy, and some of the spectroscopic redshifts have appeared in previous SPT publications. We have used a variety of instruments: GMOS-S<sup>4</sup> on Gemini South, FORS2 (Appenzeller et al., 1998) on VLT, LDSS3 on Magellan-Clay, and the IMACS camera on Magellan Baade (in long-slit mode and with the GISMO<sup>5</sup> complement).

A detailed description of the configurations, observing runs and reductions will be presented elsewhere (J. Ruel et al., in prep). For a given cluster we target bright galaxies that lie on the clusters' red sequence and observe these galaxies with a combination of filter and disperser that yields a low-resolution spectrum around their Ca 2 H&K lines and 4000Å break. CCD reductions are made using standard packages, including COSMOS (Kelson, 2003) for IMACS data and IRAF<sup>6</sup> for GMOS and FORS2. Redshift measurements are made by cross-correlation with the RVSAO package (Kurtz & Mink, 1998) and a proprietary template fitting method that uses SDSS DR2 templates. Results are then visually confirmed using strong spectral features.

In Table 3.2, the source for every spectroscopic redshift is listed, along with the number of cluster members used in deriving the redshift. For clusters for which we report our own spectroscopic measurements, we list an instrument name and observation date; we give a literature reference for those for which we report a value from the literature. In Table 3.3, we report spectroscopic redshifts for 57 clusters, of which 36 had no previous spectroscopic redshift in the literature. Unless otherwise noted, the reported cluster redshift is the robust biweight average of the redshifts of all spectroscopically confirmed cluster members, and the cluster redshift uncertainty is found from bootstrap resampling.

## 3.4 Methodology

In this section, we describe the analysis methods used to: 1) extract cluster redshift estimates and place redshift limits; 2) empirically verify the estimates of catalog purity; and 3) measure rBCG positions.

<sup>4</sup><http://www.gemini.edu/node/10625>

<sup>5</sup><http://www.lco.cl/telescopes-information/magellan/instruments/imacs/gismo/gismoquickmanual.pdf>

<sup>6</sup><http://iraf.noao.edu>

**Table 3.2:** Spectroscopic Follow-Up

Cluster	Inst	Obs	#	Refs	Cluster	Inst	Obs	#	Ref
SPT-CLJ0000-5748	GMOS-S	Sep 2010	26	–	SPT-CLJ2058-5608	GMOS-S	Sep 2011	9	–
SPT-CLJ0205-5829	IMACS	Sep 2011	9	a	SPT-CLJ2100-4548	FORS2	Aug 2011	19	–
SPT-CLJ0205-6432	GMOS-S	Sep 2011	15		SPT-CLJ2104-5224	FORS2	Jun 2011	23	–
SPT-CLJ0233-5819	GMOS-S	Sep 2011	10		SPT-CLJ2106-5844	FORS2	Dec 2010	15	–
SPT-CLJ0234-5831	GISMO	Oct 2010	22	b		GISMO	Jun 2010	3	i
SPT-CLJ0240-5946	GISMO	Oct 2010	25	–	SPT-CLJ2118-5055	FORS2	May 2011	25	–
SPT-CLJ0254-5857	GISMO	Oct 2010	35	b	SPT-CLJ2124-6124	GISMO	Sep 2009	24	–
SPT-CLJ0257-5732	GISMO	Oct 2010	22	–	SPT-CLJ2130-6458	GISMO	Sep 2009	47	–
SPT-CLJ0317-5935	GISMO	Oct 2010	17	–	SPT-CLJ2135-5726	GISMO	Sep 2010	33	–
SPT-CLJ0328-5541	–	–	–	c	SPT-CLJ2136-4704	GMOS-S	Sep 2011	24	–
SPT-CLJ0431-6126	–	–	–	c	SPT-CLJ2136-6307	GISMO	Aug 2010	10	–
SPT-CLJ0433-5630	GISMO	Jan 2011	22	–	SPT-CLJ2138-6007	GISMO	Sep 2010	34	–
SPT-CLJ0509-5342	GMOS-S	Dec 2009	18	d, e	SPT-CLJ2145-5644	GISMO	Sep 2009	37	–
SPT-CLJ0511-5154	GMOS-S	Sep 2011	15	–	SPT-CLJ2146-4633	IMACS	Sep 2011	17	–
SPT-CLJ0516-5430	GISMO	Sep 2010	48	f	SPT-CLJ2146-4846	GMOS-S	Sep 2011	26	–
SPT-CLJ0521-5104	–	–	–	e	SPT-CLJ2148-6116	GISMO	Sep 2009	30	–
SPT-CLJ0528-5300	GMOS-S	Jan 2010	20	d, e	SPT-CLJ2155-6048	GMOS-S	Sep 2011	25	–
SPT-CLJ0533-5005	LDSS3	Dec 2008	4	d	SPT-CLJ2201-5956	–	–	–	c
SPT-CLJ0534-5937	LDSS3	Dec 2008	3	–	SPT-CLJ2300-5331	GISMO	Oct 2010	24	–
SPT-CLJ0546-5345	GISMO	Feb 2010	21	g	SPT-CLJ2301-5546	GISMO	Aug 2010	11	–
	GMOS-S	Dec 2009	2	e	SPT-CLJ2331-5051	GMOS-S	Aug 2010	28	–
SPT-CLJ0551-5709	GISMO	Sep 2010	34	d		GISMO		50	d
SPT-CLJ0559-5249	GMOS-S	Nov 2009	37	d, e	SPT-CLJ2332-5358	GISMO	Jul 2009	24	–
SPT-CLJ2011-5725	–	–	–	f	SPT-CLJ2337-5942	GMOS-S	Aug 2010	19	d
SPT-CLJ2012-5649	–	–	–	c	SPT-CLJ2341-5119	GMOS-S	Aug 2010	15	d
SPT-CLJ2022-6323	GISMO	Oct 2010	37	–	SPT-CLJ2342-5411	GMOS-S	Sep 2010	11	–
SPT-CLJ2023-5535	–	–	–	f	SPT-CLJ2351-5452	–	–	–	h
SPT-CLJ2032-5627	GISMO	Oct 2010	31	–	SPT-CLJ2355-5056	GISMO	Sep 2010	37	–
SPT-CLJ2040-5725	GISMO	Aug 2010	5	–	SPT-CLJ2359-5009	GISMO	Aug 2010	21	–
SPT-CLJ2043-5035	FORS2	Aug 2011	21	–		GMOS-S	Dec 2009	9	–
SPT-CLJ2056-5459	GISMO	Aug 2010	12	–					

**Instruments** [Inst]: GMOS-S on Gemini South 8m, IMACS on Magellan Baade 6.5m, GISMO complement to IMACS on Magellan Baade 6.5m, LDSS3 on Magellan Clay 6.5, FORS2 on VLT Antu 8m; Observing dates [Obs]: dates each data taken;

**Number of galaxies** [#]: Number of galaxies used in deriving redshifts;

**References** [Refs]: <sup>a</sup> Stalder et al. (2013), <sup>b</sup> Williamson et al. (2011), <sup>c</sup> Struble & Rood (1999), <sup>d</sup> High et al. (2010), <sup>e</sup> Sifon et al. (2012), <sup>f</sup> Böhringer et al. (2004), <sup>g</sup> Brodwin et al. (2010), <sup>h</sup> Buckley-Geer et al. (2011),

<sup>i</sup> Foley et al. (2011)



### 3.4.1 Photometric Redshifts

Using the procedure described in §3.3.2, we obtain ground-based imaging data and galaxy catalogs that in most cases allow us to identify an obvious overdensity of red-sequence galaxies within approximately an arcminute of the SPT candidate position. For these optically confirmed cluster candidates, we proceed to estimate a photometric redshift.

In this work, we employ three methods (which we refer to Method 1, 2, and 3 in the following sections) to estimate cluster redshifts from optical imaging data. Two methods (Method 1 and 2) use the color of the galaxies in the cluster red sequence, and the third (Method 3) uses the average of red-sequence galaxy photometric redshifts estimated with a neural-network algorithm, trained with the magnitudes of similar galaxies. In the optical analysis for our two previous cluster catalog releases (High et al., 2010; Williamson et al., 2011), we relied on Method 1 for the results and Method 3 as a cross-check. In this work, we improve the precision of the measured redshifts by applying multiple redshift estimation algorithms and combining the results. Through cross-checks during the analysis, we find that these methods have different failure modes and that comparing the results provides a way of identifying systems that require additional attention (including systems where the cluster’s central region is contaminated by foreground stars or the cluster resides in a crowded field).

All three methods use the single-stellar-population (SSP) models of Bruzual & Charlot (BC03; 2003). These models allow us to transform the location of the red-sequence overdensity in color space to a redshift estimate. A model for the red galaxy population as a function of redshift is built assuming a single burst of star formation at  $z_f = 3$  followed by passive evolution thereafter. Models are selected over a range of metallicities and then calibrated to reproduce the color and tilt of the red sequence in the Coma cluster (Eisenhardt et al., 2007) at  $z = 0.023$ . The calibration procedure is described in more detail in Song et al. (2012a). The red sequence model prescribed in a similar way has been demonstrated to adequately describe the bright end of the cluster red sequence (Blakeslee et al., 2003; Tran et al., 2007; Muzzin et al., 2009; High et al., 2010; Mancone et al., 2010; Stott et al., 2010; Song et al., 2012a). These models are used in determining exposure times and appropriate filter combinations for imaging observations, and in the calculation of redshifts and redshift limits from those observations.

#### Photometric Redshift Measurement Methods

In Method 1, a cluster is confirmed by identifying an excess of galaxies with colors consistent with those derived from BC03 (simultaneously for all observed filters), after subtracting the background surface density. The background-subtracted galaxy number is extracted from an aperture within a radius of  $(3.5, 2.5, 1.5)'$  from the SPT candidate position and uses galaxies with photometric color uncertainties  $\leq (0.25, 0.35, 0.45)$  and apparent magnitudes brighter than  $m^* + (3, 2, 1)$  (or the magnitude limit of the data) in the red sequence based on the same BC03 models, for  $z < 0.2$ ,  $0.2 < z < 0.6$ , and  $z > 0.6$  respectively. The background measurement is obtained by applying the same criteria outside of the cluster search aperture. The redshift is estimated from the most significant peak in this red-sequence galaxy excess. Improvements over the implementation in H10 include using additional colors ( $r-z$  and  $g-i$ , plus NIR colors) in the red-sequence fitting, using the deeper photometry available from coadded images, and sampling the entire CCD mosaic rather than a single CCD for better background estimation. Method 2 is similar in that it searches for an overdensity of red-sequence galaxies. This

method, used to estimate the redshifts for a sample of 46 X-ray-selected clusters (Šuhada et al., 2012), is described and tested in more detail in Song et al. (2012a). It includes a measure of the background surface density based on the entire imaged sky area surrounding each cluster candidate and subtracts the background from the red galaxy counts in an aperture of 0.8 Mpc. Only galaxies with luminosity  $> 0.4L^*$  and magnitude uncertainty  $\leq 0.25$  are used, and the aperture and luminosity are recalculated for each potential redshift. Originally as described in Song et al. (2012a), we search for an overdensity of red-sequence galaxies using two or three available color-redshift combinations simultaneously for every cluster; essentially, we scan outwards in redshift using the following color combinations:  $g-r$  and  $g-i$  for  $z < 0.35$ ,  $g-i$  and  $r-i$  and  $r-z$  for  $0.3 < z < 0.75$ ,  $r-z$  and  $i-z$  for  $z > 0.75$ . The cluster photometric redshift is extracted from the peak of the galaxy overdensity in redshift space. The redshift is then refined by fitting the red-sequence overdensity distribution in redshift space with a Gaussian function. The version used here (which is the same as the method used in Šuhada et al. 2012) has one more refinement, in which the colors of the galaxies that lie in the peak redshift bin identified by the overdensity method are converted into individual galaxy photometric redshifts. In this conversion we assume that the galaxies are red-sequence cluster member galaxies, and the photometric redshift uncertainty reflects the individual photometric color errors. A final cluster redshift is calculated as an inverse-variance-weighted mean of these galaxy photometric redshifts.

Method 3 shares the same principle as the other two in that it involves searching for a density peak in the galaxy distribution near the position of the SPT candidate. We first select individual red cluster members using location relative to the SPT candidate position and galaxy color as the criteria for cluster membership. For the redshifts presented here, this is done visually using pseudo-color coadded images for each cluster, although in principle this could be automated. Galaxy selection is not confined by a specific radial distance from SZ centers as in the other two methods, nor by photometric uncertainties. Selected galaxies are then fed into Artificial Neural Networks (ANNz; Collister & Lahav, 2004), which is trained using the same BC03 models used in the other methods. ANNz returns redshift estimates for individual galaxies, and a peak in galaxy redshift distribution is adopted as the initial cluster redshift. Then, as in Method 2, individual galaxy photometric redshifts are averaged using inverse-variance weighting to produce the cluster photometric redshift. With this initial estimate of the redshift, we then perform an outlier rejection using iterative  $1\sigma$  clipping, where the  $1\sigma$  corresponds to the root-mean-square (RMS) variation of the measured galaxy photometric redshift distribution. Once the rejection is carried out, we refine the cluster photometric redshift estimate using the weighted mean of the non-rejected sample of cluster galaxies. No outlier rejection is undertaken if there are fewer than 20 selected galaxies in the original sample.

Method 3 is a good cross-check, as well as a stand-alone redshift estimator, because we can visually confirm which galaxies contribute to the redshift determination. Although this method requires photometry in more than just two bands, it appears to be less susceptible to the problems in two-band methods that are associated with pileup of red sequence galaxies at redshifts where the  $4000\text{\AA}$  break is transitioning out of a band.

Next we characterize redshift estimates from each method using spectroscopically confirmed clusters. We use 47 clusters with spectroscopic redshifts ( $z_{\text{spec}}$ ) where only *griz* data are used for photometric redshift estimation. In this process, photometric redshift ( $z_{\text{phot}}$ ) biases (namely, smooth trends of photometric redshift offset as a function of redshift) are measured and corrected in Method 1 and 2, while no significant bias correction is necessary for Method

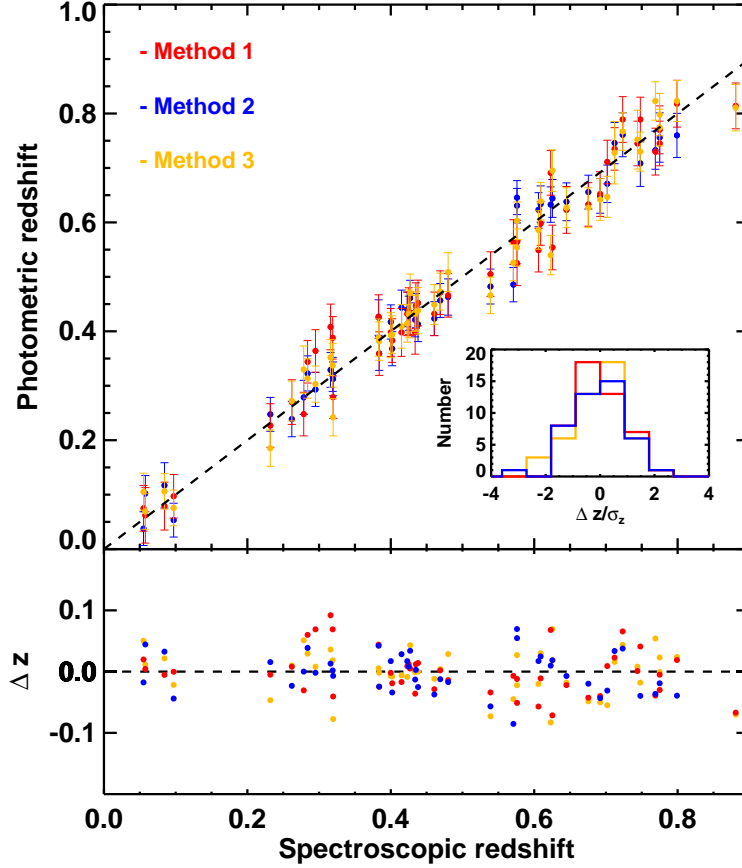


**Figure 3.1:** *Top:* Photometric redshift  $z_{\text{phot}}$  versus spectroscopic redshift  $z_{\text{spec}}$  for each redshift estimation method for 47 spectroscopically confirmed clusters at  $z < 0.9$  where we use only *griz* photometry. *Bottom:* the distribution of the photometric redshift residuals  $\Delta z = z_{\text{phot}} - z_{\text{spec}}$  as a function of  $z_{\text{spec}}$ . *Inset:* the normalized residual distributions, which all have  $\text{RMS}(\Delta z / \sigma_{z_{\text{phot}}}) \sim 1$ . The RMS scatter of  $\Delta z / (1 + z)$  is 0.028, 0.023 and 0.024 for Methods 1, 2 and 3, respectively.

3. Bias corrections depend on several factors, such as filters used for data, redshift of clusters, and the depth of the data. They are separately measured in those different cases per method as a function of  $(1+z)$  at a level of 0.01-0.03 in redshift for clusters with redshift measured in *griz* filters, *Spitzer*-only, and *BVRI* filters at  $z > 0.5$ . The largest bias correction is needed for clusters observed from SWOPE using *BVRI* filters with maximum correction of 0.13 at around  $z \sim 0.4$  where the filter transitions from *B-V* to *V-R* occurs to capture the red sequence population. This affects two clusters in the final sample. Once biases are removed, we examine the photometric-to-spectroscopic redshift offsets to characterize the performance of each method. We find the RMS in the quantity  $\Delta z / (1 + z_{\text{spec}})$ , where  $\Delta z = z_{\text{phot}} - z_{\text{spec}}$  to have values of 0.028, 0.023, and 0.024 in Methods 1, 2, and 3, respectively (see Figure 3.1). We note that some of the bias and systematic error, especially at higher redshift, could be due to the mismatch between the SEDs in the red sequence model and the cluster population, which could arise from variations in star formation history or AGN activity.

Our goal is not only to estimate accurate and precise cluster redshifts, but also to accurately

characterize the uncertainty in these estimates. To this end, we use the spectroscopic subsample of clusters to estimate a systematic floor  $\sigma_{\text{sys}}$  in addition to the statistical component. We do this by requiring that the reduced  $\chi^2$  describing the normalized photometric redshift deviations from the true redshifts  $\chi_{\text{red}}^2 = \sum (\Delta z / \sigma_{z_{\text{phot}}})^2 / N_{\text{dof}}$  have a value  $\chi_{\text{red}}^2 \sim 1$  for each method, where  $\sigma_{z_{\text{phot}}}$  is the uncertainty in measured  $z_{\text{phot}}$  and  $N_{\text{dof}}$  is the number of degrees of freedom. We adopt uncertainties  $\sigma_{z_{\text{phot}}}^2 = \sigma_{\text{stat}}^2 + \sigma_{\text{sys}}^2$  and adjust  $\sigma_{\text{sys}}$  to obtain the correct  $\chi_{\text{red}}^2$ . In this tuning process we also include redshift estimates of the same cluster from multiple instruments when that cluster has been observed multiple times. This allows us to test the performance of our uncertainties over a broader range of observing modes and depths than is possible if we just use the best available data for each cluster.

For Method 1 we separately measure the systematic floor  $\sigma_{\text{sys}}$  for each different photometric band set. For the *grizKS* instruments (Megacam, IMACS, LDSS3, MOSAIC2, NEWFIRM), we estimate  $\sigma_{\text{sys}} = 0.039$ ; for the *BVRI* instrument (Swope),  $\sigma_{\text{sys}} = 0.033$ ; and for *Spitzer*-only,  $\sigma_{\text{sys}} = 0.070$ . In Method 2, we find  $\sigma_{\text{sys}} = 0.030$  for the *griz* instruments (Megacam, IMACS, LDSS3, MOSAIC2). For Method 3 we estimate  $\sigma_{\text{sys}} = 0.028$  for the *griz* instruments. Once this individual estimation and calibration is done, we conduct an additional test on the redshift estimation methods, again using the spectroscopic subsample. The purpose of this test is to see how the quality of photometry (i.e., follow-up depth) affects the estimations. We divide the spectroscopic sample into two groups: in one group, the photometric data is kept at full depth, while the photometric data in the other group is manually degraded to resemble the data from the shallowest observations in the total follow-up sample. To create the ‘shallow’ catalogs, we add white noise to the full-depth coadds and then extract and calibrate catalogs from these artificially noisier images. Results of this test show that the accuracy of the photometric redshift estimation is affected by the poorer photometry, but that this trend is well captured by the statistical uncertainties in each estimation method.

### Combining Photo-z Estimates to Obtain $z_{\text{comb}}$

Once redshifts and redshift uncertainties are estimated with each method independently, we compare the different redshift estimates of the same cluster. Note that this comparison is not possible for Swope or *Spitzer*-only redshifts, which are measured only with Method 1. Outliers at  $\geq 3\sigma$  ( $>6\%$ ) in  $1+z_{\text{phot}}$  are identified for additional inspection. In some cases, there is an easily identifiable and correctable issue with one of the methods, such as misidentification of cluster members. If, however, it is not possible to identify an obvious problem, the outliers are excluded from the combining procedure. This outlier rejection, which occurs only in two cases, causes less than 0.05 change in the combined  $z_{\text{phot}}$  in both cases.

We combine the individual estimates into a final best redshift estimate,  $z_{\text{comb}}$ , using inverse-variance weighting and accounting for the covariance between the methods, which we expect to be non-zero given the similarities in the methods and the common data used. Correlation coefficients for the photometric redshift errors among the different methods are measured using the spectroscopic sample. The measured correlation coefficient,  $r_{ij}$ , between each pair of methods is 0.11 (Method 1 & 2), 0.40 (Method 2 & 3) and 0.19 (Method 1 & 3).

With the correlation coefficients we construct the optimal combination of the individual estimates as:

$$z_{\text{comb}} = \frac{1}{\sum_{ij} W_{ij}} \sum_i \sum_j W_{ij} z_j, \quad (3.1)$$

where  $W_{ij} = C_{ij}^{-1}$ , and the covariance matrix  $C_{ij}$  is comprised of the square of the individual uncertainties along the diagonal elements ( $\sigma_i^2$ ) and the product of the measured correlation coefficient and the two individual uncertainty components (i.e.,  $r_{ij}\sigma_i\sigma_j$ ) on the off-diagonal elements. The associated uncertainty is

$$\sigma_{z_{\text{comb}}}^2 = \frac{1}{\sum_{ij} W_{ij}}. \quad (3.2)$$

Because of the positive correlations between the three methods' errors, the errors on  $z_{\text{comb}}$  are larger than would be the case for combining three independent estimates; however, we do see an improvement in the performance of the combined redshifts relative to the individual estimates that is consistent with the expectation given the correlations. The performance of this combined redshift method is presented in Fig. 3.2; the residual distribution is roughly Gaussian, and the associated uncertainties provide a good description of the scatter of the redshift estimates about the spectroscopic redshifts (the RMS variation of  $\Delta z/\sigma_{z_{\text{phot}}}$  is 1.04). The benefit from combining different measurements is evidenced from the tighter distribution in the redshift versus  $z_{\text{spec}}$  plot; the RMS scatter of  $\Delta z/(1 + z_{\text{spec}})$  is 0.017, corresponding to a  $\sim 40\%$  improvement in the accuracy relative to the accuracy of a single method.

### *Spitzer* Photometric Redshifts

For clusters where we do not have deep enough optical data to estimate a redshift but that do have *Spitzer* coverage, we use the algorithm used in Method 1 to measure the redshifts using *Spitzer*-only colors in the same manner as we do with optical data. Overdensities of red galaxies in clusters have been identified using *Spitzer*-only color selection at high redshift, where the IRAC bands are probing the peak of the stellar emission (Stern et al., 2005; Papovich, 2008), rather than bracketing the 4000Å break. Note that the concerns about the impact of recent star formation or AGN activity on photometric redshift estimates are not as serious in the IRAC bands as in the optical bands, because the portion of the spectrum probed is less sensitive to these potential sources of contamination. In our sample, the comparison of *Spitzer*-only redshifts with spectroscopically derived redshifts shows good performance, indicating that the assumption of a well-developed red-sequence appears to hold out to  $z \gtrsim 1$  (e.g., Bower et al., 1992; Eisenhardt et al., 2008; Muzzin et al., 2009). Note that the possibility of the cluster being at lower redshift is already ruled out from the available optical data for these candidates.

Figure 3.3 shows the performance of the *Spitzer*-only redshifts in eight clusters where spectroscopic redshifts are available. Although the accuracy in  $z_{\text{phot}}$  is lower ( $\Delta z/(1 + z) \approx 0.049$ ) than those derived from optical-only or optical-IRAC colors, the performance is reliable. We flag these cases in the final table to make note of this difference in method. The larger uncertainties of *Spitzer*-only derived redshifts are possibly due to the broad width of IRAC filters and the fact that AGN emission or vigorous star formation can shift the location of the 1.6μm bump.

### Redshift Limits

In most cases there is an obvious, rich overdensity of red cluster galaxies in our follow-up imaging, from which it is straightforward to confirm the galaxy cluster giving rise to the SZ signal and to estimate the cluster redshift. For unconfirmed candidates, it is not possible to

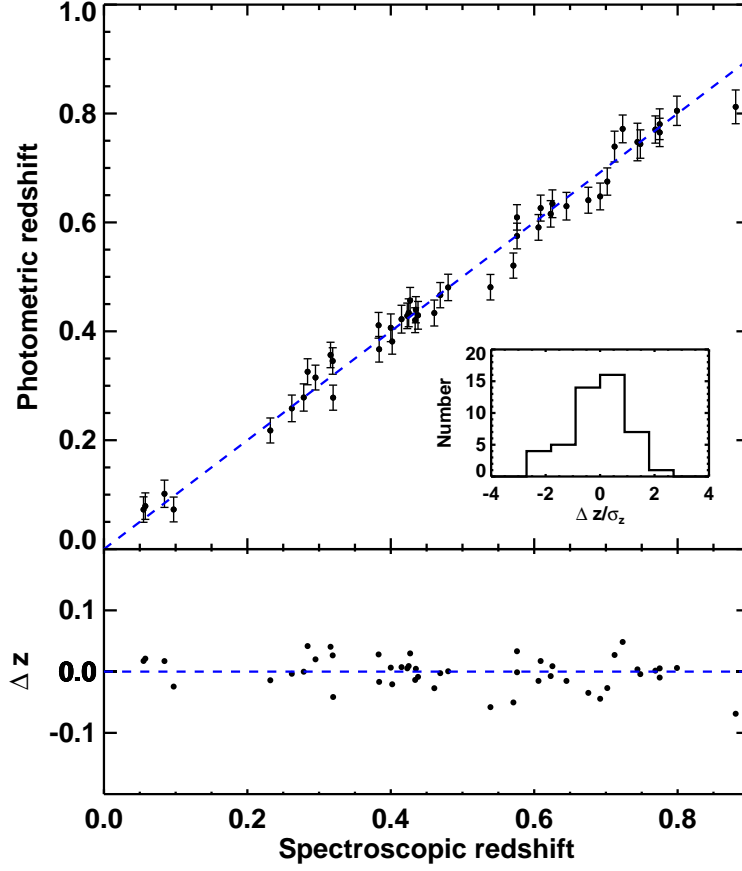


**Figure 3.2:** *Top:* Weighted mean photometric redshift  $z_{\text{comb}}$  versus spectroscopic redshift using the same sub-sample as in Fig. 3.1. *Bottom:* the distribution of the redshift errors. The RMS scatter in  $\Delta z/(1+z_{\text{spec}})=0.017$ . *Inset:* histogram of the normalized redshift error distribution, which is roughly Gaussian with  $\text{RMS} \simeq 1$ .

say with absolute certainty that no optical/NIR counterpart exists; with real, finite-depth optical and NIR data, the possibility always exists that the cluster is distant enough that no counterpart would have been detected at the achieved optical/NIR depth. Assigning a relative probability to these two interpretations of an optical/NIR non-detection (i.e., a false detection in the SZ data or a higher-redshift cluster than the optical/NIR observations could detect) is especially important for interpreting the SZ cluster sample cosmologically. To this end, we calculate a lower redshift limit for every SZ-selected candidate for which no counterpart has been found. Because the optical/NIR follow-up data is not homogeneous, we do this separately for each unconfirmed candidate.

To estimate the depth of the optical/NIR coadded images, we utilize a Monte-Carlo based technique described in Ashby et al. (2009). In brief, we perform photometry of the sky in various apertures at 1500 random positions in each image. To measure the sky noise, we then fit a Gaussian function to the resulting flux distribution (excluding the bright tail which is biased by real sources in the image). Taking the measured sky noise from 3''-diameter apertures, we add a PSF-dependent aperture correction. A redshift limit is derived for each

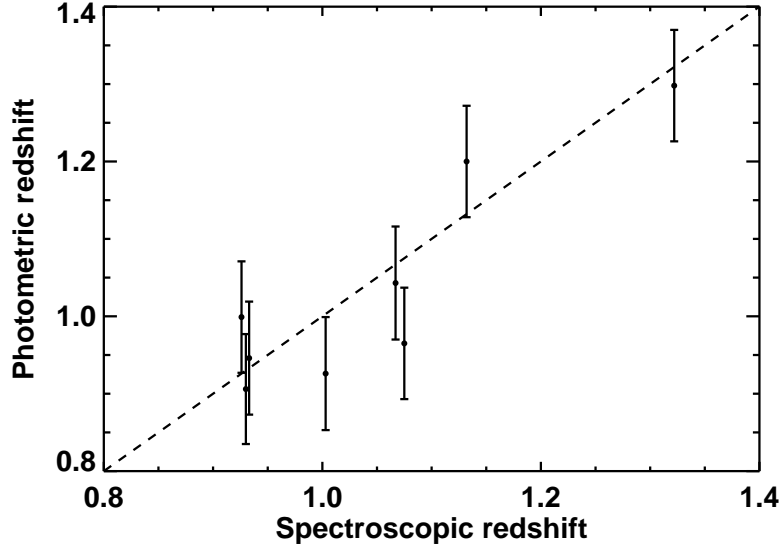


**Figure 3.3:** Photometric redshift vs.  $z_{\text{spec}}$  for clusters where only the *Spitzer* IRAC  $3.6\mu\text{m}$ - $4.5\mu\text{m}$  colors are used. In all cases where we present *Spitzer* photo- $z$ 's, we have optical data to rule out the presence of a low-redshift cluster.

filter by matching a  $0.4L^*$  red-sequence galaxy from the BC03 model to the measured  $10\sigma$  magnitude limit. We use the redshift limit from the second deepest filter with regards to  $0.4L^*$  red-sequence objects, as we require a minimum of two filters to measure a redshift. These redshift limits are compared to limits derived by comparing observed number counts of galaxies as a function of magnitude to distributions derived from much deeper data (Zenteno et al., 2011). We find the two independent redshift limit estimations are in good agreement. For cluster candidates with *Spitzer*/IRAC observations, the redshift estimation is not limited by the depth of the optical data, and we use the IRAC data to calculate a lower redshift limit for these candidates. The IRAC data are highly uniform, with depth sufficient to extract robust photometry down to  $0.1L^*$  out to a redshift of  $z = 1.5$ . In principle,  $\sim 0.5L^*$  photometry should be sufficient for redshift estimation; however, we adopt  $z = 1.5$  as a conservative lower redshift limit for any unconfirmed candidates with IRAC data.

### 3.4.2 NIR Overdensity Estimates for Unconfirmed Candidates

For cluster candidates for which we are unable to estimate a redshift, we can in principle go beyond a simple binary statement of “confirmed/unconfirmed” using NIR data. Even if there is not a sufficient number of galaxies in the NIR data to estimate a red sequence, there is information in the simple overdensity of objects (identified in a single NIR band) within a certain radius of an SPT candidate, and we can use this information to estimate the probability of that candidate being a real, massive cluster. We can then use this estimate to sharpen our estimate of the purity of the SPT-selected cluster sample. We calculate the single-band NIR overdensity for all unconfirmed candidates using *WISE* data, and we compare that value to the same statistic estimated on blank-field data. We perform the same procedure using *Spitzer*/IRAC and NEWFIRM data for unconfirmed candidates that were

targeted with those instruments. For comparison, we also calculate the same set of statistics for each confirmed cluster above  $z = 0.7$ .

We estimate the galaxy overdensity within a  $1 \text{ arcmin}^2$  aperture. To increase the signal-to-noise of the estimator, we assume an angular profile shape for the cluster galaxy distribution and fit the observed distribution to this shape. The assumed galaxy density profile is a projected  $\beta$  model with  $\beta = 1$  (the same profile assumed for the SZ signal in the matched-filter cluster detection algorithm in R13). We have tried using a projected NFW profile as well, and the results do not change in any significant way (due to the relatively low signal-to-noise in the NIR data). The central amplitude, background amplitude, scale radius, and center position (with respect to the center of the SZ signal in SPT data) are free parameters in the fit. Priors are placed on  $\theta_s$ , the scale radius, and  $\Delta\theta$ , the SZ-NIR positional offset, based on the NIR galaxy distributions measured in SPT-selected clusters known to be real and typical of the clusters in this sample. The number of galaxies above background within  $1 \text{ arcmin}^2$ —which we will call  $\Sigma_{1'}$ —is then calculated from the best-fit profile. The same procedure is repeated on fields not expected to contain massive galaxy clusters, and the value of  $\Sigma_{1'}$  for every SPT candidate is compared to the distribution of  $\Sigma_{1'}$  values in the blank fields. The key statistic is the fraction of blank fields that had a  $\Sigma_{1'}$  value larger than a given SPT candidate, and that value is recorded as  $P_{\text{blank}}$  in Table 3.3 for every high-redshift ( $z \geq 0.7$ ) or unconfirmed candidate. This technique, including using the blank-field statistic as the primary result, is similar to the analysis of WISE data in the direction of unconfirmed *Planck* Early SZ clusters in Sayers et al. (2012), although that analysis used raw galaxy counts within an aperture rather than profile fitting.

The model fitting is performed using a simplex-based  $\chi^2$  minimization, with any parameter priors enforced by adding a  $\chi^2$  penalty. The positional offset  $\chi^2$  penalty is  $\Delta\chi^2 = (\Delta\theta/\sigma_{\Delta\theta})^2$ , where  $\sigma_{\Delta\theta}$  is chosen to be  $0.25'$ , based on the SZ/BCG offset distribution in Fig. 3.7 and the value of  $r_{200}$  for a typical-mass SPT cluster at high redshift.<sup>7</sup> A prior is enforced on the scale radius from below and above by adding  $\chi^2$  penalties of  $(\theta_s/\theta_{s,\text{max}})^2$  and  $(\theta_{s,\text{min}}/\theta_s)^2$ , where  $\theta_{s,\text{max}}$  is chosen to be  $0.75'$  based on the  $\theta_s$  distribution in known high-redshift SPT clusters with NIR data, and  $\theta_{s,\text{min}}$  is chosen to be  $0.125'$  to prevent the fitter from latching onto small-scale noise peaks.

For *Spitzer*/IRAC and *WISE*, the fit is performed on the  $3.6\mu\text{m}$  and the  $3.4\mu\text{m}$  data, respectively; for NEWFIRM, the fit is performed on the  $K_s$ -band data. For both *Spitzer*/IRAC and NEWFIRM, a single magnitude threshold is used for every candidate; this threshold is determined by maximizing the signal-to-noise on the  $\Sigma_{1'}$  estimator on known clusters while staying safely away from the magnitude limit of the shallowest observations. The *Spitzer*/IRAC data is very uniform, and the  $3.6\mu\text{m}$  magnitude threshold chosen is 18.5 (Vega). The NEWFIRM  $K_s$ -band data is less uniform, but a magnitude threshold of 18 (Vega) is safe for all observations. For these instruments (IRAC and NEWFIRM), the blank fields on which the fit is performed come from the *Spitzer* Deep Wide-Field Survey (SDWFS) region (Ashby et al., 2009), which corresponds to the Bootes field of the NOAO Deep Wide-Field Survey (NDWFS; Jannuzi & Dey, 1999). The depth of the SDWFS/NDWFS observations for both instruments (19.8 in Vega for *Spitzer*/IRAC  $3.6\mu\text{m}$  and 19.5 in Vega for NEWFIRM  $K_s$ ) is more than sufficient for our chosen magnitude thresholds.

For *WISE*, in which the non-uniform sky coverage results in significant variation in magnitude

<sup>7</sup> $r_{200}$  is defined as the radius within which the average density is 200 times the mean matter density in the Universe.



limits, we perform the blank-field fit on data in the immediate area of the cluster (within a  $\sim 20'$  radius). Under the assumption that the *WISE* magnitude limit does not vary over this small an angular scale, we use all detected galaxies brighter than 18th magnitude (Vega) in both the cluster and blank-field fits.

### 3.4.3 Identifying rBCGs in SPT Clusters

An rBCG in this work is defined as the brightest galaxy among the red-sequence galaxies for each cluster. We employ the terminology rBCGs, rather than BCGs, to allow for the rare possibility of an even brighter galaxy with significant amounts of ongoing star formation, because the selection is restricted by galaxy colors along the cluster red sequence. We visually inspect pseudo-color images built with the appropriate filter combinations (given the cluster redshift) around the SZ candidate position. We search a region corresponding to the projected cluster virial region, defined by  $\theta_{200}$ , given the mass estimate from the observed cluster SPT significance  $\xi$  and photometric redshift  $z_{\text{phot}}$ .

There are 12 clusters out of the 158 with measured photometric redshifts (excluding the candidates with redshift limits) that are excluded from the rBCG selections. Eight of those are excluded due to contamination by a bright star that obscures more than one third of the area of the  $3\sigma$  SPT positional uncertainty region. Another cluster is excluded due to a bleed trail making the rBCG selection ambiguous, and three other clusters are excluded due to a high density in the galaxy population that, given the delivered image quality, makes it impossible to select the rBCG.

## 3.5 Results

The complete list of 224 SPT cluster candidates with SZ detection significance  $\xi \geq 4.5$  appears in Table 3.3. The table includes SZ cluster candidate positions on the sky [RA Dec], SZ detection significance [ $\xi$ ], and spectroscopic redshift [ $z_{\text{spec}}$ ] when available. For confirmed clusters, the table includes photometric redshift and uncertainty [ $z_{\text{comb}} \pm \sigma_{z_{\text{comb}}}$ ], estimated as described in §3.4.1. Unconfirmed candidates are assigned redshift lower limits, estimated as described in §3.4.1.

We also report a redshift quality flag for each  $z_{\text{phot}}$  in Table 3.3. For most of the confirmed clusters with reliable photometric redshift measurements, we set Flag = 1. There is one cluster (SPT-CL J2146-4846) for which the three individual photometric redshifts are not statistically consistent ( $\gtrsim 3\sigma$  outliers) for which we set Flag = 2. We still report the combined redshift for that cluster as in other secure systems. We have 6 cases where we only use Swope + Method 1, and 25 cases where we only use *Spitzer* + Method 1 for redshift estimation, both cases marked with Flag = 3. We note that the photometric redshift bias correction for two clusters (SPT-CL J0333-5842 and SPT-CL J0456-6141) is at a higher level than the typical bias correction on other clusters (see ?? for more detail on the bias correction. There are 2 cases (SPT-CL J0556-5403 and SPT-CL J0430-6251) where we quote only a Method 1 redshift even for MOSAIC or IMACS data, marked with Flag = 4. In the coadded optical images for SPT-CL J0556-5403, we identify an overdensity of faint red galaxies at the location of the SPT candidate. This optical data is too shallow, however, to allow for secure redshift estimation, but we are able to measure a redshift by combining this data with NEWFIRM imaging. This cluster is the only candidate where we rely on photometric redshift from *i-K<sub>s</sub>*.

SPT-CL J0430-6251 is in a field very crowded with large scale structure, making redshift estimation difficult.

In the Appendix, we discuss certain individually notable candidates—such as associations with known clusters that appear to be random superpositions and candidates with no optical/NIR confirmation but strong evidence from the NIR overdensity statistic.

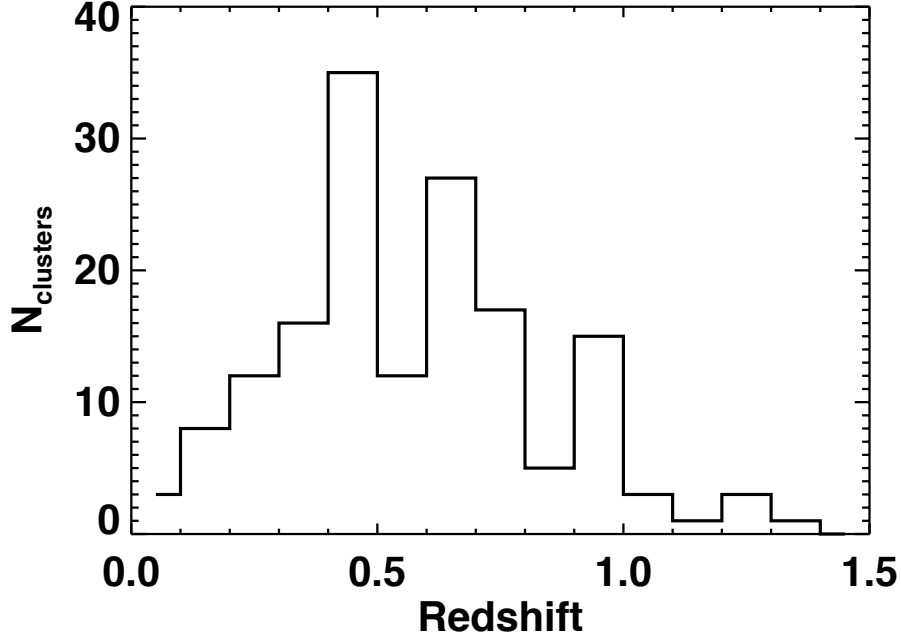


**Figure 3.4:** Redshift histogram of 158 confirmed clusters, in bins of  $\Delta z = 0.1$ . Note that about 18% of the total sample comes from  $z \geq 0.8$ .

### 3.5.1 Redshift Distribution

The redshift distribution for the 158 confirmed clusters is shown in Fig. 3.4. The median redshift is  $z = 0.57$ , with 28 systems ( $\sim 18\%$  of the sample) lying at  $z > 0.8$ . The cluster with the highest photometric redshift is SPT-CL J2040-4451 at  $z = 1.35 \pm 0.07$  (estimated using *Spitzer*/IRAC data) and the highest-redshift spectroscopically confirmed cluster is SPT-CL J0205-5829 at  $z = 1.32$ . (This cluster is discussed in detail in Stalder et al. 2013.)

The high fraction of SPT clusters at  $z > 0.8$  is a consequence of the redshift independence of the SZ surface brightness and the arcminute angular resolution of the SPT, which is well-matched to the angular size of high- $z$  clusters. X-ray surveys, in contrast, are highly efficient at finding nearby clusters, but the mass limit of an X-ray survey will increase with redshift due to cosmological dimming. ROSAT cluster surveys lack the sensitivity to push to these high redshifts except in the deepest archival exposures. XMM-Newton archival surveys (e.g., Lloyd-Davies et al., 2011; Fassbender et al., 2011) and coordinated surveys of contiguous regions (e.g., Pacaud et al., 2007; Šuhada et al., 2012) have sufficient sensitivity to detect systems like those found by SPT, but the solid angle surveyed is currently smaller. For example, the Fassbender et al. (2011) survey for high redshift clusters will eventually cover

approximately  $80 \text{ deg}^2$ , whereas the mean sky density of the SPT high-redshift and high-mass systems is around one every  $25 \text{ deg}^2$ . Therefore, one would have expected the Fassbender et al. (2011) XDCP survey to have found around three clusters of comparable mass to the SPT clusters, which is in fact consistent with their findings. The vast majority of the high redshift X-ray-selected sample available today is of significantly lower mass than SPT selected samples, simply because the X-ray surveys do not yet cover adequate solid angle to find these rare, high mass systems.

Clusters samples built from NIR galaxy catalogs have an even higher fraction of high-redshift systems than SZ-selected samples—for example, in the IRAC Shallow Cluster Survey (ISCS; Eisenhardt et al., 2008) a sample of 335 clusters has been identified out to  $z \sim 2$ , a third of which are at  $z > 1$ . However, the typical ISCS cluster mass is  $\sim 10^{14} M_{\odot}$  (Brodwin et al., 2007), significantly lower than the minimum mass of the SPT high-redshift sample. As with the X-ray selected samples, the *Spitzer* sample includes some massive clusters, including the recently discovered IDCS J1426.5+3508 at  $z = 1.75$ , which was subsequently also detected in the SZ (Stanford et al., 2012; Brodwin et al., 2012). However, the *Spitzer* surveys to date do not cover the required solid angle to find these massive systems in the numbers being discovered by SPT.

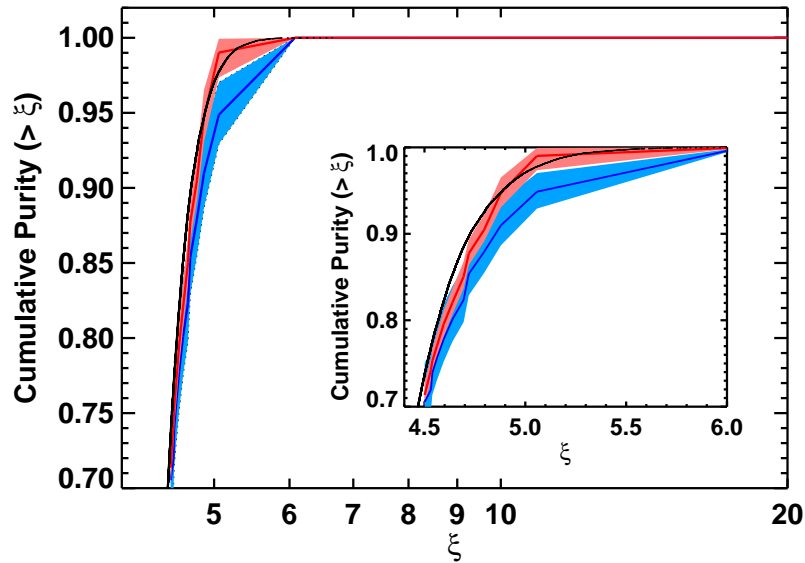


**Figure 3.5:** Cumulative purity estimates derived from the optical/NIR followup compared to simulated purity predictions (black line). The inset plot is zoomed-in to the  $\xi$  range between 4.5 and 6.0 and binned more finely. The purity is calculated from the follow-up confirmation rate: 1) (blue) assuming all clusters without a clear optical or NIR counterpart are false SZ detections (i.e., 100% optical completeness) and all optical confirmations are robust (100% optical purity); and 2) (red) assuming, as justified in the text, 97% optical completeness and 96% optical purity but taking into account clusters confirmed through other means such as X-ray observations.  $1\sigma$  uncertainties in the purity estimates from follow-up are shown with shaded blue or red regions (see Section 3.5.2).

### 3.5.2 Purity of the SPT Cluster Candidates

For a cluster sample to be useful for cosmological purposes, it is important to know the purity of the sample, defined as

$$f_{\text{pure}} = \frac{N_{\text{real}}}{N_{\text{tot}}} = 1 - \frac{N_{\text{false}}}{N_{\text{tot}}}, \quad (3.3)$$

where  $N_{\text{tot}}$  is the total number of cluster candidates,  $N_{\text{real}}$  is the number of candidates corresponding to real clusters, and  $N_{\text{false}}$  is the number of false detections. For an SZ-selected cluster sample with reasonably deep and complete optical/NIR follow-up, a first-order estimate of  $N_{\text{real}}$  is simply the number of candidates with successfully estimated redshifts. In Fig. 3.5, we show two estimations of purity for the 720 deg<sup>2</sup> SPT-SZ sample; the first in blue, assuming that all cluster candidates with no redshift measurements are noise fluctuations, and the other in red, taking into account incompleteness of our follow-up data. The blue/red shaded regions in the figure correspond to the  $1\sigma$  uncertainties on the purity, estimated from Poisson noise on  $N_{\text{false}}$  for the blue region and as described below for the red region. We also show the expected purity, estimated from the total number of candidates in the sample presented in this work combined with the false detection rate from the simulations used to test the SZ cluster finder (R13 Figure 1).

The possibility of real clusters beyond the redshift reach of our optical/NIR redshift estimation techniques makes the blue line in Figure 3.5 a lower limit to the true purity of the sample. As discussed in §3.4.2, we use single-band NIR data to estimate the probability that each unconfirmed candidate is a “blank field”, i.e., a field with typical or lower-than-typical NIR galaxy density. Candidates with no optical/NIR confirmation but with a low blank field probability  $P_{\text{blank}}$ , are potential high-redshift systems that merit further follow-up study. These systems can also give an indication of how much we underestimate our sample purity when we assume any optical/NIR non-confirmation is a spurious SPT detection. By definition, a low  $P_{\text{blank}}$  implies some NIR overdensity towards the SPT detection, but perhaps not large enough to be an SPT-detectable cluster. We can roughly calibrate the  $P_{\text{blank}}$  values to SPT detectability by investigating the results of the NIR overdensity estimator on solidly confirmed, high-redshift SPT clusters. There are 19 clusters with spectroscopic redshifts above  $z = 0.7$ , and the average *Spitzer*/IRAC  $P_{\text{blank}}$  value for these clusters is 0.04, while the average WISE  $P_{\text{blank}}$  value is 0.05. Only three of these clusters have NEWFIRM data, and the average NEWFIRM  $P_{\text{blank}}$  value is 0.07. Only one cluster in this high- $z$  spectroscopic sample has an IRAC  $P_{\text{blank}} > 0.1$ , while three have WISE  $P_{\text{blank}} > 0.1$ . So a rough threshold for SPT-type clusters appears to be  $P_{\text{blank}} \leq 0.1$ . We have nine unconfirmed cluster candidates that meet this criterion in at least one of the NIR catalogs, including five that are at  $P_{\text{blank}} \leq 0.05$ . If we assumed all of the  $P_{\text{blank}} \leq 0.05$  clusters were real, it would imply that the completeness of the optical/NIR redshift estimation was  $\sim 97\%$ , i.e., we have 163 real clusters of which we were able to estimate redshifts for 158.

Conversely, the possibility of false associations of spurious SZ detections with optical/NIR overdensities would act in the other direction. Tests of one of the red-sequence methods on blank-field data produced a significant red-sequence detection on approximately 4% of fields without SPT detected clusters. Assuming that the cross-checks with other methods would remove some of these, we can take this as an upper limit to this effect.

We therefore provide a second estimate of purity from the optical/NIR confirmation rate, taking into account the possibility of real clusters for which we were unable to successfully estimate a redshift (redshift completeness  $< 100\%$ ) and spurious optical/NIR associations

with SPT noise peaks (redshift purity  $< 100\%$ ). From the above arguments, we assume 97% for redshift completeness and 96% for redshift purity. For each value of SPT significance  $\xi$ , we use binomial statistics to ask how often a sample of a given purity with total candidates  $N(> \xi)$  would produce the observed number of successful optical/NIR redshift estimates  $N_{\text{conf}}(> \xi)$ , given the redshift completeness and false rate. An extra constraint is added to this calculation based on data independent of the optical/NIR imaging that confirms many of the SPT candidates as real, massive galaxy clusters. Specifically, we assume an SPT candidate is a real, massive cluster independent of the optical/NIR imaging data (and remove the possibility of that candidate being a false optical/NIR confirmation of an SPT noise peak) if: 1) it is associated with a ROSAT Bright Source Catalog source; 2) we have obtained X-ray data in which we can confirm a strong, extended source; or 3) we have obtained spectroscopic data and measured a velocity dispersion for that system. The red solid line and shaded region in Figure 3.5 show the maximum-likelihood value and 68% limits for the true purity of the SPT sample under these assumptions.

The purity measured in this work is in good agreement with the model for the SPT sample purity. In particular, all clusters with  $\xi > 6$  have identified optical counterparts with photometric redshift estimates. This is consistent with the expectation of the model and a demonstration that the SPT selected galaxy cluster sample is effectively uncontaminated at  $\xi > 6$ . With decreasing significance, the number of noise fluctuations in the SPT maps increases compared to the number of real clusters on the sky, and the purity decreases. The cumulative purity of the sample is  $\sim 70\%$  above  $\xi = 4.5$  and reaches  $\sim 100\%$  above  $\xi = 5.9$ . Of course, if one requires optical confirmation in addition to the SPT detection, then the sample is effectively 100% pure over the full sample at  $\xi > 4.5$ .

We note that there is no significant difference in false detection rate (based on optical confirmation alone) between cluster candidates selected with 150 GHz data alone and those detected with the multiband strategy (see §3.3.1 for details). Roughly 1/4 of the survey area was searched for clusters using 150 GHz data only, and in that area we have 12 unconfirmed candidates, including one above  $\xi = 5$ ; in the 3/4 of the area selected using multiband data, we have 54 unconfirmed candidates, including five above  $\xi = 5$ . These totals are consistent within  $1\sigma$  Poisson uncertainties.

The high purity of the SPT selected cluster sample is comparable to the purity obtained in previous X-ray cluster surveys (i.e. Vikhlinin et al., 1998; Mantz et al., 2008; Vikhlinin et al., 2009), indicating that these intracluster medium based selection techniques, when coupled with optical follow-up, provide a reliable way to select clean samples of clusters for cosmological analysis.

### 3.5.3 rBCG Offsets in SPT Clusters

The position of the rBCG in galaxy clusters is a property of interest for both astrophysical and cosmological cluster studies, as it is a possible indication of a cluster's dynamical state. In relaxed clusters, it is expected that dynamical friction will tend to drive the most massive galaxies to the bottom of the cluster potential well, which would coincide with the centroid of the X-ray and SZ signatures. On the other hand, in cases of merging systems one would expect two different rBCGs, and one or both could appear well-separated from the X-ray or SZ centroid. Several studies have shown a tight correlation between the X-ray centroid and the rBCG position (Lin & Mohr, 2004; Haarsma et al., 2010; Mann & Ebeling, 2012; Stott et al., 2012), although Fassbender et al. (2011) provide evidence that at high redshift the

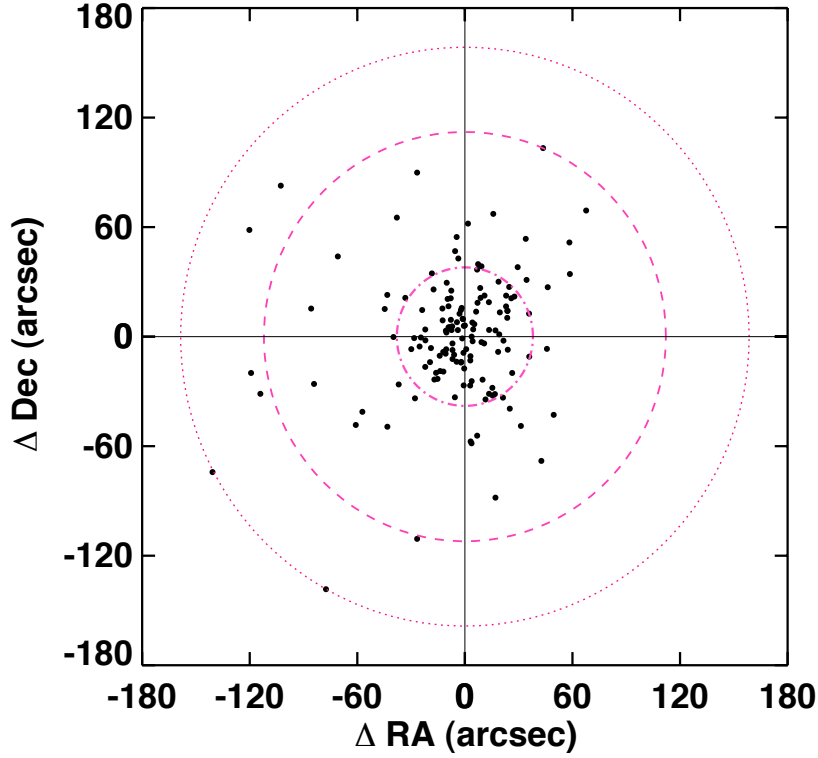


**Figure 3.6:** rBCG positions are plotted as offsets from SPT candidate positions for 146 systems with clearly defined rBCGs. The magenta concentric circles enclose 68% (dash-dot line), 95% (dashed line) and 99% (dotted line) of the whole rBCG sample and have radii of  $38.0''$ ,  $112.1''$  and  $158.6''$ .

BCG distribution is less centrally peaked. Here we examine the rBCG positions with respect to the centroid of the SZ signal in the SPT cluster sample.

The position of each rBCG is listed in Table 3.3, and the offsets from the SZ centroids in arcsec are plotted in Figure 3.6. The rings correspond to different fractions of the full population of clusters: 68%, 95%, and 99%. These rings have radii of  $38.0''$ ,  $112.1''$  and  $158.6''$ , respectively. The rBCG population is centrally concentrated with the bulk of the SPT selected clusters having rBCGs lying within about  $1'$  of the candidate position.

Given the broad redshift range of the cluster sample, the rBCG distribution in cluster coordinates  $r/r_{200}$  is more physically interesting. We use the cluster redshifts from this work and the SZ-derived masses from R13 to calculate  $r_{200}$  for each cluster. The red line in Figure 3.7 is the cumulative distribution of the rBCGs as a function of  $r/r_{200}$ . In this distribution, 68% of the rBCGs lies within  $0.17r_{200}$ , 95% within  $0.43r_{200}$  and 99% within  $0.70r_{200}$ .

We check for any effects of mm-wave selection and redshift estimation on the rBCG offset distribution by splitting the sample three ways: 1) clusters selected using 150 GHz data only vs. clusters selected using multiband data; 2) clusters with spectroscopic redshifts vs. clusters with photometric redshifts only; 3) clusters with secure photometric redshifts (Flag = 1) vs. clusters with flagged redshifts (Flag > 1, see §5.5 for details). We see no evidence that the rBCG offsets (in units of  $r_{200}$ ) in these subsamples are statistically different. A Kolmogorov-Smirnov (KS) test results in probabilities of 84%, 39%, and 34% that these

respective subsamples are drawn from the same underlying distribution.

We investigate the importance of the SPT candidate positional uncertainty by modeling the expected radial distribution in the case where all rBCGs are located exactly at the cluster center. The  $1\sigma$  SPT positional uncertainty for a cluster with a pressure profile given by a spherical  $\beta$  model with  $\beta = 1$  and scale size  $\theta_c$ , detected by SPT at significance  $\xi$ , is given by

$$\Delta\theta = \sqrt{(\theta_{\text{beam}}^2 + (k\theta_c)^2)/\xi}, \quad (3.4)$$

where  $\theta_{\text{beam}}$  is the beam FWHM, and  $k$  is a factor of order unity (see Story et al. 2011 for more details). With this information, we estimate the expected cumulative distribution of the observed rBCG offsets, assuming a Gaussian with the appropriate width for each cluster; this is equivalent to assuming the underlying rBCG distribution is a delta function centered at zero offset with respect to the true cluster SZ centroid. Results are shown as the blue dotted curve in Fig. 3.7. It is clear that the observed distribution of rBCG offsets is broader than that expected if all rBCGs were located exactly at the cluster center. We conduct a Kolmogorov-Smirnov (KS) test to address the similarity of the two distributions. The hypothesis that the two distributions are drawn from the same parent distribution has a probability of 0.09%, suggesting that the observed rBCG offset distribution cannot be easily explained by the SPT positional uncertainties alone.

Because the SPT candidate positional uncertainties  $\Delta\theta$  are roughly the same, one can expect that our ability to measure the underlying rBCG distribution will weaken as we push to higher redshift where the cluster virial regions subtend smaller angles on the sky. We test this by dividing the sample into four redshift bins with similar numbers of members. The KS tests confirm our expectations; using redshift bins of 0.0-0.40, 0.40-0.54, 0.54-0.73 and  $z > 0.73$  we find the probability that the observed and positional error distributions are drawn from the same parent distribution is 0.11%, 0.008%, 1.97% and 43.4%, respectively. Thus, with the current cluster sample, we cannot detect any extent in the rBCG distribution beyond a redshift  $z \sim 0.7$ . If we assume the underlying rBCG offset distribution is Gaussian, the KS test shows a maximum probability of 5.3% for a Gaussian distributed width of  $0.074r_{200}$  with the probability of consistency dropping below 0.1% for  $\sigma > 0.08r_{200}$ . Therefore, while the Gaussian is not a particularly good fit, the measured distribution strongly favors  $\sigma < 0.08r_{200}$ . We test whether our SZ-selected cluster sample exhibits similar rBCG offsets to those seen in previous X-ray studies. To do this, we adopt the previously published BCG offset distribution from the X-ray studies as the underlying BCG offset distribution for our sample and then convolve this distribution with the SPT candidate positional uncertainties. If rBCGs in SZ-selected clusters are no different from those in these previously studied samples, then we would expect the KS test probability of consistency to be high. We explore two samples: X-ray model 1 (Lin & Mohr 2004; green line in Figure 3.7) and X-ray model 2 (Mann & Ebeling 2012; magenta line in Figure 3.7). The probability of consistency between the SPT sample and X-ray model 1 is 41%, and the probability of consistency between the SPT sample and X-ray model 2 is 0.46%. We also examine another X-ray sample (Stott et al., 2012) which produces a very similar result with our X-ray model 2 with the probability of consistency of 0.55%.

It appears likely that the differences between the two previously published X-ray samples can be explained in terms of differences in the BCG selection. The measured rBCG offset distribution presented in this work agrees with the Lin & Mohr (2004) sample, in which the BCGs were defined as the brightest  $K$ -band galaxy projected within the virial radius  $\theta_{200}$  with

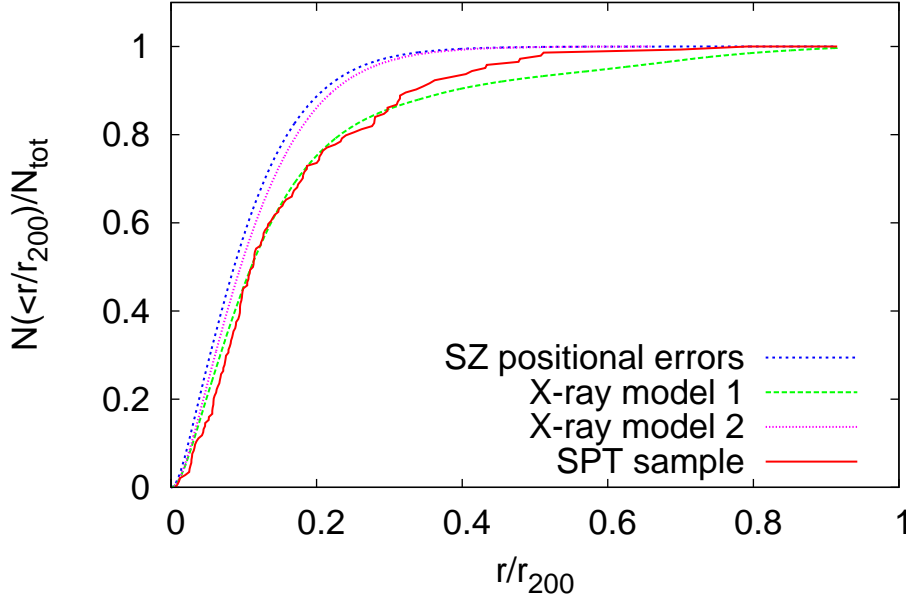


**Figure 3.7:** Normalized cumulative distribution of rBCG offsets from SPT candidate positions as a function of  $r/r_{200}$  for the SPT cluster sample (red line), the expected distribution given SPT positional uncertainties if all rBCGs were at exactly the center of the true SZ centroid (blue line), and the expected distribution given SPT positional uncertainties if the underlying distribution of offsets matched those of an X-ray selected cluster sample (green line; Lin & Mohr, 2004). The KS probability that the observed rBCG distribution and the SPT positional error distribution are drawn from the same parent distribution is 0.09%, but the observed distribution is statistically consistent with the distribution from the X-ray-selected sample convolved with the SPT positional uncertainty distribution. There is no evidence in the rBCG offset distribution that SPT-selected clusters are more merger-rich than X-ray-selected clusters.

spectroscopic redshift consistent with the cluster redshift. This BCG selection is very similar to the SPT rBCG selection, with the main difference being that we do not have spectroscopic redshifts for all rBCG candidates in the SPT sample. The agreement between the SZ- and X-ray-selected samples in this case suggests that there are no strong differences between the merger fractions in these two cluster samples.

The Mann & Ebeling (2012) BCG sample, in contrast, was assembled using bluer optical bands, which are more sensitive to the star formation history. In addition, in cases where a second concentration of galaxies was found within the projected virial region, the central galaxy of the galaxy concentration coincident with the X-ray emission peak was chosen as the BCG, regardless of whether it was brighter or not (Mann, private communication). This selection criteria would make it difficult to identify significantly offset BCGs, which would be more likely to be present in merging systems. Similarly, the Stott et al. (2012) BCG sample was assembled using *i*-band data and a prior on the offset that excludes any offset greater than 500 kpc. Such a prior would also bias the measured distribution against large offsets due to ongoing merger activity.

The rBCG offset distribution measured in the SPT SZ-selected sample of clusters does not provide any compelling evidence that SZ-selected clusters differ in their merger rate as com-



pared to X-ray-selected clusters. It will be possible to test this more precisely once we have the more accurate X-ray cluster centers with consistent rBCG selections. Currently, the X-ray properties of only 15 SPT SZ-selected clusters have been published (Andersson et al., 2011; Benson et al., 2013); however, over 100 additional SPT selected clusters have been approved for observation in on-going programs with Chandra and XMM-Newton. With those data in hand we will be able to measure the rBCG offset distribution over the full redshift range of SPT clusters, allowing us to probe for evolution in the merger rates with redshift.

### 3.6 Conclusions

The SPT-SZ survey has produced an approximately mass-limited, redshift-independent sample of clusters. Approximately 80% of these clusters are newly discovered systems; the SPT survey has significantly increased the number of clusters discovered through the SZ effect and the number of massive clusters detected at high redshift. In this paper, we present optical/NIR properties of 224 galaxy cluster candidates selected from 720 deg<sup>2</sup> of the SPT survey that was completed in 2008 and 2009. The results presented here constitute the subset of the survey in which the optical/NIR follow-up is essentially complete.

With a dedicated pointed follow-up campaign using ground- and space-based optical and NIR telescopes, we confirm 158 out of 224 SPT cluster candidates and measure their photometric redshifts. We show that 18% of the optically confirmed sample lies at  $z > 0.8$ , the median redshift is  $z = 0.57$ , and the highest redshift cluster is at  $z = 1.35 \pm 0.07$ . We have undertaken a cross-comparison among three different cluster redshift estimators to maximize the precision in the presented photometric redshifts. For each cluster, we combine the redshift estimates from the three methods, accounting for the covariance among the methods. Using 57 clusters with spectroscopic redshifts, we calibrate the photometric redshifts and uncertainties and demonstrate that our combining procedure provides a characteristic final cluster redshift accuracy of  $\Delta z / (1 + z) = 0.017$ .

For the 66 candidates without photometric redshift measurements, we calculate lower redshift limits. These limits are set by the depth of the optical/NIR imaging and the band combinations used. For nine of these candidates there is evidence from NIR data that the cluster is a high redshift system, and that we simply need deeper NIR data to measure a photometric redshift.

Under the assumption that all 66 candidates without photometric redshift measurements are noise fluctuations, we estimate the purity of the SPT selected cluster sample as a function of the SPT detection significance  $\xi$ . Results are in good agreement with expectations for sample purity, with no single unconfirmed system above  $\xi = 6$ ,  $> 95\%$  purity above  $\xi = 5$ , and  $\sim 70\%$  purity for  $\xi > 4.5$ . By requiring an optical/NIR counterpart for each SPT candidate, the purity in the final cluster sample approaches 100% over the full  $\xi > 4.5$  sample. The purity of the SPT cluster sample simplifies its cosmological interpretation.

Next, we examine the measured rBCG offset from the SZ candidate positions to explore whether SZ-selected clusters exhibit similar levels of ongoing merging as X-ray selected samples. We show that the characteristic offset between the rBCG and the candidate position is  $\sim 0.5'$ . We examine the radial distribution of rBCG offsets as a function of scaled cluster radius  $r/r_{200}$  and show that a model where we include scatter due to SPT positional uncertainties assuming all BCGs are at cluster centers has only a 0.09% chance of consistency with the observed distribution. That is, the observed distribution is broader than would be

expected from SPT positional uncertainties alone. If we assume the rBCG offset distribution is Gaussian, the observations rule out a Gaussian width of  $\sigma > 0.08r_{200}$ , however, even with smaller width a Gaussian distribution is only marginally consistent with the data. When comparing the SPT rBCG distribution with a X-ray selected cluster sample with a similar rBCG selection criteria (Lin & Mohr, 2004), the SPT and X-ray selected rBCG distributions are similar, suggesting that their merger rates are also similar. Comparisons to other X-ray selected samples are complicated by differences in rBCG selection criteria. For example, comparing to Mann & Ebeling (2012), which selects BCGs using bluer optical bands, we find a significantly less consistent rBCG distribution compared to SPT. We conclude that SZ and X-ray selected cluster samples show consistent rBCG distributions, and note that BCG selection criteria can have a significant effect in such comparisons.

With the full 2500 deg<sup>2</sup> SZ survey completed in 2011, we are now working to complete the confirmations and redshift measurements of the full cluster candidate sample. Scaling from this 720 deg<sup>2</sup> sample with effectively complete optical follow-up, we estimate that the full survey will produce  $\sim 500$  confirmed clusters, with approximately 100 of them at  $z > 0.8$ . This sample of clusters will enable an important next step in cluster cosmological studies as well as the first detailed glimpse of the high redshift tail of young, massive clusters.

*Acknowledgments:* The South Pole Telescope program is supported by the National Science Foundation through grant ANT-0638937. Partial support is also provided by the NSF Physics Frontier Center grant PHY-0114422 to the Kavli Institute of Cosmological Physics at the University of Chicago, the Kavli Foundation, and the Gordon and Betty Moore Foundation. The Munich group acknowledges support from the Excellence Cluster Universe and the DFG research program TR33 The Dark Universe. Galaxy cluster research at Harvard is supported by NSF grant AST-1009012, and research at SAO is supported in part by NSF grants AST-1009649 and MRI-0723073. The McGill group acknowledges funding from the National Sciences and Engineering Research Council of Canada, Canada Research Chairs program, and the Canadian Institute for Advanced Research.

Optical imaging data from the Blanco 4 m at Cerro Tololo Interamerican Observatories (programs 2005B-0043, 2009B-0400, 2010A-0441, 2010B-0598) and spectroscopic observations from VLT programs 086.A-0741 and 286.A-5021 and Gemini program GS-2009B-Q-16 were included in this work. Additional data were obtained with the 6.5 m Magellan Telescopes and the Swope telescope, which are located at the Las Campanas Observatory in Chile. This work is based in part on observations made with the Spitzer Space Telescope (PIDs 60099, 70053), which is operated by the Jet Propulsion Laboratory, California Institute of Technology under a contract with NASA. Support for this work was provided by NASA through an award issued by JPL/Caltech. The Digitized Sky Surveys were produced at the Space Telescope Science Institute under U.S. Government grant NAG W-2166. The images of these surveys are based on photographic data obtained using the Oschin Schmidt Telescope on Palomar Mountain and the UK Schmidt Telescope. The plates were processed into the present compressed digital form with the permission of these institutions.

*Facilities:* Blanco (MOSAIC), Blanco (NEWFIRM), Gemini-S (GMOS), Magellan:Baade (IMACS), Magellan:Clay (LDSS3), South Pole Telescope, *Spitzer*/IRAC, Swope, VLT:Antu (FORIS2), *WISE*

### 3.7 Notable clusters

**SPT-CL J0337-6207** This candidate is optically unconfirmed but has small NIR blank-field probability in at least one data set ( $P_{\text{blank}} = 0.5\%$  in WISE data—also,  $P_{\text{blank}} = 18.2\%$  in NEWFIRM data—see §3.4.2 for details).

**SPT-CL J0428-6049** This candidate is optically unconfirmed but has a high SPT significance ( $\xi = 5.1$ ) and small NIR blank-field probability in at least one data set ( $P_{\text{blank}} = 0.5\%$  in WISE data, see §3.4.2 for details). Though  $P_{\text{blank}} = 69.0\%$  in NEWFIRM data, there is clear visual evidence of a NIR overdensity in the NEWFIRM images, but at  $\sim 40''$  from the SPT position. Such a large offset is heavily disfavored by the fitting procedure, such that the model that minimizes the overall  $\chi^2$  for the NEWFIRM data is effectively a blank field. The position of the WISE overdensity is consistent with the SPT position.

**SPT-CL J0458-5741** This cluster is listed as optically unconfirmed, but it is also listed in Table 2 of R13 as coincident with the low-redshift cluster ACO 3298 (at a separation of  $77''$ ). We see a clear red-sequence overdensity in our Magellan/IMACS data at  $z \simeq 0.2$ , centered on the Abell cluster position. The best-fit SZ core radius for this candidate is  $2.5'$ , which implies an SPT positional uncertainty of  $\sim 0.5'$ , in which case a  $77''$  offset is only a  $\sim 2\sigma$  outlier. However, visual inspection of a lightly filtered SPT map shows that the SZ signal is coming from two distinct components, one of which corresponds to the Abell cluster position, and neither of which would have been significant enough to be included in the R13 catalog on its own. For this reason, we leave the  $\theta_c = 2.5'$  candidate, which blends the SZ signal from the two individual components, as unconfirmed.

**SPT-CL J2002-5335** This candidate is optically unconfirmed but has small NIR blank-field probability in at least one data set ( $P_{\text{blank}} = 7.5\%$  in WISE data—see §3.4.2 for details).

**SPT-CL J2032-5627** This cluster is listed in Table 2 of R13 as coincident with the  $z = 0.06$  cluster ClG 2028.3-5637 / ACO 3685 (at a separation of  $115''$  from the literature Abell cluster position) and as coincident with the  $z = 0.14$  cluster RXC J2032.1-5627 (at a separation of  $87''$  from the reported REFLEX cluster position). However, from our Magellan/IMACS imaging data, we estimate a red-sequence redshift of  $z = 0.31 \pm 0.02$ , and, using the red-sequence measurements as a criterion for cluster member selection, we have obtained spectra for 32 cluster members using GISMO and have measured a robust spectroscopic redshift of  $z_{\text{spec}} = 0.2840$ . Examination of the REFLEX spectroscopic catalog (Guzzo et al., 2009) reveals that their spectroscopic observations yielded five galaxies near their reported redshift of  $z_{\text{spec}} = 0.1380$  but also six galaxies within 2% of the value we derive from our GISMO observations ( $z_{\text{spec}} = 0.2840$ ). The value of  $z_{\text{spec}} = 0.0608$  for ACO 3685 is from only one galaxy (and, while reported in Struble & Rood 1999, is originally from Fetisova 1981). We conclude that there are two clear optical overdensities at different redshifts along the line of sight to this SZ/X-ray system, and that the literature redshift of  $z = 0.0608$  for ACO 3685 is probably incorrect. Because of the redshift dependence of the SPT selection function (see, e.g., Vanderlinde et al. 2010), it is likely that the bulk of the SZ signal is coming from the higher-redshift cluster. We have obtained XMM-Newton data on this system, and the X-ray and SZ signals have very similar morphology, indicating that the X-ray signal is also predominantly

associated with the higher-redshift system. This makes it likely that the  $z = 0.2840$  system is a massive cluster and that the  $z = 0.1380$  system is a low-mass interloper, possibly the cluster originally identified as ClG 2028.3-5637 / ACO 3685. SPT-CL J2032-5627 is discussed further—including weak lensing data from Magellan/Megacam—in High et al. (2012).

**SPT-CL J2035-5614** This candidate is optically unconfirmed but has small NIR blank-field probability in at least one data set ( $P_{\text{blank}} = 0.1\%$  in WISE data—see §3.4.2 for details).

**SPT-CL J2039-5723** This candidate is optically unconfirmed but has a small SZ core radius ( $0.5'$ ) and small NIR blank-field probability in at least one data set ( $P_{\text{blank}} = 1.2\%$  in WISE data and  $8.7\%$  in NEWFIRM data—see §3.4.2 for details).

**SPT-CL J2121-5546** This candidate is optically unconfirmed but has small NIR blank-field probability in at least one data set ( $P_{\text{blank}} = 0.9\%$  in WISE data—also,  $P_{\text{blank}} = 11.5\%$  in NEWFIRM data—see §3.4.2 for details).

**SPT-CL J2136-5535** This candidate is optically unconfirmed but has small NIR blank-field probability in at least one data set ( $P_{\text{blank}} = 5.2\%$  in WISE data—see §3.4.2 for details).

**SPT-CL J2152-4629** This candidate is optically unconfirmed but has a high SPT significance ( $\xi = 5.6$ ), a small SZ core radius ( $0.25'$ ), and small NIR blank-field probability in at least one data set ( $P_{\text{blank}} = 8.0\%$  in WISE data; also  $P_{\text{blank}} = 10.6\%$  in *Spitzer*/IRAC data and  $20.0\%$  in NEWFIRM data—see §3.4.2 for details). This is the only candidate with *Spitzer*/IRAC  $P_{\text{blank}} < 20\%$  for which we were not able to estimate a redshift.

**SPT-CL J2343-5556** This candidate is optically unconfirmed but has small NIR blank-field probability in at least one data set ( $P_{\text{blank}} = 5.6\%$  in WISE data and  $21.0\%$  in NEWFIRM data—see §3.4.2 for details).

**Table 3.3:** All candidates above  $\xi = 4.5$  in 720 deg<sup>2</sup> of the SPT-SZ survey.

SPT ID	Position		$\xi$	$z_{\text{spec}}^a$	$z_{\text{comb}} \pm \sigma_{z_{\text{comb}}}$ (or redshift lower limit)	Flag <sup>b</sup>	NIR blank field		probability <i>Sptizer</i>	$P_{\text{blank}}(\%)^c$		rBCG Position		Imaging Ref. <sup>d</sup>
	RA (deg)	Dec (deg)					NEWFIRM	<i>Sptizer</i>		WISE		RA (deg)	Dec (deg)	
SPT-CLJ0000-5748	0.2496	-57.8066	5.48	0.702	$0.68 \pm 0.03$	1	—	—	—	—	—	0.2503	-57.8093	1,2
SPT-CLJ0201-6051	30.3933	-60.8592	4.83	—	$> 1.0$	—	61.3	—	—	100.0	—	—	—	1
SPT-CLJ0203-5651	30.8309	-56.8612	4.98	—	$> 1.0$	—	28.1	—	—	56.5	—	—	—	1
SPT-CLJ0205-5829	31.4437	-58.4855	10.54	1.322	$1.30 \pm 0.07$	3	8.0	2.0	—	1.8	—	31.4510	-58.4803	1
SPT-CLJ0205-6432	31.2786	-64.5461	6.02	0.744	$0.75 \pm 0.03$	1	6.8	0.5	—	17.3	—	31.3244	-64.5583	1
SPT-CLJ0209-5452	32.3491	-54.8794	4.52	—	$0.42 \pm 0.03$	1	—	—	—	—	—	32.3494	-54.8720	1
SPT-CLJ0211-5712	32.8232	-57.2157	4.77	—	$> 1.0$	—	26.7	—	—	56.1	—	—	—	1
SPT-CLJ0216-5730	34.1363	-57.5100	4.72	—	$> 1.0$	—	43.4	—	—	80.6	—	—	—	1,2
SPT-CLJ0216-6409	34.1723	-64.1562	5.54	—	$0.64 \pm 0.03$	1	—	—	—	—	—	34.1599	-64.1599	1
SPT-CLJ0218-5826	34.6251	-58.4386	4.54	—	$0.57 \pm 0.03$	1	—	—	—	—	—	34.6267	-58.4421	1,2
SPT-CLJ0221-6212	35.4382	-62.2044	4.71	—	$> 1.2$	—	75.7	—	—	84.9	—	—	—	1
SPT-CLJ0230-6028	37.6410	-60.4694	5.88	—	$0.74 \pm 0.08$	3	—	11.3	—	0.3	—	37.6354	-60.4628	3
SPT-CLJ0233-5819	38.2561	-58.3269	6.64	0.663	$0.76 \pm 0.07$	3	4.2	0.0	—	—	—	38.2541	-58.3269	1
SPT-CLJ0234-5831	38.6790	-58.5217	14.65	0.415	$0.42 \pm 0.03$	1	—	—	—	—	—	38.6762	-58.5236	1
SPT-CLJ0239-6148	39.9120	-61.8032	4.67	—	$> 1.1$	—	44.2	—	—	38.0	—	—	—	1,2
SPT-CLJ0240-5946	40.1620	-59.7703	9.04	0.400	$0.41 \pm 0.03$	1	—	—	—	—	—	40.1599	-59.7635	3
SPT-CLJ0240-5952	40.1982	-59.8785	4.65	—	$0.62 \pm 0.03$	3	—	—	—	—	—	40.2048	-59.8732	5
SPT-CLJ0242-6039	40.6551	-60.6526	4.92	—	$> 1.5$	—	—	51.5	—	64.9	—	—	—	2
SPT-CLJ0243-5930	40.8616	-59.5132	7.42	—	$0.65 \pm 0.03$	1	—	—	—	—	—	40.8628	-59.5172	3
SPT-CLJ0249-5658	42.4068	-56.9764	5.44	—	$0.23 \pm 0.02$	1	—	—	—	—	—	42.3918	-56.9870	1
SPT-CLJ0253-6046	43.4605	-60.7744	4.83	—	$0.44 \pm 0.02$	1	—	—	—	—	—	43.4508	-60.7499	1
SPT-CLJ0254-5857	43.5729	-58.9526	14.42	0.438	$0.43 \pm 0.03$	1	—	—	—	—	—	43.5365	-58.9718	3
SPT-CLJ0254-6051	43.6015	-60.8643	6.71	—	$0.44 \pm 0.02$	1	—	—	—	—	—	43.5884	-60.8689	1
SPT-CLJ0256-5617	44.1009	-56.2973	7.54	—	$0.63 \pm 0.03$	1	—	—	—	—	—	44.0880	-56.3031	3
SPT-CLJ0257-5732	44.3516	-57.5423	5.40	0.434	$0.42 \pm 0.02$	1	—	—	—	—	—	44.3373	-57.5484	1
SPT-CLJ0257-5842	44.3924	-58.7117	5.38	—	$0.42 \pm 0.02$	1	—	—	—	—	—	44.4374	-58.7045	1
SPT-CLJ0257-6050	44.3354	-60.8450	4.76	—	$0.48 \pm 0.03$	1	—	—	—	—	—	44.3386	-60.8358	2
SPT-CLJ0258-5756	44.5563	-57.9438	4.50	—	$> 1.0$	1	—	—	—	17.4	—	—	—	1,2
SPT-CLJ0300-6315	45.1430	-63.2643	4.88	—	$> 1.5$	—	—	31.6	—	63.6	—	—	—	1
SPT-CLJ0301-6456	45.4780	-64.9470	4.94	—	$0.65 \pm 0.03$	1	—	—	—	—	—	45.4809	-64.9492	1
SPT-CLJ0307-6226	46.8335	-62.4336	8.32	—	$0.61 \pm 0.03$	1	—	—	—	—	—	46.8495	-62.4028	3
SPT-CLJ0311-6354	47.8283	-63.9083	7.33	—	$0.30 \pm 0.02$	1	—	—	—	—	—	47.8229	-63.9157	1
SPT-CLJ0313-5645	48.2604	-56.7554	4.82	—	$0.63 \pm 0.03$	1	—	—	—	—	—	48.2912	-56.7420	1
SPT-CLJ0316-6059	49.2179	-60.9849	4.59	—	$> 1.5$	—	—	26.4	—	26.9	—	—	—	1
SPT-CLJ0317-5935	49.3208	-59.5856	5.91	0.469	$0.47 \pm 0.02$	1	—	—	—	—	—	49.3160	-59.5915	1
SPT-CLJ0320-5800	50.0316	-58.0084	4.54	—	$> 1.0$	—	—	—	—	38.1	—	—	—	1,2
SPT-CLJ0324-6236	51.0530	-62.6018	8.59	—	$0.74 \pm 0.03$	1	—	0.3	—	0.0	—	51.0511	-62.5988	3
SPT-CLJ0328-5541	52.1663	-55.6975	7.08	0.084	$0.10 \pm 0.03$	1	—	—	—	—	—	52.1496	-55.7124	1
SPT-CLJ0333-5842	53.3195	-58.7019	4.54	—	$0.49 \pm 0.04$	3	—	—	—	—	—	53.3322	-58.7060	5
SPT-CLJ0337-6207	54.4720	-62.1176	4.88	—	$> 1.3$	—	18.2	—	—	0.5	—	—	—	1
SPT-CLJ0337-6300	54.4685	-63.0098	5.29	—	$0.46 \pm 0.03$	1	—	—	—	—	—	54.4744	-63.0155	1

Table 3.3 – continued from previous page

SPT ID	Position		$\xi$	$z_{\text{spec}}^a$	$z_{\text{comb}} \pm \sigma_{z_{\text{comb}}}$ (or redshift lower limit)	Flag <sup>b</sup>	NIR blank field probability NEWFIRM	$P_{\text{blank}}(\%)^c$ WISE	rBCG Position		Imaging Ref. <sup>d</sup>
	RA (deg)	Dec (deg)							RA (deg)	Dec (deg)	
SPT-CLJ0341-5731	55.3979	-57.5233	5.35	—	$0.64 \pm 0.02$	1	—	—	55.3955	-57.5244	1
SPT-CLJ0341-6143	55.3485	-61.7192	5.60	—	$0.63 \pm 0.03$	1	—	—	55.3488	-61.7208	1
SPT-CLJ0343-5518	55.7634	-55.3049	5.98	—	$0.49 \pm 0.02$	1	—	—	55.7581	-55.3111	1
SPT-CLJ0344-5452	56.0926	-54.8726	5.41	—	$1.01 \pm 0.07$	3	8.0	17.6	—	—	1
SPT-CLJ0344-5518	56.2101	-55.3036	5.02	—	$0.36 \pm 0.02$	1	—	—	56.1816	-55.3179	1
SPT-CLJ0345-6419	56.2518	-64.3326	5.57	—	$0.93 \pm 0.07$	3	3.4	0.1	56.2518	-64.3343	1
SPT-CLJ0346-5839	56.5746	-58.6535	4.96	—	$0.74 \pm 0.07$	3	—	0.4	56.5754	-58.6532	1
SPT-CLJ0351-5636	57.9312	-56.6099	4.65	—	$0.38 \pm 0.03$	1	—	—	57.9446	-56.6349	1
SPT-CLJ0351-5944	57.8654	-59.7457	4.61	—	$> 1.0$	—	20.4	60.4	—	—	2
SPT-CLJ0352-5647	58.2366	-56.7992	7.11	—	$0.66 \pm 0.03$	1	—	—	58.2759	-56.7608	3
SPT-CLJ0354-5904	58.5611	-59.0741	6.49	—	$0.41 \pm 0.03$	1	—	—	58.6166	-59.0971	1
SPT-CLJ0354-6032 <sup>2</sup>	58.6744	-60.5386	4.57	—	$1.06 \pm 0.07$	3	8.1	1.9	58.6604	-60.5462	2
SPT-CLJ0402-6129	60.7066	-61.4988	4.83	—	$0.53 \pm 0.04$	3	—	—	60.7213	-61.4973	5
SPT-CLJ0403-5534	60.9479	-55.5829	4.88	—	$> 1.5$	—	71.1	60.5	—	—	1
SPT-CLJ0403-5719	60.9670	-57.3241	5.75	—	$0.43 \pm 0.02$	1	—	—	60.9679	-57.3285	1
SPT-CLJ0404-6510	61.0556	-65.1817	4.75	—	$0.15 \pm 0.02$	1	—	—	61.0934	-65.1703	1
SPT-CLJ0406-5455	61.6922	-54.9205	5.82	—	$0.73 \pm 0.03$	1	3.3	19.6	61.6857	-54.9257	1
SPT-CLJ0410-5454	62.6154	-54.9016	5.06	—	$> 1.0$	—	76.8	35.0	—	—	1
SPT-CLJ0410-6343	62.5158	-63.7285	5.79	—	$0.49 \pm 0.02$	1	—	—	62.5207	-63.7311	1
SPT-CLJ0411-5751	62.8433	-57.8636	5.16	—	$0.75 \pm 0.02$	1	—	25.3	62.8174	-57.8517	1
SPT-CLJ0411-6340	62.8597	-63.6810	6.41	—	$0.14 \pm 0.02$	1	—	—	62.8676	-63.6853	1
SPT-CLJ0412-5743	63.0245	-57.7202	5.29	—	$0.38 \pm 0.03$	1	—	—	63.0442	-57.7383	1
SPT-CLJ0416-6359	64.1618	-63.9964	6.06	—	$0.30 \pm 0.02$	1	—	—	64.1735	-64.0060	1
SPT-CLJ0423-5506	65.8153	-55.1036	4.51	—	$0.21 \pm 0.04$	3	—	—	65.8108	-55.1143	5
SPT-CLJ0423-6143	65.9366	-61.7183	4.65	—	$0.71 \pm 0.04$	3	—	13.9	65.9323	-61.7293	5
SPT-CLJ0426-5455	66.5205	-54.9201	8.86	—	$0.63 \pm 0.03$	1	—	—	66.5171	-54.9253	3
SPT-CLJ0428-6049	67.0291	-60.8302	5.06	—	$> 1.1$	—	69.0	0.5	—	—	1
SPT-CLJ0430-6251 <sup>3</sup>	67.7086	-62.8536	5.20	—	$0.38 \pm 0.04$	4	—	—	—	—	1
SPT-CLJ0431-6126	67.8393	-61.4438	6.40	0.058	$0.08 \pm 0.02$	1	—	—	67.8053	-61.4533	1
SPT-CLJ0433-5630	68.2522	-56.5038	5.35	0.692	$0.65 \pm 0.03$	1	—	—	68.2545	-56.5190	1
SPT-CLJ0441-5859	70.4411	-58.9931	4.54	—	$> 1.1$	—	—	27.7	—	—	5
SPT-CLJ0444-5603 <sup>4</sup>	71.1130	-56.0566	5.30	—	$0.98 \pm 0.07$	3	0.4	0.0	71.1077	-56.0556	1
SPT-CLJ0446-5849	71.5160	-58.8226	7.44	—	$1.16 \pm 0.07$	3	—	5.6	71.5138	-58.8247	1
SPT-CLJ0452-5945	73.1282	-59.7622	4.50	—	$> 0.7$	—	—	39.4	—	—	5
SPT-CLJ0456-5623	74.1745	-56.3868	4.76	—	$0.66 \pm 0.03$	1	—	—	—	—	2
SPT-CLJ0456-6141	74.1496	-61.6840	4.84	—	$0.41 \pm 0.03$	3	—	—	74.1361	-61.6902	5
SPT-CLJ0458-5741	74.6021	-57.6952	4.91	—	$> 1.0$	—	—	52.5	—	—	2
SPT-CLJ0502-6113	75.5400	-61.2315	5.09	—	$0.66 \pm 0.03$	1	—	—	75.5630	-61.2314	1
SPT-CLJ0509-5342	77.3360	-53.7046	6.61	0.461	$0.43 \pm 0.02$	1	—	—	77.3392	-53.7036	1,2
SPT-CLJ0511-5154	77.9202	-51.9044	5.63	0.645	$0.63 \pm 0.03$	1	—	—	—	—	1*
SPT-CLJ0514-5118	78.6859	-51.3100	4.82	—	$> 1.2$	—	28.2	49.7	—	—	1
SPT-CLJ0516-5430	79.1480	-54.5062	9.42	0.295	$0.31 \pm 0.02$	1	—	—	79.1557	-54.5007	1,2

Table 3.3 – continued from previous page

SPT ID	Position		$\xi$	$z_{\text{spec}}^a$	$z_{\text{comb}} \pm \sigma_{z_{\text{comb}}}$ (or redshift lower limit)		Flag <sup>b</sup>	NIR blank field probability		$P_{\text{blank}}(\%)^c$		rBCG Position		Imaging Ref. <sup>d</sup>
	RA (deg)	Dec (deg)						NEWFIRM	<i>Spitzer</i>	<i>WISE</i>		RA (deg)	Dec (deg)	
SPT-CLJ0521-5104	80.2983	-51.0812	5.45	0.675	$0.64 \pm 0.02$	1	–	–	–	–	–	80.3106	-51.0718	1*
SPT-CLJ0522-5026	80.5190	-50.4409	4.87	–	$0.51 \pm 0.03$	1	–	–	–	–	–	80.5000	-50.4696	1*
SPT-CLJ0527-5928	81.8111	-59.4833	4.71	–	$> 0.9$	–	–	–	–	25.5	–	–	–	2
SPT-CLJ0528-5300	82.0173	-53.0001	5.45	0.768	$0.77 \pm 0.03$	1	–	0.0	–	0.0	–	82.0221	-52.9982	1*
SPT-CLJ0529-5238	82.2923	-52.6417	4.52	–	$> 1.1$	–	–	–	–	81.8	–	–	–	1*
SPT-CLJ0532-5647	83.1586	-56.7893	4.51	–	$> 0.9$	–	–	–	–	39.0	–	–	–	2
SPT-CLJ0533-5005	83.3984	-50.0918	5.59	0.881	$0.81 \pm 0.03$	1	–	0.0	–	18.4	–	83.4144	-50.0845	2
SPT-CLJ0534-5937	83.6018	-59.6289	4.57	0.576	$0.57 \pm 0.02$	1	–	–	–	–	–	83.6255	-59.6152	2
SPT-CLJ0537-5549	84.2578	-55.8268	4.55	–	$> 1.1$	–	–	–	–	28.4	–	–	–	2
SPT-CLJ0538-5657	84.5865	-56.9530	4.63	–	$> 1.5$	–	–	21.8	–	25.1	–	–	–	2
SPT-CLJ0539-5744	84.9998	-57.7432	5.12	–	$0.76 \pm 0.03$	1	–	0.0	–	0.0	–	84.9950	-57.7424	2
SPT-CLJ0546-5345	86.6541	-53.7615	7.69	1.066	$1.04 \pm 0.07$	3	–	0.0	–	0.0	–	86.6569	-53.7587	1*
SPT-CLJ0551-5709	87.9016	-57.1565	6.13	0.423	$0.43 \pm 0.02$	1	–	–	–	–	–	87.8981	-57.1414	2
SPT-CLJ0556-5403	89.2016	-54.0630	4.83	–	$0.93 \pm 0.04$	4	17.1	–	–	0.0	–	89.2018	-54.0582	2
SPT-CLJ0559-5249	89.9245	-52.8265	9.28	0.609	$0.63 \pm 0.02$	1	–	–	–	–	–	89.9301	-52.8242	2
SPT-CLJ2002-5335	300.5113	-53.5913	4.53	–	$> 1.0$	–	–	–	–	7.5	–	–	–	1
SPT-CLJ2005-5635	301.3385	-56.5902	4.68	–	$> 0.6$	–	–	–	–	71.3	–	–	–	1
SPT-CLJ2006-5325	301.6620	-53.4286	5.06	–	$> 1.5$	–	66.8	–	52.3	71.8	–	–	–	1
SPT-CLJ2007-4906	301.9663	-49.1105	4.50	–	$1.25 \pm 0.07$	3	–	0.9	–	5.9	–	301.9692	-49.1085	1
SPT-CLJ2009-5756	302.4261	-57.9480	4.68	–	$0.63 \pm 0.03$	1	–	–	–	–	–	–	–	1
SPT-CLJ2011-5228 <sup>5</sup>	302.7810	-52.4734	4.55	–	$0.96 \pm 0.04$	1	–	–	–	51.6	–	302.7814	-52.4709	1
SPT-CLJ2011-5725 <sup>6</sup>	302.8526	-57.4214	5.43	0.279	$0.28 \pm 0.03$	1	–	–	–	–	–	302.8624	-57.4197	1
SPT-CLJ2012-5342	303.0822	-53.7137	4.65	–	$> 0.7$	–	–	–	–	11.0	–	–	–	1
SPT-CLJ2012-5649	303.1132	-56.8308	5.99	0.055	$0.07 \pm 0.02$	1	–	–	–	–	–	303.1142	-56.8270	2
SPT-CLJ2013-5432	303.4968	-54.5445	4.75	–	$> 1.0$	–	49.7	–	–	63.4	–	–	–	1
SPT-CLJ2015-5504	303.9884	-55.0715	4.64	–	$> 0.6$	–	87.3	–	–	67.0	–	–	–	1
SPT-CLJ2016-4954	304.0181	-49.9122	5.01	–	$0.26 \pm 0.02$	1	–	–	–	–	–	304.0067	-49.9067	1
SPT-CLJ2017-6258	304.4827	-62.9763	6.45	–	$0.57 \pm 0.03$	1	–	–	–	–	–	304.4730	-62.9950	3
SPT-CLJ2018-4528	304.6076	-45.4807	4.64	–	$0.40 \pm 0.03$	1	–	–	–	–	–	304.6164	-45.4761	1
SPT-CLJ2019-5642	304.7703	-56.7079	5.25	–	$0.15 \pm 0.03$	1	–	–	–	–	–	304.8137	-56.7122	2
SPT-CLJ2020-4646	305.1936	-46.7702	5.09	–	$0.17 \pm 0.02$	1	–	–	–	–	–	305.1973	-46.7748	1
SPT-CLJ2020-6314	305.0301	-63.2413	5.37	–	$0.58 \pm 0.02$	1	–	–	–	–	–	305.0350	-63.2471	2
SPT-CLJ2021-5256	305.4690	-52.9439	5.31	–	$0.11 \pm 0.02$	1	–	–	–	–	–	305.4725	-52.9509	1
SPT-CLJ2022-6323	305.5235	-63.3973	6.58	0.383	$0.41 \pm 0.02$	1	–	–	–	–	–	305.5410	-63.3971	2,4
SPT-CLJ2023-5535	305.8377	-55.5903	13.41	0.232	$0.22 \pm 0.02$	1	–	–	–	–	–	305.9069	-55.5697	2,3
SPT-CLJ2025-5117	306.4836	-51.2904	9.48	–	$0.20 \pm 0.02$	1	–	–	–	–	–	306.4822	-51.2744	1
SPT-CLJ2026-4513	306.6140	-45.2256	5.53	–	$0.71 \pm 0.03$	1	–	–	–	18.8	–	306.6180	-45.2338	1
SPT-CLJ2030-5638	307.7067	-56.6352	5.47	–	$0.39 \pm 0.03$	1	–	–	–	–	–	307.6886	-56.6322	2,4
SPT-CLJ2032-5627	308.0800	-56.4557	8.14	0.284	$0.33 \pm 0.02$	1	–	–	–	–	–	308.0586	-56.4368	2
SPT-CLJ2034-5936	308.5408	-59.6007	8.57	–	$0.92 \pm 0.07$	3	–	0.2	–	25.9	–	308.5414	-59.6034	2
SPT-CLJ2035-5251	308.8026	-52.8527	9.99	–	$0.47 \pm 0.02$	1	–	–	–	–	–	–	–	1
SPT-CLJ2035-5614	308.9023	-56.2407	4.55	–	$> 1.0$	–	–	–	–	0.1	–	–	–	1

Table 3.3 – continued from previous page

SPT ID	RA (deg)	Position Dec (deg)	$\xi$	$z_{\text{spec}}^a$	$z_{\text{comb}} \pm \sigma_{z_{\text{comb}}}$ (or redshift lower limit)	Flag <sup>b</sup>	NIR blank field NEWFIRM	probability <i>Spitzer</i>	$P_{\text{blank}}(\%)^c$ <i>WISE</i>	rBCG Position RA (deg) Dec (deg)	Imaging Ref. <sup>d</sup>
SPT-CLJ2039-5723	309.8246	-57.3871	4.69	—	$> 1.2$	—	9.2	—	1.2	—	1,2
SPT-CLJ2040-4451	310.2468	-44.8599	6.28	—	$1.35 \pm 0.07$	3	29.9	4.6	3.6	310.2384 -44.8593	1
SPT-CLJ2040-5230	310.1255	-52.5052	4.70	—	$> 1.0$	—	44.4	—	20.2	—	1
SPT-CLJ2040-5342	310.2195	-53.7122	5.88	—	$0.57 \pm 0.04$	1	—	—	—	—	1
SPT-CLJ2040-5725	310.0631	-57.4287	6.38	0.930	$0.91 \pm 0.07$	3	—	0.9	15.0	310.0552 -57.4209	1,2
SPT-CLJ2043-5035	310.8285	-50.5929	7.81	0.723	$0.77 \pm 0.03$	1	—	0.6	0.4	—	1
SPT-CLJ2043-5614	310.7906	-56.2351	4.72	—	$0.69 \pm 0.03$	1	—	—	—	310.7788 -56.2390	1
SPT-CLJ2045-6026	311.3649	-60.4469	4.77	—	$> 0.5$	—	86.3	—	94.6	—	1
SPT-CLJ2046-4542	311.5620	-45.7111	4.54	—	$> 1.0$	—	—	—	65.3	—	1
SPT-CLJ2048-4524	312.2268	-45.4150	4.56	—	$> 1.0$	—	—	—	96.6	—	1
SPT-CLJ2051-6256	312.8027	-62.9348	5.17	—	$0.47 \pm 0.02$	1	—	—	—	312.8230 -62.9407	1
SPT-CLJ2055-5456	313.9941	-54.9366	6.61	—	$0.11 \pm 0.02$	1	—	—	—	313.9838 -54.9273	2
SPT-CLJ2056-5106	314.0723	-51.1163	4.70	—	$> 1.0$	—	43.0	—	45.4	—	1
SPT-CLJ2056-5459	314.2199	-54.9892	6.05	0.718	$0.84 \pm 0.07$	3	—	0.3	9.3	314.2232 -54.9858	2
SPT-CLJ2057-5251	314.4105	-52.8567	4.52	—	$> 1.5$	—	—	82.1	65.8	—	1
SPT-CLJ2058-5608	314.5893	-56.1454	5.02	0.606	$0.59 \pm 0.02$	1	—	—	—	314.5930 -56.1464	1
SPT-CLJ2059-5018	314.9324	-50.3049	4.79	—	$0.39 \pm 0.02$	1	—	—	—	314.9220 -50.3029	1
SPT-CLJ2100-4548	315.0936	-45.8057	4.84	0.712	$0.74 \pm 0.03$	1	—	1.2	6.9	—	1
SPT-CLJ2100-5708	315.1502	-57.1347	5.11	—	$0.59 \pm 0.03$	1	—	—	—	315.1470 -57.1385	1
SPT-CLJ2101-5542	315.3106	-55.7027	5.04	—	$0.22 \pm 0.02$	1	—	—	—	315.3040 -55.6940	1
SPT-CLJ2101-6123	315.4594	-61.3972	5.28	—	$0.60 \pm 0.03$	1	—	—	—	315.4326 -61.4047	1
SPT-CLJ2103-5411	315.7687	-54.1951	4.88	—	$0.46 \pm 0.02$	1	—	—	—	315.7792 -54.1945	1
SPT-CLJ2104-5224	316.2283	-52.4044	5.32	0.799	$0.81 \pm 0.03$	1	—	65.7	3.0	316.2120 -52.4079	1
SPT-CLJ2106-5820	316.5144	-58.3459	4.81	—	$> 1.0$	—	79.4	—	60.6	—	1
SPT-CLJ2106-5844	316.5210	-58.7448	22.08	1.132	$1.20 \pm 0.07$	3	—	0.0	0.1	316.5194 -58.7412	2
SPT-CLJ2106-6019	316.6642	-60.3299	4.98	—	$0.97 \pm 0.03$	1	2.5	—	1.0	316.6449 -60.3385	1
SPT-CLJ2106-6303	316.6596	-63.0510	4.90	—	$> 1.0$	—	19.6	—	16.7	—	1
SPT-CLJ2109-4626	317.4516	-46.4370	5.51	—	$0.98 \pm 0.09$	3	—	1.1	0.6	317.4557 -46.4376	1
SPT-CLJ2109-5040	317.3820	-50.6773	5.17	—	$0.47 \pm 0.03$	1	—	—	—	317.4016 -50.6815	1
SPT-CLJ2110-5244	317.5502	-52.7486	6.22	—	$0.61 \pm 0.02$	1	—	—	—	317.5520 -52.7496	1
SPT-CLJ2111-5338	317.9217	-53.6496	5.65	—	$0.43 \pm 0.03$	1	—	—	—	317.9357 -53.6477	1
SPT-CLJ2115-4659	318.7995	-46.9862	5.60	—	$0.34 \pm 0.02$	1	—	—	—	318.8064 -46.9797	1
SPT-CLJ2118-5055	319.7291	-50.9329	5.62	0.625	$0.63 \pm 0.03$	1	—	—	—	—	1
SPT-CLJ2119-6230	319.8846	-62.5096	4.55	—	$0.72 \pm 0.03$	1	—	—	—	319.8765 -62.5106	1
SPT-CLJ2120-4728 <sup>7</sup>	320.1594	-47.4776	5.98	—	$0.99 \pm 0.07$	3	8.7	0.5	2.1	320.1638 -47.4750	1
SPT-CLJ2121-5546	320.2715	-55.7780	4.79	—	$> 0.8$	—	11.5	—	0.9	—	2
SPT-CLJ2121-6335	320.4269	-63.5843	5.43	—	$0.23 \pm 0.02$	1	—	—	—	320.4303 -63.5973	1
SPT-CLJ2124-6124	321.1488	-61.4141	8.21	0.435	$0.44 \pm 0.02$	1	—	—	—	321.1577 -61.4077	1
SPT-CLJ2125-6113	321.2902	-61.2292	4.74	—	$> 1.5$	—	—	91.8	17.2	—	1,2
SPT-CLJ2127-6443	321.9939	-64.7288	4.54	—	$> 1.0$	—	—	—	80.2	—	1
SPT-CLJ2130-4737	322.6622	-47.6257	4.83	—	$> 1.5$	—	76.9	22.4	68.5	—	1
SPT-CLJ2130-6458	322.7285	-64.9764	7.57	0.316	$0.36 \pm 0.02$	1	—	—	—	322.7343 -64.9779	1,2



Table 3.3 – continued from previous page

SPT ID	RA (deg)	Position Dec (deg)	$\xi$	$z_{\text{spec}}^a$	$z_{\text{comb}} \pm \sigma_{z_{\text{comb}}}$ (or redshift lower limit)	Flag <sup>b</sup>	NIR blank field NEWFIRM	probability <i>Spitzer</i>	$P_{\text{blank}}(\%)^c$ <i>WISE</i>	rBCG Position RA (deg) Dec (deg)	Imaging Ref. <sup>d</sup>
SPT-CLJ2131-5003	322.9717	-50.0647	4.83	—	$0.45 \pm 0.02$	1	—	—	—	322.9637 -50.0624	1
SPT-CLJ2133-5411	323.2978	-54.1845	4.58	—	$> 1.5$	—	—	48.7	32.0	—	1
SPT-CLJ2135-5452	323.9060	-54.8773	4.61	—	$> 1.0$	—	—	—	53.4	—	1
SPT-CLJ2135-5726	323.9158	-57.4415	10.43	0.427	$0.46 \pm 0.02$	1	—	—	—	323.9059 -57.4418	2,4
SPT-CLJ2136-4704	324.1175	-47.0803	6.17	0.425	$0.43 \pm 0.03$	1	—	—	—	324.1640 -47.0716	1
SPT-CLJ2136-5519	324.2392	-55.3215	4.65	—	$> 1.5$	—	—	35.2	62.1	—	1
SPT-CLJ2136-5535 <sup>8</sup>	324.0898	-55.5853	4.58	—	$> 1.2$	—	—	—	5.2	—	1
SPT-CLJ2136-5723	324.1209	-57.3923	4.55	—	$> 1.0$	—	—	—	40.0	—	2,4
SPT-CLJ2136-6307	324.2334	-63.1233	6.25	0.926	$1.00 \pm 0.07$	3	—	0.2	1.4	324.2239 -63.1143	1,2
SPT-CLJ2137-6437	324.4178	-64.6235	4.60	—	$0.91 \pm 0.07$	3	—	3.7	12.8	324.4337 -64.6234	1
SPT-CLJ2138-6007	324.5060	-60.1324	12.64	0.319	$0.34 \pm 0.02$	1	—	—	—	324.5036 -60.1317	2,4
SPT-CLJ2139-5420	324.9669	-54.3396	4.81	—	$0.24 \pm 0.02$	1	—	—	—	324.9713 -54.3410	1
SPT-CLJ2140-5331	325.0304	-53.5199	4.55	—	$0.51 \pm 0.02$	1	—	—	—	325.0287 -53.5037	1
SPT-CLJ2140-5727	325.1380	-57.4564	5.08	—	$0.40 \pm 0.03$	1	—	—	—	—	2
SPT-CLJ2142-4846	325.5693	-48.7743	4.53	—	$> 0.8$	—	—	—	96.1	—	1
SPT-CLJ2145-5644	326.4694	-56.7477	12.30	0.480	$0.48 \pm 0.02$	1	—	—	—	326.5298 -56.7422	2
SPT-CLJ2146-4633	326.6473	-46.5505	9.59	0.933	$0.95 \pm 0.07$	3	—	0.2	1.5	—	1
SPT-CLJ2146-4846	326.5346	-48.7774	5.88	0.623	$0.62 \pm 0.02$	2	—	—	—	326.5246 -48.7813	1
SPT-CLJ2146-5736	326.6963	-57.6138	5.94	—	$0.61 \pm 0.02$	1	—	—	—	326.6954 -57.6310	2
SPT-CLJ2148-4843	327.0971	-48.7287	4.64	—	$0.98 \pm 0.07$	3	—	0.6	1.1	—	1
SPT-CLJ2148-6116	327.1798	-61.2791	7.27	0.571	$0.52 \pm 0.02$	1	—	—	—	327.1617 -61.2655	1,2
SPT-CLJ2149-5330	327.3770	-53.5014	4.79	—	$0.60 \pm 0.03$	1	—	—	—	327.4331 -53.5176	1
SPT-CLJ2150-6111	327.7177	-61.1954	4.70	—	$> 1.1$	1	25.4	—	15.7	—	1
SPT-CLJ2152-4629	328.1943	-46.4947	5.60	—	$> 1.5$	—	20.0	10.6	8.0	—	1
SPT-CLJ2152-5143	328.0034	-51.7245	4.53	—	$0.41 \pm 0.03$	1	—	—	—	327.9829 -51.7226	1
SPT-CLJ2152-5633	328.1458	-56.5641	5.84	—	$> 1.5$	—	—	20.2	55.5	—	1,2
SPT-CLJ2155-5103	328.8747	-51.0508	4.52	—	$> 1.1$	—	—	—	34.1	—	1
SPT-CLJ2155-5225	328.8941	-52.4169	4.77	—	$0.62 \pm 0.03$	1	—	—	—	328.8997 -52.4194	1
SPT-CLJ2155-6048	328.9850	-60.8072	5.24	0.539	$0.48 \pm 0.02$	1	—	—	—	328.9811 -60.8174	1
SPT-CLJ2158-4702	329.6901	-47.0348	4.56	—	$> 0.9$	—	—	—	64.4	—	1
SPT-CLJ2158-4851	329.5737	-48.8536	4.61	—	$> 0.8$	—	36.3	—	58.5	—	1
SPT-CLJ2158-5615	329.5975	-56.2588	4.54	—	$> 1.1$	—	—	—	53.6	—	1
SPT-CLJ2158-6319	329.6390	-63.3175	4.54	—	$> 1.1$	—	—	—	99.7	—	1
SPT-CLJ2159-6244	329.9922	-62.7420	6.08	—	$0.43 \pm 0.02$	1	—	—	—	329.9944 -62.7539	2
SPT-CLJ2200-5547	330.0304	-55.7954	4.80	—	$> 1.0$	—	23.5	—	19.7	—	1
SPT-CLJ2201-5956	330.4727	-59.9473	13.99	0.097	$0.07 \pm 0.02$	1	—	—	—	330.4723 -59.9454	2
SPT-CLJ2202-5936	330.5483	-59.6021	4.89	—	$0.42 \pm 0.03$	1	—	—	—	330.5522 -59.6037	1
SPT-CLJ2259-5432	344.9820	-54.5356	4.78	—	$0.46 \pm 0.03$	1	—	—	—	344.9765 -54.5260	3
SPT-CLJ2259-5617	344.9974	-56.2877	5.29	—	$0.15 \pm 0.02$	1	—	—	—	345.0044 -56.2848	1,2
SPT-CLJ2300-5331	345.1765	-53.5170	5.29	0.262	$0.26 \pm 0.02$	1	—	—	—	345.1655 -53.5199	2
SPT-CLJ2301-5046	345.4585	-50.7823	4.58	—	$> 1.5$	—	—	64.3	83.7	—	1
SPT-CLJ2301-5546	345.4688	-55.7758	5.19	0.748	$0.74 \pm 0.03$	1	—	0.2	0.0	345.4595 -55.7842	1

Table 3.3 – continued from previous page

SPT ID	RA (deg)	Position Dec (deg)	$\xi$	$z_{\text{spec}}^a$	$z_{\text{comb}} \pm \sigma_{z_{\text{comb}}}$ (or redshift lower limit)	Flag <sup>b</sup>	NIR blank field NEWFIRM	probability <i>Spitzer</i>	$P_{\text{blank}}(\%)^c$ <i>WISE</i>	rBCG Position RA (deg) Dec (deg)	Imaging Ref. <sup>d</sup>
SPT-CLJ2302-5225 <sup>9</sup>	345.6464	-52.4329	4.60	—	$> 1.0$	—	—	—	83.3	—	1
SPT-CLJ2311-5011	347.8427	-50.1838	4.64	—	$> 1.5$	—	38.4	—	69.7	—	1
SPT-CLJ2312-5820	348.0002	-58.3419	4.78	—	$0.83 \pm 0.05$	1	—	1.3	0.0	347.9912 -58.3428	1
SPT-CLJ2329-5831	352.4760	-58.5238	4.95	—	$0.81 \pm 0.03$	1	2.3	0.0	0.1	352.4627 -58.5128	1
SPT-CLJ2331-5051	352.9584	-50.8641	8.04	0.576	$0.61 \pm 0.02$	1	—	—	—	352.9631 -50.8650	2
SPT-CLJ2332-5358	353.1040	-53.9733	7.30	0.402	$0.38 \pm 0.02$	1	—	—	—	353.1144 -53.9744	1,2
SPT-CLJ2334-5953	353.6989	-59.8892	4.53	—	$> 1.5$	—	71.7	—	26.1	—	1
SPT-CLJ2337-5942	354.3544	-59.7052	14.94	0.775	$0.76 \pm 0.03$	1	—	0.3	0.0	354.3651 -59.7013	2
SPT-CLJ2341-5119	355.2994	-51.3328	9.65	1.003	$0.93 \pm 0.07$	3	—	0.2	0.9	355.3015 -51.3290	1,2
SPT-CLJ2342-5411	355.6903	-54.1887	6.18	1.075	$0.96 \pm 0.07$	3	7.4	2.4	9.6	355.6913 -54.1848	1*
SPT-CLJ2343-5521	355.7574	-55.3641	5.74	—	$> 1.5$	—	—	66.3	50.8	—	1,2
SPT-CLJ2343-5556	355.9290	-55.9371	4.58	—	$> 1.2$	—	20.5	—	5.6	—	1*
SPT-CLJ2351-5452	357.8877	-54.8753	4.89	0.384	$0.37 \pm 0.02$	1	—	—	—	357.9086 -54.8816	1*
SPT-CLJ2355-5056	358.9551	-50.9367	5.89	0.320	$0.28 \pm 0.02$	1	—	—	—	358.9477 -50.9280	2
SPT-CLJ2359-5009	359.9208	-50.1600	6.35	0.775	$0.78 \pm 0.03$	1	—	0.0	0.3	359.9284 -50.1672	2

<sup>a</sup> Spectroscopic redshift listed where available. Details on references and observations are given in Table 3.2.

<sup>b</sup> Photometric redshift quality flag. 1-secure, 2-statistically inconsistent between three methods, 3-Swope or *Spitzer* IRAC colors only used, and 4-only one method used (except Swope and *Spitzer*-only case).

<sup>c</sup> Probability of finding a random position in the sky richer than the SPT cluster candidate, using single-band NIR galaxy overdensity. Only calculated for unconfirmed candidates and confirmed clusters at  $z > 0.7$ .

<sup>d</sup> Cross-reference to imaging data. Only the deepest imaging data source is noted in this table. Internal references refer to Table 3.1. Ref. 1\* indicates that BCS imaging data was used.

1 optical group on N  $z \sim 0.3$ .

2 optical only  $z \sim 1.0$ .

3 very complex region, optical group on NW  $z \sim 0.4$ , another group on SW  $z \sim 0.65$ .

4 optical group within  $1'$  aperture  $z \sim 0.35$ .

5 strong lensing arc.

6 strong lensing arc.

7 optical group on SW  $z \sim 0.4$ .

8 optical group within  $1'$  aperture  $z \sim 0.15$ .

9 optical group on SE  $z \sim 0.4$ .

# A Multiband Study of the Galaxy Populations of the First Four Sunyaev–Zeldovich Effect selected Galaxy Clusters

## 4.1 Abstract

We present first results of an examination of the optical properties of the galaxy populations in SZE selected galaxy clusters. Using clusters selected by the South Pole Telescope survey and deep multiband optical data from the Blanco Cosmology Survey, we measure the radial profile, the luminosity function, the blue fraction and the halo occupation number of the galaxy populations of these four clusters with redshifts ranging from 0.3 to 1. Our goal is to understand whether there are differences among the galaxy populations of these SZE selected clusters and previously studied clusters selected in the optical and the X-ray. The radial distributions of galaxies in the four systems are consistent with NFW profiles with a galaxy concentration of 3 to 6. We show that the characteristic luminosities in *griz* bands are consistent with passively evolving populations emerging from a single burst at redshift  $z = 3$ . The faint end power law slope of the luminosity function is found to be on average  $\alpha \approx -1.2$  in *griz*. Halo occupation numbers (to  $m^* + 2$ ) for these systems appear to be consistent with those based on X-ray selected clusters. The blue fraction estimated to  $0.36L^*$ , for the three lower redshift systems, suggests an increase with redshift, although with the current sample the uncertainties are still large. Overall, this pilot study of the first four clusters provides no evidence that the galaxy populations in these systems differ significantly from those in previously studied cluster populations selected in the X-ray or the optical.

GALAXIES: CLUSTERS: GENERAL — GALAXIES: EVOLUTION — GALAXIES: FORMATION — COSMOLOGY: OBSERVATIONS

## 4.2 Introduction

Galaxy clusters can be readily discovered or selected using optical or IR emission from their member galaxies, X-ray emission from the hot intracluster medium and now even by the impact of this intracluster medium on the cosmic microwave background temperature toward these systems. First, from optical observations, Abell (1958) identified, catalogued and characterized clusters of galaxies using classification criteria like *compactness*, *distance*, and *richness*. Later, new optical surveys added other optical properties to the clusters. Luminosity function, radial profile, blue fraction, dwarf-to-giant ratio, among others, became tools for understanding different physical processes in the galaxy cluster environment.

With the advent of space based astronomy new properties of clusters of galaxies were discovered. Strong X-ray emission made the galaxy clusters some of the most luminous objects in the Universe, and their properties like X-ray luminosity, temperature, and mass have been compiled in several X-ray selected cluster surveys (see, Giacconi et al., 1972; Voges et al., 1999, 2000; Böhringer et al., 2004, for example).

In the infra-red regime, the properties of clusters have been studied mainly relying on the X-ray or optical cluster identification (see, de Propris et al., 1999; Lin et al., 2003, 2004; Toft et al., 2004; De Propris et al., 2007; Muzzin et al., 2007a,b; Roncarelli et al., 2010, among others). From IR selected clusters, some of the first studies analyzed the cluster populations based on individual clusters (Stanford et al., 1997, 2005). Later, systematic searches of clusters in the infrared became feasible with the operation of space telescopes and with ground based telescopes with advanced IR detectors. Surveys such as FLAMEX (Elston et al., 2006), UKIDSS (van Breukelen et al., 2006), FLS (Muzzin et al., 2008) and the IRAC Shallow Survey (Eisenhardt et al., 2008) have delivered cluster catalogs, at high redshift, allowing initial systematic characterization of the galaxy populations on those systems.

In the millimeter regime, the use of the Sunyaev-Zel'dovich Effect (SZE, Sunyaev & Zel'dovich, 1972) as a selection method for cluster of galaxies has recently produced the first results (Staniszewski et al., 2009; Vanderlinde et al., 2010). The use of the SZE effect for cluster detection has several advantages. A catalog of SZE selected clusters is approximately mass limited, nearly redshift independent and the observable signature is closely related to the cluster mass (Birkinshaw, 1999; Carlstrom et al., 2002), making it less prone to be biased in the selection. In particular, an SZE selected cluster sample provides an opportunity to systematically study the galaxy populations and its redshift evolution in clusters of the same mass range over a wide range of redshift.

In this paper we use tools developed for optical studies to analyze the galaxy populations of the first four SZE selected clusters published by the South Pole Telescope (SPT) collaboration (Staniszewski et al., 2009). As well as being among the first SZ selected systems, these clusters are among the most well studied. This sample has been imaged deeply in the optical Blanco Cosmology Survey, studied in the X-ray (Andersson et al., 2011), targeted spectroscopically for redshifts (High et al., 2010), and the BCS data have been used to estimate weak lensing masses (McInnes et al., 2009). Also these four systems span a broad range in redshift and mass, much like the larger samples that have been published so far (Vanderlinde et al., 2010; Williamson et al., 2011). In this pilot study, we study the luminosity function, the radial profile, the Halo Occupation number and the blue fraction, in an effort to answer a basic question: Are the galaxy populations from these first SZE selected clusters any different than the populations in clusters selected by other means?

The paper is organized as follows: §2 describes the observations and data reduction. In section

§3, properties of the clusters, such as redshift and mass, are described. In §4 we study the galaxy populations in the clusters, presenting the main results. Conclusion of this study are presented at section §5. Magnitudes are quoted in AB system.

We assume a flat,  $\Lambda$ CDM cosmology with  $H_0 = 100h \text{ km s}^{-1} \text{ Mpc}^{-1}$ ,  $h = 0.702$ , and matter density  $\Omega_m = 0.272$ , according to WMAP7 + BAO +  $H_0$  data (Komatsu et al., 2011).

## 4.3 Observations and Data Reduction

### 4.3.1 Blanco Cosmology Survey

The Blanco Cosmology Survey<sup>1</sup> (BCS) project was awarded 60 nights from the NOAO (National Optical Astronomy Observatory) survey program starting in semester 2005B. Data were gathered in 2005–2008 using the Blanco 4-meter telescope located at Cerro Tololo Inter-American Observatory<sup>2</sup> in Chile. The telescope is equipped with a wide field camera called the Mosaic2 imager, which consists of an array of eight  $2K \times 4K$  CCDs. The pixel scale of Mosaic2 imager is 0.27 arc-second per pixel, leading to a field of view of about 0.36 square degree. The observations were carried out to obtain a deep, four band photometric survey ( $g$ ,  $r$ ,  $i$  and  $z$ ) of two  $50 \text{ deg}^2$  patches of the southern sky centered at  $23^{\text{h}}00^{\text{m}}, -55^{\circ}12''$  and  $05^{\text{h}}30^{\text{m}}, -55^{\circ}47''$ . These regions were chosen to enable observations by three mm-wavelength survey experiments (the SPT, the Atacama Pathfinder Experiment (APEX) and the Atacama Cosmology Telescope (ACT) experiments). On photometric nights we also observed several standard star fields that contain stars with known magnitudes. This approach allows the calibration of our data to the standard magnitude system. In addition, we obtained deep imaging of several fields overlapping published spectroscopic surveys to enable calibration of photo- $z$ 's using samples of many thousands of spectroscopic redshifts. The data volume we collected for the BCS observation was about 20 to 30 Gigabytes/night.

The first three seasons (2005 to 2007) of the BCS imaging data were processed in 2008 and 2009 using version 3 of the data management system developed for the upcoming Dark Energy Survey (DES). Details of the DES data management system can be found in Ngeow et al. (2006) and Mohr et al. (2008). A brief description is presented in this paper. Data parallel processing was carried out primarily on NCSA's TeraGrid IA-64 Linux cluster. The pipeline processing middleware developed within the DES data management system provides the infrastructure for the automated and robust execution of our parallel pipeline processing on the TeraGrid cluster.

To remove the instrumental signatures, the raw BCS images were processed using the following corrections: crosstalk correction, overscan correction, bias subtraction, flat fielding, fringe and illumination correction. Bad columns and pixels, saturated pixels and bright star halos, and bleed trails are masked automatically. Wide field imagers have field distortions that generally deviate significantly from a simple tangent plane, and there are typically telescope pointing errors as well. The AstrOmatic code SCAMP (Bertin, 2006) was used to refine the astrometric solution by matching the detected stars in BCS images to the USNO-B catalog. We adopted the  $PV$  distortion model that maps detector coordinates to sky coordinate using a third order polynomial expansion of distortions, across each CCD, relative to a tangent plane. The DES

<sup>1</sup><http://cosmology.illinois.edu/BCS/>

<sup>2</sup>Cerro Tololo Inter-American Observatory (CTIO) is a division of the U.S. National Optical Astronomy Observatory (NOAO), which is operated by the Association of Universities for Research in Astronomy (AURA), under contract with the National Science Foundation.

data management system is using an experimental version of the AstrOmatic tool **SExtractor** (Bertin & Arnouts, 1996). This experimental version includes model fitting photometry and improved modes of star-galaxy classification to detect and catalog astronomical objects in the images. We harvested a wide range of photometric and astrometric measurements (and their uncertainties) for each object during this cataloging.

For the photometric nights that include observation of the standard star fields, we determined the band dependent (atmospheric) extinction coefficients ( $k$ ) together with CCD and band dependent photometric zeropoints ( $a$ ) and instrumental color terms ( $b$ ). Specifically, the equation we constructed for each star in the standard star fields is  $m_{inst} - m_{std} = \sum_i w_i \times [a_i + b_i(\Delta C)] + kX$ , where  $w_i = 1$  if the standard star is on CCD  $i$ ;  $w_i = 0$  otherwise. In this equation,  $m_{inst}$  and  $m_{std}$  are the instrumental and the true magnitudes for the standard stars, respectively,  $\Delta C$  is the color offset of the standard stars from a reference color, and  $X$  is the airmass. The standard star fields include the SDSS Stripe 82 fields and the Southern Standard Stars Network fields<sup>3</sup>. The resulting photometric solutions were then used to calibrate the magnitudes for other astronomical objects observed on the same night.

The nightly reduced and astrometric refined images were remapped and coadded to a pre-defined grid of tiles (which is a rectangular tangent plane projection, with  $\sim 36$  arc-minute on a side (hereafter the BCS tiles) in the sky using another AstrOmatic tool, **SWarp** (Bertin et al., 2002). During this coaddition we carry out a PSF homogenization across each tile and within each band to match the PSF to median delivered seeing in that part of the sky. The zeropoints for the flux scales for these input remap images are determined using different sources of photometric information, including direct photometric zeropoints which are derived from the photometric solution on photometric nights, relative photometric zeropoints determined using all pairs of images that overlap on the sky and the color behavior of the stellar locus (High et al., 2009). We determine the zeropoints for all images by doing a least squares solution using the constraints described above. During co-addition, we use a weighted mean combine option in **SWARP**. The coadded images are built in each band for a given coadd tile, then a  $\chi^2$  image (Szalay et al., 1999) is created for detection and cataloging to ensure each object will have measurements in the *griz* bands extracted from the same portion of the object.

### 4.3.2 Completeness

For this work we estimate the completeness of the BCS tiles from the comparison of their *griz* source count histograms and those extracted from the deeper Canada-France-Hawaii-Telescope Legacy Survey survey (CFHTLS, Brimiouille et al., 2008, private communication). Specifically, we used count histograms from the D-1 1 sq. degree patch at high galactic latitude ( $l = 172.0^\circ$ ;  $b = -58.0^\circ$ ) from the CFHTLS Deep Field, whose magnitude limit is beyond  $r=27$  and the seeing is better than  $1.0''$  and  $0.9''$  for *g* and *riz*, respectively<sup>4</sup>. Dividing both count histograms (see Fig. 4.1) we can estimate the level of completeness in the different tiles in each band. We can use this completeness estimate for each field to account for the missing objects as we approach the full depth of the photometry. Table 4.1 contains the magnitude limits in each band corresponding to 50% and 90% completeness for the tiles used in our analysis.

<sup>3</sup>[http://www-star.fnal.gov/Southern\\_ugriz/index.html](http://www-star.fnal.gov/Southern_ugriz/index.html)

<sup>4</sup>Details can be found at <http://www.ast.obs-mip.fr/article212.html>

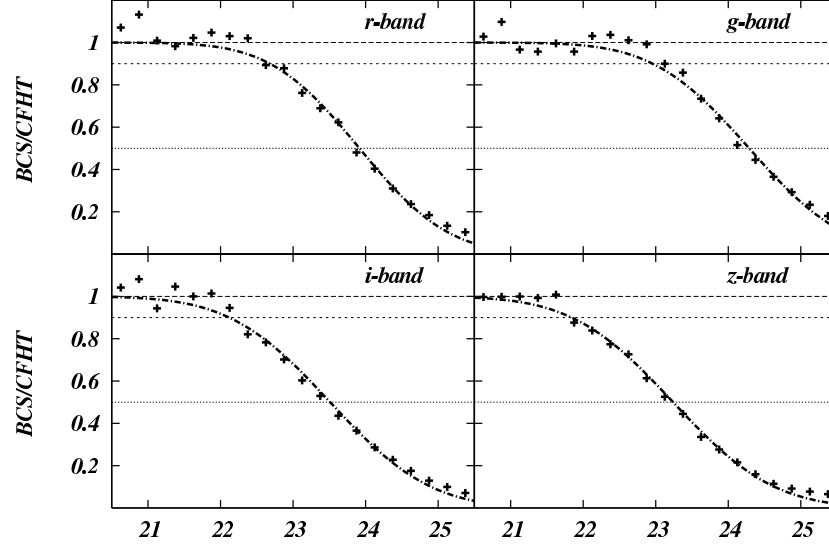


**Figure 4.1:** We estimate the completeness of our BCS coadds by comparing objects counts from them with counts from deeper CFHT data. The resulting completeness curve is fitted by an error function, which later is used to correct for the missing galaxies and to define 90% and 50% completeness limits for analysis. Here is an example for the SPT-CL J0516-5430 field.

**Table 4.1:** Completeness limits for each tile for each filter for 90%/50% completeness

ID	R.A.	decl.	g	r	i	z
	[deg]	[deg]	500 sec	600 sec	1350 sec	705 sec
SPT-CL J0516-5430	79.15569	-54.50062	23.18/24.24	22.73/23.87	22.20/23.47	21.87/23.19
SPT-CL J0509-5342	77.33908	-53.70351	23.72/24.78	23.29/24.51	23.10/24.23	22.45/23.78
SPT-CL J0528-5300	82.02212	-52.99818	23.70/24.62	23.42/24.32	22.93/23.94	22.23/23.37
SPT-CL J0546-5345	86.65700	-53.75861	23.34/24.31	22.87/23.90	22.48/23.64	21.97/23.08

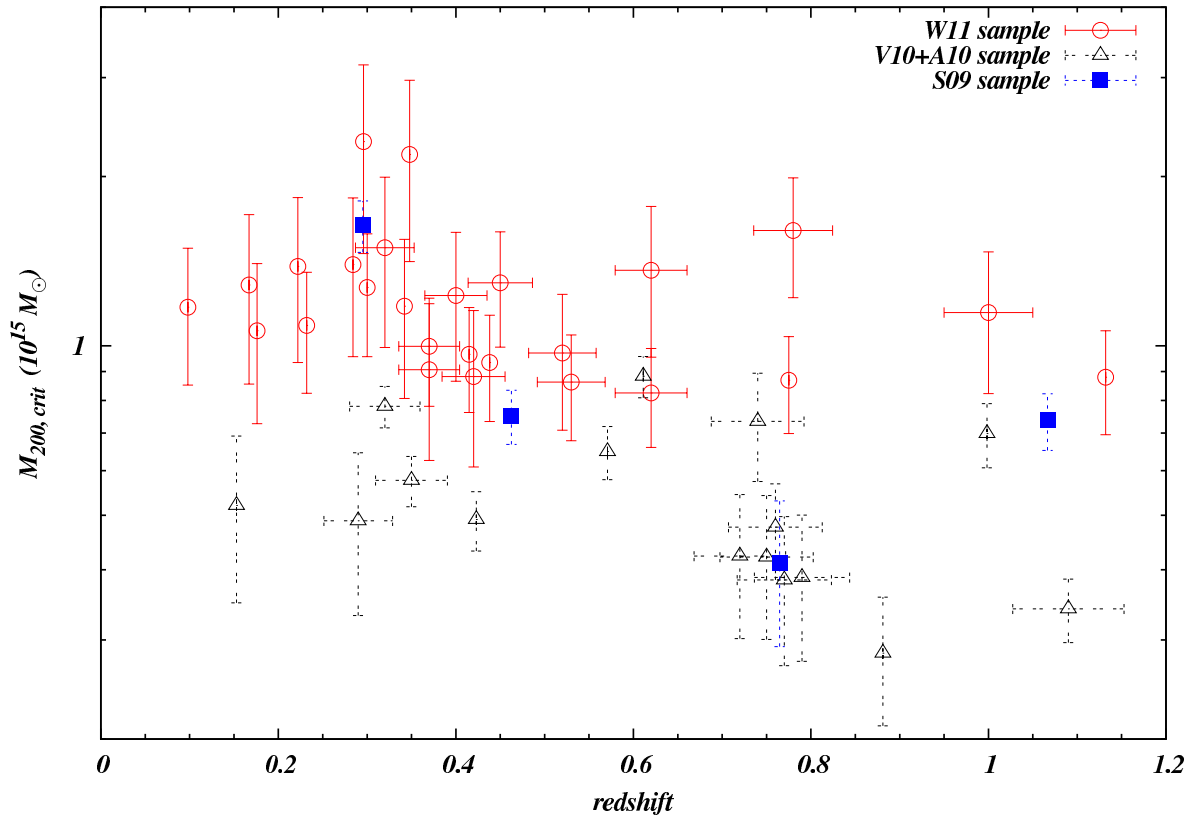


**Figure 4.2:** Masses and redshifts of the SPT cluster sample published to date. Open circles are from Williamson et al. (2011), open triangles are from Andersson et al. (2011) and Vanderlinde et al. (2010), and filled squares from Staniszewski et al. (2009), the sample here studied. The  $M_{200, crit}$  mass estimations come from X-ray observations where that is possible, or from the SPT detection significance. In the latter case, masses have been converted from their native estimation  $M_{200, mean}$  to  $M_{200, crit}$  assuming a concentration parameter of  $c = 5$  for the halo mass (see Table 4.2) under assumed cosmology. It can be seen that our sample spans on the redshift and mass space for the latest SPT sample.

#### 4.4 Basic Properties of these SPT Clusters

The basic properties of these SPT selected clusters, including the characteristics of the optical counterparts are presented in Staniszewski et al. (2009) and are further discussed in follow on papers (Menanteau et al., 2009; McInnes et al., 2009; High et al., 2010; Andersson et al., 2011). Several spectroscopic redshifts are now available as well as Chandra X-ray observations, providing dramatically improved mass information which enables the kind of galaxy population study we undertake here. Despite being a small sample, these four clusters are among the most well studied SZ selected systems and their mass and redshift distributions range are similar to the whole SPT published cluster sample (see Fig. 4.2). In particular, these masses and redshifts are used to estimate the projected cluster virial radius in which the optical properties are measured. These properties are presented below.



#### 4.4.1 Redshifts

The spectroscopic redshifts of the four cluster are now available (Table 4.2). SPT-CL J0516-5430, a known cluster identified in the Abell supplementary southern catalog (AS0520, Abell et al., 1989) and in the REFLEX survey (RXC J0516.65430, Böhringer et al., 2004), had a redshift of 0.294 (Guzzo et al., 1999) and 0.2952 (Böhringer et al., 2004), values obtained using 8 galaxy spectra from the ESO Key Programme.

For the other three clusters, spectroscopic data has recently been acquired. Using LDSS-3 on Magellan Clay telescope, High et al. (2010) reported redshifts of 0.7648 for SPT-CL 0528-5300 and 0.4626 for SPT-CL 0509-5342. For SPT-CL J0546-5345, Brodwin et al. (2010) used IMACS on Baade Magellan telescope to measure a redshift of 1.0665.

**Table 4.2:** X-ray masses, spectroscopic redshifts and cluster parameters.

ID	$M_{200,Y_X}^a$ [ $10^{14}M_\odot$ ]	$z$	$r_{200,Y_X}^b$ [Mpc]	$r_{200,Y_X}$ [arcmin]	$\xi^c$ S/N	$c_{red\ gal}^d$	$c_{all\ gal}^e$
SPT-CL J0516-5430	$16.38 \pm 1.72$	$0.2952^f$	2.21	8.34	9.42	$4.65^{+0.81}_{-0.73}$	$2.79^{+0.63}_{-0.52}$
SPT-CL J0509-5342	$7.51 \pm 0.83$	$0.4626^g$	1.61	4.54	6.61	$3.18^{+3.50}_{-1.39}$	$1.94^{+7.44}_{-1.36}$
SPT-CL J0528-5300	$4.11 \pm 1.19$	$0.7648^g$	1.17	2.61	5.45	$5.93^{+5.78}_{-2.58}$	$3.23^{+1.37}_{-0.55}$
SPT-CL J0546-5345	$7.37 \pm 0.85$	$1.0665^h$	1.27	2.57	7.69	$4.02^{+1.98}_{-1.37}$	$4.04^{+1.92}_{-1.31}$

<sup>a</sup>  $1.38 \times M_{500}$  from Andersson et al. (2011), assuming a concentration parameter of  $c = 5$  for the mass halo.

<sup>b</sup>  $1.51 \times r_{500,Y_X}$  from Andersson et al. (2011), assuming a concentration parameter of  $c = 5$  for the mass halo.

<sup>c</sup> The S/N measured in 150 GHz SPT maps from from Vanderlinde et al. (2010).

<sup>d</sup> Concentration parameter from the NFW fitting of the red galaxies.

<sup>e</sup> Concentration parameter from the NFW fitting of the all galaxies.

<sup>f</sup> Spectroscopic redshift from Böhringer et al. (2004).

<sup>g</sup> Spectroscopic redshift from High et al. (2010).

<sup>h</sup> Spectroscopic redshift from Brodwin et al. (2010).

#### 4.4.2 Cluster masses

As mentioned in §4.4, the optical analyses performed in this work require an estimate of the projected cluster virial radius. For this purpose, along with spectroscopic redshifts, X-ray masses estimations are used. We adopt mass estimates defined with respect to the critical density.

As it has been previously mentioned, SPT-CL 0516-5430 is a previously known cluster, and its mass has also been estimated. With the name of RXC J0516.6-5430 in the REFLEX survey, Zhang et al. (2006) used XMM-Newton to find a  $M_{500}$  of  $(6.4 \pm 2.1) 10^{14} M_\odot$ . Also, recent X-ray observations of the four clusters have been performed, and the mass estimation of SPT-CL 0517-5430 has been refined.

Using *Chandra* and *XMM-Newton*, Andersson et al. (2011) reported X-ray measurements of 15 of the 21 SZE selected clusters presented in Vanderlinde et al. (2010). The observations of those clusters, which include the original first four clusters, have been designed to deliver around 1500 photons within  $0.5r_{500}$ , in order to enable measurement of the ICM mass and ICM temperature, allowing a mass estimation through a  $M_{500} - Y_X$  scaling relation (Vikhlinin et al., 2009) with approximately 15% accuracy.

From X-ray  $M_{500,Y_X}$  and spectroscopic redshifts Andersson et al. (2011) estimated the physical  $r_{500,Y_X}$ , both defined with respect to the critical density. Here, those  $r_{500,Y_X}/M_{500,Y_X}$  are transformed to  $r_{200,Y_X}/M_{200,Y_X}$  using the Navarro, Frenk, & White (Navarro et al., 1997, hereafter 'NFW' profile) radial mass profile with concentration of 5 for the dark matter halo, which implies  $r_{200,Y_X} = 1.51 \times r_{500,Y_X} / M_{200,Y_X} = 1.38 \times M_{500,Y_X}$  conversion. The angular projection is calculated using the spectroscopic redshifts.  $M_{200,Y_X}$  as well as  $r_{200,Y_X}$  are listed in Table 4.2.

## 4.5 Cluster Galaxy Populations

The galaxy populations in clusters have been studied using several techniques and selection processes. Clusters of galaxies have been selected mainly from optical images (Abell, 1958; Abell et al., 1989; Koester et al., 2007, for example) and through their X-ray emission (Ebeling et al., 1996; Vikhlinin et al., 1998; Böhringer et al., 2004, among others). A selection of clusters based on their Sunyaev-Zeldovich signature promises a less biased selection method, as it is likely to be less affected by projections or false clusters like optical surveys (Lucey, 1983; Sutherland, 1988; Collins et al., 1995; Cohn et al., 2007), and its mass selection function is nearly redshift independent, making the cluster sample more homogeneous than X-ray surveys in redshift space. Also, the SPT survey will be able to find the most massive clusters of galaxies in the Universe (Carlstrom et al., 2002, 2011). Once completed, the size, redshift extent and the degree of completeness of the SZE selected cluster sample will be ideal for statistical analysis of astrophysical properties in high mass clusters. Here we focus on the first four SPT selected clusters, which are all high mass systems extending over a broad redshift range.

### 4.5.1 Radial distribution of galaxies

The radial distribution of galaxies in clusters can be used to further our understanding of the cluster environment physics. For example, from N-body and gas dynamical simulations, which include radiative cooling, star formation, SN feedback, UV heating, etc., Nagai & Kravtsov (2005) produced radial distributions consistent with observations of X-ray selected cluster samples from Carlberg et al. (1997) and Lin et al. (2004). Saro et al. (2006), using hydrodynamical simulations, also showed an agreement between the radial distribution of the simulated galaxies and X-ray and optically selected clusters from Popesso et al. (2007a).

For the following analysis we define the cluster center to be the position of the observed brightest cluster galaxy member (BCG; coordinates are listed in Table 4.1), which agree with its X-ray center (Andersson et al., 2011). In order to compare different studies we estimate the concentration parameter from the NFW surface density profile. We obtain the NFW surface density by integrating the three-dimensional number density profile  $n(x) = n_0 x^{-1} (1 + x)^{-2}$  along the line-of-sight (see Bartelmann, 1996) where  $x = c_g r / r_{200}$ ,  $n_0$  is the normalization and  $c_g$  is the concentration parameter. On stacked cluster data it is customary to fit both parameters,  $n_0$  and  $c_g$ . In our case the NFW fit is done over single cluster data to a common magnitude limit, and this leads to considerable uncertainties in the parameters of the NFW profile. In order to minimize this problem, we introduce the *observed* number of galaxies in the equation. Integrating the NFW surface density over the projected area we can derive  $n_0 = n_0(n_{obs}, c_g)$  allowing us to fit the NFW density profile as a single parameter function. Also, after a statistical background correction, a background fitting is performed along with the NFW fit. Such background fit is limited within the Poisson uncertainty of the observed background.

The radial surface density profiles are constructed using both the red+blue and the red galaxy population defined from the color-magnitude diagram of the red sequence (see sec. 4.5.4). The galaxy population is also selected performing a cut in brightness, selecting galaxies which are fainter than the BCG and brighter than a common limit of  $0.36L^*$ . The error bars are computed using small number statistics (Gehrels, 1986). The background is statistically subtracted and a second correction is applied fitting it to a radius of  $3r_{200}$ . Finally the data

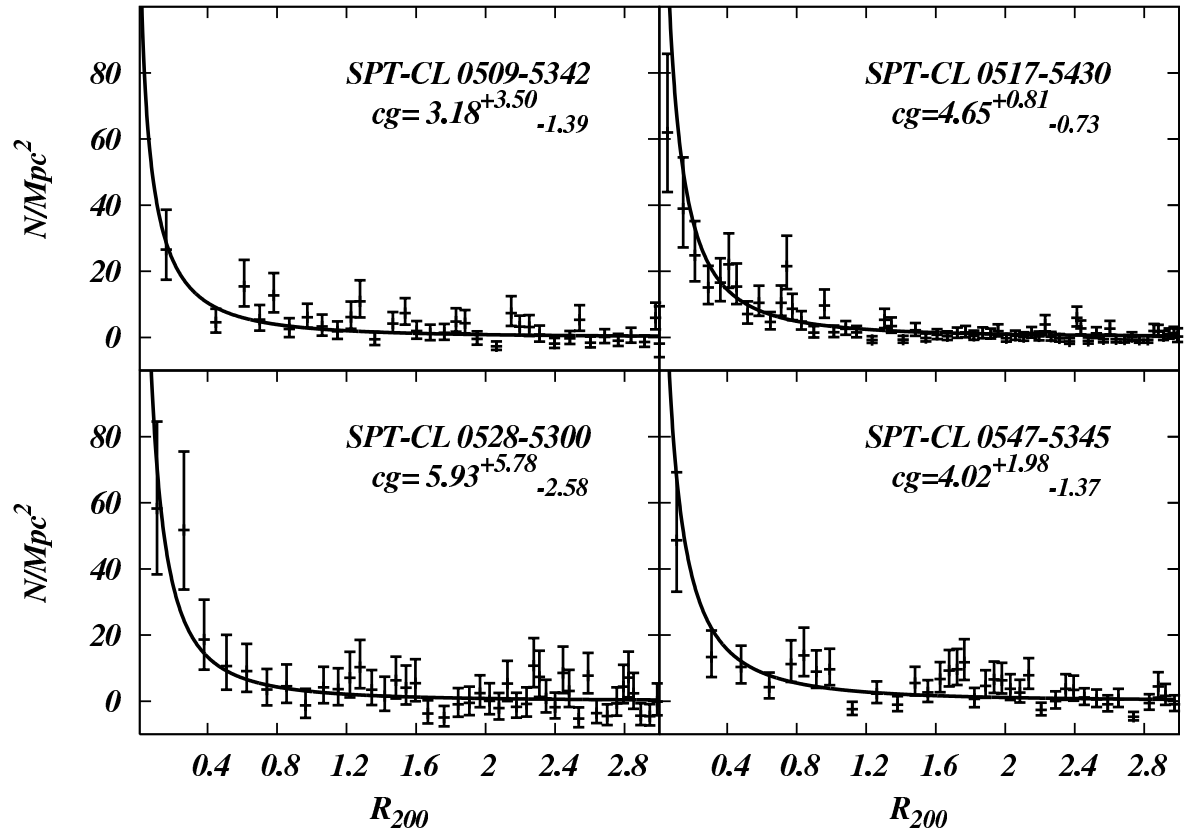


**Figure 4.3:** Radial profiles for the red galaxy population to  $0.36L^*$  (same as blue fraction), binned to obtain similar signal to noise. These profiles are centered on the BCG and extend to  $3r_{200}$  to allow the background and the cluster profile to be fit simultaneously. All radial profiles are consistent with NFW profiles with concentrations  $c \sim 4$ .

is presented using radial bins of constant signal-to-noise of 3.5 (see Fig. 4.3).

Some corrections are applied to these profiles. In the area calculation for each radial bin in Fig. 4.3, the area covered by saturated stars was excluded in order to avoid an under estimation of the surface density. This is especially important in the case of SPT-CL J0509-5342 where several bright stars close to the BCG are blocking the detection of galaxy cluster members, covering about 50% of the area at a radius of  $0.4r_{200}$ .

The concentration parameters found are shown in Table 4.2. With a concentration in the range of  $c \approx 3 - 6$ , the clusters agree at  $1\sigma$  confidence. We note that the blue+red distribution tends to be less concentrated than the red population alone, which is consistent with previous analyses where a higher concentration is seen in the red population (e.g. Goto et al., 2004). The concentration we find is in agreement with concentrations drawn from X-ray selected clusters of galaxies. For example, Carlberg et al. (1997) found a  $c_g$  of  $3.70^{+3.99}_{-1.38}$  at 95% confidence, using 16 clusters from the CNOC survey with a median redshift of  $\sim 0.3$  for a similar mass range ( $2 \times M_{\odot}^{14}$ - $6.6 \times M_{\odot}^{15}$ ; Carlberg et al. (1996)). Lin et al. (2004), from stacked 2MASS K-band data on 93 nearby X-ray selected clusters, found a value of  $c_g = 2.90^{+0.21}_{-0.22}$  in a wider  $3 \times M_{\odot}^{13}$ - $2 \times M_{\odot}^{15}$  range. Both are consistent with our results.

We also found agreement between our concentration parameter and the concentration parameter found for optical selected clusters. Biviano & Poggianti (2009) found, studying 19 intermediate redshift ( $0.4 \lesssim z \lesssim 0.8$ ;  $0.7 \lesssim M_{200} \lesssim 13.6 \times 10^{14} M_{\odot}$ ) EDisCS+MORPHS clusters, a concentration parameter of  $c = 3.2^{+4.6}_{-2.0}$ . Also, Johnston et al. (2007) found, using the SDSS sample, a concentration parameter of  $c_{200|14} = 4.1 \pm 0.2_{stat} \pm 1.2_{sys}$  for a cluster mass of  $M = 10^{14} h^{-1} M_{\odot}$ . In summary, we find no evidence that SZE selected clusters exhibit different galaxy radial distributions than in optical and X-ray selected clusters.

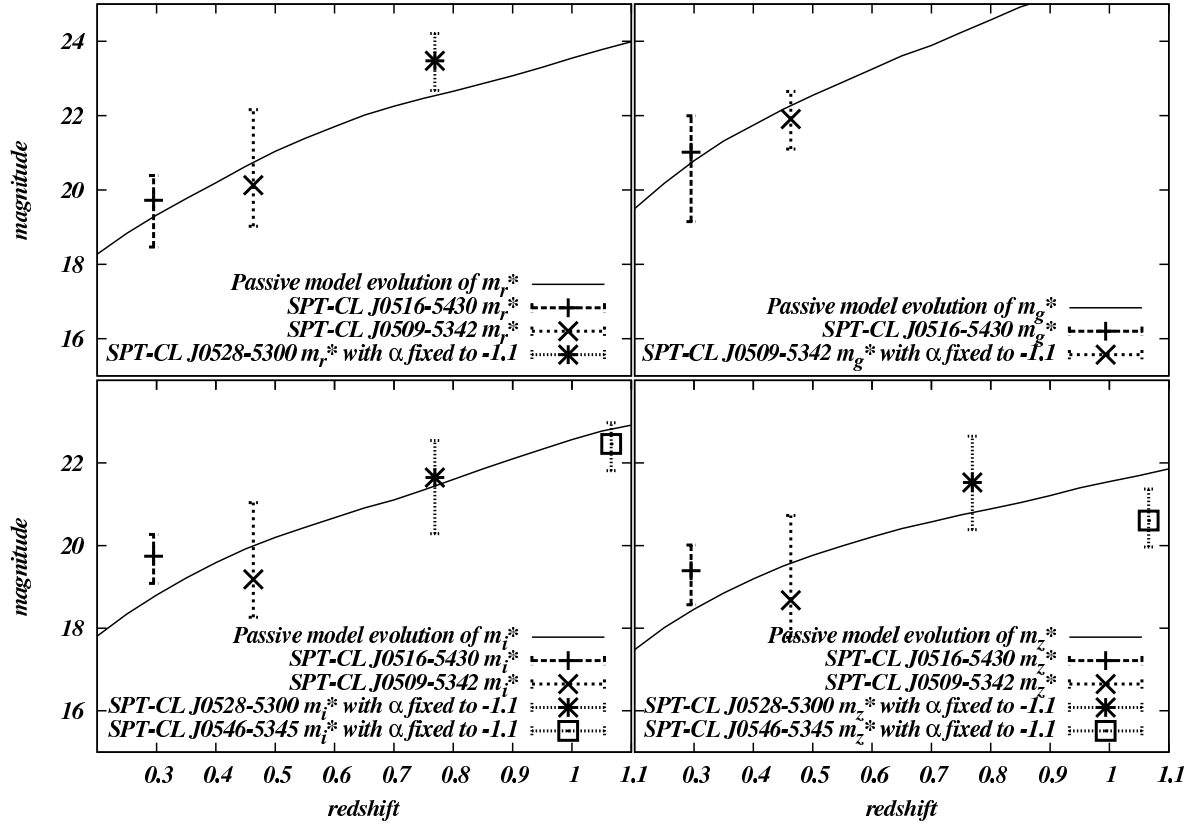


**Figure 4.4:** Here we plot the  $m^*$  (with  $1\sigma$  uncertainties) for each band that results from Schechter function fits to the luminosity function with free parameters  $m^*$ ,  $\phi^*$  and  $\alpha$  ( $\alpha$  fixed where noted). We limit the range of  $m^*$  to be fainter than the identified BCG for each cluster. The continuous line represents a passive evolution single burst model at  $z = 3$  from Bruzual & Charlot (2003). It is clear that these SPT selected clusters have galaxy populations consistent with this simple evolution model.

### 4.5.2 Luminosity functions

The luminosity function (LF) is an important tool for testing theories of galaxy formation and evolution. For example, ever more complex simulations can be tested against the LF, as an observational constraint, to probe our understanding of the evolution of galaxies in the cluster's environment (Romeo et al., 2005; Saro et al., 2006). With clusters of similar masses we can study the LF as a function of redshift and with the LF parameters we can calculate the Halo Occupation Number (HON) and test the  $N$ - $M$  scaling relation (Lin et al., 2004, 2006).

The LF can be described by the three parameter Schechter function (Schechter, 1976),

$$\phi(m) = 0.4 \ln(10) \Phi^* 10^{0.4(m^* - m)(\alpha + 1)} \exp(-10^{0.4(m^* - m)})$$

where  $\Phi^*$  is the normalization,  $m^*$  is the characteristic magnitude and  $\alpha$  accounts for the faint end power law behavior of the function.

The construction of the LF is done assuming that the *observed* LF in the cluster area is the superposition of the cluster LF and the background/foreground non-cluster LF. To recover the cluster LF we subtract the galaxy source count, rescaled by the area, from the observed LF. Given the wide range in redshift we present the LF in the four *griz* bands.

The area of the cluster is defined by our estimation of  $r_{200}$  (see §4.4.2 and Table 4.2), and the area of the background is the tile area ( $36' \times 36'$ ) minus the cluster area. The bright end limit of the LF is defined by the cluster's BCG while the faint end limit is defined by its completeness at 90% or 50%, depending on the redshift, in each band. Below the 100% completeness, the 0.5 mag bins are corrected using the error function fitted to the BCS/CFHT comparison galaxy count histograms described in §5.3.4 and shown in Fig. 4.1. Finally, the number of galaxies, background corrected, is divided by cluster volume (in  $\text{Mpc}^3$ ) and the uncertainty is assumed Poissonian in the total number of galaxies (cluster plus background). Below we extract  $m^*$  and  $\alpha$  from our cluster sample and compare them to previous results drawn from X-ray and optical selected clusters of galaxies.

#### Evolution of $m^*$

Studies of  $m^*$  evolution in clusters have been done in different wavelengths and with different selection methods. These studies indicate that the stellar populations in many of the cluster galaxies have evolved passively after forming at high redshift (see, e.g., Gladders et al., 1998; De Lucia et al., 2004; Holden et al., 2004; Muzzin et al., 2008, and references therein). There are several indications that  $m^*$  evolution can be described from a single stellar populations (SSP) synthesis model as optical and X-ray selected clusters. All four of these SPT selected clusters in our study show red sequences (see Fig. 4.11), and their color evolution is consistent with colors derived from a single stellar population (SSP) synthesis model.

In order to perform a direct comparison of the brightness and evolution of the characteristic magnitude, we let all the LF variables vary, where possible, and compare  $m^*$  in *griz* bands derived from the LF fitting to that based on the SSP model. The SSP model we use for the red galaxy population is constructed using a Bruzual & Charlot synthesis model (BC03; Bruzual & Charlot, 2003) for the red galaxy populations, assuming a single burst of star formation at  $z=3$  followed by passive evolution to  $z=0$ . We use six different models with six distinct metallicities to match the tilt of the color magnitude relation at low redshift, and we add scatter in the metallicity-luminosity relation to reproduce the intrinsic scatter in the

color-magnitude relation. These models are then calibrated, using 51 X-ray clusters that have available SDSS magnitudes drawn from the DR7 database. Details of the model used can be found in Song et al (submitted). As shown in Fig. 4.4, the SSP model and  $m^*$  in each band are in good agreement, showing that the SSP model is an appropriate description of both the colors and the magnitudes of the more evolved early type galaxies in this sample of SZE selected clusters. We will use this agreement to carry out a more constrained study of the luminosity function.

### Faint end slope

To learn about the  $\alpha$  behavior we take advantage of the agreement shown in § 5.5.2 between SSP model and the data. We adopt  $m^*$  from the model (see Table 4.3) and fit for  $\Phi^*$  and  $\alpha$  for each cluster individually. The study of the faint end slope  $\alpha$  provides us with information about the faint galaxy populations in the cluster with respect to the more evolved bright end, which is dominated by luminous early type galaxies. This relation gives us insight into competing processes in the hierarchical structure formation scenario, including the accretion of faint galaxies by the cluster, causing a steep  $\alpha$ , and the evolution of galaxies inside the cluster through galaxy merging, dynamical friction, star formation quenching and other processes. Using the *amoeba* simplex minimization routine (Press et al., 1992),  $\Phi^*$  and  $\alpha$  are chi-square fitted, and their uncertainties are determined by gridding in parameter space (see the LF in Fig. 4.5, 4.6, 4.7, 4.8, and their contour confidence regions at Fig. 4.9).

From the literature, we find that our average  $\alpha \approx -1.2$  is in agreement at the  $1\sigma$  level with previous studies which used samples constructed with different selection methods. For example, from an optical work, De Propris et al. (2003) used 60 clusters at  $z < 0.11$  from 2dFGRS in the  $b_J$  band finding  $\alpha = -1.28 \pm 0.03$ . Paolillo et al. (2001) found, on a composite LF of 39 Abell clusters, an  $\alpha$  of  $-1.07^{+0.09}_{-0.07}$ ,  $-1.11^{+0.09}_{-0.07}$  and  $-1.09^{+0.12}_{-0.11}$  for Gunn  $g$ ,  $r$  and  $i$  respectively. From X-ray selected samples Lin et al. (2004) created a composite K-band LF of 93 clusters, finding that the faint-end slope is well fitted by  $-1.1 \lesssim \alpha \lesssim -0.84$  in agreement with our findings within the errors. Popesso et al. (2005), using 97 X-ray selected clusters with SDSS photometry, for a redshift  $z < 0.25$ , found that a better representation of the data is given by two Schechter functions, characterized by a bright and a faint end slope. Comparing to the bright end of the double Schechter function with local background subtraction (which is the most similar case), the bright end slope, in  $1 \text{ Mpc } h^{-1}$ , has a slope  $\alpha$  of  $-1.23 \pm 0.11$ ,  $-1.05 \pm 0.13$ ,  $-1.17 \pm 0.13$ , and  $-1.06 \pm 0.12$  in  $g$ ,  $r$ ,  $i$ , and  $z$ , respectively, also agreeing with our findings at the  $1\sigma$  level.

From IR selected clusters Muzzin et al. (2008) detected 99 clusters and groups of galaxies and constructed the LF in  $3.6\mu\text{m}$ ,  $4.5\mu\text{m}$ ,  $5.8\mu\text{m}$ , and  $8.0\mu\text{m}$ . Although the  $3.6\mu\text{m}$  band is redward of our *griz* photometry, the LF constructed seems to be consistent with  $\alpha \approx -1$ .

The agreement found between the multiband LF parameters calculated for our SZE selected clusters, and previous studies of galaxy cluster LFs indicates that the galaxy populations in these SZE selected clusters are not very different from those in clusters selected by other means.



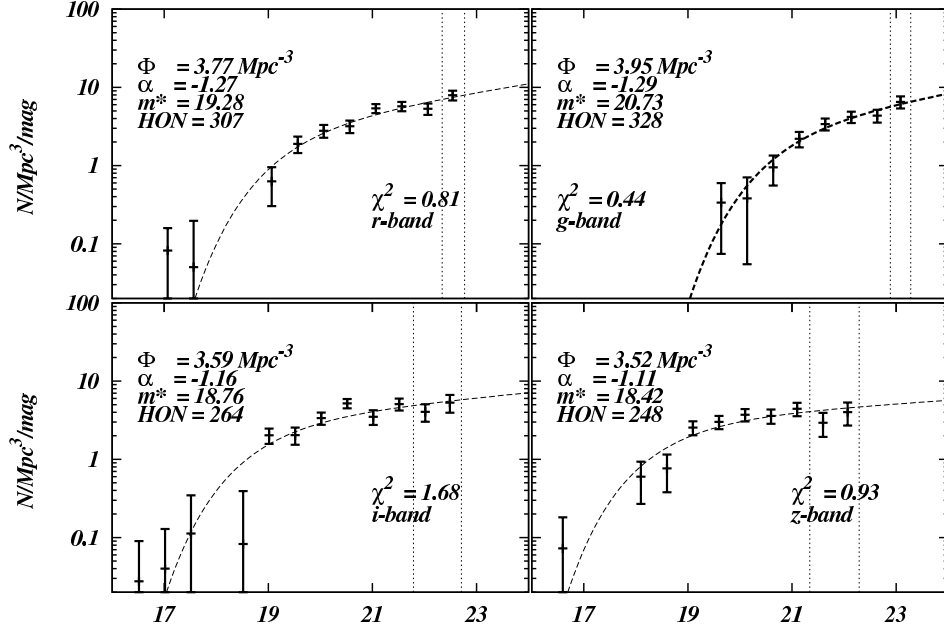


**Figure 4.5:** Here we plot the luminosity function with best fit Schechter function for each band in SPT-CL J0516-5430. Note that the BCG had been removed. Best fit parameters are shown on the figure, while Table 4.3 includes best fit and  $1\sigma$  uncertainties. 100% and 90% completeness limits are noted with vertical dotted lines in each panel.

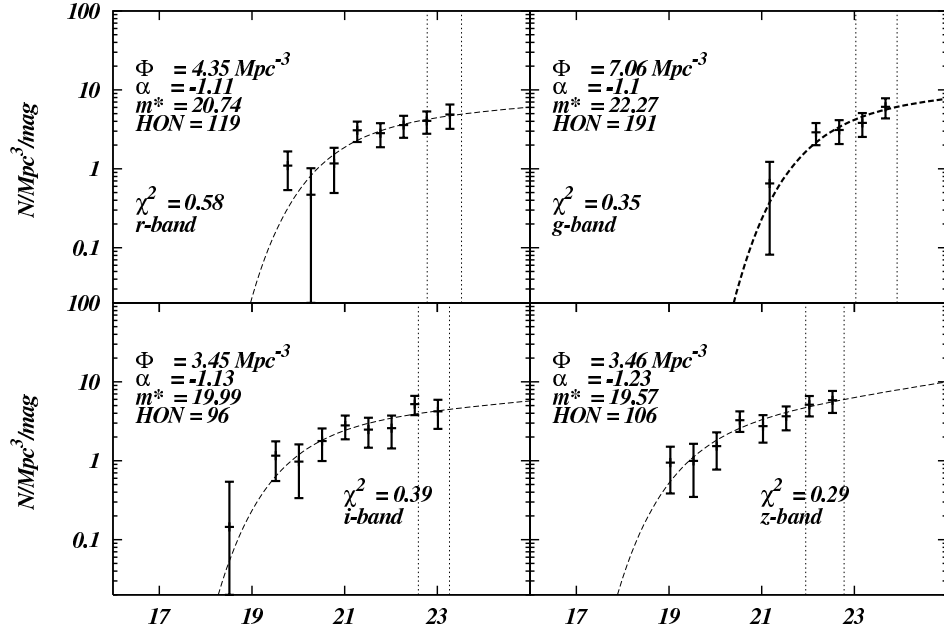


**Figure 4.6:** Same as Fig. 4.5 but for SPT-CL J0509-5342.

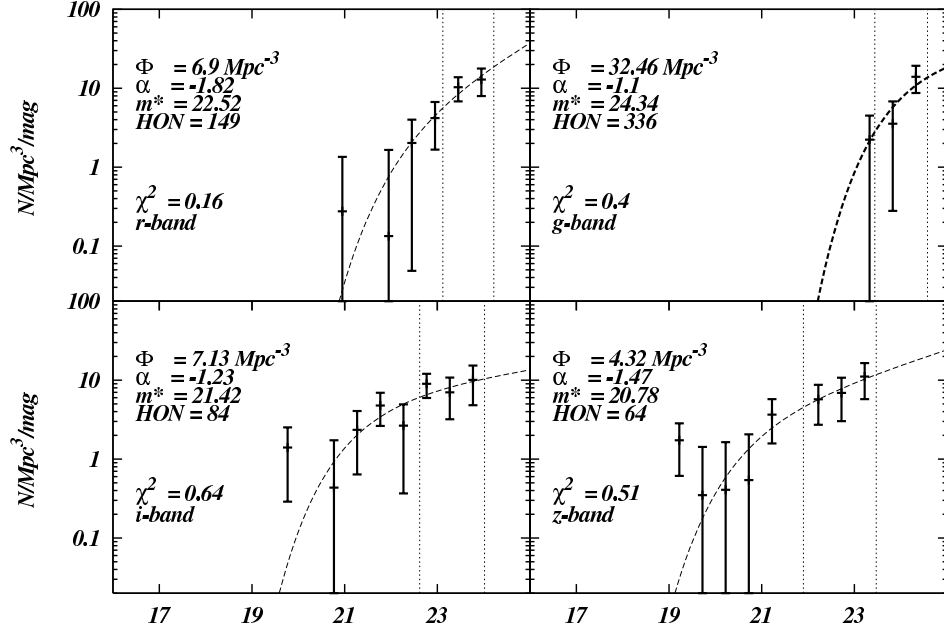


**Figure 4.7:** Same as Fig. 4.5 but for SPT-CL J0528-5300 with the 100% and 50% completeness limits noted with vertical dotted lines in each panel.

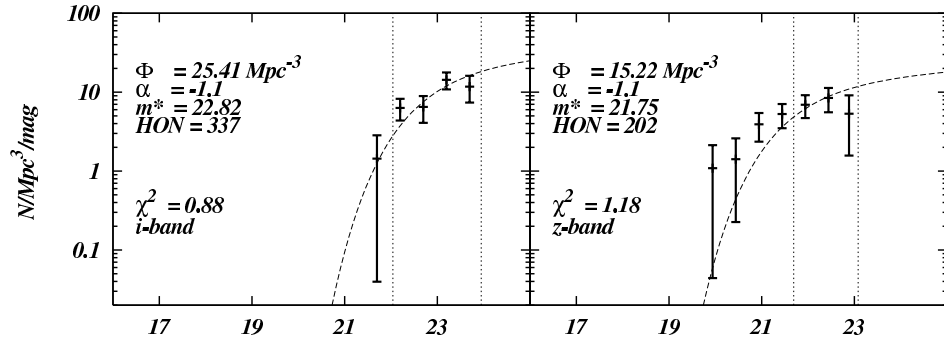


**Figure 4.8:** Same as Fig. 4.7 for SPT-CL J0546-5345 with only  $i$  and  $z$  bands.

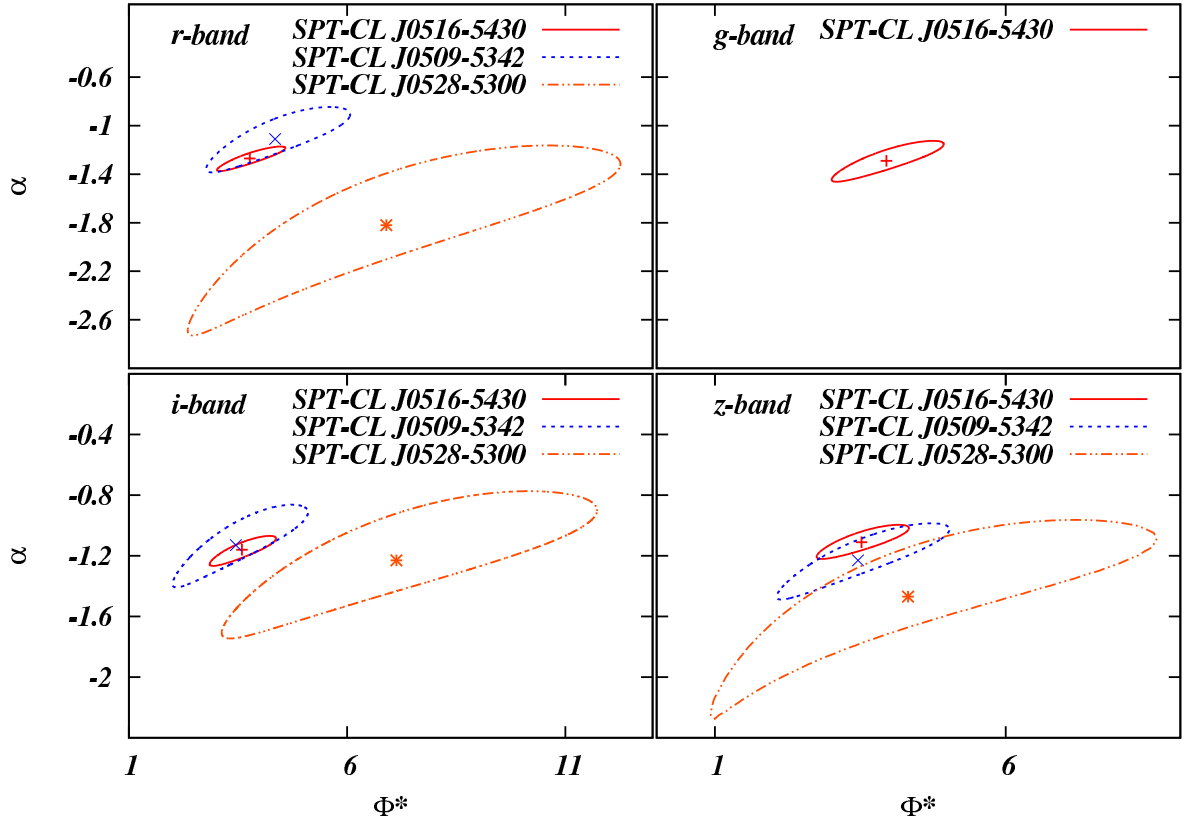


**Figure 4.9:** We plot the 68% confidence region for the LF parameters for each cluster and band combination. Panels are arranged by band with confidence regions for each cluster where a fit for  $\alpha$  and  $\Phi^*$  was possible. The current data suggest steeper than normal faint end parameters  $\alpha$  in two of the clusters and there is a tendency for the higher redshift systems to have higher characteristic galaxy densities, as expected in an evolving Universe. Values including those at fixed  $\alpha$  are given in Table 4.3.

Table 4.3: HON parameters

ID	$\Phi_g^*$ [ $Mpc^{-3}$ ]	$\alpha_g$	$m_g^*$	$HON$ ( $m_g^* + 2$ )	$\chi^2$	$\Phi_r^*$ [ $Mpc^{-3}$ ]	$\alpha_r$	$m_r^*$	$HON$ ( $m_r^* + 2$ )	$\chi^2$
SPT-CL J0516-5430	$3.95^{+0.98}_{-0.94}$	$-1.29^{+0.16}_{-0.18}$	20.73	$327^{+157}_{-112}$	0.44	$3.78^{+0.81}_{-0.76}$	$-1.27^{+0.10}_{-0.10}$	19.28	$308^{+105}_{-83}$	0.81
SPT-CL J0509-5342	$7.07^{+1.11}_{-1.11}$	$-1.1^a$	22.27	$191^{+30}_{-30}$	0.35	$4.36^{+1.71}_{-1.59}$	$-1.11^{+0.26}_{-0.28}$	20.74	$119^{+95}_{-57}$	0.58
SPT-CL J0528-5300	—	—	24.34	—	—	$6.89^{+5.37}_{-4.54}$	$-1.82^{+0.66}_{-0.91}$	22.52	$149^{+691}_{-122}$	0.16
SPT-CL J0546-5345	—	—	25.92	—	—	—	—	23.85	—	—
ID	$\Phi_i^*$ [ $Mpc^{-3}$ ]	$\alpha_i$	$m_i^*$	$HON$ ( $m_i^* + 2$ )	$\chi^2$	$\Phi_z^*$ [ $Mpc^{-3}$ ]	$\alpha_z$	$m_z^*$	$HON$ ( $m_z^* + 2$ )	$\chi^2$
SPT-CL J0516-5430	$3.59^{+0.78}_{-0.74}$	$-1.17^{+0.10}_{-0.10}$	18.76	$266^{+88}_{-71}$	1.67	$3.52^{+0.82}_{-0.77}$	$-1.11^{+0.11}_{-0.11}$	18.42	$248^{+89}_{-71}$	0.93
SPT-CL J0509-5342	$3.45^{+1.65}_{-1.40}$	$-1.13^{+0.27}_{-0.28}$	19.99	$96^{+87}_{-49}$	0.39	$3.45^{+1.58}_{-1.38}$	$-1.23^{+0.24}_{-0.26}$	19.57	$105^{+92}_{-53}$	0.29
SPT-CL J0528-5300	$7.15^{+4.57}_{-4.02}$	$-1.23^{+0.46}_{-0.52}$	21.42	$84^{+148}_{-58}$	0.64	$4.34^{+4.25}_{-3.46}$	$-1.47^{+0.50}_{-0.82}$	20.78	$65^{+265}_{-56}$	0.51
SPT-CL J0546-5345	$25.43^{+4.03}_{-4.04}$	$-1.1^a$	22.83	$337^{+53}_{-53}$	0.88	$15.2^{+3.57}_{-5.58}$	$-1.1^a$	21.75	$202^{+74}_{-74}$	1.19

<sup>a</sup>  $\alpha$  set to fixed value.  $m^*$  from model of passive evolution.

### 4.5.3 Halo Occupation Number

Based on the Press & Schechter formalism (Press & Schechter, 1974), the halo occupation distribution (HOD) is a powerful analytical tool for understanding the physical processes driving galaxy formation (Seljak, 2000; Berlind et al., 2003). Also the HOD can be used to constrain cosmological parameters (Zheng & Weinberg, 2007).

One of the key ingredients in the HOD formalism is  $\langle N \rangle(M)$ , the mean number of galaxies per halo or the Halo Occupation Number (HON). In the hierarchical scenario, the HON is expected to increase slower than the mass. While a fraction of the accreted galaxies merged, the galaxy production becomes less efficient as larger haloes are also hotter and less efficient in gas cooling (Cole et al., 2000). Observationally, several studies with cluster samples selected optically and through their X-ray emission have been performed, reinforcing that picture. For example, from samples of optically selected clusters and groups, Marinoni & Hudson (2002) found  $N \propto M^{0.83 \pm 0.15}$  for systems with  $M \gtrsim 10^{13} h_{75}^{-1} M_{\odot}$ . Also, Muzzin et al. (2007b) found  $N_{500} \propto M_{500}^{0.71 \pm 0.11}$  in the  $\sim 2 \times 10^{14} M_{\odot} - 2 \times 10^{15} M_{\odot}$  mass range. In the X-ray selection method counterpart, Lin et al. (2004) found, from a sample of 93 nearby clusters and groups,  $N \propto M^{0.87 \pm 0.04}$ . Combining X-ray and optically selected clusters, Popesso et al. (2007a) found  $N \propto M_{200}^{0.92 \pm 0.03}$ . A similar picture was found by Rines et al. (2004), who used nearby X-ray luminous Abell clusters of mass  $\sim 3 \times 10^{14} h^{-1} M_{\odot}$  and found  $N \propto M^{0.74 \pm 0.15}$ .

Here we test whether the HON of SZE selected clusters exhibits a  $N \propto M^{\beta}$ , with  $\beta < 1$ , behavior shown by other selection methods.

Due to the small sample presented here, our approach is to construct the HON and compare our results to the  $N$ - $M$  scaling relation and evolution constraints obtained by Lin et al. (2004, 2006). That scaling relation is appropriate in this analysis as it covers the mass and redshift range of this SZE sample. The scaling relation was constructed using X-ray selected clusters in the  $3 \times 10^{13} M_{\odot} - 2 \times 10^{15} M_{\odot}$  mass range using nearby clusters with 2MASS K-band photometry, and later, Lin et al. (2006), counting galaxies to the depth  $m^*+2$ , expanded the study to the 0-0.9 redshift range showing that the relation does not strongly evolve.

The Lin et al. (2004)  $N$ - $M$  relation is,

$$N_{200} = (36 \pm 3)(M_{200}/(10^{14} h_{70}^{-1} M_{\odot}))^{0.87 \pm 0.04}$$

To calculate  $N_{200}$  we integrate the cluster luminosity function to  $L(m_{MODEL}^* + 2)$  using the parameters of the Schechter luminosity function fit,  $\phi_*$ ,  $L_*$  and  $\alpha$  computed in §5.4.2. The total number of galaxies is

$$N = 1 + N^s, \text{ with } N^s = V \phi_* \int_{y_{low}}^{\infty} y^{\alpha} e^{-y} dy$$

where the 1 comes from the BCG, which is not part of the LF fitting,  $V$  is the cluster volume, and  $y_{low} = L_{low}/L_*$ . We use the derived  $M_{200, Y_X}$  masses and uncertainties as explained in §4.4.2 from Andersson et al. (2011) Chandra and XMM observations. The uncertainty in  $N_{200}$  is estimated by propagating the  $1 \sigma$  uncertainty in  $\phi_*$  and  $\alpha$  through the integration of the LF to  $m^* + 2$ .

The  $N_{200}$  with their X-ray mass for the four clusters in the four observed band, along with the HON relation found by Lin et al. (2004), are shown in Fig. 4.10. Agreement between these SPT clusters and the published results on the X-ray selected sample is good. As with the concentration and the LF faint end, there is no significant evidence that the galaxy properties differ from those already extracted from previous X-ray selected cluster samples.

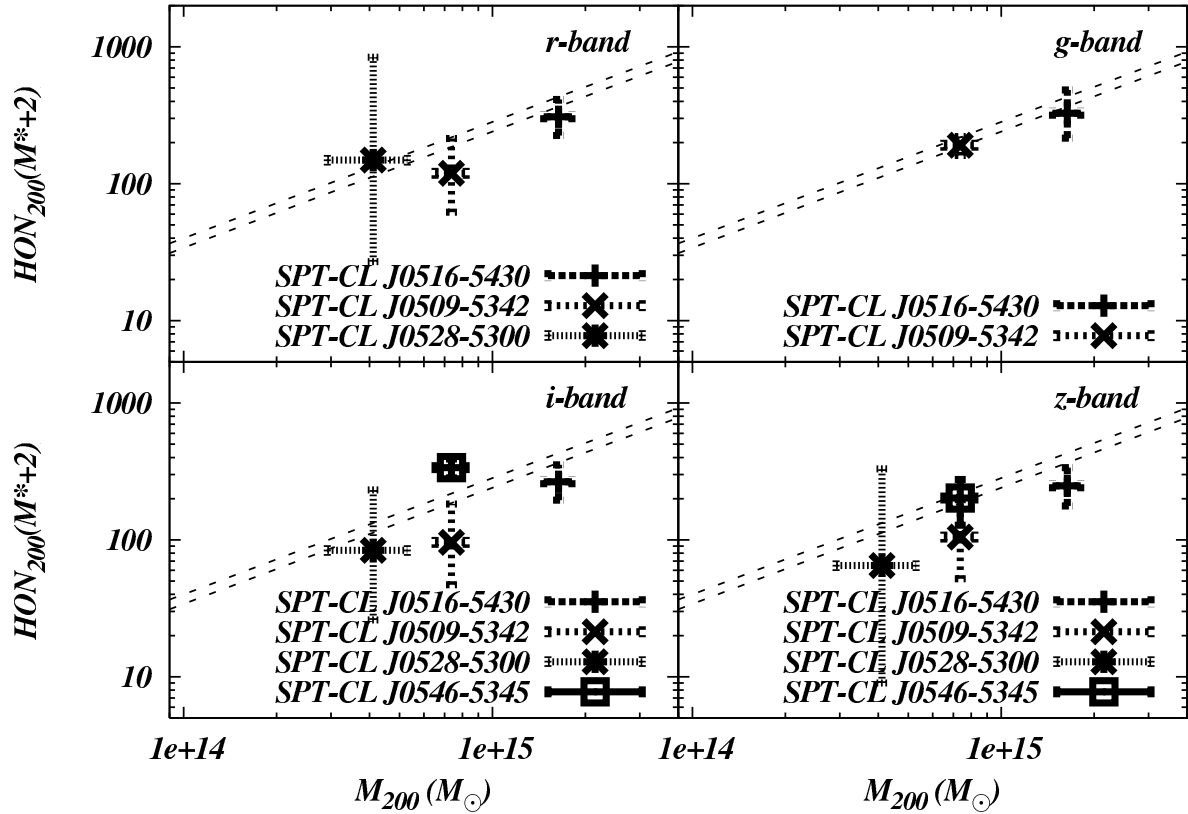


**Figure 4.10:** We present the halo occupation number ( $HON(m^{*+2})$ ) within each band for each cluster where the LF is measured in more than three bins. Masses and uncertainties on the horizontal axis come from X-ray analysis of Chandra observations (Andersson et al., 2011). HON uncertainties are derived from the variation of HON due to the  $1\sigma$  uncertainty in the LF ( $\alpha$  and  $\Phi^*$ ). The dotted lines show the HON derived from a K-band analysis of a large sample of X-ray selected clusters (Lin et al., 2004, 2006). These SPT selected clusters appear to be neither richer nor poorer.

#### 4.5.4 Blue fractions

Another property of the galaxy populations used to study their evolution in clusters of galaxies is the blue fraction ( $f_b$ ). In their seminal work Butcher & Oemler (1984, BO hereafter), using a samples of 33 optically selected clusters of galaxies, estimated  $f_b$  and showed that it increased with look-back time (termed the Butcher-Oemler effect). Later studies, such as Rakos & Schombert (1995) ( $0 < z < 1$ ) and Margoniner & de Carvalho (2000) ( $0.03 \lesssim z \lesssim 0.38$ ), using optically selected clusters, also have found a strong increase in  $f_b$  with redshift.

With the advent of new optical surveys with hundreds or thousands of clusters the analyses have been strengthened statistically. Using a sample of  $\approx 1000$  clusters, in a wide redshift range ( $0 \lesssim z \lesssim 0.9$ ), drawn from the Red-Sequence Cluster Survey (RCS), Loh et al. (2008) found a mild correlation between the red fraction and redshift. Hansen et al. (2009), using thousands of clusters and groups from SDSS, found an evolving  $f_b$  in the two redshift bins studied (0.1-0.25 and 0.25-0.3), also noticing that  $f_b$  evolution was weaker for optical masses above  $10^{14} h^{-1} M_\odot$ .

Studies using samples of X-ray selected clusters, have been contradictory. Kodama & Bower (2001) used a sample of seven clusters, in the redshift range of 0.23-0.43, and found a blue fraction trend consistent with BO, while Fairley et al. (2002), using a sample of eight clusters in a 0.23-0.58 redshift range found virtually no trend with redshift. More recently, Urquhart et al. (2010) used CFHT MegaCam  $g$  and  $r$  photometry on 34 X-ray selected clusters in the redshift range 0.15-0.41 to study  $f_b$  correlation with other intrinsic cluster properties, found that  $f_b$  correlated with mass ( $T_X$ ) and redshift.

Also there are environmental factors to be considered. Smail et al. (1998) used 10 X-ray selected clusters at similar redshift (0.22 to 0.28) and found a low blue fraction of  $\bar{f}_b = 0.04 \pm 0.02$  with a variation of  $\Delta f_b = 0.06$ , explained by 'small accretion events' which contribute blue members to the clusters without much increase of other parameters such as mass or X-ray luminosity. Such events could be a source of scatter in the galaxy populations of clusters selected by any selection method. To analyze  $f_b$  correlation with other cluster parameters De Propris et al. (2004) used a sample of clusters from 2dF Galaxy Redshift Survey (2dFGRS) at redshift  $< 0.11$ , finding a large variation ( $f_b \sim 0.1$ -0.5 for  $M^* + 1.5$  at  $r_{200}$ ) from cluster to cluster.

The apparent contradiction between X-ray and optically selected samples and the sensitivity to environmental effects, raises questions about how much of the observed  $f_b$  is due to a selection method, how much it is due to the intrinsic scatter, and if these two effects can conspire to produce an apparent trend where no trend exists.

What is needed is a sample of galaxy clusters which possess two main characteristics: (1) the selection of clusters is made in a way that is independent of the quantity whose evolution is being studied to avoid possible bias (Newberry et al., 1988; Andreon & Ettori, 1999), and (2) the sample must contain the same class of clusters (i.e. same mass range) at different redshift to help in separating mass trends from redshift evolution (Andreon & Ettori, 1999). A sample of SZE selected clusters of galaxies fulfills these requirements. The selection of the SZE clusters is closely related to mass, and that mass selection is approximately independent of redshift, allowing a comparison of the same type of clusters at different epochs.

Historically  $f_b$  has been measured in different ways. Initially the average color of the E/S0 galaxies, within a radius of  $R_{30}$  from the cluster center that is the radius that contains 30% of all galaxies that belong to the cluster, and a concentration index, were use to define  $f_b$  (see Butcher & Oemler, 1984; Rakos & Schombert, 1995; Margoniner & de Carvalho, 2000; Fairley

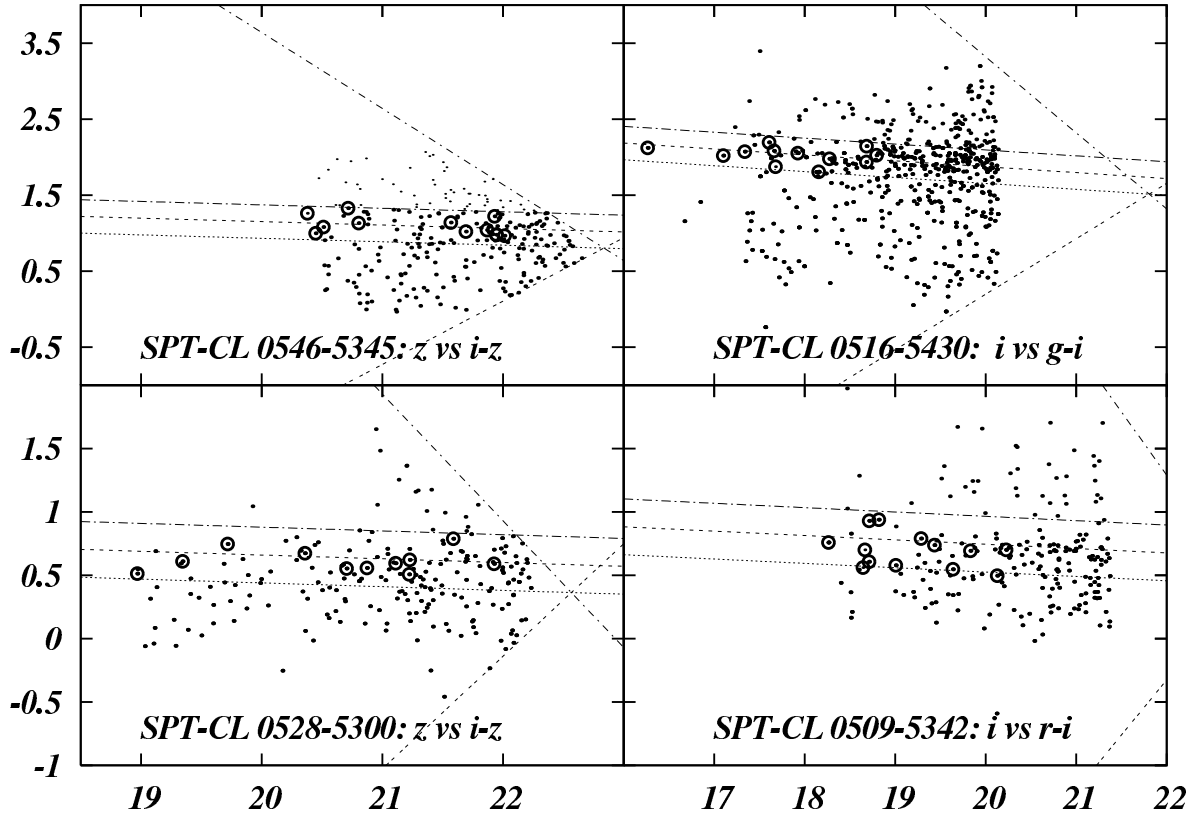


**Figure 4.11:** Color magnitude diagram for galaxies around each cluster. The blue population is defined to be more than 0.22 mags bluer than the red sequence. Selection in magnitude uses the BCG on the bright end and  $m^* + \delta$  on the faint end, where this limit corresponds to the 90% completeness limit for SPT-CL J0528-5300 ( $0.36L_{MODEL}^*$ ). The visually identified red sequence cluster galaxies are shown using circles.



et al., 2002). Another approach is using the red sequence from the color-magnitude diagram of the clusters and  $r_{200}$  (Popesso et al., 2007b; Barkhouse et al., 2007) or a combination of both methods, that is using the color-magnitude diagram but  $R_{30}$  (Kodama & Bower, 2001; Fairley et al., 2002).

Here we follow the approach of using the red sequence to define the red and blue populations, and  $r_{200}$  to define the radial extent. This ensures we are using the same portion of the cluster virial region, independent of redshift, and that we are exploring populations with colors defined with respect to a passively evolving SSP model.

The galaxies used for the  $f_b$  measurement are inside the  $r_{200}$  cluster radius and are fainter than the BCG and brighter than  $0.36L_{MODEL}^*$ . They are classified as red if they are located within  $\pm 3$  times the average dispersion of the Gaussian fit to the color-magnitude relation ( $\pm 0.22$  mag; López-Cruz et al., 2004), and blue if they are more than 0.22 mags bluer than the Red Sequence. We choose a limit of  $0.36L_{MODEL}^*$  to allow a meaningful comparison among three of our four clusters, as it is the deepest magnitude that we can detect with good completeness for the three of them. For the fourth cluster, SPT-CL J0546-5345, we currently do not have deep enough photometry for this analysis.

The color magnitude diagram used for the clusters depends on the red sequence identification: g-i/i for SPT-CL J0516-5430, r-i/i for SPT-CL J0509-5342, and i-z/z for SPT-CL J0528-5300 and SPT-CL J0546-5345 (see fig. 4.11). The blue fraction is defined as the statistically background corrected number of blue galaxies  $n_b$  divided by the total number of statistically background corrected galaxies  $n_t$ . The blue fraction and its gaussian propagated uncertainty are:

$$f_b = \frac{n_b}{n_r + n_b}; \quad \sigma_{f_b}^2 = \sum_{i=r,b} \left( \frac{\partial f}{\partial n_i} \right)^2 \sigma_{n_i}^2 \quad (4.1)$$

Where  $n_b$  and  $n_r$  are the blue and red statistically background subtracted number of galaxies:

$$n_i = N_i - \overline{N}_i^{(bkg)}$$

The uncertainties are expressed as

$$\sigma_{n_i}^2 = \sigma_{N_i}^2 + \sigma_{\overline{N}_i^{(bkg)}}^2$$

assuming  $\sigma_{N_i}$  Poissonian. The last term is calculated directly by measuring the RMS of the Gaussian distribution observed on histograms constructed from the blue and red (or total) number of galaxies background corrected in a circle of radius  $r_{200}$  on  $n$  random position outside the cluster radius ( $\text{background}(r_{200}) - \overline{\text{background}}$ ) in order to account for background variations on the observed  $36' \times 36'$  patch of the sky.

A special mention for SPT-CL 0509-5342 is required. In the center of the cluster are three bright stars leaving only a few visible galaxies; we have corrected this effect by accounting for the area masked around these stars. Nevertheless, the statistical background subtraction leads to negative blue galaxy counts in the  $\sim 0.6r_{200}$  inner part of the cluster area.

The blue fraction of three of the four clusters, at redshifts 0.295, 0.463 and 0.763, are shown in Fig. 4.12. The measurements suggest an increase with redshift, as shown for optically selected clusters, although the result could be consistent with a constant blue fraction over the range of redshift that we explored with our limited sample. Future optical follow up of SPT-SZE selected clusters using larger aperture telescopes on the high redshift end will be necessary to understand the Butcher-Oemler effect in this cluster mass range within the SZE selected sample.

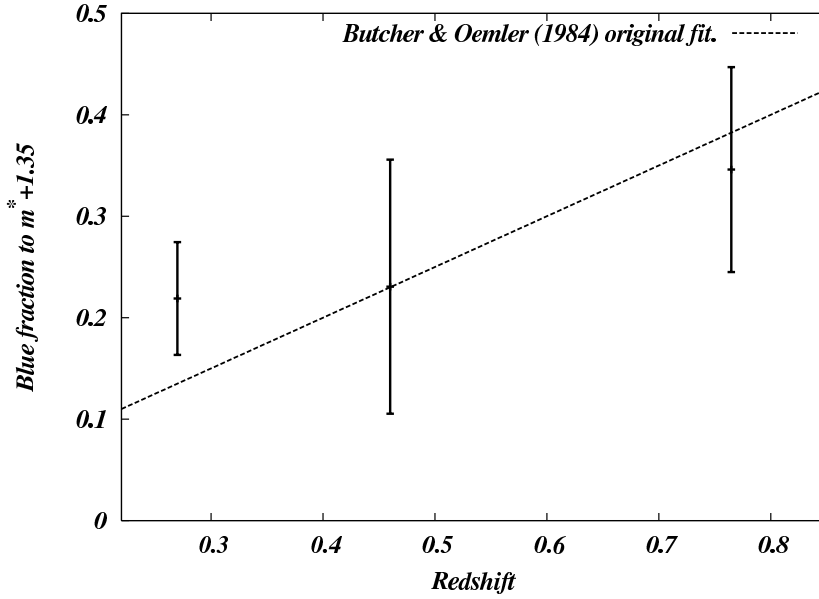


**Figure 4.12:** Blue fraction versus redshift using the populations shown in Fig. 4.11. The Butcher & Oemler (1984) relation is shown (dashed line). The blue fraction is calculated using statistical background correction within  $r_{200}$  and to a depth of  $0.36L_{MODEL}^*$  for each system.

## 4.6 Conclusions

We present the results of a careful examination of the multiband optical properties of the galaxy populations in the first four SZE selected galaxy clusters. This analysis builds upon the selection by the South Pole Telescope survey, deep multiband optical data from the Blanco Cosmology Survey, Chandra and XMM mass estimates and published spectroscopic redshifts. The radial distributions of galaxies in the four systems are consistent with NFW profiles with low concentration in the 2.2-3.6 range, although the constraints in our highest redshift clusters are weak due to the imaging depth. One system shows a clear secondary peak, which is evidence of multiple galaxy components. The observed galaxy concentrations in these SPT systems are consistent with X-ray and optical selected cluster samples as well as simulations. We showed that the characteristic luminosities in bands *griz* are consistent with passively evolving populations emerging from a single burst at redshift  $z = 3$ . This is observed by direct comparison of the *griz*  $m^*$  measurements with the evolution of the red sequence expected from the SSP model.

The slope of the luminosity function,  $\alpha$ , in all four bands showed an average of  $-1.2$  consistent with previous studies and roughly independent of redshift, although in the high redshift systems the constraints are weaker and the  $\Phi - \alpha$  contours are much more extended (see Fig. 4.9) due to the depth of the data.

Halo occupation numbers (to  $m^* + 2$ ) for these systems appear to be consistent with the relation measured in X-ray selected clusters. As shown previously (Lin et al., 2004), this well behaved and simple galaxy populations is unfortunately not easy to use as a mass indicator with optical data alone, because the HON varies with the adopted virial radius of the cluster. The blue fractions  $f_b$  observed in these systems are consistent with those seen in clusters

selected using other means. Although the measured  $f_b$  suggest a redshift evolution (as optical studies show), it is within the errors also consistent with a constant  $f_b$ . It is clear that definitive conclusions should be drawn with a larger number of clusters for more robust statistics. A larger sample and deeper multiband data on the high redshift end is needed.

The SPT selection provides a powerful means of choosing similar mass systems over a broad range of redshift, making the future larger cluster sample particularly interesting for this study.

In summary, our systematic analysis of the galaxy populations in the first SZE selected galaxy clusters spanning the redshift range  $0.3 < z < 1.1$  provides no clear evidence that the galaxy populations in these SPT selected clusters differ from populations studied in other X-ray and optically selected samples. An extension of our analysis to the full SPT sample will enable a more precise test of the effects of selection. In addition, comparison of the observed properties of the SPT cluster galaxy populations and their evolution to numerical simulations of galaxy formation should allow for clean tests of the range of physical processes that are responsible in determining the formation and evolution of cluster galaxies.

*Acknowledgments:* The South Pole Telescope is supported by the National Science Foundation through grant ANT-0638937. Partial support is also provided by the NSF Physics Frontier Center grant PHY-0114422 to the Kavli Institute of Cosmological Physics at the University of Chicago, the Kavli Foundation, and the Gordon and Betty Moore Foundation. AZ, JM, GB and JL acknowledge the support of the Excellence Cluster Universe in Garching. This paper includes data gathered with the Blanco 4-meter telescope, located at the Cerro Tololo Inter-American Observatory in Chile, which is part of the U.S. National Optical Astronomy Observatory, which is operated by the Association of Universities for Research in Astronomy (AURA), under contract with the National Science Foundation. This work is based in part on observations obtained with the Chandra X-ray Observatory (CXO), under contract SV4-74018, A31 with the Smithsonian Astrophysical Observatory which operates the CXO for NASA. We are very grateful for the efforts of the Chandra, XMM, and CTIO support staff without whom this paper would not be possible. Support for M.B. was provided by the W. M. Keck Foundation. B.S. acknowledges support from the Brinson Foundation.



# Galaxy Populations in the 26 most massive Galaxy Clusters in the South Pole Telescope SZE Survey

## 5.1 Abstract

We present a study of the optical properties of the 26 most massive galaxy clusters selected within the SPT-SZ 2500 deg<sup>2</sup> survey. This Sunyaev-Zel'dovich effect selected sample spans a redshift range  $0.1 < z < 1.13$ . We measure the galaxy radial distribution, the luminosity function (LF) and the halo occupation number (HON) using optical data with a typical depth of  $m^* + 2$ , adjusting the band used to lie redward of the 4000 Å break at each redshift. The total stacked radial profile is consistent with a Navarro-Frenk-White profile with a concentration of  $2.71^{+0.38}_{-0.33}$  for the red sequence and  $2.25 \pm 0.33$  for the total population. Stacking the data in multiple redshift bins shows no redshift evolution in the concentration when all galaxies are used, and a preference for weak evolution when only red sequence galaxies are used. The stacked LF shows a faint end slope  $\alpha = -1.06^{+0.04}_{-0.01}$ , and the redshift evolution of the characteristic magnitude  $m^*$  is consistent with a passively evolving Simple Stellar Population (SSP) model over the full redshift range. By adopting the SSP model predictions for the characteristic magnitude  $m^*$ , we explore the redshift evolution in the faint end slope  $\alpha$  and characteristic galaxy density  $\phi^*$ . We find a  $2\sigma$  evidence of evolution from  $\alpha \sim -0.9$  on the high redshift end to  $\alpha \sim -1.14$  at redshift zero; the data show that the density  $\phi^*$  of galaxies with characteristic magnitude  $m^*$  evolves as  $E^2(z)$ , consistent with the self-similar expectation. The measured HON–mass relation has a normalization in good agreement with previous studies at low redshift. Our data shows a preference for a HON redshift evolution, with clusters at higher redshift containing fewer galaxies per unit mass to  $m^* + 3$  than their low- $z$  counterparts.

GALAXIES: CLUSTERS: GENERAL – GALAXIES: EVOLUTION – GALAXIES: FORMATION – COSMOLOGY: OBSERVATIONS – SUNYAEV-ZEL'DOVICH EFFECT

## 5.2 Introduction

Clusters have long been recognised as important laboratories for the study of galaxy formation and evolution (e.g., Dressler, 1980; Butcher & Oemler, 1984). With the advent of the new generation of mm-wave survey telescopes like the South Pole Telescope (Carlstrom et al., 2011), the Atacama Cosmology Telescope (ACT, Fowler et al., 2007) and Planck (Planck Collaboration et al., 2011a), it has become possible to select galaxy clusters over large fractions of the extragalactic sky using the thermal Sunyaev-Zel'dovich effect (SZE), which arises from the inverse Compton scattering of CMB photons off the hot electrons in the intracluster medium (Sunyaev & Zel'dovich, 1972). For the SPT-SZ arcminute angular resolution  $2500 \text{ deg}^2$  survey, it has been demonstrated that the cluster samples selected using this signature are close to mass limited (Reichardt et al., 2013), extend to at least redshift  $z = 1.47$  (Bayliss et al., 2013) and have purity exceeding 95% from the SZE selection alone (Song et al., 2012b). These cluster samples, selected using cluster gas signatures as opposed to cluster galaxy signatures, are ideal for evolutionary studies of the cluster galaxy populations.

By studying the evolution of the cluster galaxy luminosity function (LF) we can address the changes in the cluster populations in a statistical manner. It has been shown, that while the bright population is consistent with a stellar population passively evolving, the faint-end of the red sequence LF (rLF) grows increasingly shallow at higher redshifts (e.g De Lucia et al., 2007; Gilbank et al., 2008; Rudnick et al., 2009). Furthermore, the same studies hint to a weak correlation of the luminosity function faint end slope,  $\alpha$ , with mass. At the same time, previous studies have shown that the Halo Occupation Number (HON), or the integral of the LF per unit mass, seems to be invariant with redshift (Lin et al., 2004), which points to a continuous galaxy transformation within the cluster. This transformation can also be tracked as a function of the radius, using the concentration evolution of the different species. Literature values at different redshifts seem to indicate no evolution when all galaxies within the virial radius are considered (e.g., Carlberg et al., 1997; Capozzi et al., 2012), and while the expectation is that the brightest red sequence galaxies, which dominate the bright-end of the LF, would be more concentrated than the fainter component, it is not known whether this effect is present at already at high redshift. All these components are also used in the framework of the Halo Occupation Distribution (HOD; Berlind et al., 2003), which describes how galaxies occupy the cluster as a function of the location, velocity distribution, and luminosity. A particularly robust observable for studies of large samples of cluster is the integral of the number of galaxies more luminous than some threshold that inhabit the cluster virial region. This is the Halo Occupation Number.

In this work we extract the radial distribution, luminosity function and the HON of an SZE selected cluster sample to address cluster galaxy evolution questions cleanly within a uniformly selected sample of the most massive clusters in the Universe. Our goal is to study how the galaxy components, separated into the red subsample and the full sample within the virial radius, change across cosmic time. By making reference to previous studies that have been carried out on X-ray and optically selected cluster samples, we have the opportunity to begin to address the importance of sample selection in these studies.

The paper is organized as follows: Section 2 describes the observations and data reduction. In Section 3, we describe our tools and the simulations used to test them. In Section 4 we present the main results of the study of the galaxy populations in the SPT selected massive cluster sample. Conclusions of this study are presented in Section 5. Magnitudes are quoted

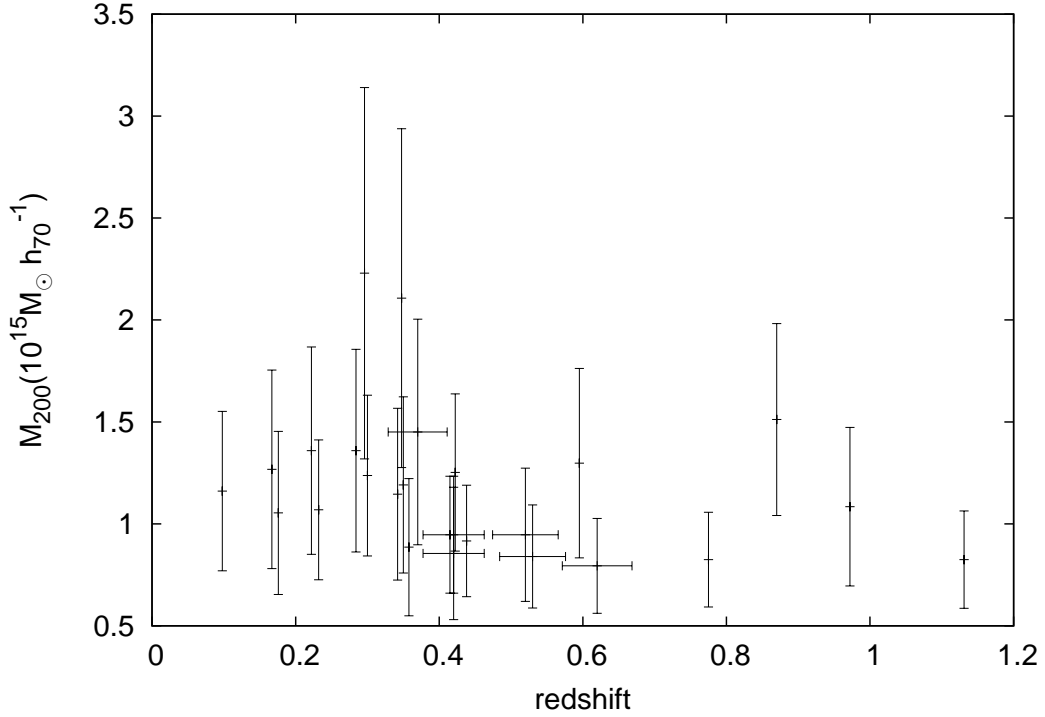


**Figure 5.1:** Mass-redshift distribution of our sample.

in the AB system. We assume a flat,  $\Lambda$ CDM cosmology with  $H_0 = 70.2 \text{ km s}^{-1} \text{ Mpc}^{-1}$ , and matter density  $\Omega_M = 0.272$ , according to WMAP7 + BAO + H0 data (Komatsu et al. 2011). Masses are defined as  $M_{\Delta, \text{crit}} = \frac{4\pi r^3 \Delta}{3} \Delta \rho_{\text{crit}}$ , where  $\rho_{\text{crit}} = 3H^2/8\pi G$  is the critical density of the Universe.

### 5.3 Observations and Data Reduction

In this work we use a sample of the most massive galaxy clusters in the total  $2500 \text{ deg}^2$  SPT survey area that was originally presented in Williamson et al. (2011). The sample consists of 26 galaxy clusters in the mass range  $M_{200} \geq 7 \times 10^{14} h_{70}^{-1} M_{\odot}$  extending to redshift  $z = 1.13$ . The optical photometric and spectroscopic data used in this paper come from multiple observatories and they have been processed using several pipelines. The data reductions for a portion of the dataset are outlined in several papers (High et al., 2010; Williamson et al., 2011; Song et al., 2012b). In the following subsections we summarize the data and the processing and calibration.

#### 5.3.1 mm-wave Observations

The clusters presented here are the most massive systems in the SPT-SZ survey area, which consists of a contiguous  $2500 \text{ deg}^2$  region defined by the boundaries  $20^{\text{h}} \leq \text{R.A.} \leq 24^{\text{h}}, 0^{\text{h}} \leq \text{R.A.} \leq 7^{\text{h}}$  and  $-65^{\circ} \leq \text{decl.} \leq -40^{\circ}$ . Mass estimation for the clusters has been carried out in a staged manner, using first simulations (Vanderlinde et al., 2010), and then using a small

number of X-ray  $Y_X$  measurements (Benson et al., 2013; Reichardt et al., 2013). For details on the SPT data processing where are several papers that describe the method in detail (Staniszewski et al., 2009; Vanderlinde et al., 2010; Shirokoff et al., 2011).

### 5.3.2 Redshifts and Cluster Masses

Cluster redshifts appear in the discovery paper (Williamson et al., 2011), but since then spectroscopic redshifts have become available for six of the systems (Song et al., 2012b; Ruel et al., 2012; Sifon et al., 2012; Planck Collaboration et al., 2011c). Where possible we use spectroscopic redshifts. The redshifts are listed in Table 5.1. This table contains the SPT cluster name (with reference to other names where they exist), the SPT sky position of the cluster (RA and DEC), the redshift (to two significant digits if a photo-z and to three if a spectroscopic redshift), the SPT S/N  $\xi$ , the estimated cluster mass, the virial radius in arc minutes and the BCG position (RA and DEC).

**Table 5.1:** SPT Cluster List.

Object Name	R.A. deg.	decl. deg.	$z$	SN	$M_{200}$ $10^{14} h_{70}^{-1} M_{\odot}$	$R_{200}$	RA <sub>BCG</sub> deg.	DEC <sub>BCG</sub> deg.
SPT-CL J0040-4407	10.202	-44.131	0.350	10.1	$12.4 \pm 1.8 \pm 3.2$	6.52	10.2083	-44.1306
SPT-CL J0102-4915 <sup>1</sup>	15.728	-49.257	0.870	39.5	$16.2 \pm 2.5 \pm 3.0$	3.74	15.7408X	-49.272X
SPT-CL J0232-4421 <sup>2</sup>	38.070	-44.351	0.284	11.4	$14.1 \pm 2.0 \pm 4.0$	8.03	38.0680	-44.3467
SPT-CL J0234-5831	38.670	-58.520	0.415	14.7	$9.8 \pm 1.6 \pm 1.3$	5.30	38.6762	-58.5236
SPT-CL J0243-4833 <sup>14</sup>	40.910	-48.557	0.53	13.8	$8.7 \pm 1.5 \pm 1.1$	4.26	40.9120	-48.5608
SPT-CL J0245-5302 <sup>3</sup>	41.378	-53.036	0.300	19.3	$12.8 \pm 2.0 \pm 2.4$	7.45	41.2750	-52.9925
SPT-CL J0254-5856	43.563	-58.949	0.438	14.3	$9.4 \pm 1.5 \pm 1.4$	5.03	43.5365	-58.9718
SPT-CL J0304-4401 <sup>14</sup>	46.064	-44.030	0.52	8.0	$9.8 \pm 1.6 \pm 2.1$	4.49	46.0878	-44.0439
SPT-CL J0411-4819 <sup>14</sup>	62.811	-48.321	0.42	14.8	$10.1 \pm 1.6 \pm 1.5$	5.25	62.8154	-48.3175
SPT-CL J0417-4748 <sup>14</sup>	64.340	-47.812	0.62	13.9	$8.3 \pm 1.3 \pm 1.0$	3.75	64.3463	-47.8133
SPT-CL J0438-5419 <sup>4</sup>	69.569	-54.321	0.422	22.3	$13.1 \pm 2.1 \pm 2.2$	5.75	69.5738	-54.3224
SPT-CL J0549-6204 <sup>14</sup>	87.326	-62.083	0.32	12.6	$15.1 \pm 2.1 \pm 4.6$	6.68	87.3331	-62.0871
SPT-CL J0555-6405 <sup>14</sup>	88.851	-64.099	0.42	7.1	$8.9 \pm 1.7 \pm 2.2$	5.07	88.8537	-64.1056
SPT-CL J0615-5746	93.957	-57.778	0.972	11.1	$11.5 \pm 1.6 \pm 2.8$	3.12	93.9656	-57.7802
SPT-CL J0628-4143 <sup>5</sup>	97.201	-41.720	0.176	8.1	$10.7 \pm 1.8 \pm 2.9$	10.98	97.2073	-41.7270
SPT-CL J0638-5358 <sup>6</sup>	99.693	-53.974	0.222	11.1	$14.0 \pm 2.0 \pm 4.1$	9.83	99.6882	-53.9731
SPT-CL J0645-5413 <sup>7</sup>	101.360	-54.224	0.167	10.0	$13.0 \pm 1.9 \pm 3.9$	12.23	101.3725	-54.2268
SPT-CL J0658-5556 <sup>8</sup>	104.625	-55.949	0.296	22.0	$23.3 \pm 2.9 \pm 8.1$	9.20	104.6777	-55.9766
SPT-CL J2023-5535 <sup>9</sup>	305.833	-55.590	0.232	14.8	$11.0 \pm 1.8 \pm 2.0$	8.73	305.9069	-55.5697
SPT-CL J2031-4037 <sup>10</sup>	307.960	-40.619	0.342	9.4	$11.9 \pm 1.8 \pm 3.3$	6.55	307.9492	-40.6152
SPT-CL J2106-5844	316.515	-58.744	1.132	22.1	$8.9 \pm 1.4 \pm 1.3$	2.59	316.5194	-58.7412
SPT-CL J2201-5956 <sup>11</sup>	330.462	-59.944	0.098	14.5	$11.8 \pm 2.0 \pm 2.6$	19.11	330.4723	-59.9454
SPT-CL J2248-4431 <sup>12</sup>	342.181	-44.527	0.348	20.7	$22.1 \pm 2.8 \pm 7.3$	7.96	342.1832	-44.5308
SPT-CL J2325-4111 <sup>13</sup>	351.294	-41.194	0.358	7.2	$9.2 \pm 1.6 \pm 2.3$	5.79	351.2988	-41.2035
SPT-CL J2337-5942	354.347	-59.703	0.775	16.8	$8.8 \pm 1.4 \pm 1.0$	3.27	354.3651	-59.7013
SPT-CL J2344-4243	356.176	-42.719	0.595	12.1	$13.7 \pm 1.9 \pm 3.6$	4.55	356.1830	-42.7201

<sup>1</sup>ACT-CL J0102-4915; <sup>2</sup>RXC J0232.2-4420; <sup>3</sup>ABELL S0295, ACT-CL J0245-5302; <sup>4</sup>ACT-CL J0438-5419;  
<sup>5</sup>ABELL 3396, RXC J0628.8-4143; <sup>6</sup>ABELL S0592, RXC J0638.7-5358. ACT-CL J0638-5358; <sup>7</sup>ABELL 3404,  
RXC J0645.4-5413, ACT-CL J0645-5413; <sup>8</sup>Bullet, RXC J0658.5-5556, ACT-CL J0658-5557; <sup>9</sup>RXC  
J2023.4-5535; <sup>10</sup>RXC J2031.8-4037; <sup>11</sup>ABELL 3827, RXC J2201.9-5956; <sup>12</sup>ABELL S1063, RXC J2248.7-4431;  
<sup>13</sup>ABELL S1121; <sup>14</sup>Photometric redshift;

Williamson et al. (2011) reported  $M_{200,\text{mean}}$  and  $M_{500,\text{crit}}$  masses for each cluster. We use the reported  $M_{500,\text{crit}}$  masses and convert them to  $M_{200,\text{crit}}$  (hereafter  $M_{200}$ ), using a Navarro-Frenk-White profile (NFW; Navarro et al., 1997) and a concentration-mass relation from Duffy et al. (2008). Results are shown in Table 5.1 along with the corresponding angular projected radii  $r_{200,\text{crit}}$ , (hereafter  $r_{200}$ ) given assumed cosmology.



### 5.3.3 Optical Imaging

The present cluster sample has been imaged with several instruments and telescopes, and with different goals in mind: from shallow photometry for photometric redshift estimations to deep observations for weak lensing analysis (see Table 5.2 for a list of the telescopes/instruments used). This rendered a heterogeneous dataset. Furthermore, to 'homogenize' the sample we set a common luminosity limit of  $m^* + 2$  (being  $m^*$  the characteristic magnitude of the luminosity function) at  $10\sigma$  for each cluster, re-observing several of them in order to achieve that goal. The data reduction was performed by three different pipelines and they are summarized below.

#### Mosaic2 Imager

The Mosaic2 imager was a prime focus camera on the Blanco 4m telescope until 2012 when it was decommissioned in favour of the new wide field DECam imager. Mosaic2 contained eight  $2048 \times 4096$  CCD detectors. However, one of the amplifiers of one CCD has not worked for the last three years while these observations were carried out. Given the fast optics at the prime focus on the Blanco, the pixels subtend  $0.27''$  on the sky. Total field of view is  $36.8$  arcmin on a side for a total solid angle per exposure of  $\sim 0.4 \text{ deg}^2$ . More details on the Mosaic2 imager can be found in the online CTIO documentation<sup>1</sup>.

The data from the Mosaic2 imager for this analysis is reduced using a development version of the Dark Energy Survey Data Management Pipeline (DESDM) (Desai et al., 2012b). In the DESDM pipeline the data from each night first undergo detrending corrections, which include cross-talk correction, overscan correction, trimming, bias subtraction, as well as fringe corrections for  $i$  and  $z$  bands. Astrometric calibration is done using SCAMP (Bertin, 2006) and using the USNO-B catalog as the astrometric reference. Co-addition is done using SWARP (Bertin et al., 2002). The single epoch images contributing to the coadd are brought to a common zeropoint using stellar sources common to pairs of images. The final photometric calibration of the coadd images is carried out using the stellar color-color locus, with reference to the median SDSS stellar locus (Covey et al., 2007), as a constraint on the zeropoint offsets between neighboring bands, while the absolute calibration comes from 2MASS (Skrutskie et al., 2006).

Mosaic2 data has been acquired over the period of 2005 to 2012, both for the Blanco Cosmology Survey (BCS; Desai et al., 2012b) and for the SPT targeted cluster followup. A detailed description of the image corrections, calibration and typical photometric and astrometric quality appears in Desai et al. (2012b).

#### WFI, IMACS and Megacam

Clusters outside the BCS footprint were observed using various instruments, including WFI, IMACS and Megacam. This study required somewhat deeper imaging than the photometric redshift estimation strategy, so the Wide Field Imager (WFI) on the MPG 2.2-meter telescope at La Silla was used to acquire deeper imaging in B-, V-, R-, and I- filters. The initial imaging from IMACS on Magellan (Dressler et al., 2003; Osip et al., 2008) was typically deep enough to use in this study, so did not require additional observations. We also use g, r, and i band

<sup>1</sup><http://www.ctio.noao.edu/mosaic/manual/index.html>

data acquired with the Megacam imager on Magellan (McLeod et al., 1998) for an ongoing cluster weak lensing program (High et al., 2012, Dietrich et al. in prep).

The processing of the WFI and IMACS data were done with the PHOTPIPE pipeline (Rest et al., 2005; Garg et al., 2007; Miknaitis et al., 2007). WFI data were calibrated in a procedure analogous to the Mosaic2 data. The colors of stars in the science data were matched and calibrated via the Stellar Locus Regression (SLR) technique to a stellar sequence locus generated from a catalog of synthetic stellar spectra from the PHOENIX library (Brott & Hauschildt, 2005). The synthetic stellar locus was calculated in the WFI instrument magnitude system using CCD, filter, telescope, and atmospheric throughput measurements. As with the other data, the absolute calibrations were measured with respect to 2MASS point sources in each field.

The Megacam data reduction was carried out at the Smithsonian Astrophysical Observatory (SAO) Telescope Data Center using the SAO Megacam reduction pipeline, and also calibrated using the SLR technique. See High et al. (2012) for a more detailed description of the observation strategy and data processing.

## FORS2

For four clusters at  $z \geq 0.75$  in this sample, we acquired VLT/FORS2 data. FORS2 imaging in b-, I-, and z-band was obtained for 14 clusters under program Nos. 087.A-0843 and 088.A-0796(A) (PI Bazin), 088.A-0889(A,B,C) (PI Mohr) and 286.A-5021(A) (DDT, PI Carlstrom). Observations were carried out in queue mode and were in clear but not generally photometric conditions. The nominal exposure times for the different bands are 480 s (b), 2100 s (I), 3600 s (z). These were achieved by coadding dithered exposures with 160 s (b), 175 s (I), and 120 s (z). Deviations from the nominal exposure times are present for some fields due to repeated observations when conditions violated specified constraints or observing sequences that could not be completed during the semester for which they were allocated. Data reduction and calibration was performed with the THELI pipeline (Erben et al., 2005; Schirmer, 2013). Twilight flats were used for flatfielding. The I- and z-band data were defringed using fringe maps made with night sky flats constructed from the data themselves. To avoid over-subtracting the sky background, the background subtraction was modified from the pipeline standard as described by Applegate et al. (2012).

The FORS2 field-of-view is so small that only a few astrometric standards are found in the common astrometric reference catalogs. Many of them are saturated in our exposures. While we used the overlapping exposures from all passbands to map them to a common astrometric grid, the absolute astrometric calibration was done using mosaics of F606W images centered on our clusters from the complimentary ACS/HST programs 12246 (PI Stubbs) and 12477 (PI High).

Because data were generally not taken in photometric conditions, the photometric calibration was also carried out using data from the HST programs. We derived a relation between F814W magnitudes and the FORS2 I Bessel filter

$$m_I - m_{F814W} = -0.052 + 0.0095(m_{F606W} - m_{F814W}) ,$$

from the Pickles (1998) stellar library, which is valid for stars with  $(m_{F606W} - m_{F814W}) < 1.7$  mag. After the absolute photometric calibration of the FORS2 I-band from this relation, the relative photometric calibrations of the other bands were fixed using a stellar locus regres-

**Table 5.2:** Optical imagers

Site	Telescope	Aperture (m)	Camera	Filters <sup>a</sup>	Field	Pixel scale ( $''$ )
Cerro Tololo	Blanco	4	MOSAIC-II	<i>griz</i>	$36' \times 36'$	0.27
Las Campanas	Magellan/Baade	6.5	IMACS f/2	<i>griz</i>	$27'.4 \times 27'.4$	0.200
Las Campanas	Magellan/Clay	6.5	Megacam	<i>gri</i>	$25' \times 25'$	0.16
La Silla	2.2 MPG/ESO	2.2	WFI	<i>BVRI</i>	$34' \times 33'$	0.238
Paranal	VLT	8.2	FORS2	<i>b<sub>j</sub>Iz</i>	$6'.8 \times 6'.8$	0.25

**Notes:** Optical and infrared cameras used in SPT follow-up observations.

<sup>a</sup> Not all filters were used on every cluster.

sion in the  $(m_b, m_{F606W}, m_I, m_z)$  color-space. The inclusion of F606W data in this process was necessary because the stellar locus in  $(m_b, m_I, m_z)$  colors has no features.

### 5.3.4 Completeness

In the majority of cases the photometry is complete to a  $10\sigma$  level or better to a depth of  $m^* + 2$  and no correction due to incompleteness is needed. For the small fraction of the sample for which this limit is not reached a correction is applied to enable analysis to a common depth relative to the cluster galaxy characteristic magnitude. The correction follows our previous work in Zenteno et al. (2011): We compare the *griz* count histograms to the deeper Canada-France-Hawaii-Telescope Legacy Survey (CFHTLS, Brimiouille et al., 2008, private communication)<sup>2</sup> by dividing both count histograms. The resulting curve is fit by an error function which is used to account for the missing objects as we approach to the  $m^* + 2$  common depth. All clusters covered by WFI-*BVRI* and VLT-*Iz* bands reach  $m^* + 2$  to a  $10\sigma$  level and no correction is applied in those cases.

## 5.4 Cluster Galaxy Populations: tools

For the following analysis we use the position of the observed brightest galaxy cluster (BCG) as a proxy of the cluster center (coordinates listed in Table 5.1) and its luminosity as a limit on the bright end, to reduce the foreground contamination. The relation between the BCG position and the SPT centre is discussed elsewhere (Song et al., 2012b). Error bars in variables are estimated with  $\chi^2$  statistics, where the confidence limits are defined as constant  $\chi^2$  boundaries (Press et al., 1992).

### 5.4.1 Radial Distribution of Galaxies

While simulations of DM present a consistent and clear picture of the DM density profiles where the concentration shows strong trends with redshift and a weak trends with mass (e.g.,  $c(z) = 5.71 \times (1+z)^{-0.47} (M/M_{\text{pivot}})^{-0.084}$ , Duffy et al., 2008), simulations of subhaloes, where the galaxies are expected to live, are less clear. In DM simulations it is found that the radial distribution of subhaloes is roughly independent of host halo mass and redshift. Also, not many high mass subhalo are found in the core of the host halo as they rapidly loss mass due

<sup>2</sup>count histograms come from the D-1 1 sq. degree patch at  $l = 172.0^\circ$  and  $b = -58.0^\circ$  with a magnitude limit beyond  $r=27$  and a seeing better than  $1.0''$

to dynamical friction and tidal stripping (e.g., Angulo et al., 2009). When baryon physics is included, the cores of the radial profiles steepen as the more tightly bound baryons survive better in the central regions than DM only subhaloes (Nagai & Kravtsov, 2005; Dolag et al., 2009).

On the observational side, no redshift trends have been found to date. Observations of the galaxy distribution have been carried out in clusters with different redshifts and masses. For example, using a local sample of 93 groups and clusters with masses in the  $3 \times 10^{13} M_{\odot} - 2 \times 10^{15} M_{\odot}$  range, and at  $z < 0.06$ , Lin et al. (2004, hereafter L04) found a concentration of  $c_{g,200c} = 2.9^{+0.21}_{-0.22}$  with no evidence of a mass dependence. At a higher redshift,  $0.15 \leq z \leq 0.4$ , Budzynski et al. (2012) found  $c_{g,200c} \approx 2.6$  independently of both cluster mass and redshift, using 55,121 groups and clusters from the SDSS-DR7.

Muzzin et al. (2007a), using 15 CNOC clusters at  $0.19 < z < 0.55$ , found a concentration of  $4.13 \pm 0.57$ . At a much higher redshift ( $z \approx 1$ ), Capozzi et al. (2012), using 15 clusters with an average mass of  $M_{200} = 3.9 \times 10^{14} M_{\odot}$ , found a concentration of  $c_{g,200c} = 2.8^{+1.0}_{-0.8}$ , completely consistent with the lower redshift cluster samples.

Those results point to no evolution in the concentration up to a redshift of 1. We use the SPT-SZ selected sample to test this picture using a uniformly selected sample over a broad redshift range.

The radial surface density profiles are constructed extracting both all and red galaxies up to a projected radius of  $3r_{200}$  (when possible). Red galaxies are selected if their colour lies within a  $\pm 3\sigma (\pm 0.22)$  range around the predicted red sequence for that redshift (López-Cruz et al., 2004, see § 5.5.2 for details).

The radial binning is done in two ways, depending on how the data are combined and fitted. One configuration is used if the fit is done over the stacked profile of all clusters, and another if a simultaneous fitting on multiple individual profiles (multi-fit hereafter) is performed. The principle behind both choices is that the number of galaxies per radial bin should be high enough for  $\chi^2$  statistics to be valid, which we chose to be  $\gtrsim 15$  members. For the multi-fit method, which involves fitting multiple individual cluster radial profiles, we bin the data in  $0.05 \times r_{200}$  with the first bin and bins beyond  $r_{200}$  twice as wide. For the stacked case, in which the individual cluster bins can be much finer, we use bins of  $0.02 \times r_{200}$  size with the first one twice as wide and the background counterpart beyond  $r_{200}$  being 5 times larger. The stacking of data using this binning is shown in Fig. 5.2.

As in Zenteno et al. (2011), we have masked the saturated stars in the field and corrected for the effective area covered. This is done by gridding the data within a radial bin tangentially using an angular bin of 2 degrees (i.e. dividing the radial bin into 180 tangentially arranged bins). Bins that fall within masked areas are discarded from the radial area calculation. Also, as a quality control, if two thirds or more of the area of the ring is lost then the bin is discarded. This typically happens at the detector edges.

To compare with previous studies we fit a projected NFW profile to our radial distribution. This density is modeled as the number of galaxies in a cylinder within rings divided by the ring area. This number can be described analytically integrating the NFW profile along the line of sight (e.g., Bartelmann, 1996):

$$N_{\text{cyl}}(r) = 4\pi\rho_s r_s^3 f(x) \quad (5.1)$$

$$f(x) = \begin{cases} \ln \frac{x}{2} + \frac{2}{\sqrt{x^2-1}} \arctan \sqrt{\frac{x-1}{x+1}} & \text{if } x > 1, \\ \ln \frac{x}{2} + \frac{2}{\sqrt{1-x^2}} \operatorname{arctanh} \sqrt{\frac{1-x}{x+1}} & \text{if } x < 1 \\ \ln \frac{x}{2} + 1 & \text{if } x = 1 \end{cases}$$

where  $\rho_s$  is the central density,  $r_s = r_{200}/c_g$  is the scale radius,  $r_{200}$  the radius at which the cluster density reach  $200 \times \rho_{\text{crit}}$ ,  $c_g$  is the galaxy concentration and  $x = c_g r / r_{200}$ . We can parametrize this as a function of the number of galaxies within a cylinder of  $r_{200}$  radius:

$$N_{\text{cyl}}^{r_{200}} = 4\pi\rho_s r_s^3 f(c_g).$$

Combining this with Eq. 5.1 we can write the projected profile as a function of  $N_{\text{cyl}}^{r_{200}}$ , the projected number of galaxies within  $r_{200}$ :

$$N_{\text{cyl}}(r) = N_{\text{cyl}}^{r_{200}} \frac{f(x)}{f(c_g)} \quad (5.2)$$

Thus, in the end we fit  $c_g$ ,  $N_{\text{cyl}}^{r_{200}}(M)$  plus a flat background  $N_{\text{bkg}}$  to our data. Note that even if all cluster galaxy distributions had the same shape, we would still expect the number of galaxies within the virial region  $N_{\text{cyl}}^{r_{200}}(M)$  to exhibit a cluster mass dependence.

Due to the heterogeneity of our optical imaging dataset we have radial profiles extending from one to several  $r_{200}$ , and it is not possible to define a region for background estimation that is uncontaminated by the cluster. We approach this problem in two ways: (1) we simply discard the background information and combine the data over the region where all clusters have coverage ( $\sim 1r_{200}$ , see Fig. 5.2) and (2) we fit simultaneously all clusters making use of the common NFW shape parameters while marginalising over individual cluster backgrounds. That is, we fit each cluster by fixing a common  $c_g$  and  $N_{\text{cyl}}^{r_{200}}$  but marginalizing over the individual cluster background  $N_{\text{bkg}}$ . While in the former case the  $\chi_{\text{stack}}^2$  comes from the single fit, in the latter the stack  $\chi_{\text{stack}}^2$  is calculated as the sum of the individual cluster  $\chi_i^2$  contributions. Errors are reported as the projection of the  $1\sigma$  contour for 1 parameter ( $\Delta\chi_{\text{stack}}^2 = 1$ ) for  $c_g$  and  $N_{\text{cyl}}^{r_{200}}$ .

Although the mass range in the current sample is small there are mass dependencies which need to be accounted for at the stacking and multi-fit processes. We do this by varying  $N_{\text{cyl}}^{r_{200}}$  from Eq. 5.2 as a function of the cluster mass  $M$  in the following way:

$$N_{\text{cyl}}^{r_{200}}(M) = N_{\text{cyl,piv}}^{r_{200}} \left[ \frac{M}{M_{\text{piv}}} \right]^\gamma$$

where  $\gamma = 0.87$  (L04) and the pivotal mass  $M_{\text{piv}} = 10^{15} M_\odot$ .

### 5.4.2 Luminosity Function

As galaxy clusters grow by accreting galaxies from the cosmic web over time, these galaxies are also transformed by processes such as merging and ram pressure stripping, formation of new stars and the ageing of their stellar populations (e.g., Dressler, 1980; Butcher & Oemler, 1984; Lin et al., 2004; Lopes et al., 2013; Gu et al., 2013). The evolution of the cluster luminosity function encodes information about these physical processes and is therefore an important tool. For example, by studying the bright end of the cluster LF, which is dominated

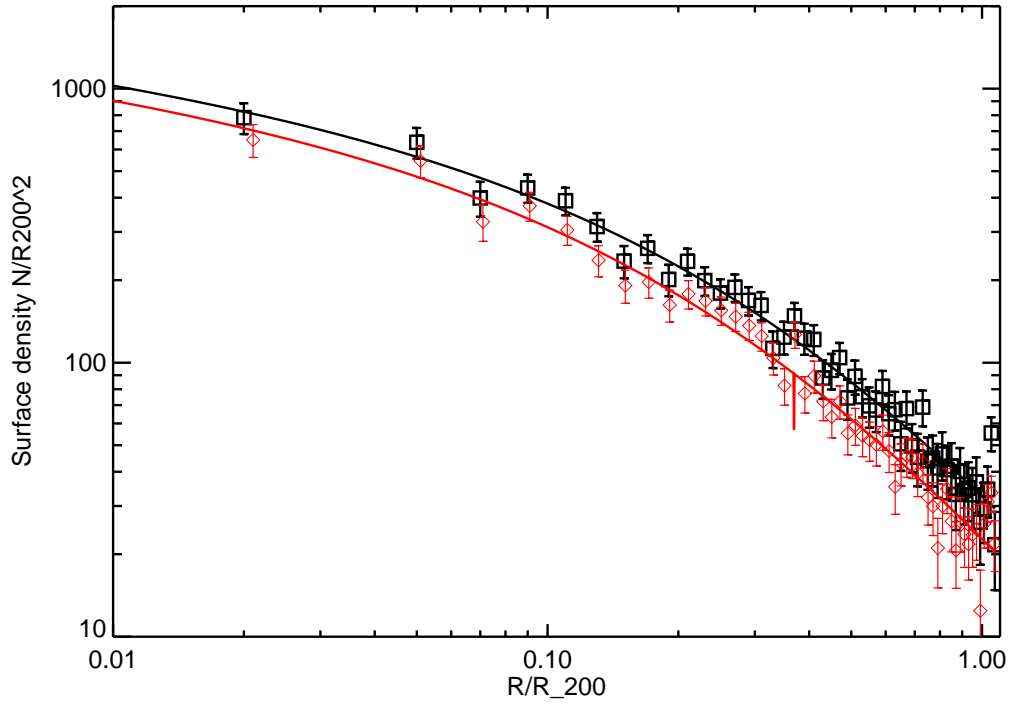


**Figure 5.2:** Radial profile of the stacked sample up to  $r_{200}$ , using all galaxies (black) and red sequence galaxies (red). These profiles are well fit by NFW profiles with concentrations of  $2.25 \pm 0.33$  and  $2.71^{+0.38}_{-0.33}$ , respectively.

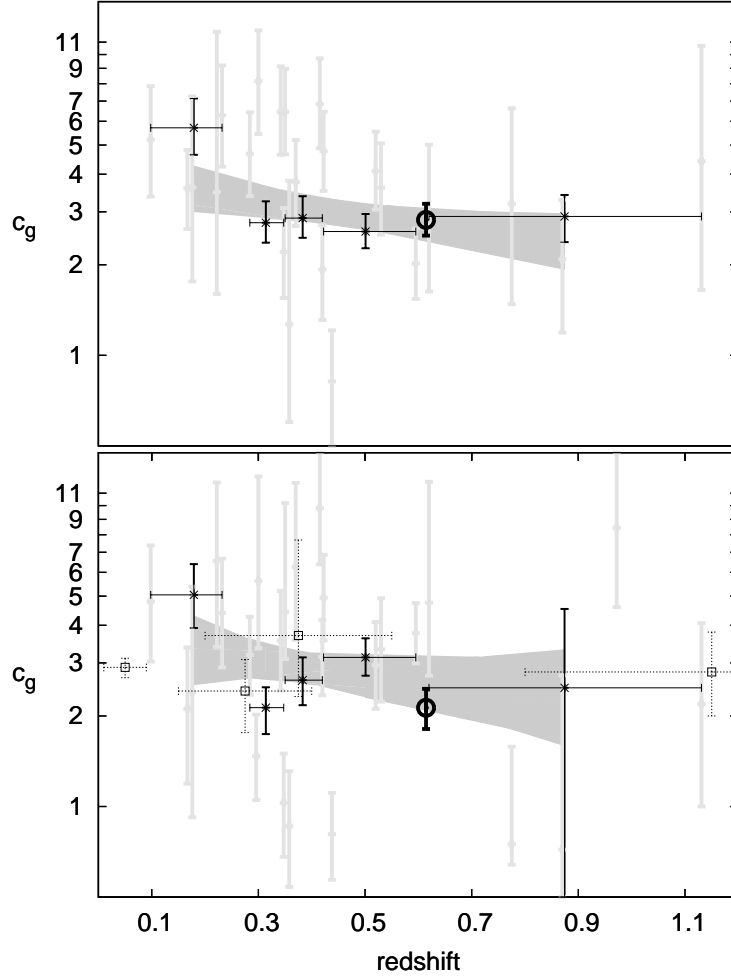


**Figure 5.3:** Cluster NFW concentration parameter evolution for red sequence selected galaxies (top panel) and all galaxies (bottom panel) within projected  $r_{200}$ . In grey points are the individual cluster fits, and the five black points are the concentrations found by simultaneously fitting to ensembles of 5 clusters each. The central open circle corresponds to the concentration extracted from the fit of the stacked sample up to  $r_{200}$  (see Fig. 5.2). There is no evidence for redshift evolution in the total sample given a slope of  $-0.80 \pm 1.05$ , and some preference for a redshift evolution of the red subsample given the slope of  $-0.87 \pm 0.53$ .

by luminous early-type galaxies, several studies have shown that the evolution is consistent with a passively evolving stellar population (e.g., de Propris et al., 1999; Lin et al., 2006; Andreon et al., 2008; Capozzi et al., 2012), independent of the cluster dynamical state (De Propris et al., 2013). This indicates that the cluster galaxies have their stellar component in place at high redshift ( $z \gtrsim 2 - 3$ ; e.g., Mancone et al., 2010).

The individual cluster LF is constructed using sources within a projected  $r_{200}$ , centered on the BCG. We perform a statistical background subtraction (using background region at  $r > 1.5r_{200}$ ) to an  $m^* + 2$  depth or even deeper. In general, we make use of the photometry up to a  $10\sigma$  level. The projected, background-corrected LF is then de-projected using an NFW profile with a concentration of  $c_{\text{corr}} = 2.66$ , which corresponds to the weighted mean value of the multi-fit solutions in Fig. 5.3 (bottom panel). Finally, the cluster LF is divided into the different magnitude bins and scaled by the cluster volume in Mpc.

Corrections due to masked regions and background over-subtraction are applied here as well. In the case of masked regions within  $r_{200}$  we correct for the missing cluster galaxies using the NFW profile with the concentration  $c_{\text{corr}}$ . Also, using the same model, we correct for the over subtraction due to cluster galaxies contaminating the background dominated region. This oversubtraction can be expressed by an extra term  $N_{\text{clus,true}}^{>1.5r_{200}}$  in the background:

$$N_{\text{clus,obs}}^{r_{200}} = N_{\text{total}}^{r_{200}} - A_N \times (N_{\text{back}}^{>1.5r_{200}} + N_{\text{clus,true}}^{>1.5r_{200}}) \quad (5.3)$$

where  $A_N$  is the area normalization between cluster and background. Under the assumption that there is no luminosity segregation and that the galaxy distribution is well described by an NFW model with a given concentration, we can connect the oversubtraction to the galaxies within  $r_{200}$  as  $N_{\text{clus,true}}^{>1.5r_{200}} = \alpha(c_g) N_{\text{clus,true}}^{r_{200}}$ . Combining with Eq. 5.3 we have a correction:

$$N_{\text{clus,true}}^{r_{200}} = \frac{N_{\text{clus,obs}}^{r_{200}}}{(1 - A_N \times \alpha(c_g))}.$$

Finally, four of the clusters have only imaging from VLT/FORS with a FOV of  $7' \times 7'$ , covering less than  $1.5r_{200}$ . On those cases the background area is re-defined as the area at  $r > r_{200}$ . For two of these clusters, SPT-CLJ2337-5942 and SPT-CLJ0615-5746, at  $z = 0.775$  and  $0.972$  respectively, the correction is of the order of  $\sim 48\%$  while for the rest of the sample the correction is around  $\sim 12 \pm 4\%$ .

Once the LF is constructed we fit it by the three parameter Schechter function (SF) (Schechter, 1976),

$$\phi(m) = 0.4 \ln(10) \phi^* 10^{0.4(m^* - m)(\alpha + 1)} \exp(-10^{0.4(m^* - m)}).$$

We fit the SF to the stack and the individual luminosity functions. In the single cluster case, simulations show that there is little constraint on  $m^*$  if the three variables are allowed to float within our typical luminosity range (see §5.4.4), so our approach is to extract the parameters  $\phi^*$ ,  $m^*$  and  $\alpha$  by fixing one parameter and leaving the other two to float. Specifically, for the  $m^*$  evolution analysis, we fix  $\alpha$ .

For the stacked LF we fit all three parameters. We bring the data to a common frame fitting in the space of  $m - m_{\text{mod}}^*$ , using a Simple Stellar Population model (see § 5.5.2 for details). Once the data are brought to this common frame, they are stacked using an inverse variance



weighted average:

$$N_j = \frac{\sum_i N_{ij}^{z=0} / \sigma_{ij}^2}{\sum_i \sigma_{ij}^2} \quad (5.4)$$

where  $N_{ij}^{z=0}$  is the number of galaxies per volume per magnitude at redshift zero, in the  $j$ th bin corresponding to the  $i$ th cluster's LF and  $\sigma_{ij}$  is the statistical poisson error associated. We obtain  $N_{ij}^{z=0}$  by correcting it by the evolutionary factor  $E^2(z)$ , where  $E(z) = \sqrt{\Omega_m(1+z)^3 + \Omega_\Lambda}$ . This scaling is appropriate for self-similar evolution where the characteristic density within the cluster virial region will scale with the critical density of the universe.

The errors of the stacked profile are computed as

$$\delta N_j = \frac{1}{(\sum_i \sigma_{ij}^2)^{1/2}}$$

We adopt  $\alpha$  from the stacked LF for the evolution study of the single cluster characteristic magnitudes  $m^*$ .

### 5.4.3 Simple Stellar Population Models

Several studies have shown that  $m^*$  evolution can be well described by a passively evolving stellar population that has formed at high redshift (de Propris et al., 1999; Andreon, 2006; Lin et al., 2006; De Propris et al., 2007; Mancone et al., 2010; De Propris et al., 2013). Empirically, these Simple Stellar Population (SSP) models have been used to predict red sequence colours that are then used to estimate cluster redshifts with characteristic uncertainties of  $\delta z \sim 0.025$  (e.g., Song et al., 2012a,b). Generally speaking, in an analysis of cluster galaxy populations over a broad redshift range it is helpful to have a model within which the evolution and  $k$ -corrections are self-consistently included to simplify the comparison of cluster populations at different redshifts within the observed bands.

In this analysis we create red sequence models for Mosaic2 and Imacs *griz*, WFI *BVRI*, and VLT *BIz* bands using the Bruzual & Charlot (2003) SSP models and the EzGal python interface (Mancone & Gonzalez, 2012). The models consist of an exponentially falling star formation rate with a decay time of 0.4 Gyr, Salpeter IMF and a formation redshift of 3. We use in total 6 different metallicities to introduce the tilt in galaxy red sequence within the color-magnitude space. To calibrate these models we adopt the measured metallicity-luminosity relation for Coma cluster galaxies (Poggianti et al., 2001). This procedure then requires a further adjustment of the luminosity to reproduce the observed colour of an  $L^*$  Coma galaxy.

This calibrated set of SSP models allows us to predict the apparent magnitudes and colours of all our cluster populations within the range of relevant observed bands. As described in § 5.5 below, by using the full sample of clusters we can test whether this set of models is consistent with the real galaxy populations. We find that the models are  $\sim 0.2$  magnitudes fainter than the populations at all redshifts. To account for this, we brighten the normalisation of our models by this amount to bring them into agreement with the data.

### 5.4.4 Simulated Catalogs

To test our methods, find the best stacking strategy and quantify possible biases, we create simulated catalogs of a typical cluster to analyse them. We re-create a galaxy cluster using

the number of galaxies in a cluster of mass  $M_{200} = 1.3 \times 10^{15} M_{\odot}$ , given the expected number of galaxies from measurements of the halo occupation number (HON at low redshift, L04) and with a concentration of 3 over a typical angular region on the sky. This corresponds to a spherical number of galaxies, within  $r_{200}$  and up to a magnitude of  $m^* + 3$ , of  $N_{\text{sph}}^{r_{200}} = 335$  and its projected value  $N_{\text{cyl}}^{r_{200}} = 443$ . Although  $m^* + 2$  is our typical depth we extend the cluster counts to  $m^* + 5$  for testing purposes. No luminosity segregation is included. We assign galaxy magnitudes to match an LF with  $\alpha = -1.2$  and  $m^* = m_{\text{model}}^*(z = 0.35)$ , while  $\phi^*$  is set by  $N_{\text{sph}}^{r_{200}}$ . The number of background galaxies used corresponds to 45,000 sources in the  $m^* - 3$  to  $m^* + 5.5$  luminosity range with a brightness distribution equivalent of the CFHTLS r-band count histogram used in § 5.3.4. The construction of the radial profiles and luminosity functions are done using the same tools as for the real clusters, accounting for masked areas due to CCD gaps, stars and missing CCDs.

As we mention in § 5.4.1, the multi-fit stack approach uses a typical bin size of  $0.05r_{200}$ , while the first bin and the bins beyond  $1r_{200}$  are twice as wide. This configuration is chosen to balance a good number of galaxies ( $\gtrsim 15$ ) per bin with the need to have narrow enough bins to be able to constrain  $c_g$ . We fit for  $c_g$  and  $N_{\text{cyl}}^{r_{200}}$  and marginalize over each individual cluster background. We demonstrate that with multi-fit fitting on 5 clusters using the region extending up to  $3r_{200}$  over 20 realizations, the concentration is recovered within  $1\sigma$  ( $3.09 \pm 0.09$ ).

Another way to use the data is to stack the cluster data up to a common maximum radius. For the current sample this is reached at  $\sim 1r_{200}$  (set by the lowest redshift cluster). As in this case there are more galaxies per bin than in the single cluster case, this gives us the chance to explore finer bins and test that our results are not biased due to the chosen bin size. We use a finer bin set of 0.04, 0.02 and  $0.1r_{200}$  for the first bin, the bins below  $r_{200}$  and the bins at  $> r_{200}$ , respectively. Simulations show that in the case of 25 clusters in the stack, the input concentration is recovered within  $1.5\sigma$  ( $3.62^{+0.48}_{-0.41}$ ). As comparison, when the same data are stacked up to  $3r_{200}$ , the input values are recovered well within  $1\sigma$ .

Using the multi-fit stack binning configuration, we also test the individual results. Fitting for the radial profile parameter  $c_g$ ,  $N_{\text{cyl}}$  and background in each individual simulated cluster, over the 100 realizations, the weighted mean of the concentration is recovered well within  $1\sigma$  ( $c_g = 2.97 \pm 0.12$ ) of the input  $c_g$ . These tests give us confidence that our binning strategy and our scripts are suited for use in extracting measurements of the concentration of the galaxy clusters in this study with biases that are at or below the statistical uncertainty.

In the case of the Luminosity Function, we use and apply the configuration and corrections described in § 5.4.2 (0.5 mag bin, count correction due to background over subtraction, star-masked areas, CCD gaps, etc.) to test our scripts and assess the level of bias and or scatter under this configuration.

Simulations demonstrate that simultaneously fitting all three SF parameters shows that only weak constraints on  $m^*$  are possible, given that the typical depth pushes to  $m^* + 2$ . To overcome this we fix one of the three parameter and explore the other two: when  $\alpha$  is fixed the weighted mean value recovered for  $m^*$  is within  $1.6\sigma$ . Conversely, if  $m^*$  is fixed,  $\alpha$  is recovered well to within  $1\sigma$ . In the case of the HON, when  $m^*$  is fixed, the true HON is recovered to  $0.6\sigma$  and to  $3.2\sigma$ s when  $\alpha$  is the variable fixed to the input value. Accordingly our first choice is to fix  $m^*$  when studying the HON.

## 5.5 Results

### 5.5.1 Radial Profile

The composite profiles for the full and red sequence selected galaxies in the full sample of clusters are shown in Fig. 5.2. The lines trace out the best fit NFW profiles, which provide a good description of the stacked galaxy profiles in both cases. The best fit concentration for the red galaxy sample is  $2.71^{+0.38}_{-0.33}$ , which is higher than that for the total population  $2.25 \pm 0.33$ . The higher concentration for the red subsample is consistent with the radial variations of red fraction found in optical studies of other cluster samples (e.g., Goto et al., 2004; Verdugo et al., 2012; Ribeiro et al., 2013; Gruen et al., 2013a).

Our measured concentration for the full sample  $2.25 \pm 0.33$  is somewhat lower when compared to previous estimates  $2.9^{+0.21}_{-0.22}$  at redshift zero (L04) and  $2.8^{+1.0}_{-0.8}$  at  $z \sim 1$  (Capozzi et al., 2012). Given the high masses of our sample, one may wonder if the differences reflect a mass dependence in the concentration. While in DM simulations more massive halos have lower concentration, the same simulations do not show such trend with galaxies. Some analyses have shown a steep inverse mass dependence with concentration (Hansen et al., 2005) although the Budzynski et al. (2012) study, which included many of the same clusters, found no such trend. They attribute the difference to different approaches in defining the radius in the two studies. A further study, with a sample with a larger mass range, is required to confirm whether a mass-concentration trend relation really exists.

The measure concentration as a function of redshift for the SPT sample is shown in Fig. 5.3. The individual cluster fits are shown in light grey, pointing to an mild evolution in the concentration when red galaxies are used (top panel) and no apparent evolution when all galaxies are selected (bottom panel). The multi-fit over five bins with five clusters in each bin confirms this picture. Special care is given to the last bin at  $z \geq 0.6$  as the individual cluster concentrations show somewhat larger scatter. Furthermore, in the red sequence galaxy sample, four of the five individual cluster fits show a similar concentration of  $\sim 2$ , while the concentration for the remaining cluster SPT-CLJ0615-5746 is beyond 20, which is bringing the mean concentration up. In the case of all galaxies SPT-CLJ0615-5746 has a slightly lower concentration. Nevertheless, the highest redshift bin contains clusters with a larger scatter in concentration.

A closer inspection of SPT-CLJ0615-5746 profile shows that it is fairly flat after  $r > 0.5r_{200}$  and the few points inside that region show almost no regular behavior. A visual inspection of the BCG (center position) confirms it as a secure identification close to the SZE center. A single anomalous result, such as a SPT-CLJ0615-5746, could bias a result. To explore this we use the jackknife method to evaluate the bias and the error of the last bin, finding the red (all) population concentration change from  $3.76^{+1.29}_{-0.91}$  ( $2.79^{+0.85}_{-0.68}$ ) to  $3.42 \pm 0.82$  ( $2.90 \pm 1.75$ ). Fitting a slope and intercept to the full sample and red subsample we find  $c_{g,\text{all}} = 3.80^{+1.44}_{+1.10} \times (1+z)^{-0.80 \pm 1.05}$  and  $c_{g,\text{red}} = 4.07^{+0.93}_{+0.67} \times (1+z)^{-0.87 \pm 0.53}$  which is consistent with no evolution within  $1\sigma$ . Also, the result from the stack over all redshifts is consistent with this formula, as expected.

### 5.5.2 Luminosity Function

Several studies have found that the steepness of the faint end depends on the band chosen (e.g., Goto et al., 2002, 2005), as bluer than the  $4000\text{\AA}$  are more sensitive to younger population. We

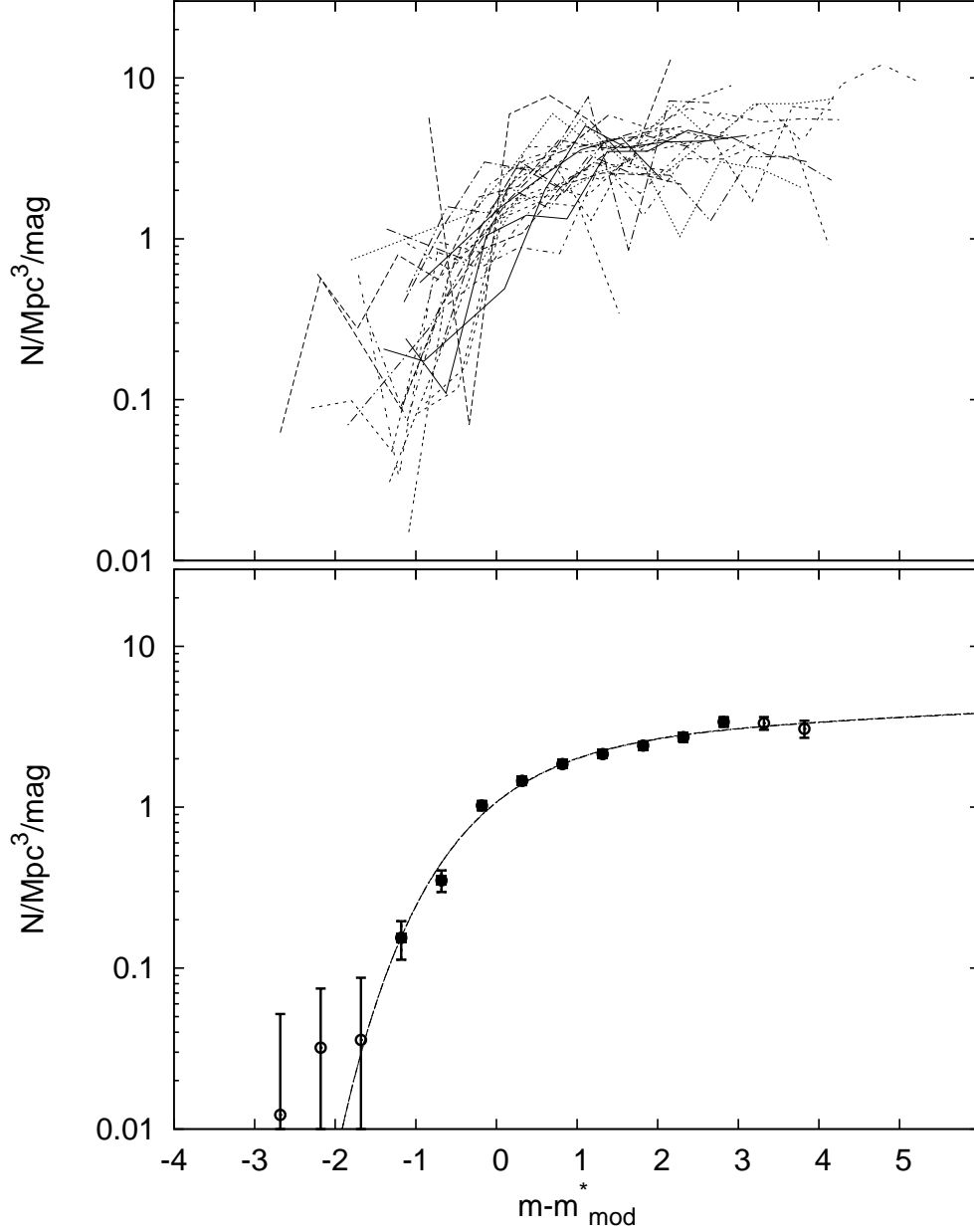


**Figure 5.4:** We plot 24 of the 26 individual LFs (top) versus  $m - m_{\text{mod}}^*$ , where  $m_{\text{mod}}^*$  is the predicted SSP characteristic luminosity at the redshift of the cluster. Each individual LF is extracted using the band redward of the 4000Å break. The two excluded clusters included the lowest redshift system where our imaging is not adequate and another system that has a foreground star field, making it difficult to identify the faint galaxy population. The weighted averaged luminosity function appears below. Filled squares are bins with ten or more contributing clusters, and open squares are bins with at least two contributing clusters. The fit for the stack is  $\phi^* = 3.01^{+0.26}_{-0.24} \text{ Mpc}^{-3} \text{ mag}^{-1}$ ,  $\alpha = -1.06^{+0.04}_{-0.01}$ , and  $m - m_{\text{mod}}^* = -0.05^{+0.09}_{-0.08} (\chi^2_{\text{red}} = 1.29)$ .

systematically select the closest band redward of the 4000Å, and are therefore less sensitive in our study to recent star formation. This mean that our band selection criteria follows this rules: *r*-band for  $0 < z \leq 0.35$ , *i*-band for  $0.35 < z \leq 0.70$ , *z*-band for  $z > 0.70$ . In the case of *BVRI* the conditions were *V*-band for  $0 < z < 0.20$ , *R*-band for  $0.20 < z < 0.40$  and *I*-band for  $z > 0.40$ . For the four clusters with VLT data ( $z \geq 0.7$ ),  $z_{Gunn}$  was used.

### Stacked Luminosity Function

For the stacked LF we use 24 clusters. The two excluded clusters are SPT-CL J2201-5956 which, with a  $z = 0.098$  and  $1.5 \times 10^{15} M_{\odot}$  mass, has a projected  $r_{200}$  outside of the field-of-view, making it all but impossible to estimate the background contribution, and SPT-CLJ0555-6406, which has a star field as a foreground that makes the cluster normalization unreliable.

As we mentioned in § 5.4.4, fitting all three variables in the LF produces large errors in the parameter exploration. To approach this problem, in the following sections we use  $m^*$  from the model or  $\alpha$  from the stacked LF to explore the other parameters. In spite of the large errors during 3 parameter SF fits, we need at minimum to check that the  $m^*$  evolution is consistent with our passively evolving SSP model. Doing this we find that a linear fit to the observed  $m^*$  distribution as a function of redshift has a zero point of  $-0.06 \pm 0.33$  and a slope of  $-0.55^{+1.00}_{-1.01}$ . That is, the normalisation of our model is consistent to within the uncertainties with the data, and the dataset over this broad range of redshift provides no evidence for a deviation from the model.

We proceed to stack the Luminosity Function using the model  $m^*$  to bring all clusters to the same relative reference frame of  $m - m_{\text{mod}}^*$ . At last, we combine the data using the weighted average in each bin (see Eq. 5.4). The stacked LF, as well as the individual LFs, for all galaxies are shown in Fig. 5.4. The open points on the faint end are those that contain contributions from at least two clusters, and the filled points contain contributions from at least ten clusters.

The fit to the stacked LF yields

$$\begin{aligned}\phi^* &= 3.01^{+0.26}_{-0.24} \text{ Mpc}^{-3} \text{ mag}^{-1} \\ \alpha &= -1.06^{+0.04}_{-0.01} \\ m - m_{\text{mod}}^* &= -0.05^{+0.09}_{-0.08}\end{aligned}$$

with a reduced  $\chi^2_{\text{red}} = 1.29$  when all data points in Fig. 5.4 are used, and when only the filled points (contributions from more than ten clusters) are used the results are  $\phi^* = 2.98^{+0.36}_{-0.31} \text{ Mpc}^{-3} \text{ mag}^{-1}$ ,  $\alpha = -1.06^{+0.05}_{-0.04}$ , and  $m - m_{\text{mod}}^* = -0.06^{+0.11}_{-0.10}$  ( $\chi^2_{\text{red}} = 2.16$ ). As the results are indistinguishable, we adopt the fit to all points as our fiducial values.

Our best fit faint end  $\alpha$  for these SZE selected clusters spanning a large range of redshift is consistent with measurements using variously selected samples at different redshifts (e.g., Gaidos, 1997; Paolillo et al., 2001; Piranomonte et al., 2001; Barkhouse et al., 2007; Popesso et al., 2005), with  $\alpha = -1.09 \pm 0.08$ ,  $-1.11^{+0.09}_{-0.07}$ ,  $-1.01^{+0.09}_{-0.07}$ ,  $-1$ , and  $-1.05 \pm 0.13$ , respectively.  $\phi^*$  is also in agreement with previous work. L04 found a best fit for their data of  $\phi^* = 4.43 \pm 0.11 h_{70}^3 \text{ Mpc}^{-3}$  for  $\alpha = -0.84 \pm 0.02$  (best fit), but found a lower  $\phi^* = 3.00 \pm 0.04 h_{70}^3 \text{ Mpc}^{-3}$  when  $\alpha$  is fixed to  $-1.1$ , noting that both  $\alpha$ 's described well their data. As our stacked LF points to a  $\alpha = -1.06^{+0.04}_{-0.01}$  we are within their range of values. As our systems are more massive and the slope of the HON is less than unity it is expected that our  $\phi^*$  solution would

be lower than that measured for lower mass systems. L04 also explore this possibility, using their 25 most massive systems, with mean mass of  $5.3 \times 10^{14} M_{\odot}$  finding  $\alpha = -0.84 \pm 0.03$  and  $\phi^* = 4.00 \pm 0.16 h_{70}^3 \text{ Mpc}^{-3}$ . Given the dependence of  $\alpha$  and  $\phi^*$  shown and the mass range, that result using a redshift zero sample of clusters and 2MASS photometry is consistent with our result.

### Evolution of $m^*$

Several previous studies have shown that the evolution of  $m^*$  for cluster galaxy populations can be described by a passively evolving stellar population formed at high redshift (de Propris et al., 1999; Andreon, 2006; De Propris et al., 2007; Lin et al., 2006; Mancone et al., 2010; De Propris et al., 2013). We test this result by fitting the LF using  $m^*$  and  $\phi^*$  as free parameters while fixing  $\alpha$  to the measurement from the stack. We compare the the obtained  $m^*$  to a Simple Stellar Population models (SSP) model that is produced as describe in Sec. 5.4.3 above.

In panel (a) of Fig. 5.5 we show a comparison between the observed  $m^*$  and our SSP model. From this figure and the  $1\sigma$  (grey) area, it is clear that the data and our SSP model is in good overall agreement. A linear fit with redshift yields an intercept of  $-0.05^{+0.12}_{-0.12}$  and a slope of  $-0.15^{+0.26}_{-0.27}$ . Thus, our SSP model of an exponential burst of star formation at  $z=3$  with a decay time of 0.4 Gyr and a Salpeter IMF tuned with a range of metallicities to reproduce the tilt of the red sequence population at low redshift provides a good description of the evolution of the cluster galaxy populations over a broad range of redshift. It is important to emphasize that our  $m^*$ 's are extracted from the band that is just redward of the 4000 Å break, a band that would be expected to be rather insensitive to recent star formation.

### Evolution of $\phi^*$

The LF normalization  $\phi^*$  is the number of galaxies per  $\text{Mpc}^3$  per unit magnitude, and it informs us, once the universal evolution of the critical density is scaled out, about possible evolution of the number density of galaxies near the characteristic magnitude in cluster environment. In our study we are using the SZE data to give us the cluster mass  $M_{200}$ , the mass within the region of the cluster that has a mean density that is 200 times the critical density. Because the critical density evolves with redshift as  $\rho_{\text{crit}} \propto E^2(z)$  where  $H(z) = H_0 E(z)$ , we expect to see a higher characteristic galaxy density at high redshift. Thus, to explore for density evolution beyond this we examine measurements of  $\phi^*/E(z)^2$  in the case where  $\alpha$  comes from the stacked LF and in the case where  $m^*$  comes from the SSP model. Results appear in panel (c) in Fig. 5.5. By fitting a linear relation for both sets of measurements ( $m^*$  model,  $\alpha$  fixed to stack value) we find best fit parameters  $2.63^{+0.21}_{-0.20}/2.96^{+0.19}_{-0.19}$  and  $0.00^{+0.46}_{-0.46}/-0.24^{+0.44}_{-0.45}$ , respectively. Both cases are consistent with no evolution at  $1\sigma$ .

As it has been already mentioned in § 5.5.2 our LF normalization is consistent with values in the low redshift regime when accounting the high masses of our clusters. At high redshift this is among the first study of its kind. Our approach to studying the characteristic galaxy density  $\phi^*$  requires good mass estimates, and until recently these were not available at redshifts  $z \sim 1$ .

### Evolution of the Faint End Slope $\alpha$

The redshift evolution of the faint end slope  $\alpha$  for all galaxies is shown in Panel (b) of Fig. 5.5. It can be seen that  $\alpha$  changes to less negative values at higher redshift with  $2\sigma$  significance.

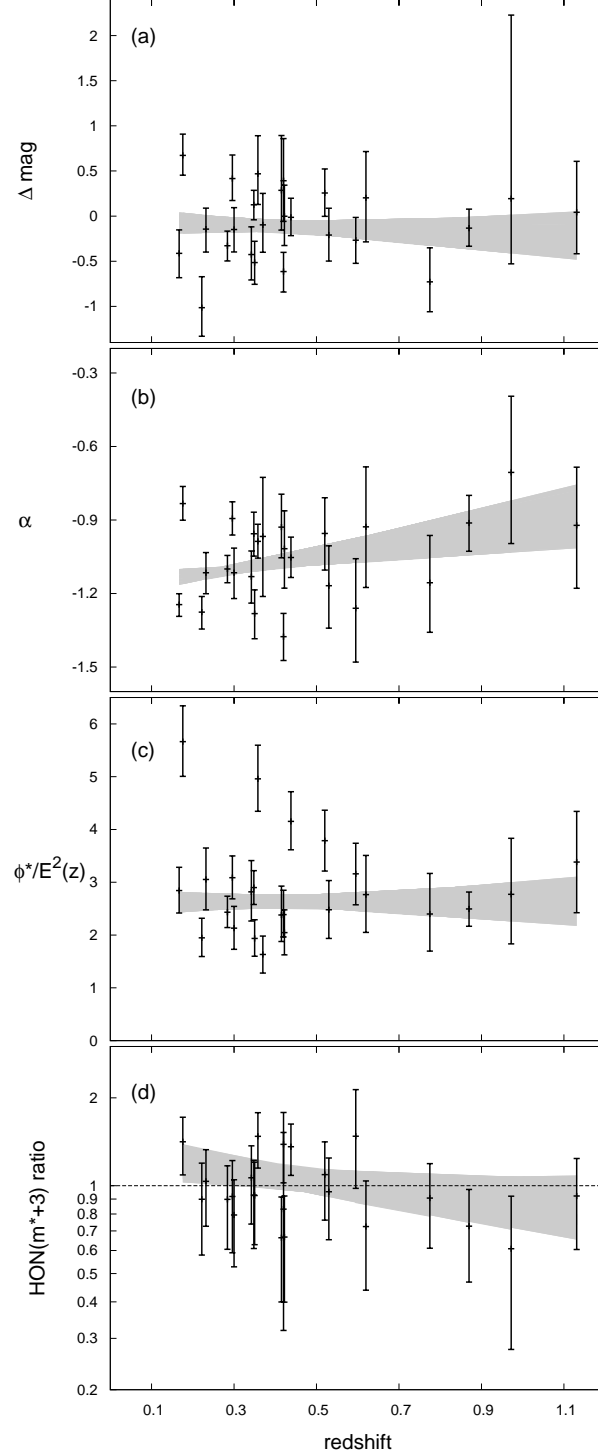


**Figure 5.5:** LF parameter evolution with redshift. As noted before, the LFs are extracted using the band redward of the  $4000\text{\AA}$  break. We fit a line in each case, marking the allowed  $1\sigma$  region. *Panel (a):* There is no significant evolution in  $\Delta \text{mag} = (m_{\text{mod}}^* - m^*)$ , indicating the SSP model provides a good description of cluster galaxies over this redshift range. *Panel (b):* Evolution of  $\alpha$  is suggested by the data with best fit line having intercept  $-1.17^{+0.04}_{-0.04}$  and slope  $0.25^{+0.11}_{-0.11}$ . *Panel (c):*  $\phi^*/E^2(z)$  extracted using fixed  $m^*$  does not evolve with redshift. *Panel (d):* Ratio of HON from this work and the redshift independent L04 prediction. Slope and intercept are found to be  $-0.60^{+0.48}_{-0.47}(0.3)$  and  $0.12^{+0.07}_{-0.08}(0.17)$  at  $1(2)\sigma$  respectively, which indicate a mild evolution where  $z = 1$  clusters have typically 30% fewer galaxies than their low redshift counterparts of the same mass.

That is, there are fewer low luminosity cluster galaxies relative to high luminosity cluster galaxies at high redshift than in the local Universe. The best fit linear relation has intercept  $-1.17^{+0.04}_{-0.04}$  and slope  $0.25^{+0.11}_{-0.11}$ .

Comparing with low- $z$  Abell Clusters, in bands redward of the  $4000\text{\AA}$ , we find a consistent picture. For example, Gaidos (1997) observed 20 Abell Clusters in the R-band obtaining  $\alpha = -1.09 \pm 0.08$ . Paolillo et al. (2001) constructed the LF using 39 Abell Clusters and found  $\alpha = -1.11^{+0.09}_{-0.07}$ , in Gunn r-band. Barkhouse et al. (2007) studied 57 Abell Clusters, in  $R_C$  band, constructing the red, blue and total LF. For the total LF they find an agreement with  $\alpha = -1$  in the region just fainter than  $m^*$  and a steeper  $\alpha$  as the photometry gets deeper, in the range that is not covered by this study. Also, Piranomonte et al. (2001) examined 80 Abell Clusters finding  $\alpha = -1.01^{+0.09}_{-0.07}$  in Gunn r-band.

At higher redshifts, in agreement with low- $z$  studies, Popesso et al. (2005) used X-ray selected samples at redshift  $\leq 0.25$  and found a faint end slope  $\alpha = -1.05 \pm 0.13$ , in r-band, for the brighter part of the LF and with a background subtraction method similar to our approach. Also, in the same redshift range, Hansen et al. (2005) showed qualitatively that  $\alpha = -1$  is a good fit to X-ray selected clusters in r-band using SDSS data.

At ever higher redshift, the observational efforts to obtain the LF are more common in the infrared, as it is expected to track the stellar mass without great sensitivity to recent star formation. Lin et al. (2006) used 27 clusters at redshifts  $0 < z < 0.9$ , assumed a fixed  $\alpha = -0.9$  found at lower redshift (L04), and which is qualitatively consistent with their high redshift sample. Muzzin et al. (2007a) found a similar slope  $\alpha = -0.84 \pm 0.08$  with a sample of 15 clusters at redshifts  $0.2 < z < 0.5$ . Using *Spitzer*, Mancone et al. (2012) found also shallower slopes, with  $\alpha_{3.6\mu m} = -0.97 \pm 0.28$  and  $\alpha_{4.5\mu m} = -0.91 \pm 0.28$  in lower mass clusters or groups at  $z \sim 1.35$ .

The literature is consistent with little evolution of  $\alpha$ , with high- $z$  cluster LFs consistently shallower (albeit with redder rest frame bands). Interestingly, there are several studies that show that the red sequence LF slope evolves strongly with shallower  $\alpha$  at higher redshifts (e.g., De Lucia et al., 2004; Goto et al., 2005; Tanaka et al., 2005; Barkhouse et al., 2007; Stott et al., 2007; Gilbank et al., 2008; Rudnick et al., 2009).

In summary, our results are consistent with the literature values and prefer a mild increase of  $\alpha$  with redshift that is significant at the  $2\sigma$  level, when all the galaxies in the virial radius are considered.

### 5.5.3 Halo Occupation Number

The HON is an ingredient of the Halo Occupation Distribution, along with the relation between the dark matter and the galaxy spatial and velocity distribution. An interesting possibility is the change of the HON as the universe evolves. Observational studies such as L04 combined two samples, one at low- $z$  (L04), and another at higher redshift from de Propris et al. (1999), showed that clusters at higher redshift having more galaxies per unit mass. Furthermore, expanding on their previous work, Lin et al. (2006) used 27 clusters in the  $0 \leq z \leq 0.9$  redshift range, finding no evidence of evolution. With a redshift parametrization of  $(1+z)^\gamma$ , Lin et al. (2006) found  $\gamma = -0.53 \pm 0.59$ . By complementing them with 93 lower redshift sample ( $z \sim 0.06$ ) a different best fit is found,  $\gamma = -0.03 \pm 0.27$ , but as the previous case, it is consistent with no evolution. More recently, Capozzi et al. (2012) estimated the HON using 15 high- $z$  clusters under similar conditions to Lin et al. (2006) ( $m_K^* + 2$  depth and  $\alpha = -0.9$ ). By comparing to a low redshift sample at  $z \sim 0.06$  (L04), they were able to find



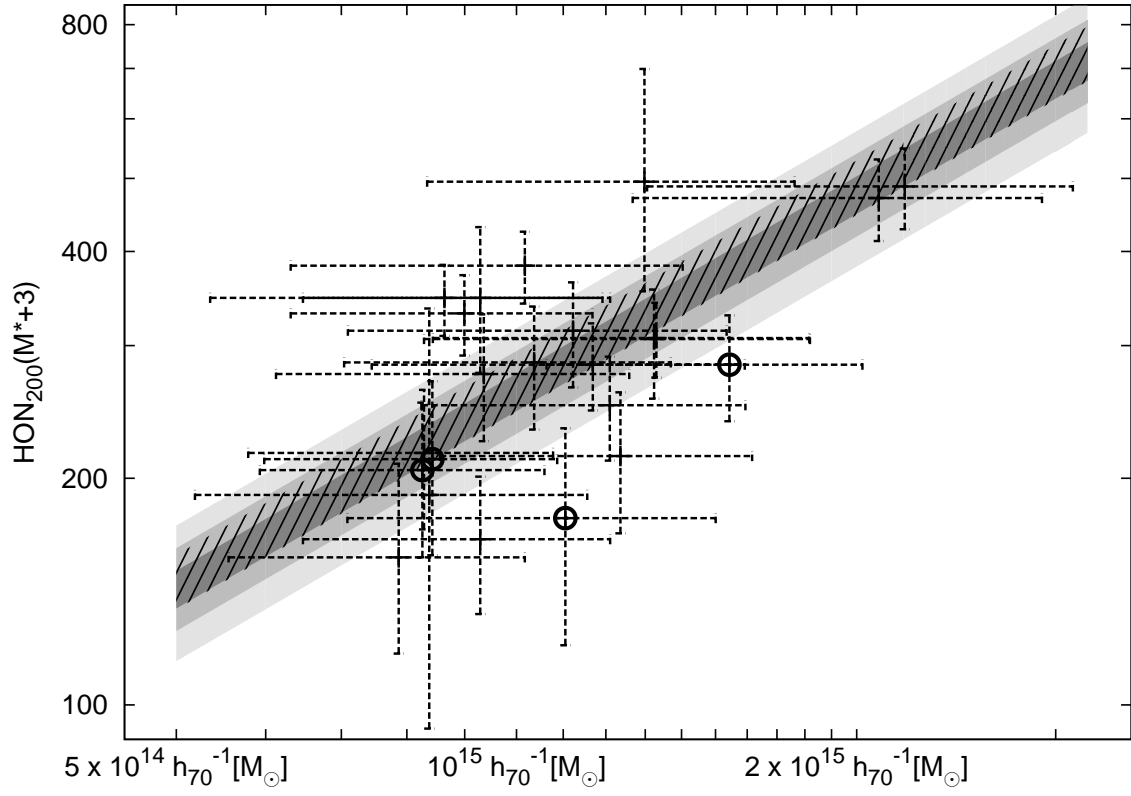


**Figure 5.6:** We plot the HON constructed using the LF extracted from the band redward of the  $4000\text{\AA}$  break versus cluster mass, as extracted from the SPT-SZ survey. The VLT data is highlighted with circles. Shaded areas correspond to the 1, 2 and 3  $\sigma$  errors in the normalization given a fixed slope of  $\gamma = 0.87$ . We find a normalization at  $M_{pivot} = 10^{15} M_{\odot}$  of  $257.04^{+18.38}_{-11.56}$  ( $1\sigma$ ) consistent with  $267 \pm 22$  from L04.

a HON redshift mass trend given by  $\gamma = -0.61^{+0.18}_{-0.20}$ , which is the opposite trend to what has been found previously.

We use a homogeneously selected cluster sample to characterize the HON as a function of mass and redshift and use that to examine possible evolutionary trends. The Halo Occupation Number is obtained by integrating the Schechter Function.

$$N = 1 + N^s, \text{ with } N^s = V\phi^* \int_{y_{\text{low}}}^{\infty} y^\alpha e^{-y} dy$$

where the first term accounts for the BCG, which is not part of the LF,  $V$  is the cluster virial volume,  $y_{\text{low}} = L_{\text{low}}/L_*$  and  $\alpha$  and  $\phi^*$  are the values obtained in previous sections. In order to compare to previous studies such as L04 we integrate the LF to  $m^* + 3$ .

As can be seen in Fig. 5.6 the range of masses in our sample is quite small, and so it is not possible to constrain both normalization and slope of the HON-mass relation. Therefore, we adopt the slope of 0.87 reported in the literature for a large sample of low redshift clusters (L04). With this slope, we measure a normalization of  $257.04^{+18.38}_{-11.56}$  ( $1\sigma$  uncertainties), which is consistent with the value found by L04 of  $267 \pm 22$ .

Furthermore, we look for possible evolution by examining the ratio between our measured HON and the value at the same mass obtained at low redshift (L04). In this analysis we enhance the HON errors using the mass uncertainties and the adopted mass slope of 0.87. As seen in panel (d) in Fig. 5.5 the measurements prefer some HON evolution. Fitting a linear relation we obtain  $-0.60^{+0.48}_{-0.47}$  (0.69) and  $0.12^{+0.07}_{-0.08}$  (0.12) for the slope and intercept, respectively (with  $1(2)\sigma$  intervals). Thus there is  $2\sigma$  evidence that galaxy clusters at high redshift have fewer galaxies per unit mass to  $m^* + 3$  than their low- $z$  counterparts.

This result is similar to Capozzi et al. (2012), but marginally inconsistent with Lin et al. (2006), where the HON was found to be consistent with no evolution. In both studies the HON was estimated in a similar fashion as we have done here, but in both those other samples the cluster population was not homogeneously selected. One possibility is that our VLT cluster LFs suffer from background-over-subtraction. As we mentioned in § 5.4.4 we use the NFW profile to correct for cluster galaxies in the defined background. While in the non-VLT data the background is defined at  $r > 1.5r_{200}$ , for the VLT cluster it is defined at  $r > 1.0r_{200}$ , which means that a larger correction is being made to the measured background. This correction is at the  $12 \pm 4\%$  level for 23 clusters, while for two of the VLT clusters (SPT-CLJ2337-5942 and SPT-CLJ0615-5746 at  $z = 0.775$  and  $0.972$ ) this correction is at the  $\sim 48\%$  level. By comparing to the other two VLT data points at Fig. 5.5, they do not look different than the VLT with lower correction values. To quantify their impact in the slope we re-fit the sample without them, obtaining a slope of  $-0.49^{+0.53}_{-0.52}$ . This new results does not change the trend of the HON albeit reduce the significance somewhat. Furthermore, if all four VLT clusters are not used in the fitting the solution for the slope becomes:  $-0.18^{+0.84}_{-0.85}$ , emphasising the importance of our high redshift VLT observed clusters to this result.

## 5.6 Conclusions

We have studied a cluster sample consisting of the 26 most massive galaxy clusters selected over the entire  $2500 \text{ deg}^2$  SPT-SZ survey footprint. The masses range between  $7.1 \times 10^{14} M_\odot$  and  $2.3 \times 10^{15} M_\odot$ , and the redshifts cover of  $0.1 \lesssim z \lesssim 1.13$ . We use the SZE mass to define the cluster virial region within which we study optical properties such as the radial profile, the luminosity function and the Halo Occupation Number.

The stacked radial profile of the whole sample is well described by an NFW model with a concentration of  $2.25 \pm 0.33$  which is low compared to results found in the literature. Differences between our study and previous works include the mass range, the redshift extent and the selection. Using SDSS clusters and groups, Hansen et al. (2005) found a strong inverse correlation between mass and concentration which may explain the lower concentration we see in our high mass sample, although Budzynski et al. (2012) did not find such correlation using a different radius definition on the same dataset. Furthermore, our low concentration measurement is driven by clusters in the higher redshift bin, which are not represented in most previously published samples (Carlberg et al., 1997; Lin et al., 2004; Budzynski et al., 2012). A more similar sample to compare to our higher redshift sample is that in Capozzi et al. (2012). Although having a lower average mass than our sample, the concentration found is  $c_g = 2.8^{+1.0}_{-0.8}$ , which is consistent with our findings within  $1\sigma$ .

We also stacked the red sequence selected galaxies radial profiles, finding them more concentrated than the total population. This is expected from the observed radial distribution of the fraction of red galaxies, which increases with lower cluster-centric radii (e.g., Goto et al., 2004; Verdugo et al., 2012; Ribeiro et al., 2013; Gruen et al., 2013a).

The redshift evolution of the concentration for all galaxies is found to be consistent with no evolution ( $(1+z)^{-0.80 \pm 1.05}$ ), while the red sequence galaxies prefer a mild evolution  $(1+z)^{-0.87 \pm 0.53}$ . Although statistically consistent with no evolution, such result could be explained as a change of the slope of the radial red fraction with redshift, such as seen in Fig. 6 in Gruen et al. (2013a) for two SPT-SZ selected clusters at redshift 0.3475 and  $\sim 0.6$ . A larger sample is required to examine this issue.

The stacked luminosity function (LF) is well fit by a Schechter function with Schechter parameters:  $\alpha = -1.06^{+0.04}_{-0.01}$ ,  $m - m_{\text{mod}}^* = -0.05^{+0.09}_{-0.08}$  and  $\phi^* = 3.01^{+0.26}_{-0.24} \text{ Mpc}^{-3} \text{ mag}^{-1}$ , with  $\chi_{\text{red}}^2 = 1.29$ . The faint end slope is found to be consistent with previous studies of local clusters (e.g., Gaidos, 1997; Paolillo et al., 2001; Piranomonte et al., 2001; Barkhouse et al., 2007) and at higher redshifts (e.g., Popesso et al., 2005; Hansen et al., 2005). Also, the  $\phi^*$  value agrees with previous work (L04,  $\phi = 4.00 \pm 0.16 h_{70}^3 \text{ Mpc}^{-3}$  for the case of the 25 most massive systems, which has a median mass roughly half of ours).

We fit the LF on single clusters using  $\alpha = -1.06$  from the stacked result to study the single cluster  $m^*$  evolution. We use the band which probes the portion of the galaxy spectrum redward of the 4000 Å break over the full redshift range. The  $m^*$  behaviour with redshift yields a slope of  $-0.15^{+0.26}_{-0.27}$ , indicating that the evolution of the characteristic luminosity in this uniformly selected sample does not deviate from the SSP model to which we compare. This model is an exponential burst at  $z = 3$  with decay time of 0.4 Gyr and a Salpeter IMF. This is broadly in agreement with previous work, that has shown cluster galaxies are general well modelled by a passively evolving stellar population that formed at redshift  $z > 1.5$  (e.g., de Propris et al., 1999; Lin et al., 2006; Andreon et al., 2008; Capozzi et al., 2012).

We used this result, fixing  $m^*$  to the SSP model predictions in the LF fit to explore the  $\alpha$  and  $\phi^*$  evolution. In the case of  $\alpha$ , we find a slope of  $0.25^{+0.22}_{-0.23}$  ( $2\sigma$  errors), indicating a preference for higher redshift clusters to have a lower faint-end LF slope with respect to their lower redshift counterparts. This is reminiscent of the strong evolution observed in red sequence LFs and may explain it if our clusters are dominated mainly by red sequence galaxies. The normalization  $\phi^*/E^2(z)$  measurements provide no significant evidence of redshift evolution when  $m^*$  is fixed to the model but prefers some evolution if  $\alpha$  is fixed to the stacked LF solution. Given that the single cluster results prefer evolution in  $\alpha$ , we take the results extracted using  $m^*$  fixed to the model as more robust.

We measured the HON, the number of galaxies within the virial region more luminous than  $m^* + 3$ , comparing it to the literature using a  $N \propto M^\gamma$  parametrization, and probing for redshift trends. Due to the small mass range in our sample, a simultaneous fit of both the normalization and the slope does not provide useful constraints. Therefore, we adopt a slope of  $\gamma = 0.87$  from the literature (L04) and fit for the normalization. We find a normalization of  $257.04^{+18.38}_{-11.56}$  at a mass  $M_{200} = 10^{15} M_\odot$ , which is consistent with the normalization of  $267 \pm 22$ , found in L04 from local clusters.

HON evolution with redshift is found at the  $2\sigma$  level, with a slope of  $-0.60^{+0.96}_{-0.95}$ , indicating that high redshift clusters are less populated than their lower redshift counterparts. This result is similar to the Capozzi et al. (2012) findings. As the  $\text{HON} \propto \phi^* \Gamma(\alpha + 2)$ , the evolution of  $\alpha$  and lack of evolution in  $\phi^*$  combine to drive the observed HON evolution (see Fig. 5.5). This suggests that while the density of galaxies near the characteristic luminosity  $L^*$  is not evolving, changes in the population of the lower luminosity galaxies occur between redshifts  $z = 1.1$  and the present. One cautionary note is that the redshift trend is strongly driven by the four clusters at  $z > 0.6$  observed with VLT, which with a FOV of  $7 \times 7$  allows for a less robust background correction. Further observations on the high redshift end with a somewhat larger field of view could resolve this issue.

*acknowledgments* The South Pole Telescope is supported by the National Science Foundation through grant ANT-0638937. Partial support is also provided by the NSF Physics Frontier Center grant PHY-0114422 to the Kavli Institute of Cosmological Physics at the University of Chicago, the Kavli Foundation, and the Gordon and Betty Moore Foundation. AZ, JM, CH and JL acknowledge the support of the Excellence Cluster Universe in Munich and the DFG Transregio program TR33: The Dark Universe. This paper includes data gathered with the Blanco 4-meter telescope, located at the Cerro Tololo Inter-American Observatory in Chile, which is part of the U.S. National Optical Astronomy Observatory, which is operated by the Association of Universities for Research in Astronomy (AURA), under contract with the National Science Foundation. Other data come from the European Southern Observatory telescopes on La Silla and Paranal. We are very grateful for the efforts of the CTIO, La Silla and Paranal support staff without whom this paper would not be possible.

## Summary & outlook

### Summary

In this Thesis we studied and characterized the galaxy populations in galaxy clusters selected by the Sunyaev–Zel’dovich Effect (SZE), a new and powerful cluster detection technique. Because of the close relationship between the thermal SZE and the cluster virial mass, SZE selected samples are similar to mass selected samples. In addition, because the relationship between the SZE signature and mass evolves only weakly with redshift, an SZE survey is delivering a cluster sample that includes cluster above a given mass at whatever redshift they exist. Furthermore, when combined with cluster redshifts in the manner outlined in this Thesis, an SZE selected sample becomes a powerful cosmological probe. The same characteristics that make an SZE-selected cluster sample a powerful probe for cosmology also make it ideal for studying the evolution of the galaxy content within clusters. In this Thesis we aimed to take advantage of these qualities to learn how the galaxy populations of clusters evolve in such dense environments. We summarize our finding as follows:

- In Chapter 3 we presented the first large-scale follow-up of an SZE-selected galaxy cluster sample. Between survey and targeted observations, over a hundred nights were invested in following up the 224 cluster candidates. We confirmed 158 clusters and measured their redshifts. We found a redshift range of  $0.1 \lesssim z \lesssim 1.35$ , confirming the expected large range of redshifts expected from an SZE-selected cluster sample. We determined the sample purity for detections at various SZE detection significance  $\xi$  levels. We found a 100% confirmation rate for detections at  $\xi > 6$ , 95% for  $\xi > 5$ , and a confirmation rate of 70% for  $\xi > 4.5$ . This demonstrates that the SZE selected samples from the SPT are very clean. We identified 146 rBCGs from the red sequence of galaxies projected within each cluster virial radius. We investigated whether the scatter in the offset between the rBCG position and the SZE centroid could be due to the positional uncertainty associated with each SPT detection. We found only a 0.09% likelihood that the SPT beam size is the sole driver of this scatter. We also compared the rBCG spatial distribution to a distribution drawn from an X-ray sample where the BCGs were selected in a similar manner. By introducing the SPT candidate positional uncertainty in an observed X-ray BCG distribution, we found a 41% probability of consistency between the two distributions. Thus, we detected the underlying physical scatter in the BCG position, and we showed that it is consistent with that found in X-ray selected samples. Because the BCG distribution is affected by recent cluster

merging, we concluded that there is no evidence that the ongoing merger rate in SZE-selected cluster samples is different than in X-ray selected ones. This builds confidence in our understanding of the SZE selection function, which is a key input for cosmological studies. The results from this chapter were used in Reichardt et al. (2013) to extract cosmological parameters, which are consistent with the standard  $\Lambda$ CDM model.

- In Chapter 4 we presented an examination of the first four SZE-selected galaxy clusters by the SPT in a representative  $0.3 < z < 1.1$  redshift range. We studied the number of galaxies within the virial radius, the radial and luminosity distribution of galaxies within the cluster, as well as their color. We constructed the galaxy surface density profile and fit an NFW profile. We found galaxy concentrations of  $c_g \approx 3$  to 6, consistent with values found for X-ray-selected clusters. We also observed a consistency between the characteristic luminosities  $m^*$  in *griz* bands and models of Simple Stellar Populations (SSP) formed from a single burst at redshift  $z = 3$ . We found the LF slope  $\alpha$  to be, on average,  $\approx -1.2$ , consistent with values found in the literature. We estimated the HON, finding it in agreement with X-ray-selected clusters. We also measured the blue fraction  $f_b$ , the fraction of blue galaxies within the total galaxy population. We found the blue fraction to evolve with redshift in agreement with other results in the literature. In summary, we found no difference with results from the literature based on other selection techniques, building confidence in the SZE cluster selection function and its power as a sampling method to study evolutionary trends in the cluster galaxy populations.

- In Chapter 5 we presented the first systematic study of the evolution of cluster galaxy populations in SZE selected clusters, using the most massive 26 clusters in the 2500 deg<sup>2</sup> SPT footprint. The clusters have masses in the range  $7.1 \times 10^{14} M_\odot \lesssim M_{200} \lesssim 2.3 \times 10^{15} M_\odot$  and redshifts  $0.1 \lesssim z \lesssim 1.13$ . We studied the total as well as the red galaxy populations within  $r_{200}$ . We identified red galaxies as those lying within  $\pm 3\sigma$  ( $\pm 0.22$  mag) of the red-sequence position.

We found that the NFW profile is a good description of both the red galaxies and the full population. The concentrations found for the red and total galaxy populations are  $2.71^{+0.38}_{-0.33}$  and  $2.25 \pm 0.33$ , respectively. The higher concentration for red-sequence galaxies is consistent with previous studies, which have found that the red galaxies preferentially populate the inner core of the galaxy cluster. Using a  $(1+z)^\gamma$  parametrization, we also explored the evolution of the galaxy population concentrations, finding that for the total population, the data are consistent with no evolution ( $\gamma = -0.80 \pm 1.05$ ) and for the red population there is a weak preference for evolution ( $\gamma = -0.87 \pm 0.53$ ).

We studied the stacked LF as well as the evolution of the individual cluster LFs. To accommodate the different bands of our observations and the different redshifts of our sample when stacking individual LFs, we used SSP models to describe  $m^*$  as a function of redshift. The models consisted of an exponentially falling star formation rate with a decay time of 0.4 Gyr, Salpeter IMF and a formation redshift of  $z = 3$ , in 6 metallicities. We normalized the models to the Coma cluster using Sloan Digital Sky Survey data and, using transmission curves for different telescope/filter combinations, generated the expected  $m^*$  for different bands. Using the aforementioned models we stacked the data in the same rest frame and fit a Schechter function. The parameters we found are  $\alpha = -1.06^{+0.04}_{-0.01}$ ,  $m - m^*_{\text{mod}} = -0.05^{+0.09}_{-0.08}$ , and  $\phi^* = 3.01^{+0.26}_{-0.24} \text{ Mpc}^{-3} \text{ mag}^{-1}$ , with

$\chi^2_{\text{red}} = 1.29$ . The data are well described by a Schechter function, and the measured parameters are consistent with values found in the literature.

We also fit the individual LFs to study evolutionary trends. Due to the relative shallowness of our data, a fit with the three LF parameters free on individual clusters does not have much constraining power. Therefore, we proceeded by fixing one parameter as we explored the other two. By setting  $\alpha = -1.06$  from the stacked result, we performed a linear fit to the  $m^*$  evolution, finding a slope of  $-0.15^{+0.26}_{-0.27}$ . This is consistent with no evolution of  $m^*$  beyond the simple passive aging of the stellar component. We used the same procedure to study the evolution in  $\alpha$  with  $m^*$  fixed. The resulting slope was  $0.25^{+0.22}_{-0.23}$ , at the  $2\sigma$  level, indicating a mild evolution with redshift; low- $z$  clusters exhibit a steeper  $\alpha$  than their high- $z$  counterparts. We also studied the evolution of the characteristic density  $\phi^*$  of galaxies with characteristic magnitude  $m^*$ , using  $m^*$  fixed and then  $\alpha$  fixed; both yielded values consistent with self-similar evolution.

We estimated the HON by integrating the LF to  $m^* + 3$ , following Lin et al. (2004). Given the small mass range, we fitted a function  $N = N_0 \times (M/M_{\text{pivot}})^s (1+z)^\gamma$  to the HON versus SZE mass with the slope  $s$  fixed. By using a fixed slope of  $s = 0.87$  taken from the literature (Lin et al., 2004) and  $\gamma = 0$ , we found a value for  $N_0$  of  $257.04^{+18.38}_{-11.56}$ , in good agreement with the normalization found in the aforementioned work ( $267 \pm 22$ ). We also investigated the evolution of the HON exploring the  $\gamma$  term. A fit of the above function rendered a slope of  $\gamma = -0.60^{+0.48}_{-0.47}$ . This indicates a preference for high- $z$  clusters to have fewer galaxies per unit mass than low- $z$  systems.

## Outlook

As we have shown, galaxy clusters detected by their SZE signature in the SPT survey are ideal for evolutionary studies of the galaxy populations in a cluster environment. As SZE surveys are being completed, they are increasingly supplemented with multi-wavelength follow-up observations. These include X-ray observations as well as deep, ground-based and space-based, optical observations for weak lensing mass estimation and spectroscopic redshifts. The resulting dataset provides a new source of information based on the clean SZE selection function that will greatly improve our understanding of the evolution of galaxies in galaxy clusters. Data collected with the aim of better understanding and constraining cluster masses will, when combined with larger samples of high- $z$  clusters, allow us to strengthen (or falsify) the evolutionary trends found in Chapter 5. In particular, the change of HON with redshift hints at an evolution of the processes that shape the cluster LF. Competing processes include the galaxy accretion rate onto clusters, the galaxy merger rate, and the star formation in clusters. Larger cluster samples plus additional observations will shed light on how those processes evolve. Also, in the high- $z$  regime, exciting science possibilities await, for example studies of star-formation rates in clusters at redshifts beyond  $z = 1$  seem to reveal two star-formation eras: an era of active star formation at  $z \gtrsim 1.4$  followed by an era of quenched star formation (e.g., Bayliss et al., 2013; Brodwin et al., 2013). By the end of the SPT Survey the number of confirmed, high-redshift clusters will increase and, when studied with powerful new instruments like KMOS and MUSE, these clusters present an opportunity to study this epoch in more detail. The results will provide insights into the mechanisms that drive galaxy formation in dense environments at early times.





# Bibliography

- Abell, G. O. 1958: *The Distribution of Rich Clusters of Galaxies.*, ApJS, 3, 211
- Abell, G. O., Corwin, Jr., H. G., & Olowin, R. P. 1989: *A catalog of rich clusters of galaxies*, ApJS, 70, 1
- Afonso, C., Albert, J. N., Andersen, J., Ansari, R., Aubourg, É., Bareyre, P., Beaulieu, J. P., Blanc, G., Charlot, X., Couchot, F., Coutures, C., et al. 2003: *Limits on Galactic dark matter with 5 years of EROS SMC data*, A&A, 400, 951
- Albrecht, A., Bernstein, G., Cahn, R., Freedman, W. L., Hewitt, J., Hu, W., Huth, J., Kamionkowski, M., Kolb, E. W., Knox, L., Mather, J. C., et al. 2006: *Report of the Dark Energy Task Force*, ArXiv Astrophysics e-prints
- Alcock, C., Allsman, R. A., Alves, D., Axelrod, T. S., Bennett, D. P., Cook, K. H., Freeman, K. C., Griest, K., Guern, J., Lehner, M. J., Marshall, S. L., et al. 1997: *The MACHO Project: 45 Candidate Microlensing Events from the First-Year Galactic Bulge Data*, ApJ, 479, 119
- Alcock, C., Allsman, R. A., Alves, D. R., Axelrod, T. S., Becker, A. C., Bennett, D. P., Cook, K. H., Dalal, N., Drake, A. J., Freeman, K. C., Geha, M., et al. 2000: *The MACHO Project: Microlensing Results from 5.7 Years of Large Magellanic Cloud Observations*, ApJ, 542, 281
- Alpher, R. A., Herman, R., & Gamow, G. A. 1948: *Thermonuclear Reactions in the Expanding Universe*, Physical Review, 74, 1198
- Andersson, K., Benson, B. A., Ade, P. A. R., Aird, K. A., Armstrong, B., Bautz, M., Bleem, L. E., Brodwin, M., Carlstrom, J. E., Chang, C. L., Crawford, T. M., et al. 2011: *X-Ray Properties of the First Sunyaev-Zel'dovich Effect Selected Galaxy Cluster Sample from the South Pole Telescope*, ApJ, 738, 48
- Andreon, S. 2006: *The buildup of stellar mass and the 3.6  $\mu$ m luminosity function in clusters from  $z = 1.25$  to  $z = 0.2$* , A&A, 448, 447
- Andreon, S. & Ettori, S. 1999: *Is the Butcher-Oemler Effect a Function of the Cluster Redshift?*, ApJ, 516, 647

- Andreon, S., Puddu, E., de Propris, R., & Cuillandre, J.-C. 2008: *Galaxy evolution in the high-redshift, colour-selected cluster RZCS 052 at  $z = 1.02$* , MNRAS, 385, 979
- Angulo, R. E., Lacey, C. G., Baugh, C. M., & Frenk, C. S. 2009: *The fate of substructures in cold dark matter haloes*, MNRAS, 399, 983
- Appenzeller, I., Fricke, K., Fürtig, W., Gässler, W., Häfner, R., Harke, R., Hess, H.-J., Hummel, W., Jürgens, P., Kudritzki, R.-P., Mantel, K.-H., et al. 1998: *Successful commissioning of FORS1 - the first optical instrument on the VLT.*, The Messenger, 94, 1
- Applegate, D. E., von der Linden, A., Kelly, P. L., Allen, M. T., Allen, S. W., Burchat, P. R., Burke, D. L., Ebeling, H., Mantz, A., & Morris, R. G. 2012: *Weighing the Giants III: Methods and Measurements of Accurate Galaxy Cluster Weak-Lensing Masses*, ArXiv e-prints
- Arnaud, M., Pratt, G. W., Piffaretti, R., Böhringer, H., Croston, J. H., & Pointecouteau, E. 2010: *The universal galaxy cluster pressure profile from a representative sample of nearby systems (REXCESS) and the  $Y_{SZ} - M_{500}$  relation*, A&A, 517, A92+
- Ashby, M. L. N., Stern, D., Brodwin, M., Griffith, R., Eisenhardt, P., Kozłowski, S., Kochanek, C. S., Bock, J. J., Borys, C., Brand, K., Brown, M. J. I., et al. 2009: *The Spitzer Deep, Wide-field Survey*, ApJ, 701, 428
- Babcock, H. W. 1939: *The rotation of the Andromeda Nebula*, Lick Observatory Bulletin, 19, 41
- Barkhouse, W. A., Yee, H. K. C., & López-Cruz, O. 2007: *The Luminosity Function of Low-Redshift Abell Galaxy Clusters*, ApJ, 671, 1471
- Bartelmann, M. 1996: *Arcs from a universal dark-matter halo profile.*, A&A, 313, 697
- Battye, R. A. & Weller, J. 2003: *Constraining cosmological parameters using Sunyaev-Zel'dovich cluster surveys*, Phys. Rev. D, 68, 083506
- Baum, W. A. 1959: *The Hertzsprung-Russell diagrams of old stellar Populations*, in IAU Symposium, Vol. 10, The Hertzsprung-Russell Diagram, ed. J. L. Greenstein, 23
- Bayliss, M. B., Ashby, M. L. N., Ruel, J., Brodwin, M., Aird, K. A., Bautz, M. W., Benson, B. A., Bleem, L. E., Bocquet, S., Carlstrom, J. E., Chang, C. L., et al. 2013: *SPT-CLJ2040-4451: An SZ-Selected Galaxy Cluster at  $z = 1.478$  With Significant Ongoing Star Formation*, ArXiv e-prints
- Bender, R., Saglia, R. P., Ziegler, B., Belloni, P., Greggio, L., Hopp, U., & Bruzual, G. 1998: *Exploring Cluster Elliptical Galaxies as Cosmological Standard Rods*, ApJ, 493, 529
- Bennett, C. L., Larson, D., Weiland, J. L., Jarosik, N., Hinshaw, G., Odegard, N., Smith, K. M., Hill, R. S., Gold, B., Halpern, M., Komatsu, E., et al. 2012: *Nine-Year Wilkinson Microwave Anisotropy Probe (WMAP) Observations: Final Maps and Results*, ArXiv e-prints

- Benson, B. A., de Haan, T., Dudley, J. P., Reichardt, C. L., Aird, K. A., Andersson, K., Armstrong, R., Ashby, M. L. N., Bautz, M., Bayliss, M., Bazin, G., et al. 2013: *Cosmological Constraints from Sunyaev-Zel'dovich-selected Clusters with X-Ray Observations in the First 178 deg<sup>2</sup> of the South Pole Telescope Survey*, ApJ, 763, 147
- Berlind, A. A., Weinberg, D. H., Benson, A. J., Baugh, C. M., Cole, S., Davé, R., Frenk, C. S., Jenkins, A., Katz, N., & Lacey, C. G. 2003: *The Halo Occupation Distribution and the Physics of Galaxy Formation*, ApJ, 593, 1
- Bertin, E. 2006: *Automatic Astrometric and Photometric Calibration with SCAMP*, in Astronomical Society of the Pacific Conference Series, Vol. 351, Astronomical Data Analysis Software and Systems XV, ed. C. Gabriel, C. Arviset, D. Ponz, & S. Enrique, 112–+
- Bertin, E. & Arnouts, S. 1996: *SExtractor: Software for source extraction.*, A&AS, 117, 393
- Bertin, E., Mellier, Y., Radovich, M., Missonnier, G., Didelon, P., & Morin, B. 2002: *The TERAPIX Pipeline*, in Astronomical Society of the Pacific Conference Series, Vol. 281, Astronomical Data Analysis Software and Systems XI, ed. D. A. Bohlender, D. Durand, & T. H. Handley, 228–+
- Birkinshaw, M. 1999: *The Sunyaev Zel'dovich Effect*, Physics Reports, 310, 97
- Biviano, A. & Poggianti, B. M. 2009: *The evolution of mass profiles of galaxy clusters*, ArXiv e-prints
- Blakeslee, J. P., Franx, M., Postman, M., Rosati, P., Holden, B. P., Illingworth, G. D., Ford, H. C., Cross, N. J. G., Gronwall, C., Benítez, N., Bouwens, R. J., et al. 2003: *Advanced Camera for Surveys Photometry of the Cluster RDCS 1252.9-2927: The Color-Magnitude Relation at  $z = 1.24$* , ApJ, 596, L143
- Böhringer, H., Schuecker, P., Guzzo, L., Collins, C. A., Voges, W., Cruddace, R. G., Ortiz-Gil, A., Chincarini, G., De Grandi, S., Edge, A. C., MacGillivray, H. T., et al. 2004: *The ROSAT-ESO Flux Limited X-ray (REFLEX) Galaxy cluster survey. V. The cluster catalogue*, A&A, 425, 367
- Bower, R. G., Lucey, J. R., & Ellis, R. S. 1992: *Precision Photometry of Early Type Galaxies in the Coma and Virgo Clusters - a Test of the Universality of the Colour / Magnitude Relation - Part Two - Analysis*, MNRAS, 254, 601
- Brimioulle, F., Lerchster, M., Seitz, S., Bender, R., & Snigula, J. 2008: *Photometric redshifts for the CFHTLS-Wide*, ArXiv e-prints
- Brodwin, M., Gonzalez, A. H., Moustakas, L. A., Eisenhardt, P. R., Stanford, S. A., Stern, D., & Brown, M. J. I. 2007: *Galaxy Cluster Correlation Function to  $z \sim 1.5$  in the IRAC Shallow Cluster Survey*, ApJ, 671, L93
- Brodwin, M., Gonzalez, A. H., Stanford, S. A., Plagge, T., Marrone, D. P., Carlstrom, J. E., Dey, A., Eisenhardt, P. R., Fedeli, C., Gettings, D., Jannuzi, B. T., et al. 2012: *IDCS J1426.5+3508: Sunyaev-Zel'dovich Measurement of a Massive IR-selected Cluster at  $z=1.75$* , ArXiv:1205.3787

- Brodwin, M., Ruel, J., Ade, P. A. R., Aird, K. A., Andersson, K., Ashby, M. L. N., Bautz, M., Bazin, G., Benson, B. A., Bleem, L. E., Carlstrom, J. E., et al. 2010: *SPT-CL J0546-5345: A Massive  $z > 1$  Galaxy Cluster Selected Via the Sunyaev-Zel'dovich Effect with the South Pole Telescope*, ApJ, 721, 90
- Brodwin, M., Stanford, S. A., Gonzalez, A. H., Zeimann, G. R., Snyder, G. F., Mancone, C. L., Pope, A., Eisenhardt, P. R., Stern, D., Alberts, S., Ashby, M. L. N., et al. 2013: *The Era of Star Formation in Galaxy Clusters*, ArXiv e-prints
- Brott, I. & Hauschildt, P. H. 2005: *A PHOENIX Model Atmosphere Grid for Gaia*, in ESA Special Publication, Vol. 576, The Three-Dimensional Universe with Gaia, ed. C. Turon, K. S. O'Flaherty, & M. A. C. Perryman, 565–+
- Bruzual, G. & Charlot, S. 2003: *Stellar population synthesis at the resolution of 2003*, MNRAS, 344, 1000
- Buckley-Geer, E. J., Lin, H., Drabek, E. R., Allam, S. S., Tucker, D. L., Armstrong, R., Barkhouse, W. A., Bertin, E., Brodwin, M., Desai, S., Frieman, J. A., et al. 2011: *The Serendipitous Observation of a Gravitationally Lensed Galaxy at  $z = 0.9057$  from the Blanco Cosmology Survey: The Elliot Arc*, ApJ, 742, 48
- Budzynski, J. M., Koposov, S. E., McCarthy, I. G., McGee, S. L., & Belokurov, V. 2012: *The radial distribution of galaxies in groups and clusters*, MNRAS, 423, 104
- Butcher, H. & Oemler, Jr., A. 1984: *The evolution of galaxies in clusters. V - A study of populations since  $Z$  approximately equal to 0.5*, ApJ, 285, 426
- Capozzi, D., Collins, C. A., Stott, J. P., & Hilton, M. 2012: *The evolution of  $K^*$  and the halo occupation distribution since  $z = 1.5$ : observations versus simulations*, MNRAS, 419, 2821
- Carlberg, R. G., Yee, H. K. C., Ellingson, E., Abraham, R., Gravel, P., Morris, S., & Pritchet, C. J. 1996: *Galaxy Cluster Virial Masses and Omega*, ApJ, 462, 32
- Carlberg, R. G., Yee, H. K. C., Ellingson, E., Morris, S. L., Abraham, R., Gravel, P., Pritchet, C. J., Smecker-Hane, T., Hartwick, F. D. A., Hesser, J. E., Hutchings, J. B., et al. 1997: *The Average Mass Profile of Galaxy Clusters*, ApJ, 485, L13+
- Carlstrom, J. E., Ade, P. A. R., Aird, K. A., Benson, B. A., Bleem, L. E., Busetti, S., Chang, C. L., Chauvin, E., Cho, H.-M., Crawford, T. M., Crites, A. T., et al. 2011: *The 10 Meter South Pole Telescope*, PASP, 123, 568
- Carlstrom, J. E., Holder, G. P., & Reese, E. D. 2002: *Cosmology with the Sunyaev-Zel'dovich Effect*, ARA&A, 40, 643
- Cease, H., DePoy, D., Derylo, G., Diehl, H. T., Estrada, J., Flaugh, B., Guarino, V., Kuk, K., Kuhlmann, S., Schultz, K., Schmitt, R. L., et al. 2008: *The Dark Energy Survey CCD imager design*, in Society of Photo-Optical Instrumentation Engineers (SPIE) Conference Series, Vol. 7014, Society of Photo-Optical Instrumentation Engineers (SPIE) Conference Series

- Ciardullo, R., Feldmeier, J. J., Jacoby, G. H., Kuzio de Naray, R., Laychak, M. B., & Durrell, P. R. 2002: *Planetary Nebulae as Standard Candles. XII. Connecting the Population I and Population II Distance Scales*, ApJ, 577, 31
- Clocchiatti, A. 2011: *Type Ia Supernovae and the discovery of the Cosmic Acceleration*, ArXiv e-prints
- Cohn, J. D., Evrard, A. E., White, M., Croton, D., & Ellingson, E. 2007: *Red-sequence cluster finding in the Millennium Simulation*, MNRAS, 382, 1738
- Cole, S., Lacey, C. G., Baugh, C. M., & Frenk, C. S. 2000: *Hierarchical galaxy formation*, MNRAS, 319, 168
- Collins, C. A., Guzzo, L., Nichol, R. C., & Lumsden, S. L. 1995: *The Edinburgh-Durham Southern Galaxy Catalogue - VII. The Edinburgh-Milano cluster redshift survey*, MNRAS, 274, 1071
- Collister, A. A. & Lahav, O. 2004: *ANNz: Estimating Photometric Redshifts Using Artificial Neural Networks*, PASP, 116, 345
- Covey, K. R., Ivezić, Ž., Schlegel, D., Finkbeiner, D., Padmanabhan, N., Lupton, R. H., Agüeros, M. A., Bochanski, J. J., Hawley, S. L., West, A. A., Seth, A., et al. 2007: *Stellar SEDs from 0.3 to 2.5  $\mu$ m: Tracing the Stellar Locus and Searching for Color Outliers in the SDSS and 2MASS*, AJ, 134, 2398
- De Lucia, G., Poggianti, B. M., Aragón-Salamanca, A., Clowe, D., Halliday, C., Jablonka, P., Milvang-Jensen, B., Pelló, R., Poirier, S., Rudnick, G., Saglia, R., et al. 2004: *The Buildup of the Red Sequence in Galaxy Clusters since  $z \sim 0.8$* , ApJ, 610, L77
- De Lucia, G., Poggianti, B. M., Aragón-Salamanca, A., White, S. D. M., Zaritsky, D., Clowe, D., Halliday, C., Jablonka, P., von der Linden, A., Milvang-Jensen, B., Pelló, R., et al. 2007: *The build-up of the colour-magnitude relation in galaxy clusters since  $z \sim 0.8$* , MNRAS, 374, 809
- De Propris, R., Colless, M., Driver, S. P., Couch, W., Peacock, J. A., Baldry, I. K., Baugh, C. M., Bland-Hawthorn, J., Bridges, T., Cannon, R., Cole, S., et al. 2003: *The 2dF Galaxy Redshift Survey: the luminosity function of cluster galaxies*, MNRAS, 342, 725
- De Propris, R., Colless, M., Peacock, J. A., Couch, W. J., Driver, S. P., Balogh, M. L., Baldry, I. K., Baugh, C. M., Bland-Hawthorn, J., Bridges, T., Cannon, R., et al. 2004: *The 2dF Galaxy Redshift Survey: the blue galaxy fraction and implications for the Butcher-Oemler effect*, MNRAS, 351, 125
- De Propris, R., Phillipps, S., & Bremer, M. N. 2013: *Deep luminosity functions and colour-magnitude relations for cluster galaxies at  $0.2 < z < 0.6$* , MNRAS, 434, 3469
- de Propris, R., Stanford, S. A., Eisenhardt, P. R., Dickinson, M., & Elston, R. 1999: *The K-Band Luminosity Function in Galaxy Clusters to  $z \sim 1$* , AJ, 118, 719
- De Propris, R., Stanford, S. A., Eisenhardt, P. R., Holden, B. P., & Rosati, P. 2007: *The Rest-Frame K-Band Luminosity Function of Galaxies in Clusters to  $z = 1.3$* , AJ, 133, 2209

- Desai, S., Armstrong, R., Ashby, M. L. N., Bayliss, B., Bazin, G., Benson, B., Bertin, E., Bleem, L., Gonzalez, A. H., High, F. W., Liu, J., et al. 2012a: *Optical followup of galaxy clusters detected by the South Pole Telescope*, ArXiv e-prints
- Desai, S., Armstrong, R., Mohr, J. J., Semler, D. R., Liu, J., Bertin, E., Allam, S. S., Barkhouse, W. A., Bazin, G., Buckley-Geer, E. J., Cooper, M. C., et al. 2012b: *The Blanco Cosmology Survey: Data Acquisition, Processing, Calibration, Quality Diagnostics, and Data Release*, ApJ, 757, 83
- Desai, S., Mohr, J., Armstrong, R., Bertin, E., Zenteno, A., Tucker, D., Song, J., Ngeow, C., Lin, H., Bazin, G., Liu, J., et al. 2011: *Results from DESDM Pipeline on Data From Blanco Cosmology Survey*, in Bulletin of the American Astronomical Society, Vol. 43, American Astronomical Society Meeting Abstracts #217, 334.03
- Dolag, K., Borgani, S., Murante, G., & Springel, V. 2009: *Substructures in hydrodynamical cluster simulations*, MNRAS, 399, 497
- Dressler, A. 1980: *Galaxy morphology in rich clusters - Implications for the formation and evolution of galaxies*, ApJ, 236, 351
- Dressler, A. M., Sutin, B. M., & Bigelow, B. C. 2003: *Science with IMACS on Magellan*, in Society of Photo-Optical Instrumentation Engineers (SPIE) Conference Series, Vol. 4834, Society of Photo-Optical Instrumentation Engineers (SPIE) Conference Series, ed. P. Guhathakurta, 255–263
- Duffy, A. R., Schaye, J., Kay, S. T., & Dalla Vecchia, C. 2008: *Dark matter halo concentrations in the Wilkinson Microwave Anisotropy Probe year 5 cosmology*, MNRAS, 390, L64
- Ebeling, H., Voges, W., Bohringer, H., Edge, A. C., Huchra, J. P., & Briel, U. G. 1996: *“Properties of the X-ray-brightest Abell-type clusters of galaxies (XBACs) from ROSAT All-Sky Survey data - I. The sample”*, MNRAS, 281, 799
- Eikenberry, S., Elston, R., Raines, S. N., Julian, J., Hanna, K., Hon, D., Julian, R., Bandyopadhyay, R., Bennett, J. G., Bessoff, A., Branch, M., et al. 2006: *FLAMINGOS-2: the facility near-infrared wide-field imager and multi-object spectrograph for Gemini*, in Society of Photo-Optical Instrumentation Engineers (SPIE) Conference Series, Vol. 6269, Society of Photo-Optical Instrumentation Engineers (SPIE) Conference Series
- Einstein, A. 1916: *Die Grundlage der allgemeinen Relativitätstheorie*, Annalen der Physik, 354, 769
- Eisenhardt, P. R., De Propriis, R., Gonzalez, A. H., Stanford, S. A., Wang, M., & Dickinson, M. 2007: *Multiaperture UBVRIZJHK Photometry of Galaxies in the Coma Cluster*, ApJS, 169, 225
- Eisenhardt, P. R. M., Brodwin, M., Gonzalez, A. H., Stanford, S. A., Stern, D., Barmby, P., Brown, M. J. I., Dawson, K., Dey, A., Doi, M., Galametz, A., et al. 2008: *Clusters of Galaxies in the First Half of the Universe from the IRAC Shallow Survey*, ApJ, 684, 905
- Eisenstein, D. J. & Hu, W. 1998: *Baryonic Features in the Matter Transfer Function*, ApJ, 496, 605

- Eisenstein, D. J., Zehavi, I., Hogg, D. W., Scoccimarro, R., Blanton, M. R., Nichol, R. C., Scranton, R., Seo, H., Tegmark, M., Zheng, Z., Anderson, S. F., et al. 2005: *Detection of the Baryon Acoustic Peak in the Large-Scale Correlation Function of SDSS Luminous Red Galaxies*, ApJ, 633, 560
- Elston, R. J., Gonzalez, A. H., McKenzie, E., Brodwin, M., Brown, M. J. I., Cardona, G., Dey, A., Dickinson, M., Eisenhardt, P. R., Jannuzi, B. T., Lin, Y., et al. 2006: *The FLAMINGOS Extragalactic Survey*, ApJ, 639, 816
- Erben, T., Schirmer, M., Dietrich, J. P., Cordes, O., Habertzettl, L., Hettterscheidt, M., Hildebrandt, H., Schmithuesen, O., Schneider, P., Simon, P., Deul, E., et al. 2005: *GaBoDS: The Garching-Bonn Deep Survey. IV. Methods for the image reduction of multi-chip cameras demonstrated on data from the ESO Wide-Field Imager*, Astronomische Nachrichten, 326, 432
- Fabian, A. C. 1994: *Cooling Flows in Clusters of Galaxies*, ARA&A, 32, 277
- Fairley, B. W., Jones, L. R., Wake, D. A., Collins, C. A., Burke, D. J., Nichol, R. C., & Romer, A. K. 2002: *Galaxy colours in high-redshift, X-ray-selected clusters - I. Blue galaxy fractions in eight clusters*, MNRAS, 330, 755
- Fassbender, R., Böhringer, H., Nastasi, A., Šuhada, R., Mühlegger, M., de Hoon, A., Kohnert, J., Lamer, G., Mohr, J. J., Pierini, D., Pratt, G. W., et al. 2011: *The x-ray luminous galaxy cluster population at  $0.9 < z \lesssim 1.6$  as revealed by the XMM-Newton Distant Cluster Project*, New Journal of Physics, 13, 125014
- Fazio, G. G., Hora, J. L., Allen, L. E., Ashby, M. L. N., Barmby, P., Deutsch, L. K., Huang, J.-S., Kleiner, S., Marengo, M., Megeath, S. T., Melnick, G. J., et al. 2004: *The Infrared Array Camera (IRAC) for the Spitzer Space Telescope*, ApJS, 154, 10
- Feast, M. W. & Walker, A. R. 1987: *Cepheids as distance indicators*, ARA&A, 25, 345
- Felten, J. E., Gould, R. J., Stein, W. A., & Woolf, N. J. 1966: *X-Rays from the Coma Cluster of Galaxies*, ApJ, 146, 955
- Fetisova, T. S. 1981: *A Catalog of Galaxy Clusters with Measured Redshifts*, Soviet Ast., 25, 647
- Finoguenov, A., Guzzo, L., Hasinger, G., Scoville, N. Z., Aussel, H., Böhringer, H., Brusa, M., Capak, P., Cappelluti, N., Comastri, A., Giodini, S., et al. 2007: *The XMM-Newton Wide-Field Survey in the COSMOS Field: Statistical Properties of Clusters of Galaxies*, ApJS, 172, 182
- Finoguenov, A., Watson, M. G., Tanaka, M., Simpson, C., Cirasuolo, M., Dunlop, J. S., Peacock, J. A., Farrah, D., Akiyama, M., Ueda, Y., Smolčić, V., et al. 2010: *X-ray groups and clusters of galaxies in the Subaru-XMM Deep Field*, MNRAS, 403, 2063
- Fixsen, D. J., Cheng, E. S., Gales, J. M., Mather, J. C., Shafer, R. A., & Wright, E. L. 1996: *The Cosmic Microwave Background Spectrum from the Full COBE FIRAS Data Set*, ApJ, 473, 576

- Foley, R. J., Andersson, K., Bazin, G., de Haan, T., Ruel, J., Ade, P. A. R., Aird, K. A., Armstrong, R., Ashby, M. L. N., Bautz, M., Benson, B. A., et al. 2011: *Discovery and Cosmological Implications of SPT-CL J2106-5844, the Most Massive Known Cluster at  $z > 1$* , ApJ, 731, 86
- Fowler, J. W., Niemack, M. D., Dicker, S. R., Aboobaker, A. M., Ade, P. A. R., Battistelli, E. S., Devlin, M. J., Fisher, R. P., Halpern, M., Hargrave, P. C., Hincks, A. D., et al. 2007: *Optical design of the Atacama Cosmology Telescope and the Millimeter Bolometric Array Camera*, Appl. Opt., 46, 3444
- Friedmann, A. 1922: *Über die Krümmung des Raumes*, Zeitschrift für Physik, 10, 377
- Gaidos, E. J. 1997: *The Galaxy Luminosity Function from Observations of Twenty Abell Clusters*, AJ, 113, 117
- Garg, A. 2008: *Microlensing candidate selection and detection efficiency for the SuperMACHO Dark Matter search*, PhD thesis, Harvard University
- Garg, A., Stubbs, C. W., Challis, P., Wood-Vasey, W. M., Blondin, S., Huber, M. E., Cook, K., Nikolaev, S., Rest, A., Smith, R. C., Olsen, K., et al. 2007: *Light Curves of Type Ia Supernovae from Near the Time of Explosion*, AJ, 133, 403
- Gehrels, N. 1986: *Confidence limits for small numbers of events in astrophysical data*, ApJ, 303, 336
- Geller, M. J. & Beers, T. C. 1982: *Substructure within clusters of galaxies*, PASP, 94, 421
- Giacconi, R., Murray, S., Gursky, H., Kellogg, E., Schreier, E., & Tananbaum, H. 1972: *The Uhuru catalog of X-ray sources.*, ApJ, 178, 281
- Gilbank, D. G., Yee, H. K. C., Ellingson, E., Gladders, M. D., Loh, Y., Barrientos, L. F., & Barkhouse, W. A. 2008: *The Red-Sequence Luminosity Function in Galaxy Clusters since  $z \sim 1$* , ApJ, 673, 742
- Giodini, S., Lovisari, L., Pointecouteau, E., Ettori, S., Reiprich, T. H., & Hoekstra, H. 2013: *Scaling Relations for Galaxy Clusters: Properties and Evolution*, Space Sci. Rev., 177, 247
- Gladders, M. D., Lopez-Cruz, O., Yee, H. K. C., & Kodama, T. 1998: *The Slope of the Cluster Elliptical Red Sequence: A Probe of Cluster Evolution*, ApJ, 501, 571
- Gladders, M. D. & Yee, H. K. C. 2005: *The Red-Sequence Cluster Survey. I. The Survey and Cluster Catalogs for Patches RCS 0926+37 and RCS 1327+29*, ApJS, 157, 1
- Gonzalez, A. H., Brodwin, M., Brown, M. J. I., Dey, A., Dickinson, M., Gettings, D., Stanford, S. A., Stern, D., Bock, J., Bussman, S., Cooray, A., et al. 2010: *A NEWFIRM Survey of the Spitzer Deep Wide Field*, in American Astronomical Society Meeting Abstracts, Vol. 216, American Astronomical Society Meeting Abstracts #216, 415.13
- Gonzalez, A. H., Sivanandam, S., Zabludoff, A. I., & Zaritsky, D. 2013: *Galaxy Cluster Baryon Fractions Revisited*, ApJ, 778, 14
- Gonzalez, A. H., Zabludoff, A. I., & Zaritsky, D. 2005: *Intracuster Light in Nearby Galaxy Clusters: Relationship to the Halos of Brightest Cluster Galaxies*, ApJ, 618, 195



- Goto, T., Okamura, S., McKay, T. A., Bahcall, N. A., Annis, J., Bernard, M., Brinkmann, J., Gómez, P. L., Hansen, S., Kim, R. S. J., Sekiguchi, M., et al. 2002: *Composite Luminosity Functions Based on the Sloan Digital Sky Survey “Cut and Enhance” Galaxy Cluster Catalog*, PASJ, 54, 515
- Goto, T., Postman, M., Cross, N. J. G., Illingworth, G. D., Tran, K., Magee, D., Franx, M., Benítez, N., Bouwens, R. J., Demarco, R., Ford, H. C., et al. 2005: *Luminosity Functions of the Galaxy Cluster MS 1054-0321 at  $z=0.83$  based on ACS Photometry*, ApJ, 621, 188
- Goto, T., Yagi, M., Tanaka, M., & Okamura, S. 2004: *Evolution of the colour-radius and morphology-radius relations in SDSS galaxy clusters*, MNRAS, 348, 515
- Gruen, D., Brimiouille, F., Seitz, S., Lee, C.-H., Young, J., Koppenhoefer, J., Eichner, T., Riffeser, A., Vikram, V., Weidinger, T., & Zenteno, A. 2013a: *Weak lensing analysis of RXC J2248.7-4431*, MNRAS, 432, 1455
- Gruen, D., Seitz, S., Kosyra, R., Brimiouille, F., Koppenhoefer, J., Lee, C.-H., Bender, R., Riffeser, A., Eichner, T., Weidinger, T., & Bierschenk, M. 2013b: *Weak lensing analysis of SZ-selected clusters of galaxies from the SPT and Planck surveys*, ArXiv e-prints
- Gu, L., Gandhi, P., Inada, N., Kawaharada, M., Kodama, T., Konami, S., Nakazawa, K., Shimasaku, K., Xu, H., & Makishima, K. 2013: *Probing of the Interactions between the Hot Plasmas and Galaxies in Clusters from  $z = 0.1$  to  $0.9$* , ApJ, 767, 157
- Gursky, H., Solinger, A., Kellogg, E. M., Murray, S., Tananbaum, H., Giacconi, R., & Cavaliere, A. 1972: *X-Ray Emission from Rich Clusters of Galaxies*, ApJ, 173, L99
- Guzzo, L., Böhringer, H., Schuecker, P., Collins, C. A., Schindler, S., Neumann, D. M., de Grandi, S., Cruddace, R., Chincarini, G., Edge, A. C., Shaver, P. A., et al. 1999: *The REFLEX cluster survey: observing strategy and first results on large-scale structure.*, The Messenger, 95, 27
- Guzzo, L., Schuecker, P., Böhringer, H., Collins, C. A., Ortiz-Gil, A., de Grandi, S., Edge, A. C., Neumann, D. M., Schindler, S., Altucci, C., & Shaver, P. A. 2009: *The REFLEX galaxy cluster survey. VIII. Spectroscopic observations and optical atlas.*, A&A, 499, 357
- Haarsma, D. B., Leisman, L., Donahue, M., Bruch, S., Böhringer, H., Croston, J. H., Pratt, G. W., Voit, G. M., Arnaud, M., & Pierini, D. 2010: *Brightest Cluster Galaxies and Core Gas Density in REXCESS Clusters*, ApJ, 713, 1037
- Haiman, Z., Mohr, J. J., & Holder, G. P. 2001: *Constraints on Cosmological Parameters from Future Galaxy Cluster Surveys*, ApJ, 553, 545
- Hamuy, M., Maza, J., Phillips, M. M., Suntzeff, N. B., Wischnjewsky, M., Smith, R. C., Antezana, R., Wells, L. A., Gonzalez, L. E., Gigoux, P., Navarrete, M., et al. 1993: *The 1990 Calan/Tololo Supernova Search*, AJ, 106, 2392
- Hansen, S. M., McKay, T. A., Wechsler, R. H., Annis, J., Sheldon, E. S., & Kimball, A. 2005: *Measurement of Galaxy Cluster Sizes, Radial Profiles, and Luminosity Functions from SDSS Photometric Data*, ApJ, 633, 122

- Hansen, S. M., Sheldon, E. S., Wechsler, R. H., & Koester, B. P. 2009: *The Galaxy Content of SDSS Clusters and Groups*, ApJ, 699, 1333
- Herschel, W. 1785: *On the Construction of the Heavens.*, Royal Society of London Philosophical Transactions Series I, 75, 213
- High, F. W., Hoekstra, H., Leethochawalit, N., de Haan, T., Abramson, L., Aird, K. A., Armstrong, R., Ashby, M. L. N., Bautz, M., Bayliss, M., Bazin, G., et al. 2012: *Weak-Lensing Mass Measurements of Five Galaxy Clusters in the South Pole Telescope Survey Using Magellan/Megacam*, ApJ, 758, 68
- High, F. W., Stalder, B., Song, J., Ade, P. A. R., Aird, K. A., Allam, S. S., Armstrong, R., Barkhouse, W. A., Benson, B. A., Bertin, E., Bhattacharya, S., et al. 2010: *Optical Redshift and Richness Estimates for Galaxy Clusters Selected with the Sunyaev-Zel'dovich Effect from 2008 South Pole Telescope Observations*, ApJ, 723, 1736
- High, F. W., Stubbs, C. W., Rest, A., Stalder, B., & Challis, P. 2009: *Stellar Locus Regression: Accurate Color Calibration and the Real-Time Determination of Galaxy Cluster Photometric Redshifts*, AJ, 138, 110
- Holden, B. P., Stanford, S. A., Eisenhardt, P., & Dickinson, M. 2004: *Evolution in the Color-Magnitude Relation of Early-Type Galaxies in Clusters of Galaxies at  $z \sim 1$* , AJ, 127, 2484
- Holder, G., Haiman, Z., & Mohr, J. J. 2001: *Constraints on  $\Omega_M$ ,  $\Omega_\Lambda$ , and  $\sigma_8$  from Galaxy Cluster Redshift Distributions*, ApJ, 560, L111
- Hu, W. 2003: *Self-consistency and calibration of cluster number count surveys for dark energy*, Phys. Rev. D, 67, 081304
- Hubble, E. 1929: *A Relation between Distance and Radial Velocity among Extra-Galactic Nebulae*, Contributions from the Mount Wilson Observatory, vol. 3, pp.23-28, 3, 23
- Jannuzi, B. T. & Dey, A. 1999: *The NOAO Deep Wide-Field Survey*, in ASP Conf. Ser. 191: Photometric Redshifts and the Detection of High Redshift Galaxies, 111–+
- Johnston, D. E., Sheldon, E. S., Wechsler, R. H., Rozo, E., Koester, B. P., Frieman, J. A., McKay, T. A., Evrard, A. E., Becker, M. R., & Annis, J. 2007: *Cross-correlation Weak Lensing of SDSS galaxy Clusters II: Cluster Density Profiles and the Mass–Richness Relation*, ArXiv e-prints
- Katayama, H., Hayashida, K., Takahara, F., & Fujita, Y. 2003: *Properties of the Brightest Cluster Galaxy and Its Host Cluster*, ApJ, 585, 687
- Kelson, D. D. 2003: *Optimal Techniques in Two-dimensional Spectroscopy: Background Subtraction for the 21st Century*, PASP, 115, 688
- Kodama, T. & Bower, R. G. 2001: *Reconstructing the history of star formation in rich cluster cores*, MNRAS, 321, 18
- Koester, B. P., McKay, T. A., Annis, J., Wechsler, R. H., Evrard, A., Bleem, L., Becker, M., Johnston, D., Sheldon, E., Nichol, R., Miller, C., et al. 2007: *A MaxBCG Catalog of 13,823 Galaxy Clusters from the Sloan Digital Sky Survey*, ApJ, 660, 239

- Komatsu, E., Smith, K. M., Dunkley, J., Bennett, C. L., Gold, B., Hinshaw, G., Jarosik, N., Larson, D., Nolte, M. R., Page, L., Spergel, D. N., et al. 2011: *Seven-year Wilkinson Microwave Anisotropy Probe (WMAP) Observations: Cosmological Interpretation*, ApJS, 192, 18
- Kravtsov, A. V., Vikhlinin, A., & Nagai, D. 2006: *A New Robust Low-Scatter X-Ray Mass Indicator for Clusters of Galaxies*, ApJ, 650, 128
- Kurtz, M. J. & Mink, D. J. 1998: *RVSAO 2.0: Digital Redshifts and Radial Velocities*, PASP, 110, 934
- Lemaître, G. 1931: *Expansion of the universe, A homogeneous universe of constant mass and increasing radius accounting for the radial velocity of extra-galactic nebulae*, MNRAS, 91, 483
- Lewis, A., Challinor, A., & Lasenby, A. 2000: *Efficient Computation of Cosmic Microwave Background Anisotropies in Closed Friedmann-Robertson-Walker Models*, ApJ, 538, 473
- Lima, M. & Hu, W. 2005: *Self-calibration of cluster dark energy studies: Observable-mass distribution*, Phys. Rev. D, 72, 043006
- Lima, M. & Hu, W. 2007: *Photometric redshift requirements for self-calibration of cluster dark energy studies*, Phys. Rev. D, 76, 123013
- Limber, D. N. 1959: *Effects of Intracuster Gas and Duct upon the Virial Theorem.*, ApJ, 130, 414
- Lin, Y., Mohr, J. J., Gonzalez, A. H., & Stanford, S. A. 2006: *Evolution of the K-Band Galaxy Cluster Luminosity Function and Scaling Relations*, ApJ, 650, L99
- Lin, Y., Mohr, J. J., & Stanford, S. A. 2003: *Near-Infrared Properties of Galaxy Clusters: Luminosity as a Binding Mass Predictor and the State of Cluster Baryons*, ApJ, 591, 749
- Lin, Y., Mohr, J. J., & Stanford, S. A. 2004: *K-Band Properties of Galaxy Clusters and Groups: Luminosity Function, Radial Distribution, and Halo Occupation Number*, ApJ, 610, 745
- Lin, Y.-T. & Mohr, J. J. 2004: *K-band Properties of Galaxy Clusters and Groups: Brightest Cluster Galaxies and Intracuster Light*, ApJ, 617, 879
- Lloyd-Davies, E. J., Romer, A. K., Mehrrens, N., Hosmer, M., Davidson, M., Sabirli, K., Mann, R. G., Hilton, M., Liddle, A. R., Viana, P. T. P., Campbell, H. C., et al. 2011: *The XMM Cluster Survey: X-ray analysis methodology*, MNRAS, 418, 14
- Loh, Y., Ellingson, E., Yee, H. K. C., Gilbank, D. G., Gladders, M. D., & Barrientos, L. F. 2008: *The Color Bimodality in Galaxy Clusters since  $z \sim 0.9$* , ApJ, 680, 214
- Lopes, P. A. A., Ribeiro, A. L. B., & Rembold, S. B. 2013: *NoSOCS in SDSS. IV. The Role of Environment Beyond the Extent of Galaxy Clusters*, ArXiv e-prints
- López-Cruz, O., Barkhouse, W. A., & Yee, H. K. C. 2004: *The Color-Magnitude Effect in Early-Type Cluster Galaxies*, ApJ, 614, 679

- Lucey, J. R. 1983: *An assessment of the completeness and correctness of the Abell catalogue*, MNRAS, 204, 33
- Majumdar, S. & Mohr, J. J. 2003: *Importance of Cluster Structural Evolution in Using X-Ray and Sunyaev-Zeldovich Effect Galaxy Cluster Surveys to Study Dark Energy*, ApJ, 585, 603
- Majumdar, S. & Mohr, J. J. 2004: *Self-Calibration in Cluster Studies of Dark Energy: Combining the Cluster Redshift Distribution, the Power Spectrum, and Mass Measurements*, ApJ, 613, 41
- Mancone, C. L., Baker, T., Gonzalez, A. H., Ashby, M. L. N., Stanford, S. A., Brodwin, M., Eisenhardt, P. R. M., Snyder, G., Stern, D., & Wright, E. L. 2012: *The Faint End of the Cluster-galaxy Luminosity Function at High Redshift*, ApJ, 761, 141
- Mancone, C. L. & Gonzalez, A. H. 2012: *EzGal: A Flexible Interface for Stellar Population Synthesis Models*, PASP, 124, 606
- Mancone, C. L., Gonzalez, A. H., Brodwin, M., Stanford, S. A., Eisenhardt, P. R. M., Stern, D., & Jones, C. 2010: *The Formation of Massive Cluster Galaxies*, ApJ, 720, 284
- Mann, A. W. & Ebeling, H. 2012: *X-ray-optical classification of cluster mergers and the evolution of the cluster merger fraction*, MNRAS, 420, 2120
- Mantz, A., Allen, S. W., Ebeling, H., & Rapetti, D. 2008: *New constraints on dark energy from the observed growth of the most X-ray luminous galaxy clusters*, MNRAS, 387, 1179
- Mantz, A., Allen, S. W., Rapetti, D., & Ebeling, H. 2010: *The observed growth of massive galaxy clusters - I. Statistical methods and cosmological constraints*, MNRAS, 406, 1759
- Margoniner, V. E. & de Carvalho, R. R. 2000: *Photometric Properties of 48 Clusters of Galaxies. I. The Butcher-Oemler Effect*, AJ, 119, 1562
- Marinoni, C. & Hudson, M. J. 2002: *The Mass-to-Light Function of Virialized Systems and the Relationship between Their Optical and X-Ray Properties*, ApJ, 569, 101
- Marriage, T. A., Acquaviva, V., Ade, P. A. R., Aguirre, P., Amiri, M., Appel, J. W., Barrientos, L. F., Battistelli, E. S., Bond, J. R., Brown, B., Burger, B., et al. 2011: *The Atacama Cosmology Telescope: Sunyaev-Zel'dovich-Selected Galaxy Clusters at 148 GHz in the 2008 Survey*, ApJ, 737, 61
- McDonald, M., Bayliss, M., Benson, B. A., Foley, R. J., Ruel, J., Sullivan, P., Veilleux, S., Aird, K. A., Ashby, M. L. N., Bautz, M., Bazin, G., et al. 2012a: *A Massive, Cooling-Flow-Induced Starburst in the Core of a Highly Luminous Galaxy Cluster*, Nature, 488, 349
- McDonald, M., Benson, B., Veilleux, S., Bautz, M. W., & Reichardt, C. L. 2012b: *An HST/WFC3-UVIS View of the Starburst in the Cool Core of the Phoenix Cluster*, ArXiv e-prints
- McDonald, M., Benson, B. A., Vikhlinin, A., Stalder, B., Bleem, L. E., de Haan, T., Lin, H. W., Aird, K. A., Ashby, M. L. N., Bautz, M. W., Bayliss, M., et al. 2013: *The Growth of Cool Cores and Evolution of Cooling Properties in a Sample of 83 Galaxy Clusters at  $0.3 < z < 1.2$  Selected from the SPT-SZ Survey*, ApJ, 774, 23

- McInnes, R. N., Menanteau, F., Heavens, A. F., Hughes, J. P., Jimenez, R., Massey, R., Simon, P., & Taylor, A. 2009: *First lensing measurements of SZ-detected clusters*, MNRAS, 399, L84
- McKellar, A. 1941: *Molecular Lines from the Lowest States of Diatomic Molecules Composed of Atoms Probably Present in Interstellar Space*, Publications of the Dominion Astrophysical Observatory Victoria, 7, 251
- McLeod, B. A., Gauron, T. M., Geary, J. C., Ordway, M. P., & Roll, J. B. 1998: *Megacam: paving the focal plane of the MMT with silicon*, in Society of Photo-Optical Instrumentation Engineers (SPIE) Conference Series, Vol. 3355, Society of Photo-Optical Instrumentation Engineers (SPIE) Conference Series, ed. S. D’Odorico, 477–486
- Melin, J.-B., Bartlett, J. G., & Delabrouille, J. 2006: *Catalog extraction in SZ cluster surveys: a matched filter approach*, A&A, 459, 341
- Menanteau, F., Hughes, J. P., Jimenez, R., Hernandez-Monteagudo, C., Verde, L., Kosowsky, A., Moodley, K., Infante, L., & Roche, N. 2009: *Southern Cosmology Survey. I. Optical Cluster Detections and Predictions for the Southern Common-Area Millimeter-Wave Experiments*, ApJ, 698, 1221
- Messier, C. 1781: *Catalogue des Nébuleuses & des amas d’Étoiles (Catalog of Nebulae and Star Clusters)*, Tech. rep.
- Miknaitis, G., Pignata, G., Rest, A., Wood-Vasey, W. M., Blondin, S., Challis, P., Smith, R. C., Stubbs, C. W., Suntzeff, N. B., Foley, R. J., Matheson, T., et al. 2007: *The ESSENCE Supernova Survey: Survey Optimization, Observations, and Supernova Photometry*, ApJ, 666, 674
- Mohr, J. J., Adams, D., Barkhouse, W., Beldica, C., Bertin, E., Cai, Y. D., da Costa, L. A. N., Darnell, J. A., Daues, G. E., Jarvis, M., Gower, M., et al. 2008: *The Dark Energy Survey data management system*, in Society of Photo-Optical Instrumentation Engineers (SPIE) Conference Series, Vol. 7016, Society of Photo-Optical Instrumentation Engineers (SPIE) Conference Series
- Molnar, S. M., Haiman, Z., Birkinshaw, M., & Mushotzky, R. F. 2004: *Constraints on the Energy Content of the Universe from a Combination of Galaxy Cluster Observables*, ApJ, 601, 22
- Mortonson, M. J., Hu, W., & Huterer, D. 2011: *Simultaneous falsification of  $\Lambda$ CDM and quintessence with massive, distant clusters*, Phys. Rev. D, 83, 023015
- Murante, G., Giovalli, M., Gerhard, O., Arnaboldi, M., Borgani, S., & Dolag, K. 2007: *The importance of mergers for the origin of intracluster stars in cosmological simulations of galaxy clusters*, MNRAS, 377, 2
- Muzzin, A., Wilson, G., Lacy, M., Yee, H. K. C., & Stanford, S. A. 2008: *The Evolution of Dusty Star Formation and Stellar Mass Assembly in Clusters: Results from the IRAC 3.6, 4.5, 5.8, and 8.0  $\mu$ m Cluster Luminosity Functions*, ApJ, 686, 966

- Muzzin, A., Wilson, G., Yee, H. K. C., Hoekstra, H., Gilbank, D., Surace, J., Lacy, M., Blindert, K., Majumdar, S., Demarco, R., Gardner, J. P., et al. 2009: *Spectroscopic Confirmation of Two Massive Red-Sequence-Selected Galaxy Clusters at  $z \sim 1.2$  in the SpARCS-North Cluster Survey*, ApJ, 698, 1934
- Muzzin, A., Yee, H. K. C., Hall, P. B., Ellingson, E., & Lin, H. 2007a: *Near-Infrared Properties of Moderate-Redshift Galaxy Clusters: Luminosity Functions and Density Profiles*, ApJ, 659, 1106
- Muzzin, A., Yee, H. K. C., Hall, P. B., & Lin, H. 2007b: *Near-Infrared Properties of Moderate-Redshift Galaxy Clusters. II. Halo Occupation Number, Mass-to-Light Ratios, and  $\Omega_m$* , ApJ, 663, 150
- Nagai, D. & Kravtsov, A. V. 2005: *The Radial Distribution of Galaxies in  $\Lambda$  Cold Dark Matter Clusters*, ApJ, 618, 557
- Nagai, D., Kravtsov, A. V., & Vikhlinin, A. 2007: *Effects of Galaxy Formation on Thermodynamics of the Intracluster Medium*, ApJ, 668, 1
- Navarro, J. F., Frenk, C. S., & White, S. D. M. 1997: *A Universal Density Profile from Hierarchical Clustering*, ApJ, 490, 493
- Newberry, M. V., Kirshner, R. P., & Boroson, T. A. 1988: *Spectra of galaxies in clusters. I - The Butcher-Oemler effect*, ApJ, 335, 629
- Ngeow, C., Mohr, J. J., Alam, T., Barkhouse, W. A., Beldica, C., Cai, D., Daues, G., Plante, R., Annis, J., Lin, H., Tucker, D., et al. 2006: *Cyber-infrastructure to support science and data management for the Dark Energy Survey*, in Society of Photo-Optical Instrumentation Engineers (SPIE) Conference Series, Vol. 6270, Society of Photo-Optical Instrumentation Engineers (SPIE) Conference Series
- Oemler, Jr., A. 1974: *The Systematic Properties of Clusters of Galaxies. Photometry of 15 Clusters*, ApJ, 194, 1
- Osip, D. J., Floyd, D., & Covarrubias, R. 2008: *Instrumentation at the Magellan Telescopes 2008*, in Society of Photo-Optical Instrumentation Engineers (SPIE) Conference Series, Vol. 7014, Society of Photo-Optical Instrumentation Engineers (SPIE) Conference Series
- Pacaud, F., Pierre, M., Adami, C., Altieri, B., Andreon, S., Chiappetti, L., Detal, A., Duc, P.-A., Galaz, G., Gueguen, A., Le Fèvre, J.-P., et al. 2007: *The XMM-LSS survey: the Class 1 cluster sample over the initial  $5 \text{ deg}^2$  and its cosmological modelling*, MNRAS, 382, 1289
- Paolillo, M., Andreon, S., Longo, G., Puddu, E., Gal, R. R., Scaramella, R., Djorgovski, S. G., & de Carvalho, R. 2001: *Luminosity function of clusters of galaxies*, A&A, 367, 59
- Papovich, C. 2008: *The Angular Clustering of Distant Galaxy Clusters*, ApJ, 676, 206
- Peebles, P. J. E. & Yu, J. T. 1970: *Primeval Adiabatic Perturbation in an Expanding Universe*, ApJ, 162, 815

- Penzias, A. A. & Wilson, R. W. 1965: *A Measurement of Excess Antenna Temperature at 4080 Mc/s.*, ApJ, 142, 419
- Percival, W. J., Cole, S., Eisenstein, D. J., Nichol, R. C., Peacock, J. A., Pope, A. C., & Szalay, A. S. 2007: *Measuring the Baryon Acoustic Oscillation scale using the Sloan Digital Sky Survey and 2dF Galaxy Redshift Survey*, MNRAS, 381, 1053
- Perlmutter, S., Aldering, G., Goldhaber, G., Knop, R. A., Nugent, P., Castro, P. G., Deustua, S., Fabbro, S., Goobar, A., Groom, D. E., Hook, I. M., et al. 1999: *Measurements of Omega and Lambda from 42 High-Redshift Supernovae*, ApJ, 517, 565
- Phillips, M. M. 1993: *The absolute magnitudes of Type IA supernovae*, ApJ, 413, L105
- Pickles, A. J. 1998: *A Stellar Spectral Flux Library: 1150-25000 Å*, PASP, 110, 863
- Piranomonte, S., Longo, G., Andreon, S., Puddu, E., Paolillo, M., Scaramella, R., Gal, R., & Djorgovski, S. G. 2001: *The Luminosity Function of 80 Abell Clusters from the CRONaRio Catalogs*, in Astronomical Society of the Pacific Conference Series, Vol. 225, Virtual Observatories of the Future, ed. R. J. Brunner, S. G. Djorgovski, & A. S. Szalay, 73–+
- Planck Collaboration, Ade, P. A. R., Aghanim, N., Argüeso, F., Arnaud, M., Ashdown, M., Aumont, J., Baccigalupi, C., Balbi, A., Banday, A. J., & et al. 2011a: *Planck early results. XIII. Statistical properties of extragalactic radio sources in the Planck Early Release Compact Source Catalogue*, A&A, 536, A13
- Planck Collaboration, Ade, P. A. R., Aghanim, N., Armitage-Caplan, C., Arnaud, M., Ashdown, M., Atrio-Barandela, F., Aumont, J., Baccigalupi, C., Banday, A. J., & et al. 2013: *Planck 2013 results. XVI. Cosmological parameters*, ArXiv e-prints
- Planck Collaboration, Ade, P. A. R., Aghanim, N., Arnaud, M., Ashdown, M., Aumont, J., Baccigalupi, C., Balbi, A., Banday, A. J., Barreiro, R. B., & et al. 2011b: *Planck early results. VIII. The all-sky early Sunyaev-Zeldovich cluster sample*, A&A, 536, A8
- Planck Collaboration, Aghanim, N., Arnaud, M., Ashdown, M., Aumont, J., Baccigalupi, C., Balbi, A., Banday, A. J., Barreiro, R. B., Bartelmann, M., & et al. 2011c: *Planck early results. IX. XMM-Newton follow-up for validation of Planck cluster candidates*, A&A, 536, A9
- Poggianti, B. M., Bridges, T. J., Mobasher, B., Carter, D., Doi, M., Iye, M., Kashikawa, N., Komiyama, Y., Okamura, S., Sekiguchi, M., Shimasaku, K., et al. 2001: *A Photometric and Spectroscopic Study of Dwarf and Giant Galaxies in the Coma Cluster. III. Spectral Ages and Metallicities*, ApJ, 562, 689
- Popesso, P., Biviano, A., Böhringer, H., & Romaniello, M. 2007a: *RASS-SDSS galaxy cluster survey. VII. On the cluster mass-to-light ratio and the halo occupation distribution*, A&A, 464, 451
- Popesso, P., Biviano, A., Romaniello, M., & Böhringer, H. 2007b: *RASS-SDSS galaxy cluster survey. VI. The dependence of the cluster SFR on the cluster global properties*, A&A, 461, 411

- Popesso, P., Böhringer, H., Romaniello, M., & Voges, W. 2005: *RASS-SDSS galaxy cluster survey. II. A unified picture of the cluster luminosity function*, A&A, 433, 415
- Press, W. & Schechter, P. 1974: *Formation of Galaxies and Clusters of Galaxies by Self-Similar Gravitational Condensation*, ApJ, 187, 425
- Press, W. H., Teukolsky, S. A., Vetterling, W. T., & Flannery, B. P. 1992, Numerical recipes in C. The art of scientific computing, ed. Press, W. H., Teukolsky, S. A., Vetterling, W. T., & Flannery, B. P. (Cambridge: University Press, —c1992, 2nd ed.)
- Rakos, K. D. & Schombert, J. M. 1995: *Color evolution from  $Z = 0$  to  $Z = 1$* , ApJ, 439, 47
- Reaves, G. 1966: *Dwarf Galaxies in the Coma Cluster*, PASP, 78, 407
- Reichardt, C. L., Stalder, B., Bleem, L. E., Montroy, T. E., Aird, K. A., Andersson, K., Armstrong, R., Ashby, M. L. N., Bautz, M., Bayliss, M., Bazin, G., et al. 2013: *Galaxy Clusters Discovered via the Sunyaev-Zel'dovich Effect in the First 720 Square Degrees of the South Pole Telescope Survey*, ApJ, 763, 127
- Rest, A., Stubbs, C., Becker, A. C., Miknaitis, G. A., Miceli, A., Covarrubias, R., Hawley, S. L., Smith, R. C., Suntzeff, N. B., Olsen, K., Prieto, J. L., et al. 2005: *Testing LMC Microlensing Scenarios: The Discrimination Power of the SuperMACHO Microlensing Survey*, ApJ, 634, 1103
- Reyes, R., Mandelbaum, R., Hirata, C., Bahcall, N., & Seljak, U. 2008: *Improved optical mass tracer for galaxy clusters calibrated using weak lensing measurements*, MNRAS, 390, 1157
- Ribeiro, A. L. B., Lopes, P. A. A., & Rembold, S. B. 2013: *NoSOCS in SDSS. III. The interplay between galaxy evolution and the dynamical state of galaxy clusters*, A&A, 556, A74
- Riess, A. G., Filippenko, A. V., Challis, P., Clocchiattia, A., Diercks, A., Garnavich, P. M., Gilliland, R. L., Hogan, C. J., Jha, S., Kirshner, R. P., Leibundgut, B., et al. 1998: *Observational Evidence from Supernovae for an Accelerating Universe and a Cosmological Constant*, AJ, 116, 1009
- Rines, K., Geller, M. J., Diaferio, A., Kurtz, M. J., & Jarrett, T. H. 2004: *CAIRNS: The Cluster and Infall Region Nearby Survey. II. Environmental Dependence of Infrared Mass-to-Light Ratios*, AJ, 128, 1078
- Roberts, M. S. 1969: *Integral Properties of Spiral and Irregular Galaxies*, AJ, 74, 859
- Robertson, H. P. 1933: *Relativistic Cosmology*, Reviews of Modern Physics, 5, 62
- Romeo, A. D., Portinari, L., & Sommer-Larsen, J. 2005: *Simulating galaxy clusters - II. Global star formation histories and the galaxy populations*, MNRAS, 361, 983
- Roncarelli, M., Pointecouteau, E., Giard, M., Montier, L., & Pello, R. 2010: *Infrared properties of the SDSS-maxBCG galaxy clusters*, A&A, 512, A20+
- Rood, H. J. 1969: *Luminosity Function and Color-Magnitude Diagram of Galaxies in a Central Zone of the Coma Cluster*, ApJ, 158, 657



- Rood, H. J. & Abell, G. O. 1973: *Luminosity Functions of Clusters of Galaxies*, *Astrophys. Lett.*, 13, 69
- Rood, H. J. & Turnrose, B. E. 1968: *The Distribution of Galaxies Near the Center of the Coma Cluster*, *ApJ*, 152, 1057
- Rubin, V. C. & Ford, Jr., W. K. 1970: *Rotation of the Andromeda Nebula from a Spectroscopic Survey of Emission Regions*, *ApJ*, 159, 379
- Rudnick, G., von der Linden, A., Pelló, R., Aragón-Salamanca, A., Marchesini, D., Clowe, D., De Lucia, G., Halliday, C., Jablonka, P., Milvang-Jensen, B., Poggianti, B., et al. 2009: *The Rest-frame Optical Luminosity Function of Cluster Galaxies at  $z < 0.8$  and the Assembly of the Cluster Red Sequence*, *ApJ*, 700, 1559
- Rudnick, G. H., Tran, K.-V., Papovich, C., Momcheva, I., & Willmer, C. 2012: *A Tale of Dwarfs and Giants: Using a  $z = 1.62$  Cluster to Understand How the Red Sequence Grew over the Last 9.5 Billion Years*, *ApJ*, 755, 14
- Ruel et al. 2012: *Optical Spectroscopy and Velocity Dispersions of South Pole Telescope Clusters*, In Preparation
- Sánchez, A. G., Scóccola, C. G., Ross, A. J., Percival, W., Manera, M., Montesano, F., Mazzei, X., Cuesta, A. J., Eisenstein, D. J., Kazin, E., McBride, C. K., et al. 2012: *The clustering of galaxies in the SDSS-III Baryon Oscillation Spectroscopic Survey: cosmological implications of the large-scale two-point correlation function*, *MNRAS*, 425, 415
- Sanderson, A. J. R., Edge, A. C., & Smith, G. P. 2009: *LoCuSS: the connection between brightest cluster galaxy activity, gas cooling and dynamical disturbance of X-ray cluster cores*, *MNRAS*, 398, 1698
- Saro, A., Borgani, S., Tornatore, L., Dolag, K., Murante, G., Biviano, A., Calura, F., & Charlot, S. 2006: *Properties of the galaxy population in hydrodynamical simulations of clusters*, *MNRAS*, 373, 397
- Saro, A., Mohr, J. J., Bazin, G., & Dolag, K. 2013: *Toward Unbiased Galaxy Cluster Masses from Line-of-sight Velocity Dispersions*, *ApJ*, 772, 47
- Sayers, J., Czakon, N. G., Bridge, C., Golwala, S. R., Koch, P. M., Lin, K.-Y., Molnar, S. M., & Umetsu, K. 2012: *Bolocam Observations of Two Unconfirmed Galaxy Cluster Candidates from the Planck Early Sunyaev-Zel'dovich Sample*, *ApJ*, 749, L15
- Schechter, P. 1976: *An analytic expression for the luminosity function for galaxies.*, *ApJ*, 203, 297
- Schirmer, M. 2013: *THELI – Convenient reduction of any optical, near- and mid-infrared imaging data*, ArXiv e-prints
- Schmidt, B. P., Suntzeff, N. B., Phillips, M. M., Schommer, R. A., Clocchiatti, A., Kirshner, R. P., Garnavich, P., Challis, P., Leibundgut, B., Spyromilio, J., Riess, A. G., et al. 1998: *The High-Z Supernova Search: Measuring Cosmic Deceleration and Global Curvature of the Universe Using Type Ia Supernovae*, *ApJ*, 507, 46

- Seielstad, G. A. & Whiteoak, J. B. 1965: *An Interferometric Investigation of the Neutral Hydrogen in Galaxies.*, ApJ, 142, 616
- Seljak, U. 2000: *Analytic model for galaxy and dark matter clustering*, MNRAS, 318, 203
- Seljak, U. & Zaldarriaga, M. 1996: *A Line-of-Sight Integration Approach to Cosmic Microwave Background Anisotropies*, ApJ, 469, 437
- Semler, D. R., Šuhada, R., Aird, K. A., Ashby, M. L. N., Bautz, M., Bayliss, M., Bazin, G., Bocquet, S., Benson, B. A., Bleem, L. E., Brodwin, M., et al. 2012: *High-redshift Cool-core Galaxy Clusters Detected via the Sunyaev-Zel'dovich Effect in the South Pole Telescope Survey*, ApJ, 761, 183
- Shirokoff, E., Reichardt, C. L., Shaw, L., Millea, M., Ade, P. A. R., Aird, K. A., Benson, B. A., Bleem, L. E., Carlstrom, J. E., Chang, C. L., Cho, H. M., et al. 2011: *Improved Constraints on Cosmic Microwave Background Secondary Anisotropies from the Complete 2008 South Pole Telescope Data*, ApJ, 736, 61
- Sifon, C., Menanteau, F., Hasselfield, M., Marriage, T. A., Hughes, J. P., Barrientos, L. F., Gonzalez, J., Infante, L., Addison, G. E., Baker, A. J., Battaglia, N., et al. 2012: *The Atacama Cosmology Telescope: Dynamical Masses and Scaling Relations for a Sample of Massive Sunyaev-Zel'dovich Effect Selected Galaxy Clusters*, ArXiv e-prints
- Skrutskie, M. F., Cutri, R. M., Stiening, R., Weinberg, M. D., Schneider, S., Carpenter, J. M., Beichman, C., Capps, R., Chester, T., Elias, J., Huchra, J., et al. 2006: *The Two Micron All Sky Survey (2MASS)*, AJ, 131, 1163
- Slipher, V. M. 1913: *The radial velocity of the Andromeda Nebula*, Lowell Observatory Bulletin, 2, 56
- Smail, I., Edge, A. C., Ellis, R. S., & Blandford, R. D. 1998: *A statistical analysis of the galaxy populations of distant luminous X-ray clusters*, MNRAS, 293, 124
- Smoot, G. F. et al. 1992: *Structure in the COBE Differential Microwave Radiometer First-Year Maps*, ApJ, 396, L1
- Solinger, A. B. & Tucker, W. H. 1972: *Relationship Between X-Ray Luminosity and Velocity Dispersion in Clusters of Galaxies*, ApJ, 175, L107
- Song, J., Mohr, J. J., Barkhouse, W. A., Warren, M. S., & Rude, C. 2012a: *A Parametrized Galaxy Catalog Simulator For Testing Cluster Finding, Mass Estimation and Photometric Redshift Estimation in Optical and Near Infrared Surveys*, ApJ, 747, 58
- Song, J., Zenteno, A., Stalder, B., Desai, S., Bleem, L. E., Aird, K. A., Armstrong, R., Ashby, M. L. N., Bayliss, M., Bazin, G., Benson, B. A., et al. 2012b: *Redshifts, Sample Purity, and BCG Positions for the Galaxy Cluster Catalog from the First 720 Square Degrees of the South Pole Telescope Survey*, ApJ, 761, 22
- Stalder, B., Ruel, J., Šuhada, R., Brodwin, M., Aird, K. A., Andersson, K., Armstrong, R., Ashby, M. L. N., Bautz, M., Bayliss, M., Bazin, G., et al. 2013: *SPT-CL J0205-5829: A  $z = 1.32$  Evolved Massive Galaxy Cluster in the South Pole Telescope Sunyaev-Zel'dovich Effect Survey*, ApJ, 763, 93

- Stanford, S. A., Brodwin, M., Gonzalez, A. H., Zeimann, G., Stern, D., Dey, A., Eisenhardt, P. R., Snyder, G. F., & Mancone, C. 2012: *IDCS J1426.5+3508: Discovery of a Massive, Infrared-selected Galaxy Cluster at  $z = 1.75$* , ApJ, 753, 164
- Stanford, S. A., Eisenhardt, P. R., Brodwin, M., Gonzalez, A. H., Stern, D., Jannuzi, B. T., Dey, A., Brown, M. J. I., McKenzie, E., & Elston, R. 2005: *An IR-selected Galaxy Cluster at  $z = 1.41$* , ApJ, 634, L129
- Stanford, S. A., Elston, R., Eisenhardt, P. R., Spinrad, H., Stern, D., & Dey, A. 1997: *An IR-Selected Galaxy Cluster at  $\zeta=1.27$* , AJ, 114, 2232
- Staniszewski, Z., Ade, P. A. R., Aird, K. A., Benson, B. A., Bleem, L. E., Carlstrom, J. E., Chang, C. L., Cho, H.-M., Crawford, T. M., Crites, A. T., de Haan, T., et al. 2009: *Galaxy Clusters Discovered with a Sunyaev-Zel'dovich Effect Survey*, ApJ, 701, 32
- Stern, D., Eisenhardt, P., Gorjian, V., Kochanek, C. S., Caldwell, N., Eisenstein, D., Brodwin, M., Brown, M. J. I., Cool, R., Dey, A., Green, P., et al. 2005: *Mid-Infrared Selection of Active Galaxies*, ApJ, 631, 163
- Story, K., Aird, K. A., Andersson, K., Armstrong, R., Bazin, G., Benson, B. A., Bleem, L. E., Bonamente, M., Brodwin, M., Carlstrom, J. E., Chang, C. L., et al. 2011: *South Pole Telescope Detections of the Previously Unconfirmed Planck Early Sunyaev-Zel'dovich Clusters in the Southern Hemisphere*, ApJ, 735, L36+
- Stott, J. P., Collins, C. A., Sahlén, M., Hilton, M., Lloyd-Davies, E., Capozzi, D., Hosmer, M., Liddle, A. R., Mehrrens, N., Miller, C. J., Romer, A. K., et al. 2010: *The XMM Cluster Survey: The Build-up of Stellar Mass in Brightest Cluster Galaxies at High Redshift*, ApJ, 718, 23
- Stott, J. P., Hickox, R. C., Edge, A. C., Collins, C. A., Hilton, M., Harrison, C. D., Romer, A. K., Rooney, P. J., Kay, S. T., Miller, C. J., Sahlén, M., et al. 2012: *The XMM Cluster Survey: the interplay between the brightest cluster galaxy and the intracluster medium via AGN feedback*, MNRAS, 422, 2213
- Stott, J. P., Smail, I., Edge, A. C., Ebeling, H., Smith, G. P., Kneib, J.-P., & Pimbblet, K. A. 2007: *An Increase in the Faint Red Galaxy Population in Massive Clusters since  $z \sim 0.5$* , ApJ, 661, 95
- Stromberg, G. 1925: *Analysis of radial velocities of globular clusters and non-galactic nebulae.*, ApJ, 61, 353
- Struble, M. F. & Rood, H. J. 1999: *A Compilation of Redshifts and Velocity Dispersions for ACO Clusters*, ApJS, 125, 35
- Sunyaev, R. A. & Zel'dovich, Y. B. 1970: *The Spectrum of Primordial Radiation, its Distortions and their Significance*, Comments on Astrophysics and Space Physics, 2, 66
- Sunyaev, R. A. & Zel'dovich, Y. B. 1972: *The Observations of Relic Radiation as a Test of the Nature of X-Ray Radiation from the Clusters of Galaxies*, Comments on Astrophysics and Space Physics, 4, 173
- Sutherland, W. 1988: *The 3-D distribution of Abell clusters*, MNRAS, 234, 159

- Szalay, A. S., Connolly, A. J., & Szokoly, G. P. 1999: *Simultaneous Multicolor Detection of Faint Galaxies in the Hubble Deep Field*, AJ, 117, 68
- Tanaka, M., Kodama, T., Arimoto, N., Okamura, S., Umetsu, K., Shimasaku, K., Tanaka, I., & Yamada, T. 2005: *The build-up of the colour-magnitude relation as a function of environment*, MNRAS, 362, 268
- Tinker, J., Kravtsov, A. V., Klypin, A., Abazajian, K., Warren, M., Yepes, G., Gottlöber, S., & Holz, D. E. 2008: *Toward a Halo Mass Function for Precision Cosmology: The Limits of Universality*, ApJ, 688, 709
- Tisserand, P., Le Guillou, L., Afonso, C., Albert, J. N., Andersen, J., Ansari, R., Aubourg, É., Bareyre, P., Beaulieu, J. P., Charlot, X., Coutures, C., et al. 2007: *Limits on the Macho content of the Galactic Halo from the EROS-2 Survey of the Magellanic Clouds*, A&A, 469, 387
- Toft, S., Mainieri, V., Rosati, P., Lidman, C., Demarco, R., Nonino, M., & Stanford, S. A. 2004:  *$K_s$ -band luminosity function of the  $z = 1.237$  cluster of galaxies  $j$ ASTROBJ $j$ RDCS J1252.9-2927 $j$ /ASTROBJ $j$* , A&A, 422, 29
- Tran, K.-V. H., Franx, M., Illingworth, G. D., van Dokkum, P., Kelson, D. D., Blakeslee, J. P., & Postman, M. 2007: *A Keck Spectroscopic Survey of MS 1054-03 ( $z = 0.83$ ): Forming the Red Sequence*, ApJ, 661, 750
- Udalski, A., Kubiak, M., & Szymanski, M. 1997: *Optical Gravitational Lensing Experiment. OGLE-2 – the Second Phase of the OGLE Project*, ACTAA, 47, 319
- Urquhart, S. A., Willis, J. P., Hoekstra, H., & Pierre, M. 2010: *An environmental Butcher-Oemler effect in intermediate redshift X-ray clusters*, ArXiv e-prints
- Šuhada, R., Song, J., Böhringer, H., Mohr, J. J., Chon, G., Finoguenov, A., Fassbender, R., Desai, S., Armstrong, R., Zenteno, A., Barkhouse, W. A., et al. 2012: *The XMM-BCS galaxy cluster survey. I. The X-ray selected cluster catalog from the initial 6 deg<sup>2</sup>*, A&A, 537, A39
- van Breukelen, C., Clewley, L., Bonfield, D. G., Rawlings, S., Jarvis, M. J., Barr, J. M., Foucaud, S., Almaini, O., Cirasuolo, M., Dalton, G., Dunlop, J. S., et al. 2006: *Galaxy clusters at  $0.6 < z < 1.4$  in the UKIDSS Ultra Deep Survey Early Data Release*, MNRAS, 373, L26
- Vanderlinde, K., Crawford, T. M., de Haan, T., Dudley, J. P., Shaw, L., Ade, P. A. R., Aird, K. A., Benson, B. A., Bleem, L. E., Brodwin, M., Carlstrom, J. E., et al. 2010: *Galaxy Clusters Selected with the Sunyaev-Zel'dovich Effect from 2008 South Pole Telescope Observations*, ApJ, 722, 1180
- Verdugo, M., Lerchster, M., Böhringer, H., Hildebrandt, H., Ziegler, B. L., Erben, T., Finoguenov, A., & Chon, G. 2012: *The Cosmic Web and galaxy evolution around the most luminous X-ray cluster: RX J1347.5-1145*, MNRAS, 421, 1949

- Vieira, J. D., Crawford, T. M., Switzer, E. R., Ade, P. A. R., Aird, K. A., Ashby, M. L. N., Benson, B. A., Bleem, L. E., Brodwin, M., Carlstrom, J. E., Chang, C. L., et al. 2010: *Extragalactic Millimeter-wave Sources in South Pole Telescope Survey Data: Source Counts, Catalog, and Statistics for an 87 Square-degree Field*, ApJ, 719, 763
- Vikhlinin, A., Kravtsov, A. V., Burenin, R. A., Ebeling, H., Forman, W. R., Hornstrup, A., Jones, C., Murray, S. S., Nagai, D., Quintana, H., & Voevodkin, A. 2009: *Chandra Cluster Cosmology Project III: Cosmological Parameter Constraints*, ApJ, 692, 1060
- Vikhlinin, A., McNamara, B. R., Forman, W., Jones, C., Quintana, H., & Hornstrup, A. 1998: *A Catalog of 200 Galaxy Clusters Serendipitously Detected in the ROSAT PSPC Pointed Observations*, ApJ, 502, 558
- Visvanathan, N. & Sandage, A. 1977: *The color-absolute magnitude relation for E and S0 galaxies. I - Calibration and tests for universality using Virgo and eight other nearby clusters*, ApJ, 216, 214
- Voges, W., Aschenbach, B., Boller, T., Bräuninger, H., Briel, U., Burkert, W., Dennerl, K., Englhauser, J., Gruber, R., Haberl, F., Hartner, G., et al. 1999: *The ROSAT all-sky survey bright source catalogue*, A&A, 349, 389
- Voges, W., Aschenbach, B., Boller, T., Brauninger, H., Briel, U., Burkert, W., Dennerl, K., Englhauser, J., Gruber, R., Haberl, F., Hartner, G., et al. 2000: *ROSAT All-Sky Survey Faint Source Catalog (Voges+ 2000)*, VizieR Online Data Catalog, 9029, 0
- Wang, L. & Steinhardt, P. J. 1998: *Cluster Abundance Constraints for Cosmological Models with a Time-varying, Spatially Inhomogeneous Energy Component with Negative Pressure*, ApJ, 508, 483
- Wang, S., Khoury, J., Haiman, Z., & May, M. 2004: *Constraining the evolution of dark energy with a combination of galaxy cluster observables*, Phys. Rev. D, 70, 123008
- Werner, M. W., Roellig, T. L., Low, F. J., Rieke, G. H., Rieke, M., Hoffmann, W. F., Young, E., Houck, J. R., Brandl, B., Fazio, G. G., Hora, J. L., et al. 2004: *The Spitzer Space Telescope Mission*, ApJS, 154, 1
- White, S. D. M., Efstathiou, G., & Frenk, C. S. 1993: *The amplitude of mass fluctuations in the universe*, MNRAS, 262, 1023
- Williamson, R., Benson, B. A., High, F. W., Vanderlinde, K., Ade, P. A. R., Aird, K. A., Andersson, K., Armstrong, R., Ashby, M. L. N., Bautz, M., Bazin, G., et al. 2011: *A Sunyaev-Zel'dovich-selected Sample of the Most Massive Galaxy Clusters in the 2500 deg<sup>2</sup> South Pole Telescope Survey*, ApJ, 738, 139
- Wright, E. L., Eisenhardt, P. R. M., Mainzer, A. K., Ressler, M. E., Cutri, R. M., Jarrett, T., Kirkpatrick, J. D., Padgett, D., McMillan, R. S., Skrutskie, M., Stanford, S. A., et al. 2010: *The Wide-field Infrared Survey Explorer (WISE): Mission Description and Initial On-orbit Performance*, AJ, 140, 1868
- Zenteno, A., Song, J., Desai, S., Armstrong, R., Mohr, J. J., Ngeow, C.-C., Barkhouse, W. A., Allam, S. S., Andersson, K., Bazin, G., Benson, B. A., et al. 2011: *A Multiband Study of the*

- Galaxy Populations of the First Four Sunyaev-Zel'dovich Effect Selected Galaxy Clusters*, ApJ, 734, 3
- Zhang, Y.-Y., Böhringer, H., Finoguenov, A., Ikebe, Y., Matsushita, K., Schuecker, P., Guzzo, L., & Collins, C. A. 2006: *X-ray properties in massive galaxy clusters: XMM-Newton observations of the REFLEX-DXL sample*, A&A, 456, 55
- Zheng, Z. & Weinberg, D. H. 2007: *Breaking the Degeneracies between Cosmology and Galaxy Bias*, ApJ, 659, 1
- Zwicky, F. 1933: *Die Rotverschiebung von extragalaktischen Nebeln*, Helvetica Physica Acta, 6, 110
- Zwicky, F. 1951: *The Coma Cluster of Galaxies*, PASP, 63, 61
- Zwicky, F. 1952: *Luminous Intergalactic Matter*, PASP, 64, 242
- Zwicky, F., Herzog, E., & Wild, P. 1968, Catalogue of galaxies and of clusters of galaxies
- Zwicky, I. F. 1942: *On the Clustering of Nebulae.*, ApJ, 95, 555

# Acknowledgments

I want express my deepest gratitude to my supervisor Joseph Mohr for his efforts in trying to get the best out of me, making me a better scientist. Without his time, advise and everlasting funding this thesis would have never been written.

I also want to thank George Hau and Brooke Gregory who were fundamental in achieving my dream.

I want to express my gratitude to colleage and friends which are part of our group and collaborations and whom friendships makes the long working hours more amenable.

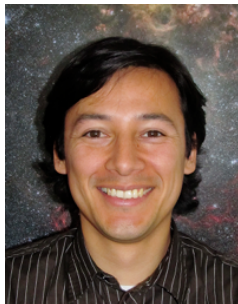
As in anything worthwhile doing there were difficult moments. I am blessed to have friends and family, people who loved me and supported me in such times. Thank you. Among them, my special gratitude is for my girlfriend Rhea-Silvia Remus. Her love has been like a permanent light that shined ever more in such moments.

For the other 99.73% of the time I thank to the same people which are too many to name, plus everybody else who is part of USM and as such contribute to a great atmosphere.





# Curriculum vitae



ALFREDO ANDRÉS ZENTENO VIVANCO  
VOLKARTSTRASSE 75, D-80636,  
MUNICH, GERMANY  
ALFREDO@USM.LMU.DE  
TEL: +49-89-2180-5982

---

## EDUCATION

### Present

**2009-** PhD. student at Ludwig-Maximilians-Universität (LMU), Advisor: Prof. Joseph Mohr.

### Past

**2009** Master of Science at the University of Illinois at Urbana-Champaign (UoI), Illinois, USA. Advisor: Prof. Joseph Mohr.

**2001** Licenciatura en Física, Pontificia Universidad Católica de Chile (PUC). Thesis: Hadron-quarks phase transition in Neutron Stars.

## OBSERVATIONAL EXPERIENCE

**2003-** Over 100 nights of experience on the 4 m Victor Blanco telescope using instruments such as Mosaic II, NEWFIRM and ISPI.

Additional telescopes for which I have acquired experience are the CTIO 0.9 m, ESO-MPG 2.2m (WFI), ESO 3.58 m NTT (EFOSC2), SOAR 4.1 m (SOI) and the 6.5 m Magellan Baade (IMACS; imaging and spectroscopy) telescopes.

## RESEARCH EXPERIENCE

### Present

**2009-** Research assistant at the LMU/Excellence Cluster studying the optical properties and photometric redshifts of SZ selected clusters of galaxies. Supervisor: Prof. Joseph Mohr.

### Past

**2007-09** Research assistant at UoI for the Blanco Cosmology Survey studying the optical properties of SZ selected clusters of galaxies.

**2006-07** Research assistant at the Cerro Tololo Inter-American Observatory (CTIO) for the Magellanic Cloud Emission Line Survey (MCELS).

**2004-06** Research assistant in CTIO for the “Equation of State: SupErNovae trace Cosmic Expansion” (ESSENCE) project. Among other responsibilities this involved observing and

programing observations for supernovae (SNe) in the 0.9-m and 4-m telescopes, reduction and photometric calibration of the data obtained and the creation of SNe light curves.

**2004-06** Research assistant in CTIO for the SuperMACHO project. It involved observations for the project and helping with data processing.

**2004** Research assistant at CTIO. I worked on developing an Integration Time Calculator for a future 30-m Giant Segmented Mirror Telescope (GMST).

**2003-04** Research assistant at CTIO. Study of the three-dimensional geometry of the Large Magellanic Cloud (LMC) using data from the 4-m Mosaic and ISPI instruments.

**2001-02** Independent collaboration with Dr. George Hau measuring the dynamics of the Shell galaxies using the spectroscopic data collected by the Anglo-Australian Telescope characterizing the dynamical behavior of a sample of 9 shell galaxies.

## TEACHING EXPERIENCE AND PUBLIC OUTREACH

**2012** Participation in the Universität Sternwarte München *Maus Tag* open day for children, showing the biggest telescopes in the world.

**2007-08** Teaching assistant for ASTRO100, basic astronomy for freshmen at UofI.

**2007** Teaching assistant for ASTRO350, introduction to cosmology, UofI.

**2001** Laboratory and teaching assistant of Electricity and Magnetism course at the PUC.

**1996-2000** Teaching assistant of Modern Physics, Intermediate Mechanics and Electromagnetism Theory. Laboratory assistant of Heat and Thermodynamics and Classical Mechanics at the PUC.

## TALKS

**Nov 2012** Optical follow up of South Pole Telescope SZ selected clusters, University of La Serena, La Serena, Chile.

**Oct 2011** Galaxy population in SPT selected galaxy clusters, ESO Chile.

**Oct 2011** Galaxy population in SPT selected galaxy clusters, PUC Chile.

**Feb 2010** Galaxy population of the first four SPT selected galaxy clusters, MPE, Garching, Germany.

**Jan 2010** Optical properties of the first four SZ-selected clusters by the SPT telescope, Ringberg Castle, Bavaria, Germany.

## AWARDS AND SCHOLARSHIPS

**1995** MINEDUC (Ministry of Education) Scholarship (90% of the university fees).

**1994** First place in communal painting, organized by the ministry of education and the municipality.

## POSITIONS OF RESPONSIBILITY

**1997 - 99** President of the Physics and Astronomy student association, PUC.

## WORKSHOPS

**2013** Conference “The Physical Link between Galaxies and their Halos” at Garching, Munich, Germany.

**2012** Dark Energy Survey International Collaboration Meeting at Garching, Munich, Germany.

**2010** Conference “Galaxy Clusters: Observations, Physics and Cosmology” at Garching, Munich, Germany.

**2010** Dark Energy Survey International Collaboration Meeting at the CIEMAT, Madrid, Spain, .

**2010** “Workshop on Gravitational Lensing, Large Scale Structure And Galaxy Evolution” at Ringberg, Bavaria, Germany.

**2008** “Great Lakes Cosmology Workshop”, Carnegie Mellon University, Pittsburgh, Pennsylvania, USA.

**2007** American Astronomical Society. Presenting the poster : “Planetary Nebulae in the Large Magellanic Cloud: Results from MCELS”, Seattle, Washington, USA.

**2004** 2004 IAOC International workshop “The Cool Universe: Observing Cosmic Dawn” in Valparaiso, Chile.

**2000** Summer congress of high energy physics in Valdivia, Chile.

## LANGUAGE SKILL

I am a native Spanish speaker and I am proficient in English. I have an A1 level in German.

## COMPUTING EXPERIENCE

I work intensively with PERL. I also use IRAF, IDL, Python, C, SQL, HTML and PHP4.

## EXTRACURRICULAR ACTIVITIES

I like to practice sports and organize and play soccer games in particular.

## REFEREED PUBLICATIONS

Number of refereed papers: 31. Total citations: 2476. H-index : 18.

### First author papers

**Zenteno, A;** (24 co-authors) 2011: *A Multiband Study of the Galaxy Populations of the First Four Sunyaev-Zel’dovich Effect Selected Galaxy Clusters*. ApJ, 734, 3

### Second author papers

Song, J.; **Zenteno, A;** (75 co-authors) 2012: *Redshifts, Sample Purity, and BCG Positions for the Galaxy Cluster Catalog from the first 720 Square Degrees of the South Pole Telescope Survey*. ApJ, 761, 22S

**Remaining Refereed publications**

- Ruel, J.; (80 co-authors) **Zenteno, A.** 2013: *Optical Spectroscopy and Velocity Dispersions of Galaxy Clusters from the SPT-SZ Survey*. arXiv:1311.4953
- Grüen, D.; (9 co-authors) **Zenteno, A.** 2013: *Weak lensing analysis of RXC J2248.7-4431*. MNRAS, 432, 1455
- Benson, B. A.; (74 co-authors) **Zenteno, A.** 2013: *Cosmological Constraints from Sunyaev-Zel'dovich-Selected Clusters with X-ray Observations in the First 178 Square Degrees of the South Pole Telescope Survey*. ApJ, 763, 147B
- Reichardt, C. L.; (78 co-authors); **Zenteno, A.** 2013: *Galaxy clusters discovered via the Sunyaev-Zel'dovich effect in the first 720 square degrees of the South Pole Telescope survey*. ApJ, 763, 127R
- Stalder, B.; (81 co-authors) **Zenteno, A.** 2013: *SPT-CL J0205-5829: A  $z = 1.32$  evolved massive galaxy cluster in the south pole telescope Sunyaev-Zel'dovich effect survey*. ApJ, 763, 93
- Semler, D. R.; (77 co-authors); **Zenteno, A.** 2012: *High-Redshift Cool-Core Galaxy Clusters Detected via the Sunyaev-Zel'dovich Effect in the South Pole Telescope Survey*. ApJ, 761, 183S
- High, F. W.; (84 co-authors); **Zenteno, A.** 2012: *Weak-Lensing Mass Measurements of Five Galaxy Clusters in the South Pole Telescope Survey Using Magellan/Megacam*. ApJ, 758, 68H
- Desai, S.; (18 co-authors); **Zenteno, A.** 2012: *The Blanco Cosmology Survey: Data Acquisition, Processing, Calibration, Quality Diagnostics and Data Release*. ApJ, 757, 83D
- McDonald, M.; (84 co-authors); **Zenteno, A.** 2012: *A massive, cooling-flow-induced starburst in the core of a luminous cluster of galaxies*. Nature, 488, 349
- Desai, S.; (22 co-authors); **Zenteno, A.** 2012: *Optical followup of galaxy clusters detected by the South Pole Telescope*. 2012JPhCS.375c2011D
- Suhada, R.; (8 co-authors) ; **Zenteno, A.**; (12 co-authors) 2012: *The XMM-BCS galaxy cluster survey. I. The X-ray selected cluster catalog from the initial 6 deg<sup>2</sup>*. A&A 537, 39
- Buckley-Geer, E. J.; (18 co-authors); **Zenteno, A.** 2011: *The Serendipitous Observation of a Gravitationally Lensed Galaxy at  $z = 0.9057$  from the Blanco Cosmology Survey: The Elliot Arc*. ApJ, 742, 48.
- Williamson, R.; (73 co-authors) **Zenteno, A.** 2011: *An SZ-selected sample of the most massive galaxy clusters in the 2500-square-degree South Pole Telescope survey*. ApJ, 738, 139
- Andersson, K.; (61 co-authors) **Zenteno, A.** 2011: *X-Ray Properties of the First Sunyaev-Zel'dovich Effect Selected Galaxy Cluster Sample from the South Pole Telescope*. ApJ, 738, 48
- Story, K.; (61 co-authors); **Zenteno, A.** 2011: *South Pole Telescope Detections of the Previously Unconfirmed Planck Early Sunyaev-Zel'dovich Clusters in the Southern Hemisphere*. ApJ, 735, L36+
- Foley, R. J.; (71 co-authors); **Zenteno, A.** 2011: *Discovery and Cosmological Implications of SPT-CL J2106-5844, the Most Massive Known Cluster at  $z > 1$* . ApJ, 731, 86
- Rest, A.; (26 co-authors); **Zenteno, A.**; (9 co-authors) 2011: *Pushing the Boundaries of Conventional Core-Collapse Supernovae: The Extremely Energetic Supernova SN 2003ma*. ApJ, 729, 88
- High, F. W.; (69 co-authors); **Zenteno, A.** 2011: *Optical Redshift and Richness Estimates for Galaxy Clusters Selected with the Sunyaev-Zel'dovich Effect from 2008 South Pole Telescope*

- Observations*. ApJ, 723, 1736
- Vanderlinde, K.; (57 co-authors); **Zenteno, A.** 2010: *Galaxy Clusters Selected with the Sunyaev-Zel'dovich Effect from 2008 South Pole Telescope Observations*. ApJ, 722, 1180
- Brodwin, M.; (65 co-authors); **Zenteno, A.** 2010: *SPT-CL J0546-5345: A Massive  $z > 1$  Galaxy Cluster Selected Via the Sunyaev-Zel'dovich Effect with the South Pole Telescope*. ApJ, 721, 90
- Vieira, J. D.; (53 co-authors); **Zenteno, A.** 2010: *Extragalactic Millimeter-wave Sources in South Pole Telescope Survey Data: Source Counts, Catalog, and Statistics for an 87 Square-degree Field*. ApJ, 719, 763
- Staniszewski, Z.; (42 co-authors); **Zenteno, A.** 2009: *Galaxy clusters discovered with a Sunyaev-Zel'dovich effect survey*. ApJ, 701, 32
- Foley, Ryan J.; (28 co-authors); **Zenteno, A.** 2008: *Constraining Cosmic Evolution of Type Ia Supernovae*. ApJ, 684, 68
- Blondin, S.; (30 co-authors); **Zenteno, A.** 2008: *Time Dilation in Type Ia Supernova Spectra at High Redshift*. ApJ, 682, 724
- Becker, A. C.; (37 co-authors); **Zenteno, A.** 2008: *Exploring the Outer Solar System with the ESSENCE Supernova Survey*. ApJ, 682, L53
- Rest, A.; (14 co-authors); **Zenteno, A.**; (13 co-authors) 2008: *Spectral Identification of an Ancient Supernova Using Light Echoes in the Large Magellanic Cloud*. ApJ, 680, 1137
- Davis, T. M.; (26 co-authors); **Zenteno, A.** 2007: *Scrutinizing Exotic Cosmological Models Using ESSENCE Supernova Data Combined with Other Cosmological Probes*. ApJ, 666, 716
- Wood-Vasey, W. M.; (35 co-authors); **Zenteno, A.** 2007: *Observational Constraints on the Nature of Dark Energy: First Cosmological Results from the ESSENCE Supernova Survey*. ApJ, 666, 694
- Miknaitis, G.; (34 co-authors); **Zenteno, A.** 2007: *The ESSENCE Supernova Survey: Survey Optimization, Observations, and Supernova Photometry*. ApJ, 666, 674

